IMPACT OF CHEMICAL STATES ON THE EFFECTIVE WORK FUNCTION OF METAL GATE AND HIGH-K DIELECTRIC MATERIALS ON NOVEL HETEROSTRUCTURES

A Dissertation

by

MARY RACHEL COAN

Submitted to the Office of Graduate Studies of
Texas A&M University
in partial fulfillment of the requirements for the degree of

DOCTOR OF PHILOSOPHY

August 2012

Major Subject: Chemical Engineering

Impact of Chemical States on the Effective Work Function of Metal Gate and High-κ Dielectric Materials on Novel Heterostructures

Copyright 2012 Mary Rachel Coan

IMPACT OF CHEMICAL STATES ON THE EFFECTIVE WORK FUNCTION OF METAL GATE AND HIGH-K DIELECTRIC MATERIALS ON NOVEL HETEROSTRUCTURES

A Dissertation

by

MARY RACHEL COAN

Submitted to the Office of Graduate Studies of
Texas A&M University
in partial fulfillment of the requirements for the degree of

DOCTOR OF PHILOSOPHY

Approved by:

Co-Chairs of Committee,	Harlan Rusty Harris
	Jorge M. Seminario
Committee Member,	Zhengdong Cheng
	Fred Strieter
Head of Department,	Charles Glover

August 2012

Major Subject: Chemical Engineering

ABSTRACT

Impact of Chemical States on the Effective Work Function of Metal Gate and High-κ Dielectric Materials on Novel Heterostructures. (August 2012)

Mary Rachel Coan, B.S., University of Rochester

Co-Chairs of Advisory Committee: Dr. Harlan Rusty Harris
Dr. Jorge M. Seminario

An experimental and theoretical approach is taken to determine the effect of a heterojunction on the effective work function in a metal/high-κ gate stack, the characteristics of aqueous hydrochloric acid cleaned (aq-HCl) GaN surface and the interface between GaN and Al_2O_3, HfO_2 and GaON. The investigation of the effect of a heterojunction on the effective work function in a metal/high-κ gate stack found that when a Ge/Si heterostructure on silicon is lightly doped and sufficiently thin, the work function can be extracted in a manner similar to that for a simple silicon substrate. Modifications to the terraced oxide structure are proposed to remove oxidation effects of the alternate channel materials. The extracted work function of TiN with various thicknesses on HfSiO is found to be in agreement with that of TiN on a silicon substrate. X-ray and ultraviolet photoelectron spectroscopy are used to observe the interface electronic states at the GaN (0001) and Al_2O_3, HfO_2 and GaON dielectric interfaces. The GaN is cleaned using aqueous HCl prior to thermal oxidation to form GaON and atomic layer deposition of Al_2O_3 and HfO_2. This was followed by a post deposition anneal. The GaN/HfO_2 and GaN/Al_2O_3 interfaces exhibited dipoles of 1.6 eV and 0.4 eV ± 0.2 eV, respectively. It is determined that the formation of an interfacial layer at the GaN/HfO_2 interface is the primary cause of the larger dipole. Due to the knowledge of the formation of an interfacial GaO_x or GaON layer during atomic layer deposition of HfO_2, a better understanding of the GaN/GaON interface is needed. To accomplish this task, the interface electronic states at the GaN(0001) and GaON interface are observed using X-ray and ultraviolet photoelectron spectroscopy (XPS and UPS). XPS and UPS analysis of the GaN/GaON interface resulted in the calculation of a -2.7 eV ± 0.2 eV

dipole assuming that the core level shifts are only representative of the GaN band bending at the interface. If it is assumed that the core level shifts are only due to the oxidation of GaN, then the exhibited dipole at the GaN/GaON interface is -1.8 eV ± 0.2 eV. Results indicate that the observed dipole is primarily caused by the polarization of the GaN. A theoretical approach is taken to provide a more complete understanding of the underlying formation mechanisms of a GaON interfacial layer during atomic layer deposition of HfO_2. First, density functional theory is used to calculate the interactions of oxygen and water with the Ga-face of GaN clusters. The GaN clusters could be used as testbeds for the actual Ga-face on GaN crystals of importance in electronics. The results reveal that the local spin plays an important role in these interactions. It is found that the most stable interactions of O_2 and the GaN clusters results in the complete dissociation of the O_2 molecule to form two Ga-O-Ga bonds, while the most stable interactions between a H_2O molecule and the GaN clusters are the complete dissociation of one of the O-H bonds to form a Ga-O-H bond and a Ga-H bond. Second, density functional theory is used to calculate the interaction of the reactants used to deposit HfO_2 and Al_2O_3 during atomic layer deposition with hydrolyzed Ga-face GaN clusters. The results suggest that while further research is needed in this area to grasp a better understanding of the interactions of Trimethylaluminum (TMA) or Tertrakis(EthylMethylAmino)Hafnium (TEMAH) with hydrolyzed GaN clusters, it is found that a Ga-N(CH_3)(CH_2CH_3) bond can form during the deposition of HfO_2 using ALD and TEMAH as the reactant without breaking the Hf-N bond. The formation of a Ga-N(CH_3)(CH_2CH_3) bond is significant because with the introduction of water into the system, the methyl and ethylmethyl groups may react to form a Ga-N-O bond which is believed to be the interfacial oxide found during deposition of HfO_2 using ALD on GaN. No Ga-C bond structure formed in any fully optimized stable structure when analyzing the interaction of TMA with hydrolyzed GaN.

DEDICATION

To my marvelous parents, and all of my astounding sisters, I share this achievement with you, and dedicating it to you is not enough to thank you for all your unconditional love, encouragement and support. You have given me my strength, courage and understanding. Without you, I do not know where I would be today. Thank you for everything.

ACKNOWLEDGEMENTS

I would like to thank my committee members, Dr. Cheng and Dr. Strieter, for their guidance and support throughout the course of this research, and for their time and effort in being members of my committee.

I thank Dr. Harris and Dr. Seminario, who have been a great support for me during these years. I would like them to know that the time that I have been under their direction and tutelage has been a wonderful learning experience. Thank you for nourishing my creativity, for patiently teaching me how to be a researcher, to seek excellence, to be productive and systematic. I hope to apply their teachings throughout my career and life.

Thank you to my friends and colleagues of the Molecular Engineering group and Harris Integrated Photonic and Electronics Laboratory (HIPER Lab), smart, great and valuable people. I would like to show my gratitude to those supporting the Henry F. Taylor Nanofabrication Facility Institute of Solid State Electronics and Electro-optics especially to Robert Atkins, Jim Gardner, and Denny Spears. I want to extend my gratitude to the agencies supporting this research, the U.S. Army Research Office, the U.S. Defense Threat Reduction Agency (DTRA) and NSF.

Thanks to the Chemical Engineering Program Coordinator, Towanna Arnold, for all the help and support during these years, and to the Chemical Engineering Department faculty and staff for making my time at Texas A&M University a great experience.

To my family, whom I miss beyond explanation, I wish to thank each of you for the gifts you have given to me, from my father I carry the courage and strength to know who I am, from my mother I carry patience and understanding, from my sisters I carry the ability to adapt, to learn from those around me, and what unconditional love truly is.

To my le to‘alua, thank you for listening to me and guiding me these last few years. You have given me the strength to continue on when no one else could, thank you.

Thank you to my New York friends and my newfound friends in Texas and in Florida, without your help this dissertation would not have been written, and without your company, help and encouragement my time in Texas and Florida would have been difficult. Thank you for everything you have done for me.

NOMENCLATURE

III-V	Column three – Column five of the periodic table materials
III-N	Column three of the periodic table – Nitrogen materials
2DEG	Two-Dimensional Electron Gas
ACM	Alternate Channel Materials
ALD	Atomic Layer Deposition
aq-HCl	Aqueous Hydrochloric Acid
BE	Binding Energy
CMOS	Complementary-symmetry Metal-Oxide-Semiconductor
C-V	Capacitance – Voltage Plot
DC	Direct Current
DFT	Density Functional Theory
E-mode	Enhancement mode
EOT	Effective Oxide Thickness
EWF	Effective Work Function
GGA	Generalized Gradient Approximation
HEMT	High Electron Mobility Transistor
High-κ	High dielectric constant compared to silicon dioxide
HJ	Heterojunction
hν	photon energy, h = Planck constant and ν = frequency of the radiation
KE	Kinetic Energy
MOH	Metal Oxide Heterojunction
MOS	Metal Oxide Semiconductor
MOSFET	Metal Oxide Semiconductor Field Effect Transistor
NMOS	n-type Metal Oxide Semiconductor
PMOS	p-type Metal Oxide Semiconductor
RF	Radio Frequency
TEM	Transmission Electron Microscopy

TEMAH	Tertrakis(EthylMethylAmino)Hafnium
TMA	Trimethylaluminium
UPS	Ultraviolet Photoelectron Spectroscopy
UV	Ultra-Violet
VBM	Valance Band Maxima
V_{fb}	Flat band Voltage
V_{th}	Threshold Voltage
WF	Work Function
XPS	X-Ray Photoelectron Spectroscopy

TABLE OF CONTENTS

Page

ABSTRACT iii

DEDICATION v

ACKNOWLEDGEMENTS vi

NOMENCLATURE viii

TABLE OF CONTENTS x

LIST OF FIGURES xii

LIST OF TABLES xxi

CHAPTER I INTRODUCTION 1

1.1 Motivation and Goals 3
1.2 Background 6
1.2.1 Work Function Tuning of Si Based Devices 8
1.2.2 Work Function Tuning of III-V Based Devices 9
1.3 Significance 10
1.4 Summary and Outline 12

CHAPTER II IMPACT OF CHEMICAL STATES ON THE EFFECTIVE WORK FUNCTION – AN EXPERIMENTAL AND THEORETICAL APPROACH 15

2.1 Introduction to the Polarization of GaN 16
2.2 Experimental Techniques 20
2.2.1 Atomic Layer Deposition 20
2.2.2 Photoemission Spectroscopy 24
2.2.3 Transmission Electron Microscopy 32
2.3 Theoretical Techniques 33
2.3.1 Sentaurus Device 33
2.3.2 *Ab initio* Molecular Orbital Theory 34
2.3.3 Basis Sets 35
2.3.4 Density Functional Theory 36
2.3.5 Hybrid Methods 36

CHAPTER III INTEGRATION OF HETEROJUNCTIONS INTO EFFECTIVE WORK FUNCTION CALCULATION 37

3.1 Introduction 37
3.2 Theoretical Equations 39
3.3 Experiment Methodology 42
3.4 Results and Discussion 43

3.5 Summary and Conclusions ... 50
3.6 Acknowledgements ... 50

CHAPTER IV BAND OFFSET MEASUREMENTS OF THE GaN/DIELECTRIC INTERFACES ... 51

4.1 Introduction ... 51
4.2 Experimental Methodology ... 52
4.3 Results and Discussion ... 55
4.4 Conclusions ... 64
4.5 Acknowledgements ... 65

CHAPTER V BAND-OFFSET MEASUREMENTS OF THE GaN/GaON INTERFACE ... 66

5.1 Introduction ... 66
5.2 Experimental Methodology ... 67
5.3 Results and Discussion ... 70
5.4 Conclusion ... 82
5.5 Acknowledgements ... 83

CHAPTER VI AB INITIO ANALYSIS OF THE INTERACTIONS OF GaN CLUSTERS WITH OXYGEN AND WATER ... 84

6.1 Introduction ... 84
6.2 Methodology ... 86
6.3 Results and Discussion ... 87
6.3.1 Testbeds ... 87
6.3.2 Oxidation of GaN Clusters Using Oxygen ... 88
6.3.3 Oxidation of GaN Clusters Using Water ... 99
6.4 Conclusions ... 111

CHAPTER VII AB INITIO ANALYSIS OF THE INTERACTIONS OF HYDROLYZED GaN CLUSTERS WITH ALD REACTANTS ... 113

7.1 Introduction ... 113
7.2 Methodology ... 115
7.3 Results and Discussion ... 116
7.3.1 TMA ... 116
7.3.2 TEMAH ... 132
7.4 Conclusions ... 141

CHAPTER VIII CONCLUSIONS AND FUTURE RESEARCH ... 143

REFERENCES AND NOTES ... 148

VITA ... 166

LIST OF FIGURES

Page

Fig. 1. Mobility versus Effective Oxide Thickness (EOT). Figurative representation of the required scaling due to Moore's Law including Si and Non-Si based channels. Motivation to study non-Si based materials. 4

Fig. 2. Investigation of work function tuning of high-κ/metal gate stack devices for the past 7 years. 7

Fig. 3. Figurative representations of a.) A bi-layer high-κ metal gate stack, b.) The terraced oxide method top view, c.) Terraced oxide method varying the interfacial oxide (SiO_x) thickness, d.) Terraced oxide method varying the high-k thickness all with metal gate electrodes shown. The bi-layer high-κ metal gate stack method implements ringed dielectric terraces of various thicknesses on a single substrate to minimize the effects of interfacial charges while varying the dielectric bulk charges, which in turn are limited to thickness of the dielectric. 9

Fig. 4. Motivation of Study. Figurative representation of the high impact research areas currently under development. Motivations to research the metal gate high-κ gate stack on alternate channel materials such as GaN. Enhancement-mode high-electron mobility transistors are needed for high-power applications. 11

Fig. 5. Proposed Research. A figurative representation of the proposed research of interfacial effects of heterojunctions and high-k dielectrics on the EWF calculation. 15

Fig. 6. Spontaneous Polarization of GaN. Schematics of the crystal structure of wurtzite Ga-face and N-face GaN. The spontaneous polarization (P_{sp}) direction is shown. Ga is pink (larger) and N is blue (smaller). 17

Fig. 7. Overall polarization induced sheet charge density, σ, and directions of the spontaneous and piezoelectric polarization (P_{SP} and P_{PE}) in Ga-face relaxed GaN/tensile strained AlGaN heterostructure and Ga-face compressive strained GaN/tensile strained AlGaN heterostructure. 17

Fig. 8. Figurative representation of GaN/AlGaN HEMTs with no surface states and no additional dipole at the high-κ/III-V interface showing the a) overall polarization fields and b) the 2DEG with no applied voltages. 18

Fig. 9. Figurative representation of GaN/AlGaN HEMTs with positive surface states and a positive dipole located at the high-κ/III-V interface showing the a) overall polarization fields and b) the 2DEG with no applied voltages. 19

Fig. 10. Figurative representation of GaN/AlGaN HEMTs with positive surface states and a negative dipole located at the high-κ/III-V interface showing the a) overall polarization fields and b) the 2DEG with no applied voltages. 19

Fig. 11. Atomic Layer Deposition of Al_2O_3. The sequential, self-limiting surface reactions that occur during the atomic layer deposition (ALD) of Al_2O_3 on GaN are displayed. 21

Fig. 12. Image of the Cambridge NanoTech Savannah Atomic Layer Deposition Tool, installed by the author. 22

Fig. 13. Cross-sectional TEM image of thermally annealed high-κ HfO_2 (11 nm) deposited using ALD, 100 cycle deposition, on Si/SiO_x. The ALD reactants used were water and TEMAH. 23

Fig. 14. Cross-sectional TEM image of thermally annealed high-κ Al_2O_3 (9 nm) deposited using ALD, 80 cycle deposition, on Si/SiO_x. The ALD reactants used were water and TMA. 23

Fig. 15. Photoelectron generation using an X-ray photon source during X-Ray photoelectron spectroscopy (XPS). The core electron is excited. 26

Fig. 16. Photoelectron generation in terms of the materials Fermi level when an X-Ray source is used as the photon supplier. The core electron is excited. 26

Fig. 17. Photoelectron generation using a UV photon source during ultraviolet photoelectron spectroscopy (UPS). The valence electron is excited. 27

Fig. 18. Figurative representation of Type I, Type II and Type III band alignments. 29

Fig. 19. Schematics of $HfSiO_2/SiO_2/SiGe$/p-Si stack. 39

Fig. 20. Charge schematic of $HfSiO_2/SiO_2/SiGe$/p-Si stack. The variables shown are defined in Table 2 and throughout the text. 40

Fig. 21. Schematic band diagrams of the SiGe/p-Si heterojunction with Si substrate Boron doping concentrations of (a) $1 \times 10^{15}\,cm^{-3}$ and (b) $1 \times 10^{19}\,cm^{-3}$ at $V_g = 0$ V. The depletion region is shaded..............................44

Fig. 22. Dependence of the Si and SiGe Surface Potentials on the (a) doping concentration of Si for the $TiN/HfO_2/SiO_2/SiGe$ with a SiGe thickness of 40 nm and (b) thickness of SiGe for the $TiN/HfO_2/SiO_2/SiGe$ with a doping concentration of $N_a = 1 \times 10^{15}/cm^3$ and $1 \times 10^{17}/cm^3$. All simulations were run using a HfO_2 thickness of 6 nm....................................45

Fig. 23. C-V curve corresponding to a specific EOT device with a heterojunction plotted against a simulated device with the same EOT without a heterojunction using SiGe as the substrate.....................................47

Fig. 24. Flat band voltage vs. *EOT* for effective work function extraction of devices with fixed interfacial SiO_2 layer, varying $HfSiO_2$ layers and a TiN contact thickness of (a) 3 nm and (b) 20 nm. 48

Fig. 25. XPS survey spectra of: a) aq-HCl GaN, b) GaN/Al_2O_3 after PDA, and c) GaN/HfO_2 after PDA. Some of the core level peaks are identified using a dotted line along with some Auger peaks with dotted circles.............55

Fig. 26. UPS spectra of the valence band maximum of: a) aq-HCl GaN, b) GaN/Al_2O_3 after PDA, and c) GaN/HfO_2 after PDA. (insert) UPS spectra of aq-HCl GaN showing the linear regressions used to determine the valence band maxima and the on-set of the secondary electrons..56

Fig. 27. Ga 3*d* XPS spectra for: a) aq-HCl GaN, b) GaN/Al_2O_3 after PDA, and c) GaN/HfO_2 after PDA. Peak fittings are the dotted and dashed lines, there are two or three peaks fitted to each plot...58

Fig. 28. Deduced bands for the aq-HCl cleaned GaN surface and GaN.......................58

Fig. 29. N 1*s* XPS spectra for: a) aq-HCl GaN, b) GaN/Al_2O_3 after PDA, and c) GaN/HfO_2 after PDA. Peak fittings are the dotted and dashed lines, there are three peaks fitted to each plot. 60

Fig. 30. Deduced bands for the interface between GaN and HfO_2 after PDA. The valence band offset (VBO), conduction band offset (CBO), band bending, and interface dipole (Δ) are represented. 61

Fig. 31. Cross-sectional TEM image of high-κ HfO_2 (9 nm) deposited using ALD on aq-HCl cleaned GaN grown on Si, an interfacial GaON or

GaON with Hf layer (2.5nm) is formed during deposition of HfO_2. No post deposition anneal was done. 62

Fig. 32. Deduced bands for the interface between GaN and Al_2O_3 after a post deposition anneal. The valence band offset (VBO), conduction band offset (CBO), band bending, and interface dipole (Δ) are represented. 64

Fig. 33. XPS survey spectra of: a) aq-HCl GaN and b) GaN/GaON. Some of the core level peaks are identified using a dotted line along with Ga Auger peaks with the dotted circle. 69

Fig. 34. Cross-sectional TEM image of GaON (3 nm) thermally grown on aq-HCl cleaned GaN grown on Si. No post deposition anneal was done. 71

Fig. 35. UPS spectra of aq-HCl GaN (GaN) and GaN/GaON (GaON). 72

Fig. 36. UPS spectra of the valence band maximum of aq-HCl GaN (GaN) and GaN/GaON (GaON). 73

Fig. 37. Ga 3*d* XPS spectra for: a) aq-HCl GaN and b) GaN/GaON. Peak fittings are the dotted and dashed lines, there are two or three peaks fitted to each plot. 75

Fig. 38. Reprint of Fig. 28 from Chapter V for the readers review. Deduced bands for the aq-HCl cleaned GaN surface and GaN. 76

Fig. 39. N 1*s* XPS spectra for: a) aq-HCl GaN and b) GaN/GaON. Peak fittings are the dotted and dashed lines, there are three or four peaks fitted to each plot. 78

Fig. 40. Deduced bands for the interface between GaN and GaON assuming all core level shifts are due to changes in bonding. The valence band offset (VBO), conduction band offset (CBO), band bending, and interface dipole (Δ) are represented. 79

Fig. 41. Deduced bands for the interface between GaN and GaON* assuming all core level shifts are due to band bending at the interface in the GaN. The valence band offset (VBO), conduction band offset (CBO), band bending, and interface dipole (Δ) are represented. 80

Fig. 42. Possible mechanisms behind the negative dipole at the GaN/GaON. Spontaneous and piezoelectric polarization, P_{SP} and P_{PE}, in the GaON and GaN resulting in an overall negative dipole, σ, at the GaN/GaON interface and Ga vacancies in the GaON, +. 81

Fig. 43. Top and side views of the optimized GaN clusters used as surface reactive centers (testbeds) of a GaN surface (without H atoms) (a) Ga-centered, (b) N-centered, and (c) Hollow-centered. Ga is pink and N is Blue..88

Fig. 44. Initial and final side views of the Ga-centered GaN structures (without H atoms) with and without oxygen being introduced to the cluster. (a-b) no oxygen atoms, (c-g) single O atom, (h) two O atoms, (i) O_2, (j) O_2 within a bonds length to a single surface Ga atom, and (k-o) O_2 with both O within a bond length to a single surface Ga atom. Below each diagram is the multiplicity, the optimized geometry relative energy, the initial geometry relative energy inside parentheses, and the smallest angle O-Ga-N (where applicable). Energies are in eV. Ga is pink, N is blue, and O is red. 89

Fig. 45. Initial and final side views of the N-centered GaN clusters (H atoms not shown) with and without oxygen introduced to the cluster. (a,b) no oxygen atoms; (c-e) single O atom, (f) O_2, and (g-l) O_2 and within a bond length to a single surface Ga atom. Below each diagram is the multiplicity, , the optimized geometry relative energy, the initial geometry relative energy inside parentheses, and the smallest angle O-Ga-N (where applicable). Energies are in eV. Ga is pink, N is blue, and O is red...93

Fig. 46. Initial and final side views of the Hollow-centered GaN clusters (without H atoms) with and without oxygen being introduced to the system. (a-d) no oxygen atoms, (e-h) single O atom, (i-l) two O atoms each within a bonds length to a different surface Ga atom, (m-p) two O atoms each within a bonds length to two different surface Ga atoms, and (q-r) O_2 double bonded. Below each diagram is the multiplicity, the optimized geometry relative energy, the initial geometry relative energy inside parentheses, and the smallest angle O-Ga-N (where applicable). Energies are in eV. Ga is pink, N is blue, and O is red. 96

Fig. 47. Initial and final side views of the Ga-centered GaN clusters (with H atoms) with water or -OH being introduced to the system. (a-b) one –OH molecule within a Ga-O bonds length to the cluster, (c-e) two –OH molecules within a Ga-O bonds length to the cluster, (f-i) three –OH molecules each within a bonds length to a surface Ga atom, (j-q) one water molecule in varying rotations and distances from a surface. Below each diagram is the multiplicity, the optimized geometry relative energy, the initial geometry relative energy inside parentheses, and the smallest angle O-Ga-N (where applicable). Energies are in

eV. Ga is pink, N is blue, and O is red. Ga atom. Ga is pink, N is blue, and O is red. 100

Fig. 48. Initial and final side views of the N-centered GaN structures (with H atoms) with water or -OH being introduced to the system. (a-b) one –OH molecule within a Ga-O bond length to the cluster, (c-d) two –OH molecules within a Ga-O bond length to the cluster, (e-f) three –OH molecules each within a bond length to a surface Ga atom, (g-k) one water molecule in varying rotations and distances from a surface Ga atom. Below each diagram are the multiplicity, the optimized geometry relative energy, and the initial geometry relative energy inside parentheses, and the smallest angle O-Ga-N (where applicable). Energies are in eV. Ga is pink, N is blue, and O is red. 105

Fig. 49. Initial (top) and final (bottom) side views of the Hollow-centered GaN structures (with H atoms) with water or -OH being introduced to the system. (a-c) one –OH molecule within a Ga-O bond length to the cluster, (d-e) two –OH molecules within a Ga-O bond length to the cluster, (f-j) three –OH molecules each within a bond length to a surface Ga atom, (k-n) one water molecule in varying rotations and distances from a surface Ga atom. Below each diagram are the multiplicity, the optimized geometry relative energy, and the initial geometry relative energy inside parentheses, and the smallest angle O-Ga-N (where applicable). Energies are in eV. Ga is pink, N is blue, and O is red. 108

Fig. 50. Initial and final side views of the Ga-centered hydrolyzed (1, 2 or 3 –OH molecules bonded to the surface) GaN structures (with H atoms) with 1 or 2 TMA molecules being introduced to the system. Each figure is labeled with the name and the multiplicity of each molecule. (a)-(f) one –OH molecule bonded to the GaN surface with 1 TMA molecule introduced, (g)-(j) two –OH molecule bonded to the surface with 1 TMA molecule introduced, (k)-(n) three –OH molecule bonded to the surface with 1 TMA molecule introduced, (o)-(p) two –OH molecule bonded to the surface with 2 TMA molecules introduced, and (q)-(t) three –OH molecules bonded to the surface with 2 TMA molecules introduced. Ga is Green, N is blue, O is red, H is white, C is black, and Al is purple. RE is Relative Energy (eV) and m is the multiplicity. (F) Signifies that the geometry failed to optimize completely due to an error, (NS) signifies that the geometry has not finished optimizing, and (Osc) signifies the geometry failed to converge due to oscillations. 117

Fig. 51. Initial and final side views of the N-centered hydrolyzed (1, 2 or 3 –OH molecules bonded to the surface) GaN structures (with H atoms) with 1 or 2 TMA molecules being introduced to the system. Each figure is labeled with the name and the multiplicity of each molecule. (a) one –OH molecule bonded to the GaN surface with 1 TMA molecule introduced and (b) three –OH molecule bonded to the surface with 1 TMA molecule introduced. Ga is Green, N is blue, O is red, H is white, C is black, and Al is purple. RE is Relative Energy (eV) and m is the multiplicity. 122

Fig. 52. Initial and final side views of the Hollow-centered hydrolyzed (1, 2 or 3 –OH molecules bonded to the surface) GaN structures (with H atoms) with 1 or 2 TMA molecules being introduced to the system. Each figure is labeled with the name and the multiplicity of each molecule. (a)-(c) one –OH molecule bonded to the GaN surface with 1 TMA molecule introduced and (d) two –OH molecule bonded to the surface with 2 TMA molecules introduced. Ga is Green, N is blue, O is red, H is white, C is black, and Al is purple. RE is Relative Energy (eV) and m is the multiplicity. (Osc) signifies failure to converge due to oscillations. 124

Fig. 53. Initial and final side views of Step 2, the stability of reacted TMA on hydrolyzed GaN. Ga-centered TMA reacted GaN structures (with H atoms) with 1 or 2 Ga-O bonds and 1 or 2 O-Al bonds. Each figure is labeled with the name and the multiplicity of each molecule. (a)-(b) one Al-O-Ga bond optimized, (c)-(d) one Al-O-Ga bond and one –OH molecule bonded to the GaN surface optimized and (e)-(g) two Al-O-Ga bonds optimized. Ga is Green, N is blue, O is red, H is white, C is black, and Al is purple. RE is Relative Energy (eV) and m is the multiplicity. (NS) signifies the molecule is not stable due to a failure in convergence. 127

Fig. 54. Initial and final side views of Step 2, the stability of reacted TMA on hydrolyzed N-GaN. N-centered TMA reacted GaN structures (with H atoms) with 1 or 2 Ga-O bonds and 1 or 2 O-Al bonds. Each figure is labeled with the name and the multiplicity of each molecule. (a) one Al-O-Ga bond optimized, (b) one Al-O-Ga bond and one –OH molecule bonded to the GaN surface optimized and (c)-(d) two Al-O-Ga bonds optimized. Ga is Green, N is blue, O is red, H is white, C is black, and Al is purple. RE is Relative Energy (eV) and m is the multiplicity. 129

Fig. 55. Initial and final side views of Step 2, the stability of reacted TMA on hydrolyzed Hollow-GaN. Hollow-centered TMA reacted GaN

structures (with H atoms) with 1, 2, or 3 Ga-O bonds and 1, 2 or 3 O-Al bonds. Each figure is labeled with the name and the multiplicity of each molecule. (a) one Al-O-Ga bond optimized, (b) one Al-O-Ga bond and one –OH molecule bonded to the GaN surface optimized, (c) two Al-O-Ga bonds optimized, and (d) three Al-O-Ga bonds optimized. Ga is Green, N is blue, O is red, H is white, C is black, and Al is purple. RE is Relative Energy (eV) and m is the multiplicity. 131

Fig. 56. Initial and final side views of the Ga-centered hydrolyzed (2 or 3 –OH molecules bonded to the surface) GaN structures (with H atoms) with 1 TEMAH molecule being introduced to the system. Each figure is labeled with the name and the multiplicity of each molecule. (a) two –OH molecules bonded to the GaN surface with 1 TEMAH molecule introduced, (b)-(d) two –OH molecules bonded to the GaN surface with 1 TEMAH molecule introduced and varying H atoms being shifted, and (e) three –OH molecules bonded to the surface with 1 TEMAH molecule introduced with a N atom shifted. Ga is Green, N is blue, O is red, H is white, C is black, and Al is purple. RE is Relative Energy (eV) and m is the multiplicity. (Osc) signifies failure to converge due to oscillations and (R) signifies the molecule is still running and has not reached its final stable state. 133

Fig. 57. Initial and final side views of the Hollow-centered hydrolyzed (2 or 3 –OH molecules bonded to the surface) GaN structures (with H atoms) with 1 TEMAH molecule being introduced to the system. Each figure is labeled with the name and the multiplicity of each molecule. (a)-(b) two –OH molecules bonded to the GaN surface with 1 TEMAH molecule introduced and (c) three –OH molecules bonded to the surface with 1 TEMAH molecule introduced with a N atom shifted. Ga is Green, N is blue, O is red, H is white, C is black, and Al is purple. RE is Relative Energy (eV) and m is the multiplicity.....................135

Fig. 58. Initial and final side views of Step 2, the stability of reacted TEMAH on hydrolyzed Ga-GaN. Ga-centered TEMAH reacted GaN structures (with H atoms) with 2 or 3 Ga-O bonds and 2 O-Hf bonds. Each figure is labeled with the name and the multiplicity of each molecule. (a) one Ga-O-Hf(NCH_2CH_3)$_2$-O-Ga bond optimized and (b) one Ga-O-Hf(NCH_2CH_3)$_2$-O-Ga bond optimized and one –OH molecule bonded to the GaN surface optimized. Ga is Green, N is blue, O is red, H is white, C is black, and Al is purple. RE is Relative Energy (eV) and m is the multiplicity. 137

Fig. 59. Initial and final side views of Step 2, the stability of reacted TEMAH on hydrolyzed N-GaN. N-centered TEMAH reacted GaN structures

(with H atoms) with 2 or 3 Ga-O bonds and 2 O-Hf bonds. Each figure is labeled with the name and the multiplicity of each molecule. (a) one Ga-O-Hf(NCH_2CH_3)$_2$-O-Ga bond optimized and (b) one Ga-O-Hf(NCH_2CH_3)$_2$-O-Ga bond optimized and one –OH molecule bonded to the GaN surface optimized. Ga is Green, N is blue, O is red, H is white, C is black, and Al is purple. RE is Relative Energy (eV) and m is the multiplicity. 139

Fig. 60. Initial and final side views of Step 2, the stability of reacted TEMAH on hydrolyzed Hollow-GaN. Hollow-centered TEMAH reacted GaN structures (with H atoms) with 2 or 3 Ga-O bonds and 2 O-Hf bonds. Each figure is labeled with the name and the multiplicity of each molecule. (a)-(b) one Ga-O-Hf(NCH_2CH_3)$_2$-O-Ga bond optimized and (c) one Ga-O-Hf(NCH_2CH_3)$_2$-O-Ga bond optimized and one –OH molecule bonded to the GaN surface optimized. Ga is Green, N is blue, O is red, H is white, C is black, and Al is purple. RE is Relative Energy (eV) and m is the multiplicity. Osc signifies the system did not reach a minimum due to oscillations. 140

LIST OF TABLES

Page

Table 1. Experimental bandgap energies and electron affinities of common semiconductors and dielectrics. Values were compiled from the references next to the semiconductor names. 31

Table 2. Tabulation of charges potentially affecting the flat band voltage including the symbols used to represent the charges throughout the paper along with assumptions regarding the charges explained within the paper. 40

Table 3. Tabulation of the numerical values of the variables used in this work. The charges located at the $HfSiO_2/SiO_2$ interface, SiO_2/Si interface + permittivity of SiGe multiplied by the surface perpendicular electric field of SiGe and the extracted effective work function values using Equation (4) using different values for the intrinsic concentrations. This analysis indicates that the calculated effective work function is within 5% of the reference. 49

Table 4. UPS valence band maximum (VBM) fitting results and XPS core level fitting results for the O 1*s*, N 1*s*, Ga 3*d*, Al 2*p*, and Hf 4*f* energy levels. All XPS data has an uncertainty of ± 0.1 eV. All UPS data has an uncertainty of ± 0.1 eV. 57

Table 5. Parameters used to calculate the GaN/dielectric interface dipole, where E_g is the band gap of the surface material, E_F is the Fermi level of the sample, E_v is the valence band of the surface material, E_c is the conduction band of the surface material, χ is the electron affinity of the surface material, ΔE_{Ga3d} is the difference in the Ga 3*d* core level of the aq-HCl GaN and the sample, ΔE_{N1s} is the difference in the N 1*s* core level of the aq-HCl GaN and the sample, VBO is the valence band offset, CBO is the conduction band offset, and Δ is the dipole at the GaN/dielectric interface. 62

Table 6. UPS valence band maximum (VBM) fitting results and XPS core level fitting results for the O 1*s*, N 1*s*, and Ga 3*d* energy levels. The XPS and UPS data has an uncertainty of ± 0.1 eV. 74

Table 7. Parameters used to calculate the GaN/oxide interface dipole, where E_g is the band gap of the surface material, E_F is the Fermi level of the sample, E_v is the valence band of the surface material, E_c is the conduction band of the surface material, χ is the electron affinity of the

surface material, ΔE_{Ga3d} is the difference in the Ga 3d core level of the aq-HCl GaN and the sample, ΔE_{N1s} is the difference in the N 1s core level of the aq-HCl GaN and the sample, VBO is the valence band offset, CBO is the conduction band offset, and Δ is the dipole at the GaN/dielectric interface. * represents calculations assuming that the core level shifts are only due to band bending at the GaN/GaON interface 80

Table 8. Total optimized energies in Hartrees for Ga-centered GaN cluster, multiplicity (m), initial (d_i) and final (d_f) distances from the O atom to the nearest surface Ga atom, smallest initial (θ_i) and final (θ_f) O-Ga-N angles in the active region, and shortest Ga-N bond length ($d_{\text{Ga-N}}$) for the Ga atom that is taking part in the oxidation and the N atom that is part of the active region GaN. 90

Table 9. Total optimized energies in Hartrees for N-centered GaN cluster, multiplicity (m), initial (d_i) and final (d_f) distances from the O atom to the nearest surface Ga atom, smallest initial (θ_i) and final (θ_f) O-Ga-N angles in the active region, and shortest Ga-N bond length ($d_{\text{Ga-N}}$) for the Ga atom that is taking part in the oxidation and the N atom that is part of the active region GaN. 94

Table 10. Total optimized energies in Hartrees for Hollow-centered GaN cluster, multiplicity (m), initial (d_i) and final (d_f) distances from the O atom to the nearest surface Ga atom, smallest initial (θ_i) and final (θ_f) O-Ga-N angles in the active region, and shortest Ga-N bond length ($d_{\text{Ga-N}}$) for the Ga atom that is taking part in the oxidation and the N atom that is part of the active region GaN. 98

Table 11. Total optimized energies in Hartrees for water oxidized Ga-centered GaN cluster, multiplicity (m), initial (d_i) and final (d_f) distances from the O atom to the nearest surface Ga atom, smallest initial (θ_i) and final (θ_f) O-Ga-N angles in the active region, and shortest Ga-N bond length ($d_{\text{Ga-N}}$) for the Ga atom that is taking part in the oxidation and the N atom that is part of the active region GaN. 103

Table 12. Total optimized energies in Hartrees for water oxidized N-centered GaN cluster, multiplicity (m), initial (d_i) and final (d_f) distances from the O atom to the nearest surface Ga atom, smallest initial (θ_i) and final (θ_f) O-Ga-N angles in the active region, and shortest Ga-N bond length ($d_{\text{Ga-N}}$) for the Ga atom that is taking part in the oxidation and the N atom that is part of the active region GaN. 106

Table 13.Total optimized energies in Hartrees for water oxidized Hollow-centered GaN cluster, multiplicity (*m*), initial (d_i) and final (d_f) distances from the O atom to the nearest surface Ga atom, smallest initial (θ_i) and final (θ_f) O-Ga-N angles in the active region, and shortest Ga-N bond length ($d_{\text{Ga-N}}$) for the Ga atom that is taking part in the oxidation and the N atom that is part of the active region GaN. 110

Table 14. Total optimized energies in Hartrees for hydrolyzed Ga-centered GaN cluster interacting with 1, 2 or 3 TMA molecules, the number of –OH molecules bonded to the GaN cluster, the number of TMA molecules, the multiplicity (*m*) used, the initial (d_i) and final distances (d_f) from the O atom to the nearest Al atom, the formation of a CH_4 molecule is determined and the shortest Ga-N bond length for the Ga atom that is taking part in the reaction and the N atom that is part of the active region GaN. (F) Signifies that the geometry failed to optimize completely due to an error, (NS) signifies that the geometry has not finished optimizing, and (Osc) signifies the geometry failed to converge due to oscillations. RE stands for relative energy.........................120

Table 15. Total optimized energies in Hartrees for hydrolyzed N-centered GaN cluster interacting with 1 or 3 TMA molecules, the number of –OH molecules bonded to the GaN cluster, the number of TMA molecules, the multiplicity (*m*) used, the initial (d_i) and final distances (d_f) from the O atom to the nearest Al atom, the formation of a CH_4 molecule is determined and the shortest Ga-N bond length for the Ga atom that is taking part in the reaction and the N atom that is part of the active region GaN. RE stands for relative energy...122

Table 16. Total optimized energies in Hartrees for hydrolyzed Hollow-centered GaN cluster interacting with 1, 2 or 3 TMA molecules, the number of –OH molecules bonded to the GaN cluster, the number of TMA molecules, the multiplicity (*m*) used, the initial (d_i) and final distances (d_f) from the O atom to the nearest Al atom, the formation of a CH_4 molecule is determined and the shortest Ga-N bond length for the Ga atom that is taking part in the reaction and the N atom that is part of the active region GaN. (F) Signifies that the geometry failed to optimize completely due to an error, (NS) signifies that the geometry has not finished optimizing, and (Osc) signifies the geometry failed to converge due to oscillations. RE stands for relative energy.........................125

Table 17. Total optimized energies in Hartrees for Step 2, the stability of reacted TMA on hydrolyzed Ga-centered GaN cluster, the number of –OH molecules bonded to the GaN cluster, the number of TMA molecules, the number of O atoms bonded to the GaN cluster, the multiplicity (*m*)

used, the initial (d_i) and final distances (d_f) from the O atom to the nearest Al atom, the formation of any new or broken bonds is determined and the shortest Ga-N bond length for the Ga atom that is taking part in the reaction and the N atom that is part of the active region GaN. (F) Signifies that the geometry failed to optimize completely due to an error, (NS) signifies that the geometry has not finished optimizing. RE stands for relative energy. 128

Table 18. Total optimized energies in Hartrees for Step 2, the stability of reacted TMA on hydrolyzed N-centered GaN cluster, the number of –OH molecules bonded to the GaN cluster, the number of TMA molecules, the number of O atoms bonded to the GaN cluster, the multiplicity (m) used, the initial (d_i) and final distances (d_f) from the O atom to the nearest Al atom, the formation of an any new or broken bonds is determined and the shortest Ga-N bond length for the Ga atom that is taking part in the reaction and the N atom that is part of the active region GaN. RE stands for relative energy. 130

Table 19. Total optimized energies in Hartrees for Step 2, the stability of reacted TMA on hydrolyzed Hollow-centered GaN cluster, the number of –OH molecules bonded to the GaN cluster, the number of TMA molecules, the number of O atoms bonded to the GaN cluster, the multiplicity (m) used, the initial (d_i) and final distances (d_f) from the O atom to the nearest Al atom, the formation of new or broken bonds is determined and the shortest Ga-N bond length for the Ga atom that is taking part in the reaction and the N atom that is part of the active region GaN. RE stands for relative energy. 131

Table 20. Total optimized energies in Hartrees for hydrolyzed Ga-centered GaN cluster interacting with 1 TEMAH molecule, the number of –OH molecules bonded to the GaN cluster, the number of TEMAH molecules, the multiplicity (m) used, the initial (d_i) and final distances (d_f) from the O atom to the nearest Hf atom, the formation of a N-H bond is determined and the shortest Ga-N bond length for the Ga atom that is taking part in the reaction and the N atom that is part of the active region GaN. (R) Signifies that the geometry has not fully optimized and is still running and (Osc) signifies the geometry failed to converge due to oscillations. RE stands for relative energy. 134

Table 21. Total optimized energies in Hartrees for hydrolyzed Hollow-centered GaN cluster interacting with 1 TEMAH molecule, the number of –OH molecules bonded to the GaN cluster, the number of TEMAH molecules, the multiplicity (m) used, the initial (d_i) and final distances (d_f) from the O atom to the nearest Hf atom, the formation of a N-H

bond is determined and the shortest Ga-N bond length for the Ga atom that is taking part in the reaction and the N atom that is part of the active region GaN. RE stands for relative energy. 136

Table 22. Total optimized energies in Hartrees for Step 2, the stability of reacted TEMAH on hydrolyzed Ga-centered GaN cluster, the number of –OH molecules bonded to the GaN cluster, the number of TEMAH molecules, the number of O atoms bonded to the GaN cluster, the multiplicity (*m*) used, the initial (d_i) and final distances (d_f) from the O atom to the nearest Hf atom, the formation of new or broken bonds is determined and the shortest Ga-N bond length for the Ga atom that is taking part in the reaction and the N atom that is part of the active region GaN. RE stands for relative energy. 138

Table 23. Total optimized energies in Hartrees for Step 2, the stability of reacted TEMAH on hydrolyzed N-centered GaN cluster, the number of –OH molecules bonded to the GaN cluster, the number of TEMAH molecules, the number of O atoms bonded to the GaN cluster, the multiplicity (*m*) used, the initial (d_i) and final distances (d_f) from the O atom to the nearest Hf atom, the formation of new or broken bonds is determined and the shortest Ga-N bond length for the Ga atom that is taking part in the reaction and the N atom that is part of the active region GaN. RE stands for relative energy. 139

Table 24. Total optimized energies in Hartrees for Step 2, the stability of reacted TEMAH on hydrolyzed Hollow-centered GaN cluster, the number of –OH molecules bonded to the GaN cluster, the number of TEMAH molecules, the number of O atoms bonded to the GaN cluster, the multiplicity (*m*) used, the initial (d_i) and final distances (d_f) from the O atom to the nearest Hf atom, the formation of new or broken bonds is determined and the shortest Ga-N bond length for the Ga atom that is taking part in the reaction and the N atom that is part of the active region GaN. RE stands for relative energy. Osc signifies the system did not reach a minimum due to oscillations. 141

CHAPTER I
INTRODUCTION

The development of Si-based microelectronic devices has led and continues to lead to many advances in electronics, computers, and telecommunications in particular, that have been a boon to modern civilization. While Si-based materials and technologies are by far the best understood semiconductors, they are not the only semiconductor material that can be used in microelectronic systems. Over the past decade a new group of semiconductor materials have begun to receive wider attention, those are the III-nitride semiconductors which are noted for their wide bandgap. Due to the nature of these materials, researchers believe that these materials can be used in devices for high power applications in environments never previously thought possible, such as pressure vessels and near nuclear reactors. Other applications of III-nitride semiconductors are in high electron mobility transistors and optical-electronic applications.

III-nitrides offer potential advancements in several research areas; however they are not very well understood. One area of significant research for both Si and III-N based devices is tuning threshold voltage of transistors. The voltage at which a device "turns on", the threshold voltage, is significant for two main reasons, the first being control which leads to low/high power devices and the second being the magnitude of the drain current. Due to the physics of the device, the threshold voltage is controlled by the effective work function of the dielectric metal gate stack. The effective work function calculation for simple structures such as field effect transistors (FET) using non-III-N based materials is well understood, but the calculation for a high electron mobility transistor that uses III-N based materials and includes a heterojunction is not well understood. This is because of the charges that are due to the heterojunction affect the threshold voltage and may also affect the calculation of the effective work function.

This dissertation follows the style of *Science*.

Another area of intense research is the band alignment at the dielectric semiconductor interface which directly affects the gate leakage current, the carrier transport and surface passivation in the gate region. The threshold voltage of a GaN/AlGaN high electron mobility transistor is strongly dependent on surface passivation due to the polarization within the materials. Any interfacial dipole at the dielectric semiconductor interface causes the threshold voltage of these devices to shift depending on the dipole's magnitude and direction. Hence, it is imperative that research into heterojunctions and dielectric III-N semiconductor interfaces continue so that we can realize the full potential of III-N based semiconductors.

These are the main motivations behind this research. In summary, this research is a interfacial engineering project that comprises of three major goals: first, an understanding of how a heterostructure will affect the current effective work function calculation methodology resulting in a novel effective work function calculation involving heterostructures; the second goal is to determine the effect of dielectrics on novel alternate channel materials in regards to the interfacial dipole in such a way that allows for the development of enhancement mode devices using alternate channel materials; and thirdly to determine the mechanism behind the deposition/growth of dielectric materials on alternate channel materials using theoretical calculations providing a more complete understanding of the dielectric/alternate channel material interface and the effect on the interfacial dipole formation. As a direct result of this project, an innovative effective work function equation that employs charges from a heterostructure can be used to more accurately determine the effective work function of metal gate high-κ dielectric gate stacks on alternate channel materials and enhancement mode III-N based devices employing high-κ metal gate stacks that will contribute to high performance and low power microelectronics.

1.1 Motivation and Goals

Over the last two decades research in advanced microprocessors have been following Moore's law and tailored to the consumer, i.e. high performance (gaming laptops, servers, etc.), low power (mobile phones, FLASH storage, etc.) and relatively thin (net books, liquid crystal displays, light emitting diode displays and etc.) electronics. These electronics and more use complementary metal oxide semiconductor (CMOS) technology which employs metal oxide semiconductor field effect transistors (MOSFET) to achieve the desired reliability and performance tailored to the customer; i.e. higher performance, increased reliability, and decreased weight. The device performance and scale of the complementary metal oxide semiconductor technology are strongly dependent on the thickness and quality of the gate oxide region (*1*). This region has been rapidly shrinking in accordance with Moore's law which calls for an increase in speed at a constant power density. However, the conventional silicon oxide with nitrogen incorporated, SiO(N), gate oxide needed to be replaced with new gate insulators for future generations of metal oxide semiconductor field effect transistors due to large gate leakage currents and high gate oxide breakdown characteristic of the thin gate oxide, $\approx$ 1.2 nm, Fig. 1 (*1*).

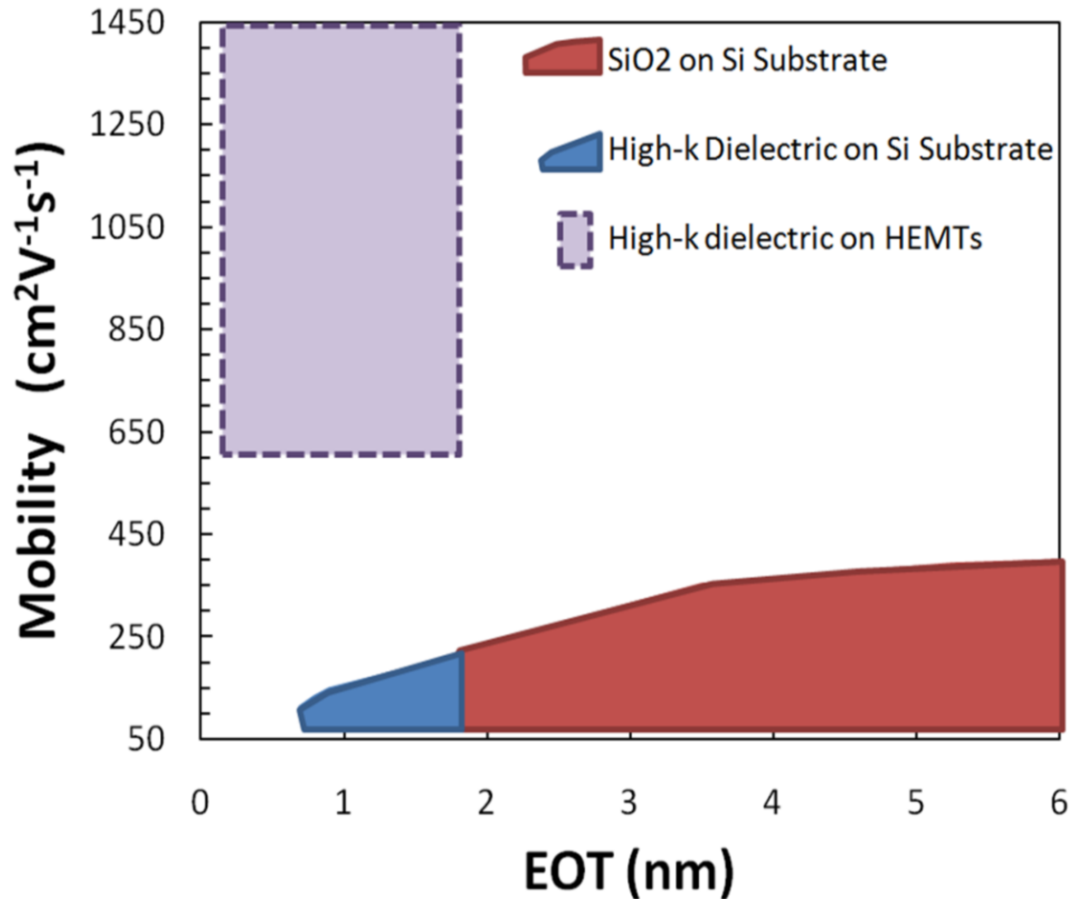

Fig. 1. Mobility versus Effective Oxide Thickness (EOT). Figurative representation of the required scaling due to Moore's Law including Si and Non-Si based channels. Motivation to study non-Si based materials.

Over the last decade, silicon oxide based gate oxides, SiO_2 and SiO(N), have been replaced with higher permittivity dielectric materials (high-κ dielectrics). High-κ dielectrics offer the ability to be physically thicker than the current silicon oxide based films while decreasing the equivalent electrical oxide thickness or effective oxide thickness (EOT) resulting in significant gate leakage reduction (*2, 3*). Another advantage of high-κ dielectrics is the ability to lower the EOT beyond which is possible for SiO_2 potentially resulting in thinner lower power devices (*2-4*). A disadvantage of

high-k dielectrics is the interaction of the high-κ material with the polysilicon electrode. Unfavorable increases in the threshold voltages (V_{th}) of polysilicon/high-κ gate stack p-type MOS and n-type MOS devices were observed and found to be due to Fermi-level pinning. Polysilicon was then replaced with metal electrodes to remove this and other problems associated with the polysilicon/high-κ gate stack (*5*).

However, using metal as the gate electrode comes with its own set of problems. First is the fact that the bulk work function (WF) of a metal on SiO_2 is not the same as the bulk WF on a high-k material resulting in favorable/unfavorable changes in the V_{th}. This change in WF is due to the interactions between the high-κ dielectric and the metal which are not fully understood along with the interactions at the high-κ/Si interface. Other problems include Fermi level pinning, metal diffusion into the dielectric and the semiconductor, thermal/chemical stability, process integration, structural variation and deviation of the WF based on film thickness, influence of bulk/interface charges from the dielectric, and agglomeration of the metal (*6-11*). Over the past several years, it has been found that Hf-based high-κ dielectric TaN metal gate stacks on Si substrates result in optimized gate leakage currents, proper V_{th}'s, larger drive currents, and can be easily integrated into current technologies (*12, 13*).

Even with these advancements in scaling of the MOS structure, to increase the speed of the device Si will need to be replaced with an alternate channel materials (ACMs) and/or III-V based materials. Recently complex heterostructures of ACMs and III-V materials have been implemented to achieve higher electron mobility in NMOS and PMOS devices (*14-17*). For an example, Ge in PMOS devices can have a strained Si_xGe_{1-x} layer on Si followed by a Si interlayer to improve the interface between the high-κ and the Si_xGe_{1-x} layer (*14*). Similarly, recent research involving MOS capacitors on GaAs, with high-κ dielectric stacks using Si as an interface passivation layer between GaAs and HfO_2, have been reported (*17*). Achievement of enhancement mode operation and threshold voltage tuning with different metal gates is a paramount concern for any ACM used because of the need to integrate these devices into current Si based technology. To achieve enhancement mode operation and V_{th} tuning the gate stack and

its interactions with a heterostructure must be well understood and the calculation of the effective work function (EWF) must be accurate. It is proposed that through extensive computer simulations, coupled with the physical and electrical characterizations of the high-κ the ACMs and vice versa, will be fully developed to form an accurate effective work function and work function tuning methodology.

1.2 Background

Over the past several years, there has been little consensus on what metal should be used as the gate metal in the high-k metal gate stacks of Si and III-V based devices. This is because the optimal electrode material should have the proper work function (WF), be chemically and thermally stable with the underlying dielectric, and should be easily integrated into the current process flow technologies. For bulk CMOS devices, the proper WF for NMOS and PMOS has been simulated be near the conduction or valence band-edge (4.1/5.2 eV for NMOS/PMOS) of Si to achieve a suitable threshold voltage (V_{th}) for maximized drive current (*8*). However, a proper WF has not been established for III-V based materials due to the infancy of ACM based device research. An overview of the research that has been completed in the field of WF extraction and tuning for the past 7 years is shown in Fig. 2 including the potential applications and the advantages/disadvantages of each device or method.

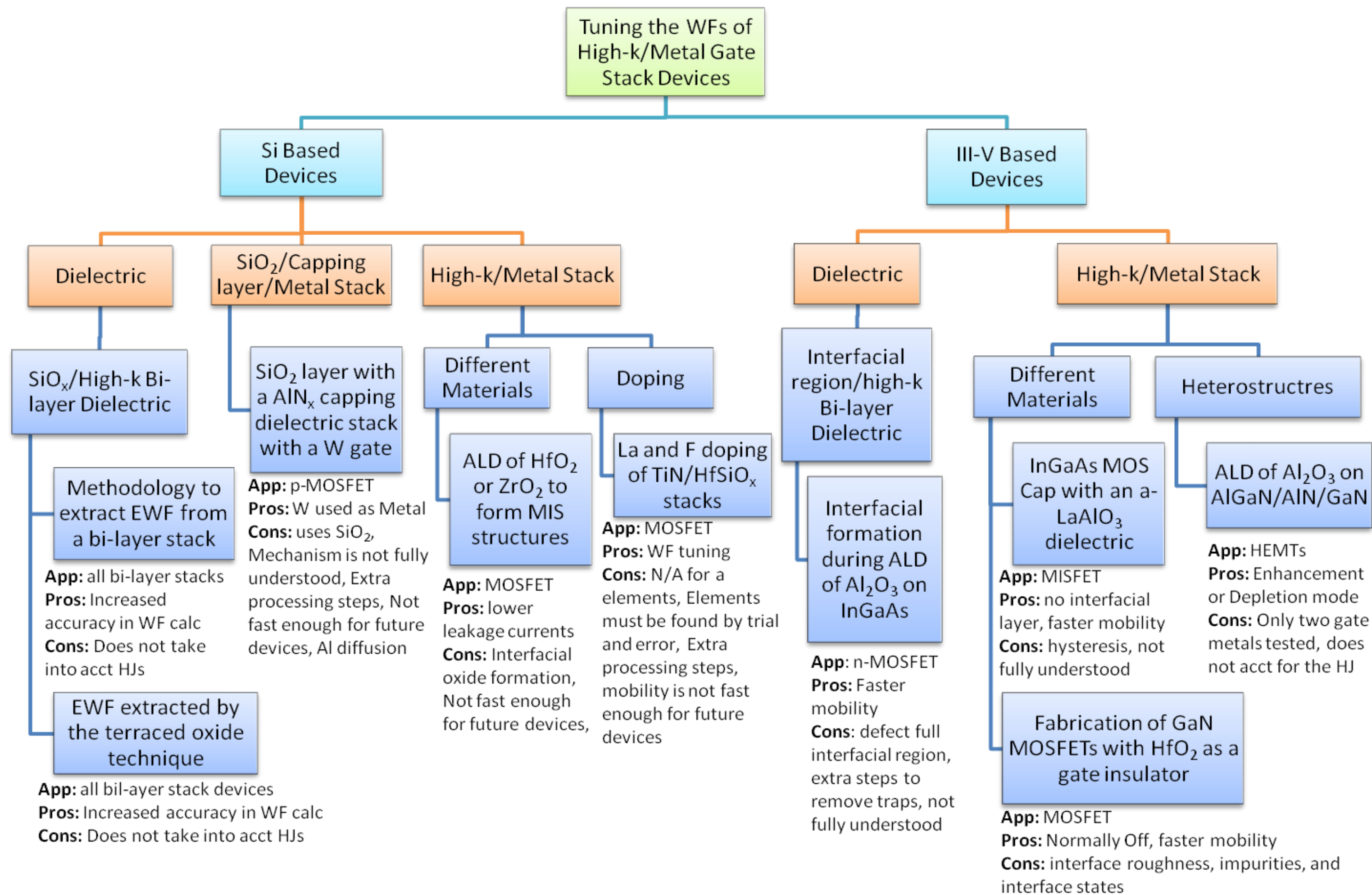

Fig. 2. Investigation of work function tuning of high-κ/metal gate stack devices for the past 7 years.

1.2.1 Work Function Tuning of Si Based Devices

Not only is determining the proper WF for ACM based simulated devices time consuming, determining the actual WF, or the effective work function (EWF), of a gate metal in contact with a dielectric is extremely complex due to interfacial and bulk charges. R. Jha and his colleagues studied the effects of charge distribution in gate dielectric stacks on the flatband voltage (V_{fb}) of Si based capacitors (*18*). A mathematical model was constructed to accurately extract the EWF of the gate metal in a high-κ metal gate stack with various charge disruptions including charges resulting from a bi-layer gate dielectric stack, Fig. 3(a), (*18*). Another EWF extraction method determined in 2004 was the terraced oxide method which can be used for SiO_2 or a high-κ bi-layer dielectric stack. This method implements ringed dielectric terraces of various thicknesses on a single substrate, Fig. 3(b-d), to minimize the effects of interfacial charges while varying the dielectric bulk charges, which in turn are limited to thickness of the dielectric (*19*).

Both these methods use Si as the substrate and account for the oxidation of the Si/high-κ interface which occurs during typical processing which had not been previously accounted for. Certain III-V substrates, such as GaAs, InGaAs and other related materials, also form an interfacial region during typical processing methods when forming a high-κ metal gate stack. Thus allowing for the above methods to extract the EWF from III-V based high-κ metal gate stacks while accounting for the interfacial and bulk charges of the dielectric stack (*20*).

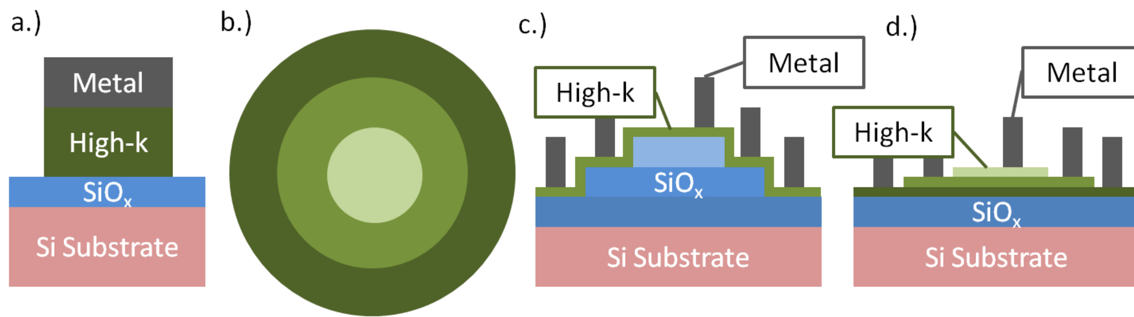

Fig. 3. Figurative representations of a.) A bi-layer high-κ metal gate stack, b.) The terraced oxide method top view, c.) Terraced oxide method varying the interfacial oxide (SiO_x) thickness, d.) Terraced oxide method varying the high-k thickness all with metal gate electrodes shown. The bi-layer high-κ metal gate stack method implements ringed dielectric terraces of various thicknesses on a single substrate to minimize the effects of interfacial charges while varying the dielectric bulk charges, which in turn are limited to thickness of the dielectric.

After experimentally determining the EWF of a metal on a certain gate stack or simulating a device to work with a certain EWF, the EWF may need to be manipulated to achieve certain electrical device characteristics, such as leakage current, V_{th} and drive current, also known as WF tuning/engineering. Different studies of Si based devices have shown that by changing the dielectric material or metal the electrical characteristics have greatly improved (*21-24*). For an example, the atomic layer deposition (ALD) of HfO_2 or ZrO_2 on a Si substrate decreases the leakage current by several orders of magnitude compared to that of SiO_2 on a Si substrate with similar effective oxide thickness (EOT) values (*21*). Other studies have shown that by capping SiO_2 with AlN_x or implanting F or incorporating La into high-κ stacks on Si substrates, the EWF can be effectively controlled or tuned by influencing interfacial bonding (*22-24*). However, many substrates are now implementing heterostructures into the channel region to increase electron/hole mobility and these interfaces have not been accounted for in the EWF extraction or tuning.

1.2.2 Work Function Tuning of III-V Based Devices

Different studies of III-V based devices have shown that by changing the dielectric material or metal the electrical characteristics have greatly improved (*25, 26*).

One of the most recent demonstrations of work function tuning on heterostructures was using high Al composition $Al_{0.72}Ga_{0.28}N$/AlN/GaN to form high electron mobility transistors (HEMTs) using Al_2O_3 as the gate dielectric and Al/Au and Ni/Au as different gate metals. G. Li and his colleagues were able to show that by changing the gate metal the V_{th} shifted 0.87 V (*27*). HEMT provide an extremely high electron mobility and low leakage currents and could be used in the future for high frequency operation. Heterostructures typically use dipoles, due to spontaneous and piezoelectric polarization (result of strain), to form high electron mobility channels. These dipoles could potentially influence the dipoles and/or charges in the surrounding materials and/or at the surrounding interfaces causing the electrical characteristics of the device to vary (*28*). To optimize these devices it is necessary to better understand the dipoles at the ACM/high-κ dielectric interface and the effects that heterostructures have on the gate stack and thus on the EWF.

1.3 Significance

Currently, III-V based devices are needed for digital applications, low-loss high-power RF switching and large DC voltage applications. A figurative description of the high impact research areas of III-V devices is shown in Fig. 4. To achieve E-mode III-V based devices the threshold voltage (V_{th}) must be controlled, i.e. positive or negative and within a certain voltage range depending on n-type or p-type devices and applications. One of the current methods being developed to control the V_{th} is tuning the WF of the gate metal. To accomplish this task a better understanding of the how the dipoles in the gate stack and in the ACMs along with the potential additional charges at the heterojunction (HJ) interfaces impact the WF is needed. In the proposed work, the potential charges that could affect the WF are examined using electrical, theoretical and physical characterization. In order to extract an accurate work function, the charges located at the: a) bulk high-κ layer, b) interface of high-κ and interfacial layer, c) bulk of the interfacial layer, d) ACM and the interfacial layer, e) space charge of the ACMs, f)

interface of the ACMs and g) high-κ/gate electrode interface must be either accounted for or measured such that no impact to or upon the extraction of the WF.

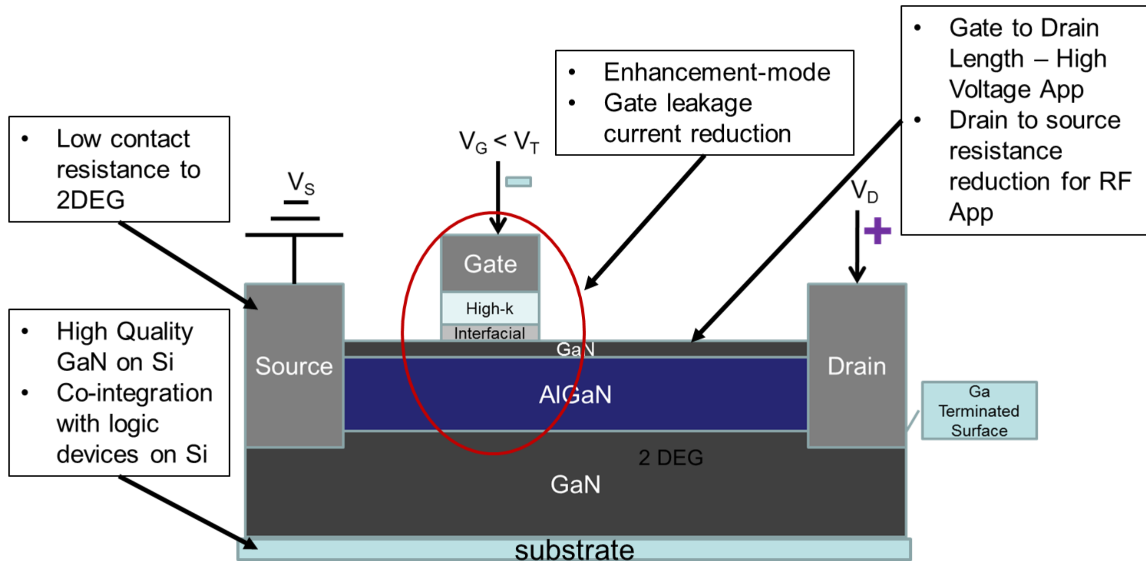

Fig. 4. Motivation of Study. Figurative representation of the high impact research areas currently under development. Motivations to research the metal gate high-κ gate stack on alternate channel materials such as GaN. Enhancement-mode high-electron mobility transistors are needed for high-power applications.

A better understanding of the band alignment, including dipole formation, at the III-N/dielectric interface is also needed. The III-N/ high-κ interface has been shown to influence the work function of the gate metal and therefore the threshold voltage (*27, 29*). Many III-N-based devices with varying gate stacks using high-κ materials such as HfO_2 and Al_2O_3 have been studied (*26, 27, 30-32*). However, previous experiments only use X-ray photoelectron spectra (XPS) to determine the band offsets. Ultraviolet photoelectron spectra (UPS) are needed to accurately determine the valence band offset between III-N/dielectric due to precision issues with XPS at low binding energies (*33-35*). In the proposed work, the band alignments of varying dielectrics on GaN are investigated using XPS, UPS and TEM analysis.

Previous research has shown that a thin GaON or GaHfON interfacial layer is formed during the atomic layer deposition (ALD) of HfO_2 on to clean GaN (0001) (*30*). Understanding the formation mechanism of this interfacial layer and its effect on the interface dipole between GaN and ALD HfO_2 is of paramount importance. Therefore the oxidation of the GaN (0001) surface with varying oxidation methods and surface structures are studied using the *ab initio* density functional theory (DFT) using varying GaN structures with the intent to understand the formation mechanism and to investigate the features of these devices as they are scaled down to nanosizes. The interfacial layer's effect on the interface dipole and the band alignment is analyzed using XPS, UPS and Transmission Electron Microscopy (TEM).

With the completion of the proposed work, the EWF can be accurately determined and the charges can be exploited to tune the WF. Tuning of the WF will allow for the integration of III-V materials into Si-based technology with a more precise knowledge of the metal gate-stack interactions with a heterostructure.

1.4 Summary and Outline

This research project is a combination of experimental and theoretical approaches to determine the effect of chemical states on the effective work function. The heterojunction and the semiconductor/dielectric interfaces have been studied to determine the effects on the effective work function calculation. Experimental approaches including X-ray photoelectron spectra, Ultraviolet photoelectron spectra, and Transmission Electron Microscopy are used to determine the band alignment of semiconductor/dielectric interfaces. Theoretical approaches including density functional theory and Sentaurus Device software are used to determine the mechanisms behind the formation of an interfacial layer at the semiconductor/dielectric interface when reaction kinetics allows and the heterojunction effect on the effective work function.

Chapter II discusses my plan of research regarding the impact of chemical states on the effective work function. A basic introduction regarding the polarization

properties of GaN is reviewed. A description of the theory and experimental approaches used in this dissertation are described. First the experimental techniques, such as atomic layer deposition (ALD), XPS/UPS, and tunneling electron microscopy (TEM), are discussed in detail; followed by a description of the theoretical techniques used, including Sentaurus Device and density functional theory (DFT) using the program Gaussian09.

Chapter III is concerned with the formation of a dielectric/semiconductor interface when an insulator (various high-κ dielectrics) is grown or deposited on a semiconductor (GaN). The basics of band alignment are discussed including the effect of a dipole. Photoemission characterization techniques (XPS and UPS) used to determine the band offsets at the dielectric/semiconductor interface are discussed.

Chapter IV describes in detail the theoretical equations, experiments, results and analysis of the integration of heterojunctions into effective work function calculations. It is found that when a SiGe/Si heterostructure on silicon is low doped and sufficiently thin, then the work function can be extracted in a manner similar to that on a simple silicon substrate.

Chapter V details the experimental investigation of the aq-HCl GaN – ALD high-κ dielectric interfaces. X-ray and ultraviolet photoelectron spectroscopy are used to observe the interface electronic states at the GaN (0001) and high-κ dielectric interfaces. The GaN/HfO_2 and GaN/Al_2O_3 interfaces exhibited dipoles of 1.6 eV and 0.4 eV ± 0.2 eV, respectively. It is found that the formation of an interfacial layer at the GaN/HfO_2 interface is the primary cause of the larger dipole.

Chapter VI details the photoemission investigation of the aq-HCl GaN – GaON interface using X-ray and ultraviolet photoelectron spectroscopy. This study resulted in GaN/GaON exhibiting a dipole of -2.7 eV ± 0.2 eV assuming that the core level shifts are only representative of the GaN band bending at the interface. If it was assumed that the core level shifts are only due to the oxidation of GaN then the exhibited dipole at the GaN/GaON was -1.8 eV ± 0.2 eV. It was found that the observed dipole is primarily due to the polarization of the GaN.

Chapter VII details the oxidation of the GaN (0001) surface with varying oxidation methods and hydrolyzed surface structures are studied using the *ab initio* density functional theory (DFT). GaN clusters are used for computation time reduction and to better understand the effects of GaN in the nano-size regime. The oxidation of the Ga-face surface of GaN (0001) clusters is discussed. The most notable interactions are between the GaN active region and O_2 and H_2O. The most stable interaction of O_2 and the active GaN region results in the complete dissociation of the O_2 molecule. While the most stable interaction between a H_2O molecule and the active GaN region is the complete dissociation of one of the O-H bonds to form a Ga-O-H bond.

Chapter VIII details the calculations of the interactions of Trimethylaluminium (TMA) and Tertrakis(EthylMethylAmino)Hafnium (TEMAH) with the hydrolyzed Ga-face of GaN clusters, which could be used as testbeds for the actual Ga-face on GaN crystals. However, an additional goal is the analysis of the nano-clusters for several other applications in nanotechnology. It is found that while further research is needed in this area to grasp a better understanding of the interactions of TMA or TEMAH with hydrolyzed GaN clusters, it was found that the formation of a Ga-N(CH_3)(CH_2CH_3) bond can form during the deposition of HfO_2 using ALD and TEMAH as the reactant without breaking the Hf-N bond. It is important to note that a Ga-CH_3 bond did not form in any fully optimized stable structures when analyzing the interaction of TMA with hydrolyzed GaN.

Chapter IX, discusses path for future research, including but not limited to further GaON analysis, continued GaN/dielectric and AlGaN/dielectric photoemission analysis and experiments that can be done to verify the theoretical mechanisms calculated within this dissertation.

Finally in Chapter X, overall conclusions drawn from Chapters IV-VIII are presented.

CHAPTER II
IMPACT OF CHEMICAL STATES ON THE EFFECTIVE WORK FUNCTION – AN EXPERIMENTAL AND THEORETICAL APPROACH

The work function of the metal is in important parameter in the device operation, but we know from years of difficult research probing the work function of metals in high-κ/metal gate devices, that it may be difficult to precisely design the threshold voltage due to the interfaces found within these devices. Thus, the interfaces of the devices will be the main focus of the proposed research. The investigation of the interfaces will be separated into two main parts: integration of a heterojunction into the calculation of the EWF and the effects of interfacial charges at the dielectric/heterostructure interface on the heterojunction and EWF. Fig. 5 is a representation of the overall proposed work.

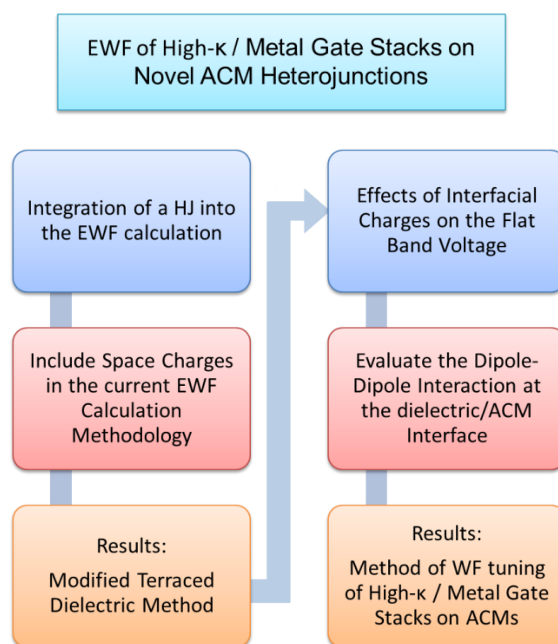

Fig. 5. Proposed Research. A figurative representation of the proposed research of interfacial effects of heterojunctions and high-k dielectrics on the EWF calculation.

The EWF calculation must account for all of the interfacial charges of the device. In the case of ACM based devices, many include complex heterostructures which can complicate the extraction of the work function because of the potential additional charges at the heterojunction and the space charge of the ACMs. Thus, integration of a heterostructure into the terraced dielectric method is pivotal.

The potential additional charges at the heterojunction and the space charge of the ACMs must be evaluated to determine their effects on the EWF. Potential sources of additional charges not currently considered in EWF extraction methods are dipole-dipole interaction between the ACM and the dielectric, dipole-dipole interaction between the dielectric/ACM heterostructure interface and charges at the interface of the dielectric/heterojunction affecting the dipole of the ACM. These charges need to be considered due to the polarization effects in certain ACMs, such as GaN and AlGaN.

2.1 Introduction to the Polarization of GaN

There is a binary polarization effect in GaN and AlGaN: the first is spontaneous polarization due to the symmetry of the wurzite structure and the large iconicity of the covalent gallium nitrogen bond (Fig. 6), the second is strain-induced piezoelectric polarization due to lattice mismatch (Fig. 7) (*36*). Piezoelectric polarization is negative for tensile and positive for compressive strained GaN or AlGaN strained layers, Fig. 7.

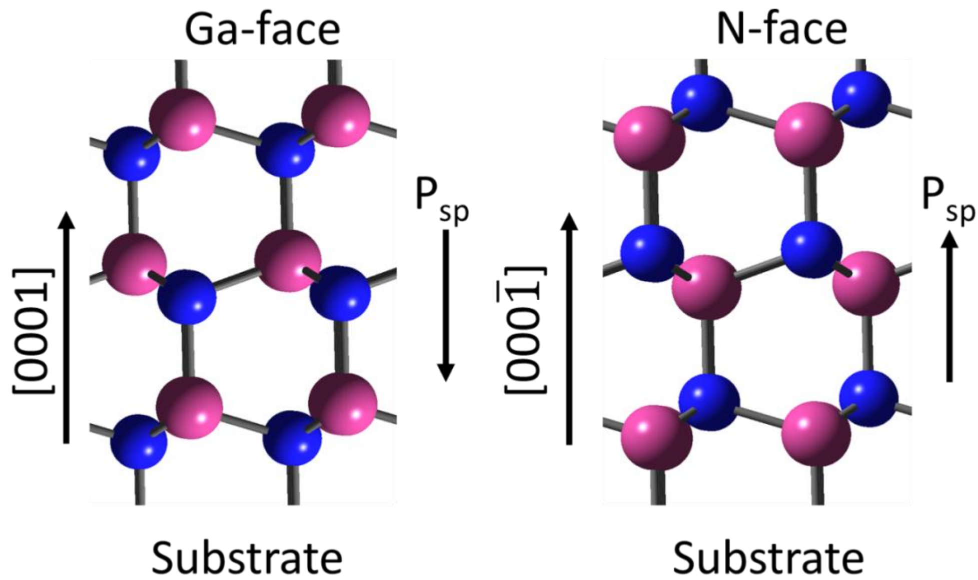

Fig. 6. Spontaneous Polarization of GaN. Schematics of the crystal structure of wurtzite Ga-face and N-face GaN. The spontaneous polarization (P_{sp}) direction is shown. Ga is pink (larger) and N is blue (smaller).

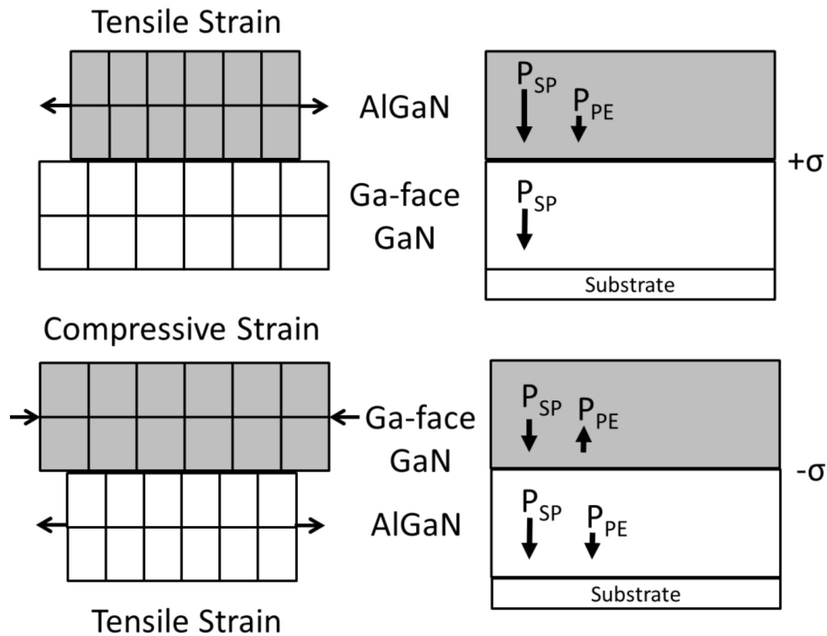

Fig. 7. Overall polarization induced sheet charge density, σ, and directions of the spontaneous and piezoelectric polarization (P_{SP} and P_{PE}) in Ga-face relaxed GaN/tensile strained AlGaN heterostructure and Ga-face compressive strained GaN/tensile strained AlGaN heterostructure.

Due to the large polarization fields, a sheet carrier concentration as high as 10^{13} cm^{-2} can be achieved in the two-dimensional electron gas (2DEG) channel of the AlGaN/GaN heterostructure without intentional doping or an applied voltage (*36*), Fig. 8. Due to the definition of a dipole, any surface contamination or additional strain due to the surface of the GaN or AlGaN being in contact with another material would result in an increase or decrease in the polarization field at the AlGaN/GaN interface therefore effecting the threshold voltage, Fig. 9 and Fig. 10.

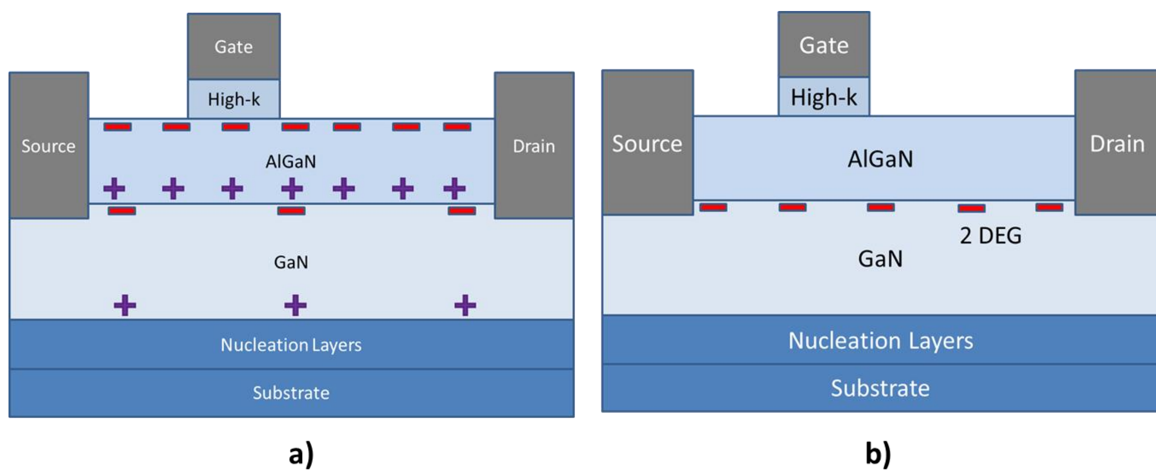

Fig. 8. Figurative representation of GaN/AlGaN HEMTs with no surface states and no additional dipole at the high-κ/III-V interface showing the a) overall polarization fields and b) the 2DEG with no applied voltages.

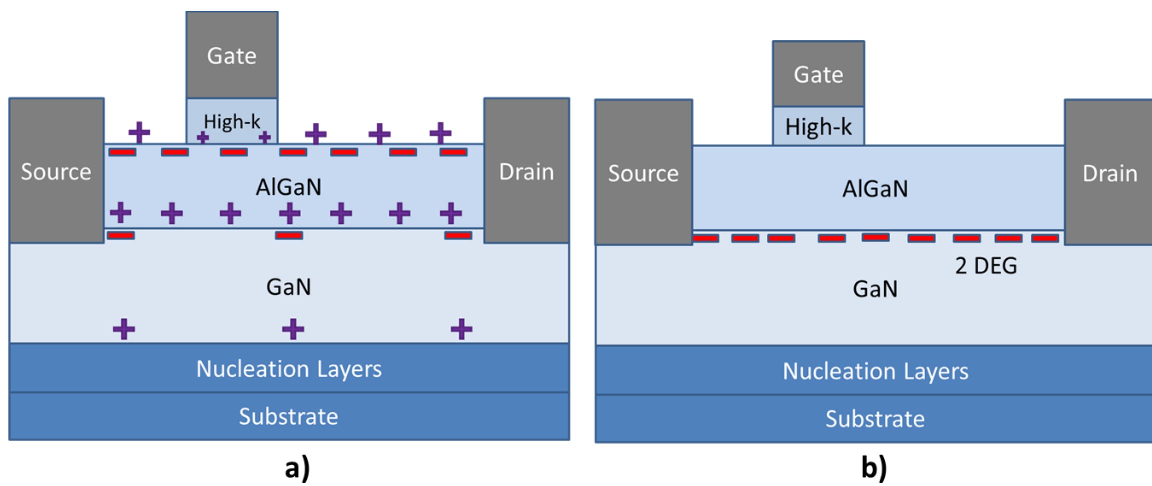

Fig. 9. Figurative representation of GaN/AlGaN HEMTs with positive surface states and a positive dipole located at the high-κ/III-V interface showing the a) overall polarization fields and b) the 2DEG with no applied voltages.

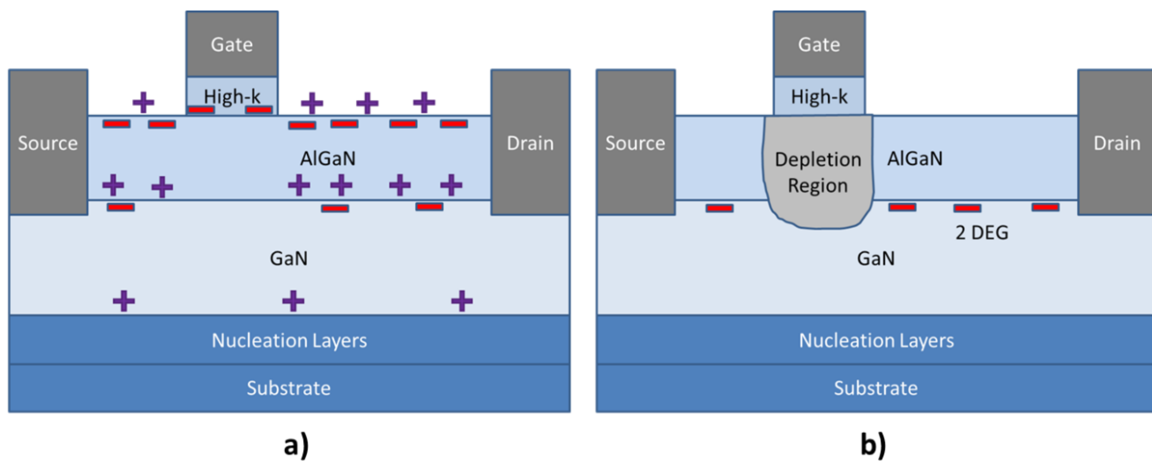

Fig. 10. Figurative representation of GaN/AlGaN HEMTs with positive surface states and a negative dipole located at the high-κ/III-V interface showing the a) overall polarization fields and b) the 2DEG with no applied voltages.

Due to the formation of spontaneous and piezoelectric polarization in GaN/AlGaN HEMTs the high-κ/III-V interfacial dipole either can increase or decrease the 2DEG in the gate stack region, at the GaN/AlGaN interface below the gate stack. An

increase in the 2DEG would cause a negative shift in the turn-on voltage, the threshold voltage (V_{th}) or the flat band voltage (V_{fb}). A decrease in the 2DEG would cause a positive shift in the turn-on voltage, the V_{th} or V_{fb}. A positive dipole at the high-κ/III-V causes the overall dipole in the AlGaN, in this case, to increase thus increasing the 2DEG in the GaN region, Fig. 9. A negative dipole at the high-κ/III-V causes the overall dipole in the AlGaN, in this case, to decrease thus causing a decrease in the 2DEG or a depletion region to form if the negative dipole is a large enough, Fig. 10. In order to facilitate GaN/AlGaN HEMTs to be integrated into Si based electronics it is necessary to shift the threshold voltage towards more positive voltages.

In this chapter, a description of the theory and experimental approaches used in this dissertation to understand the effects of chemical states on the effective work function are described. First the experimental techniques, atomic layer deposition (ALD), XPS/UPS, and tunneling electron microscopy (TEM), are discussed in detail; followed by a description of the theoretical techniques used, Sentaurus and density functional theory using the program Gaussian09.

2.2 Experimental Techniques

There are four main experimental techniques used in this study; X-ray and ultraviolet photoelectron spectroscopy (XPS and UPS), and tunneling electron microscopy (TEM). Detailed descriptions of each technique are found within this section.

2.2.1 Atomic Layer Deposition

Atomic layer deposition (ALD) is an advanced deposition technique that relies on self-limiting reactions to deposit atomically thin materials such as high-κ dielectrics. ALD processes and its applications have previously been extensively reviewed (*16, 21, 30, 31, 37-45*). A figurative representation of the sequential, self-limiting surface reactions during ALD of Al_2O_3 on GaN are displayed in Fig. 11. Most ALD processes

are founded on binary reaction sequences where two sets of surface reactions take place and deposit a binary compound film. Due to a finite number of surface sites, the reactant can only react with a finite number of surface species. Since each of the two surface reactions is self-limiting, the two reactions proceed in a sequential fashion to deposit atomically controlled film (*40*). Therefore, ALD offers extreme thickness precision, material uniformity, and quality.

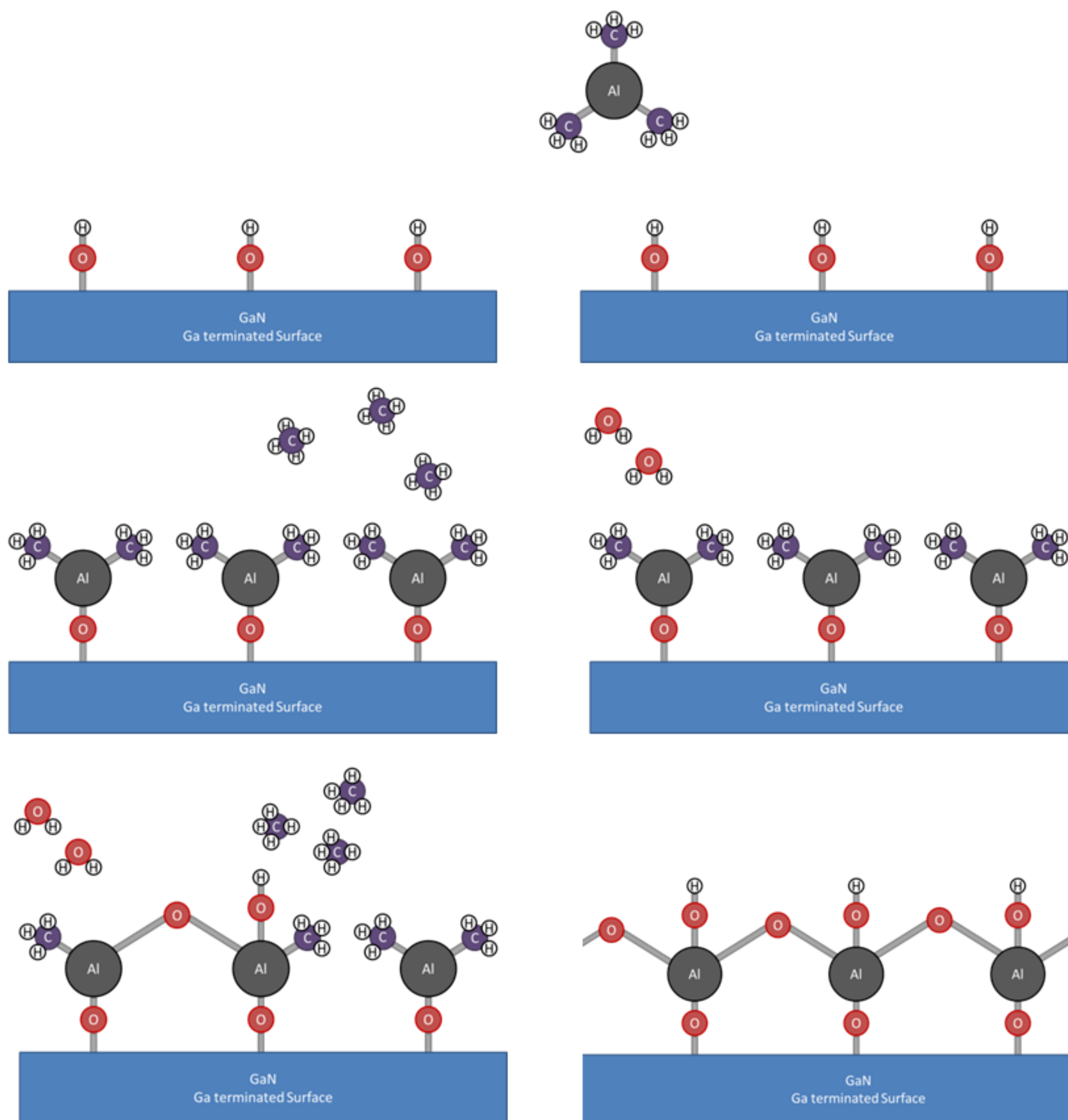

Fig. 11. Atomic Layer Deposition of Al_2O_3. The sequential, self-limiting surface reactions that occur during the atomic layer deposition (ALD) of Al_2O_3 on GaN are displayed.

There are many different materials using many varying reactants that can be deposited using ALD. In this research three reactants were used to deposit Al_2O_3 and HfO_2. Trimethylaluminium, TMA, and water are used to deposit Al_2O_3, Fig. 11, (*46*). Tetrakis(ethylmethylamino)hafnium, TEMAH, and water are used to deposit HfO_2. The atomic layer deposition tool used throughout this research was purchased from Cambridge NanoTech Savannah ALD Tool. The author equipped the ALD with water, TMA and TEMAH precursors, Fig. 12. TMA and TEMAH were purchased from Sigma-Aldrich. The author performed thickness analysis of thermally annealed ALD HfO_2 and Al_2O_3 using TEM to determine the deposition rates, examples of this analysis are found in Fig. 13 and Fig. 14. Through TEM analysis the growth rates were determined to be 1.10 Å/cycle for ALD HfO_2 and 1.25 Å/cycle for ALD Al_2O_3. The thickness profile of ALD HfO_2 and ALD Al_2O_3 can be found through Cambridge NanoTech.

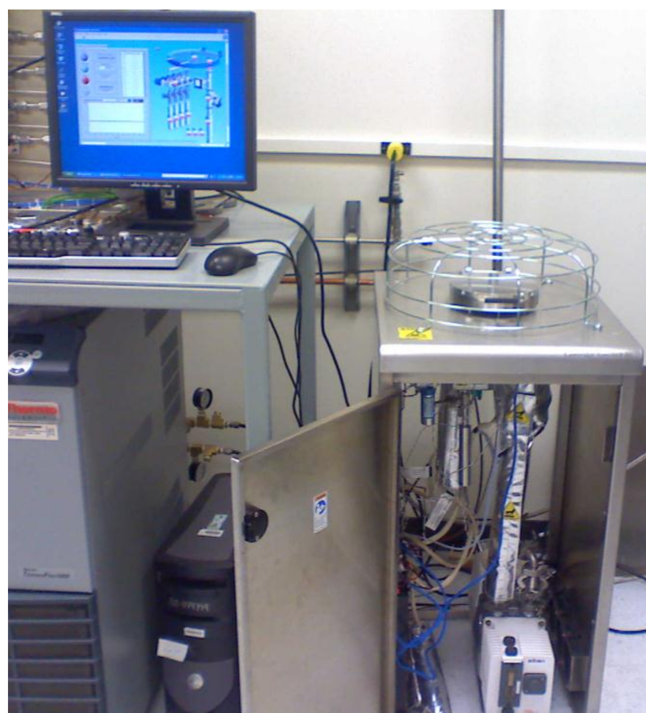

Fig. 12. Image of the Cambridge NanoTech Savannah Atomic Layer Deposition Tool, installed by the author.

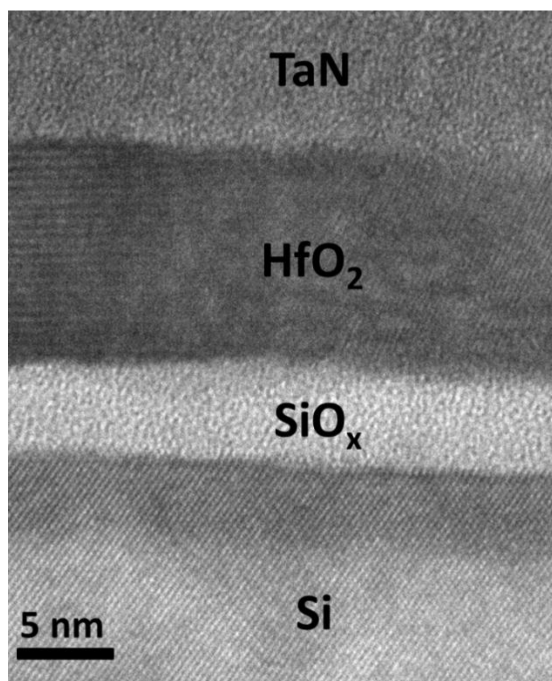

Fig. 13. Cross-sectional TEM image of thermally annealed high-κ HfO_2 (11 nm) deposited using ALD, 100 cycle deposition, on Si/SiO_x. The ALD reactants used were water and TEMAH.

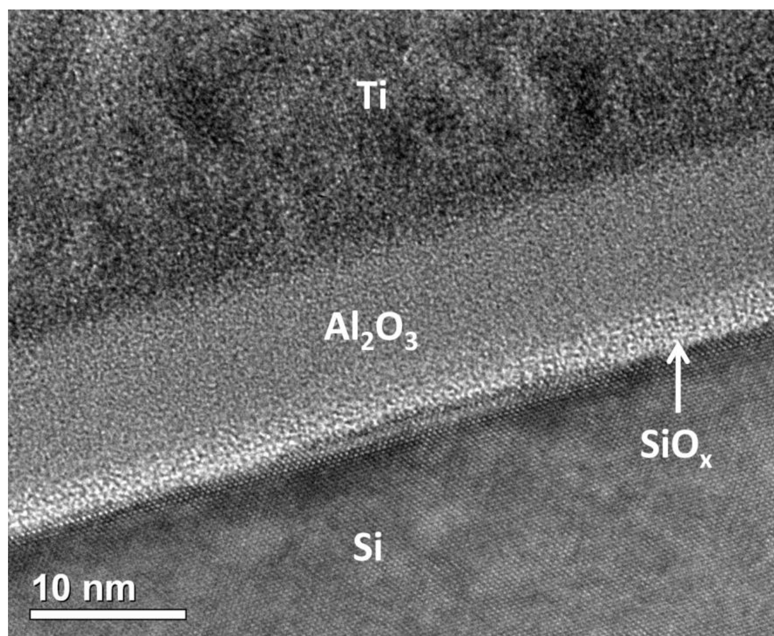

Fig. 14. Cross-sectional TEM image of thermally annealed high-κ Al_2O_3 (9 nm) deposited using ALD, 80 cycle deposition, on Si/SiO_x. The ALD reactants used were water and TMA.

2.2.2 Photoemission Spectroscopy

The primary analysis technique used in this study to determine interfacial dipoles was X-ray and Ultraviolet photoelectron spectroscopy (XPS and UPS). XPS and UPS are based on the process of photoelectron emission. Photoemission is typically thought of as occurring in three steps, Fig. 15 (*47*). In the first step, an incoming photon is absorbed by a core electron within the 10 nm of the surface. This electron is then transferred from its initial state into an excited final state at the location of absorption. This step repeats itself for all electrons that come in contact with the incoming photon. During the second step, the excited electron travels to the sample's surface with other excited electrons colliding with other electrons; these are called inelastic collisions. By the time the excited electron reaches the surface the electron has lost some of its energy. The final step is the ejection of the excited electron into the vacuum. The primary difference between XPS and UPS is the energy used to cause electrons to be emitted from the sample.

2.2.2.1 X-ray Photoelectron Spectroscopy

XPS is a technique that characterizes the composition, chemical states, and electronic states of the elements present in the first 10 nm of the material. XPS can only analyze the near surface region because of escape depth of the photoelectrons is limited to ≈ 3 – 10 nm depending on the sample and X-ray source (*48*). The energy of the X-ray source used to cause photoelectrons to be emitted from the near surface region of the sample is typically between 1200 – 2000 eV. The kinetic energy of the emitted photoelectrons is measured using energy dispersive analysis. The kinetic energy of a photoelectron (KE) is made up of three main properties; the energy of the incoming X-rays (hν), the binding energy of the electron impacted by the X-rays (BE), and the spectrometer work function (Φ). The KE is given by the following equation:

$$KE = h\nu - BE - \Phi \tag{1}$$

The binding energy of a photoelectron is the energy required to release an electron from its atomic orbital; where the initial state is its atomic orbital and its final state is a free electron state in the vacuum, Fig. 15. Binding energy is a material property and can also be defined as the energy difference between the Fermi level and a core level, such as N 1*s*, as shown in Fig. 16. The binding energy of a photoelectron is affected by the chemical element, over all energy of the sample, and the chemical states.

The XPS spectra collected during this study were recorded using a commercial Kratos Axis Ultra, utilizing a monochromated Al-K_{α} X-ray source ($h\nu = 1486.5$ eV), hybrid optics (employing a magnetic and electrostatic lens simultaneously) and a multi-channel plate and delay line detector coupled to a hemispherical analyzer. The photoelectrons take-off angle was normal to the surface of the sample and 45° with respect to the X-ray beam. All spectra were recorded using a single sweep and an aperture slot of 300x700 microns, and high resolution spectra were collected with a pass energy of 20 eV. The pressure in the analysis chamber was typically 4×10^{-9} Torr during all data acquisition. Casa XPS analysis software was used to determine the stoichiometry of samples from corrected peak areas and employing Kratos sensitivity factors for each element of interest written by Kratos. All spectra were corrected using the C 1*s* peak to 284.5 eV.

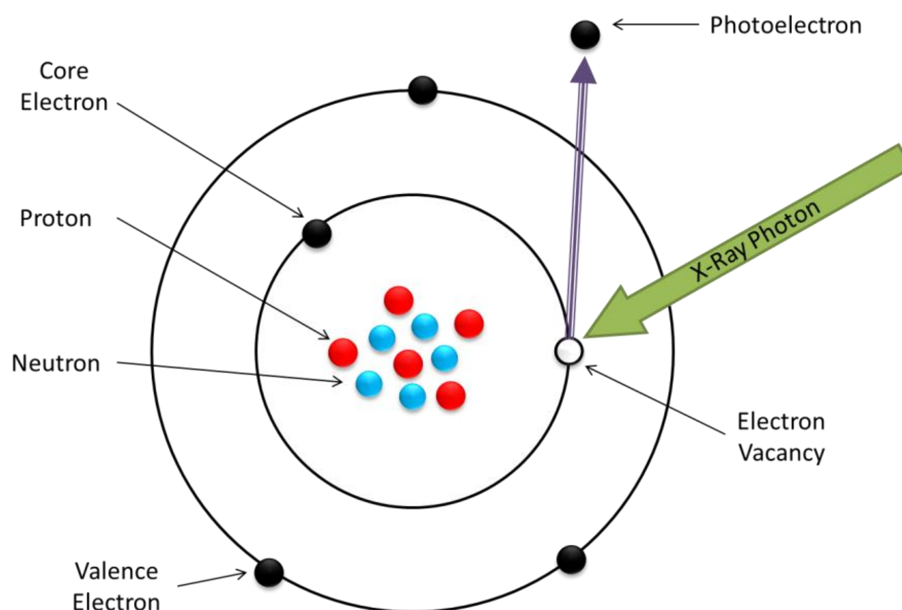

Fig. 15. Photoelectron generation using an X-ray photon source during X-Ray photoelectron spectroscopy (XPS). The core electron is excited.

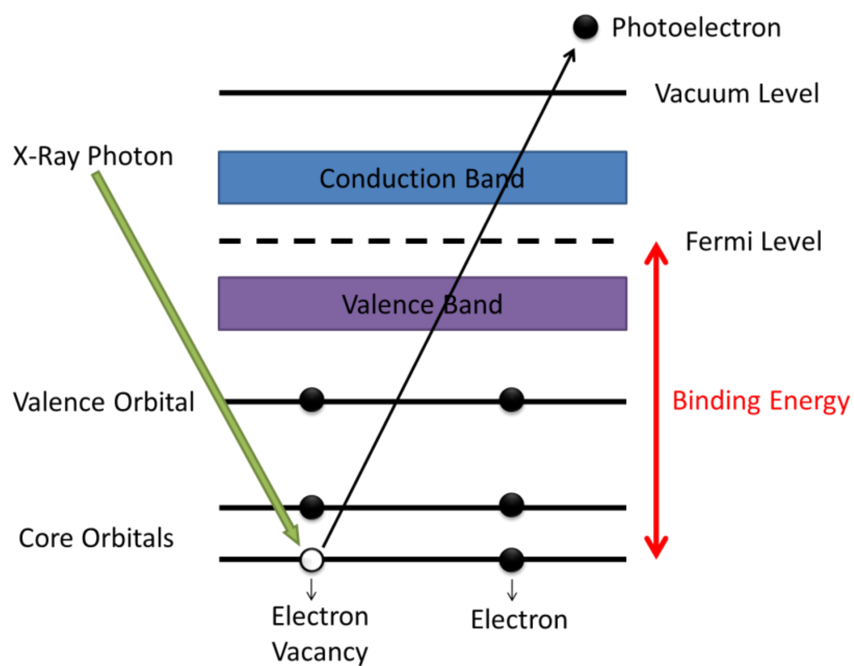

Fig. 16. Photoelectron generation in terms of the materials Fermi level when an X-Ray source is used as the photon supplier. The core electron is excited.

2.2.2.2 Ultraviolet Photoelectron Spectroscopy

UPS is an analysis technique used in this study to determine the valence electronic structure of varying materials. Unlike XPS, UPS cannot be used to as an elemental identification method. However, UPS is used to determine the material's valance band maxima (VBM) and the ionization energy. Similarly to XPS, UPS can only analyze the near surface region because of escape depth of the photoelectrons is limited to ≈ 3 – 10 nm. The energy of the ultraviolet source used to cause photoelectrons to be emitted from the near surface region of the sample is typically 21.22 eV (He I) or 40.81 eV (He II).

Due to the lower photon energy valence electrons are primarily excited and released, Fig. 17.

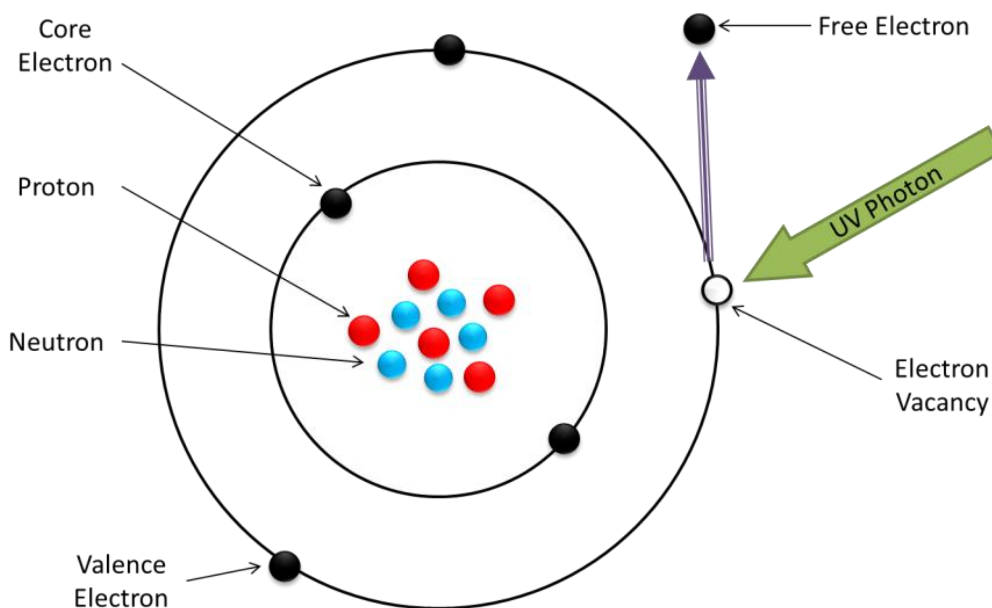

Fig. 17. Photoelectron generation using a UV photon source during ultraviolet photoelectron spectroscopy (UPS). The valence electron is excited.

In this study UPS spectra were recorded using He (I) UV-ray source (hν = 21.2 eV), hybrid optics (employing a magnetic and electrostatic lens simultaneously) and a multi-channel plate and delay line detector coupled to a hemispherical analyzer. The photoelectrons take-off angle was normal to the surface of the sample and 45° with respect to the UV beam. All spectra were recorded using a single sweep and an aperture slot of ~1000x1000 microns, and high resolution spectra were collected with a pass energy of 5 eV. The pressure in the analysis chamber was typically $4x10^{-9}$ Torr during all data acquisition. The Fermi level energy of the system was located using linear-regression at the valence-band edge of a sputtered gold foil sample.

2.2.2.3 Experimental Set-up

The cleaned GaN sample was mounted and inserted into the load lock chamber within 10 min of the aq-HCl clean. All samples were mounted on a sample plate with copper foil in contact with the top of the samples to ensure electrical grounding. Gold samples were loaded with each set of samples to acquire the reference Fermi level. The charge neutralizer was turned on. XPS survey scans were taken once the samples were loaded into the analysis chamber using the Al Kα line (1486.6 eV). UPS spectra of the four samples was acquired without the charge neutralizer following the XPS survey scans for all samples using a He I line (21.22 eV). The analyzer was biased 9.0 V with respect to the sample in order to overcome the work function of the system. With the charge neutralizer turned on, individual C 1*s*, N 1*s*, O 1*s*, Ga 2*p*, Ga 3*d* and Al 2*p* (for Al_2O_3 samples only) scans of all samples were recorded following the UPS scans. The core-level positions and intensities were acquired by linear background subtraction and fitting to a Gaussian line shape using the CasaXPS software resulting in peak positions within ± 0.1 eV uncertainty.

2.2.2.4 Band Offset Measurements Using Photoemission

A background of band alignments is needed prior to an explanation of band offset measurements using photoemission. There are three types of band alignments, Type I, Type II and Type III, illustrated in Fig. 18. Type I and type II are the most

common, however all three will be reviewed in this chapter. The band alignment at a heterojunction interface, such as GaN/AlGaN, controls the dynamics of how charge carriers flow. Band alignment at a dielectric/semiconductor interface, such as HfO_2/AlGaN or HfO_2/GaN, can also affect the dynamics of how charge carriers flow if the semiconducting material has spontaneous and piezoelectric polarizations, such as GaN and AlGaN. A dipole at the dielectric/AlGaN interface will affect the dipole in the AlGaN material which will in turn affect the overall dipole at the AlGaN/GaN interface resulting in a change in the flat band and threshold voltages for high electron mobility transistors. A dipole at the dielectric/GaN interface will also affect the polarization fields in the GaN as well.

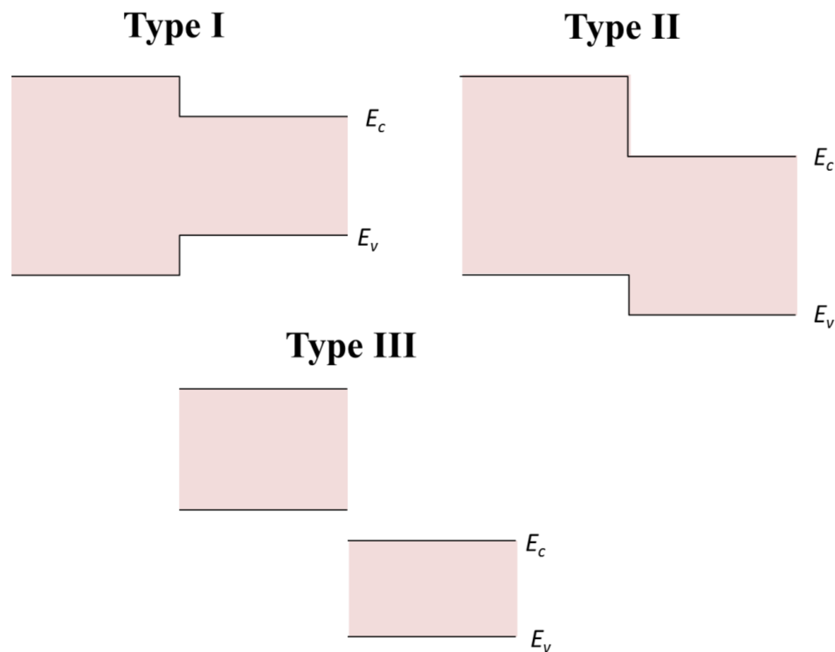

Fig. 18. Figurative representation of Type I, Type II and Type III band alignments.

Every solid material has its own energy band structure resulting in three main types of materials, insulators, semiconductors and conductors. In this chapter only the

band structures of insulators and semiconductors are discussed. An overview of the electronic structure of materials using band theory of solids can be found in the following references, (*3, 49-51*). When atoms are brought together, the outermost energy levels of the individual atoms are split into discrete energy levels. These levels overlap with energy levels from neighboring atoms, which results in the atomic spacing to decrease and the energy levels to combine to form an energy band. The energy band defines the electronic states that the electrons can occupy. As the atoms shift, or move closer or farther away from each other, to lower energies, equilibrium is established and the energy bands split to form the conduction and valence bands.

For insulators, the electrons in the valence and conduction bands are separated by a large energy gap, i.e. bandgap. In semiconductors, the conduction and valence bands are separated by a smaller bandgap. Due to the small bandgap found in semiconductors, thermal or other excitations can cause electrons to bridge the gap, hence the name semiconductor. An important parameter that enables semiconductors to conduct some current is the Fermi Level. The Fermi level is the top of the available electron energy levels at low temperatures. The Fermi level comes from Fermi-Dirac statistics. If the reader wishes to obtain a better understanding of the Fermi Level the author suggests the following references, (*50-52*).

The work function, Φ, of a semiconductor is defined as the difference in energy from the Fermi level at the surface of the semiconductor to the vacuum level. Since the Fermi level is dependent on the doping of the semiconductor, the work function of a semiconductor will not have a unique value. Therefore, the work function of a semiconductor does not accurately describe the energy relations of the bands to the vacuum energy for one particular material. The electron affinity, χ, is a more appropriate quantity to represent the relation of the semiconductor band structure to the vacuum level. Electron affinity is defined as the energy difference between the conduction band minimum and the vacuum level, thus making the energy difference independent of the doping level (*53*). The electron affinities and bandgaps for some common semiconductors and dielectrics are given in Table 1.

Table 1. Experimental bandgap energies and electron affinities of common semiconductors and dielectrics. Values were compiled from the references next to the semiconductor names.

Semiconductor and Dielectric Materials	Bandgap (eV)	Electron Affinity (eV)
Si (*53*)	1.12	4.05
GaN (*54*)	3.39	4.1
SiO_2 (*55*)	9.0	0.9
Si_3N_4 (*55*)	5.3	2.1
ALD Al_2O_3 (*56, 57*)	6.4	1.35 – 1.5
ALD HfO_2 (*58*)	5.8	1.4 - 2.5

Two major quantities are used to describe the band alignment, the conduction band offset, CBO, and the valence band offset, VBO. The CBO is the difference between the conduction bands of the second material, $E_C^{(B)}$, minus the first material, $E_C^{(A)}$: $CBO = E_C^{(B)} - E_C^{(A)}$. The VBO is the difference between the valence bands of the first material, $E_V^{(A)}$, minus the second material, $E_V^{(B)}$: $VBO = E_V^{(A)} - E_V^{(B)}$. If both the CBO and VBO are either positive or negative then the band alignment is said to be Type I. If the CBO and the VBO have opposite signs and the CBO or VBO are not larger than the largest bandgap, then the band alignment is said to be Type II. If the CBO and the VBO have opposite signs and either the CBO or VBO are larger than the largest bandgap, then the band alignment is said to be Type III (*49*).

The calculation of band offsets using photoemission is a well-established method that has been previously reported (*33, 59-62*). The method used to determine the valence band and conduction band offset is similar to Waldrop and Grant (*62*) where the

valence band maxima is referenced to a core level in the XPS for each material and the difference between the core levels is used to determine the band discontinuities. However, in our studies UPS is used to determine the energy of the valence band maxima (VBM) from the Fermi level energy and XPS is used to measure the core level shifts relative to the Fermi level. In this research the valence and conduction band offsets, VBO and CBO, are expressed as the following

$$VBO = E_{VBM}^{2} - E_{VBM}^{1} + \Delta E_{Ga3d} \tag{1}$$

$$CBO = (E_{g}^{2} - E_{VBM}^{2}) - (E_{g}^{1} - E_{VBM}^{1}) + \Delta E_{Ga3d} \tag{2}$$

where E_{VBM}^{2} and E_{VBM}^{1} are the measured VBMs of the dielectric deposited on aq-HCl GaN and the substrate (aq-HCl GaN), respectively, E_{g}^{2} and E_{g}^{1} are the band gaps of the dielectric and GaN, respectively, and ΔE_{Ga3d} is the change in band bending defined by the shift of the Ga 3*d* core level. It is important to note that a shift in the N 1*s* core level also indicates band bending, thus ΔE_{Ga3d} can be replaced by $\Delta E_{N1s} = E_{N1s}^{1} - E_{N1s}^{2}$ if the change in the core level is larger for N 1*s* versus Ga 3*d* peaks (*33*). The electron affinities are determined using the ultraviolet photoelectron spectra.

2.2.3 Transmission Electron Microscopy

This section reviews transmission electron microscopy (TEM). TEM uses a high energy electron beam transmitted through a sample with a thickness of ≥ the mean free path of the primary electron to image and analyze the microstructure of materials within the sample with a resolution of 1 – 2 Å. The electrons are focused with electromagnetic lenses and the image is recorded with digital camera. The electrons are accelerated at several hundred kV, giving wavelengths much smaller than that of light: 200kV electrons have a wavelength of 0.025Å. TEMs can be used to determine the morphology and crystallographic information of a sample by using an electron beam to image the

sample. To use TEM the sample must have a thickness that is approximately equal to or thinner than the mean free path of the primary electron in the sample. For example at 100 keV the mean free path = 150 nm for carbon and 5 nm for gold. One of the benefits of TEM over scanning electron microscopy is that TEM uses transmitted electrons therefore the resolution is not limited by secondary electrons. The typical working distance for TEM is also much shorter than that of an SEM allowing for higher resolutions on the order of 1 to 2 Angstroms. A general overview of TEM can be found in the following reference (*63*).

2.3 Theoretical Techniques

The theoretical techniques used in this research are discussed. Sentaurus device is used to model the Si/SiGe heterojunction interface assuming a given set of parameters. The results of this modeling were used to fabricate devices.

Molecular orbital theory and density functional theory were also used in this research. There are two types of molecular systems that are used to determine the mechanisms of GaN oxidation and ALD of Al_2O_3 and HfO_2 on GaN: (1) three sets of GaN clusters with a finite number of atoms interacting with either oxygen or water and (2) three sets of hydrolyzed GaN clusters with a finite number of atoms interacting with either Trimethylaluminium (TMA) or Tetrakis-(ethylmethylamino)-hafnium (TEMAH). The geometries of the molecular systems were optimized using quantum chemistry by solving the Schrödinger equation, applying appropriate correlation and approximations factors, i.e. density functional theory (DFT).

This section discusses the Sentaurus device simulation package, *ab initio* molecular orbital theory, basis sets, density functional theory, and hybrid methods.

2.3.1 Sentaurus Device

Sentaurus Device is a multidimensional device simulator used to simulate electrical characteristics of compound and Si semiconductor devices. Sentaurus Device

is part of the Technology Computer-Aided Design (TCAD) simulation package offered by Synopsys. Further information regarding Sentaurus Device can be found at the following reference, (*64*).

2.3.2 *Ab initio* Molecular Orbital Theory

The energy of a molecule can be predicted by solving the Schrödinger equation

$$\mathrm{H}\,\Psi = E\,\Psi \tag{1}$$

where H is the Hamiltonian operator, E is the energy of the molecule and Ψ is the wave-function of the particles in the system.

The full Hamiltonian is made up of kinetic (T) and potential (V) energy terms and can be written as:

$$\mathrm{H} = T + V = T^{e}(\vec{r}) + T^{n}(\vec{R}) + V^{n-e}(\vec{R},\vec{r}) + V^{e}(\vec{r}) + V^{n}(\vec{R}) \tag{2}$$

where T is the quantum mechanical representation of the kinetic energy of all nuclei and electrons, V is the electrostatic attraction and repulsion of the electrons and nuclei, T^n is the kinetic energy of the nuclei, T^e is the kinetic energy of the electrons, $V^{n\text{-}e}$ is the mutual electrostatic attraction of the electrons and the nuclei, V^e is the electrostatic repulsion among the electrons, and V^n is the electrostatic repulsion among the nuclei.

The nuclear kinetic energy term in Eq. 2, T^n, is neglected when using the Born-Oppenheimer approximation. This approximation considers that the mass of the nuclei is greater than the electron mass and therefore moves more slowly compared to the electrons. By using this approximation the Schrödinger equation can be solved using less complicated steps.

Using the proper boundary conditions and approximations, each possible solution of the time-independent Schrödinger equation corresponds to a different stationary state of the system. An example of a boundary condition is for a particle in a box with

infinitely high walls. The appropriate boundary condition for this example is that the wave function is required to go to zero at the walls (*65*). The stationary state of the system with the lowest energy is considered the ground state, i.e. the most stable state.

The solution to the Schrödinger equation is known as the spatial wavefunction. The spatial wavefunction is a function of the positions of the electrons ($\vec{r_i}$) and the nuclei ($\overrightarrow{R_I}$) and is independent of time. Molecular orbitals (MOs) can be expressed as linear combinations of the atomic orbitals. The linear combination approximation allows for approximate solutions to the molecular Schrödinger equations. Atomic orbitals, also known as the wave functions for a single electron in an atom, are solutions of the Hartree-Fock equations for a given atom. Atomic orbitals are also known as basis functions (*66*).

2.3.3 Basis Sets

For this work, Gaussian functions are used to form a complete set of functions. The general Cartesian Gaussian function is:

$$g(\alpha, \vec{r}) = cx^n y^m z^l e^{-\alpha r^2} \quad (3)$$

where n, m and l are positive integers, α is a positive orbital exponent, c is a normalization constant, r is the radial coordinate and x, y and z are the Cartesian coordinates with its origin located at the nucleus. For an example, when $n + m + l = 0$ then the Gaussian function is considered to be s-type. Linear combinations of these primitive Gaussians are used and called contracted Gaussian functions. Contracted Gaussian functions take the form of:

$$\chi_\mu = \sum_p d_{\mu p} g_p \quad (4)$$

where $d_{\mu p}$ are contraction coefficients and are fixed constants, while g_p are primitive Gaussian functions for a given basis set.

The Gaussian basis functions typically include polarization and diffusion functions through the additional of several primitives. In this dissertation the basis set used is the Los Alamos National Laboratory (LANL2DZ) basis set (*67, 68*).

2.3.4 Density Functional Theory

Calculating the wavefunction for molecules above a few atoms is computationally expensive. Density functional theory (DFT) simply states that the ground state properties of any multi-electron system can be described by simply using electron densities, or the probability an electron will be within a certain region. DFT is based on the Hohenberg-Kohn first theory (*69*), which established that properties in the ground state are functions of the electron density. The density is a variable of three degrees of freedom allowing for a reduced computation time. However to simplify the calculation even more, in 1965 Kohn-Sham (*70, 71*) demonstrated that the electron density of a system of interacting electrons can be represented with the electron density of an equivalent system of non-interactive electrons subjected to an effective external potential. A more detailed description of density functional theory can be found in the following references, (*65, 69-73*).

2.3.5 Hybrid Methods

Hybrid methods are a class of approximations used in density functional theory. Hybrid methods were first introduced by Axel Becke (*74*). By using the hybrid method some of the molecule properties are modeled more accurately, including bond lengths and vibrations. The DFT B3PW91 hybrid functional includes a combination of the Perdew-Wang-91 (*75, 76*) and has shown good energetics predictions (*77, 78*). To learn more about hybrid methods the author directs the reader to the following texts, (*74, 79-82*).

CHAPTER III
INTEGRATION OF HETEROJUNCTIONS INTO EFFECTIVE WORK FUNCTION CALCULATION[*]

In this chapter, the effects of a heterojunction on the effective work function in a metal/high-κ gate stack are studied and a new structure developed for the extraction of the work function. It is found that when a Ge/Si heterostructure on silicon is low doped and sufficiently thin, then the work function can be extracted in a manner similar to that on a simple silicon substrate. Modifications to the terraced oxide structure are proposed to remove oxidation effects of the alternate channel materials. The extracted work function of thickness variation of TiN is found to be in agreement with that of TiN on a silicon substrate.

3.1 Introduction

Alternate channel materials (ACM) have been the focus of recent research for CMOS applications, primarily with the goal of capitalizing on high mobility. Ge can be incorporated in a surface channel configuration to improve hole mobility and achieve low PMOS threshold voltage in Si CMOS, while more complex heterostructures of III-V materials can be used for higher electron mobility in NMOS devices (*15, 16*). Achieving enhancement mode operation and tuning the threshold voltage with different metal gates is a paramount concern for any ACM used. Thus an understanding of the effect of non-native metal/oxide gate stacks on heterostructures is important in introducing ACMs to the current technology landscape.

---

[*] Reprinted with permission from "Work Function Extraction of Metal Gates with Alternate Channel Materials" by M. Coan, D. Johnson, J. H. Woo, N. Biswas, V. Misra, P. Majhi, and H. R. Harris, 2012, *Journal of Vacuum Science & Technology B: Microelectronics and Nanometer Structures*, vol. 30, pp. 022202-5. Copyright 2012 by the American Institute of Physics. The article may be found at (http://avspublications.org/jvstb/resource/1/jvtbd9/v30/i2/p022202_s1).

Previous methods of extracting the work function on Si capitalized on the quality of the native SiO_2 to vary the equivalent oxide thickness (*18, 19, 83*). However, the thermal oxides of ACMs are unstable and chemically undesirable for an MOS structure (*84*). Thus the use of a deposited high-κ dielectric with minimal thermal stress is important for realizing working enhancement mode devices. The work function of the metal is an important parameter in the device operation, but we know from years of difficult research probing the work function of metals in high-κ/metal gate devices that it may be difficult to precisely design the threshold voltage. Second, the heterostructures are not necessarily simple, complicating the work function extraction. According to S.C. Song, et al and references therein, the work function could vary with the underlying substrate due to oxygen vacancies within the high-κ at the high-k/metal interface resulting in the formation of a dipole (*85*). This dipole causes the Fermi level of the gate metal to shift, thus varying the effective work function. These vacancies can be filled with oxygen from the lower portion of the high-κ layer. Oxygen can transport from the bottom oxide to the high-κ due to the oxidation enthalpy difference. However, if the bottom oxide is below a certain thickness the reverse oxygen transport will occur resulting in an increase in the oxygen vacancies within the high-κ. Therefore, if the substrate forms an interfacial oxide layer the high-κ will form oxygen vacancies resulting in a change in the effective work function (*86*). However, high-κ dielectrics in contact with Ge, for example, do not form significantly thick interfacial GeO_x layers, resulting in fewer oxidation vacancies in the high-κ layer (*87*).

Ge in PMOS devices can have a strained Si_xGe_{1-x} layer on Si followed by a Si interlayer to improve the interface between the high-κ and the Si_xGe_{1-x} layer (*14*). Similarly, recent research involving MOS capacitors on GaAs, with high-κ dielectric stacks using Si as an interface passivation layer between GaAs and HfO_2, have been reported (*17*). In this work, the SiGe/Si heterostructure is used to examine the effects of heterostructure and high-κ material on work function extraction. The terraced dielectric method is modified to account for the additional charges at the heterojunction and changes in the space charge of the semiconductor materials (*18, 83*).

3.2 Theoretical Equations

Fig. 19 illustrates the overall physical gate stack/heterostructure, while Fig. 20 and Table 2 denote the charges potentially affecting the flat band voltage (V_{FB}) for this system. Although efforts were made to minimize the formation of a high-κ/SiGe interfacial dielectric, subsequent thermal processing requires that it be taken into account (*88*). The equation that relates V_{FB} to the charges at the SiO_2/Si interface per unit area, $Q_{f\left(\frac{SiO_2}{Si}\right)}$, the SiO_2 gate dielectric charge distribution per unit volume, $\rho_{b(SiO_2)}(x)$, and *EOT*, can be found in Jha, *et al*, and is extended to a heterojunction substrate (*18*).

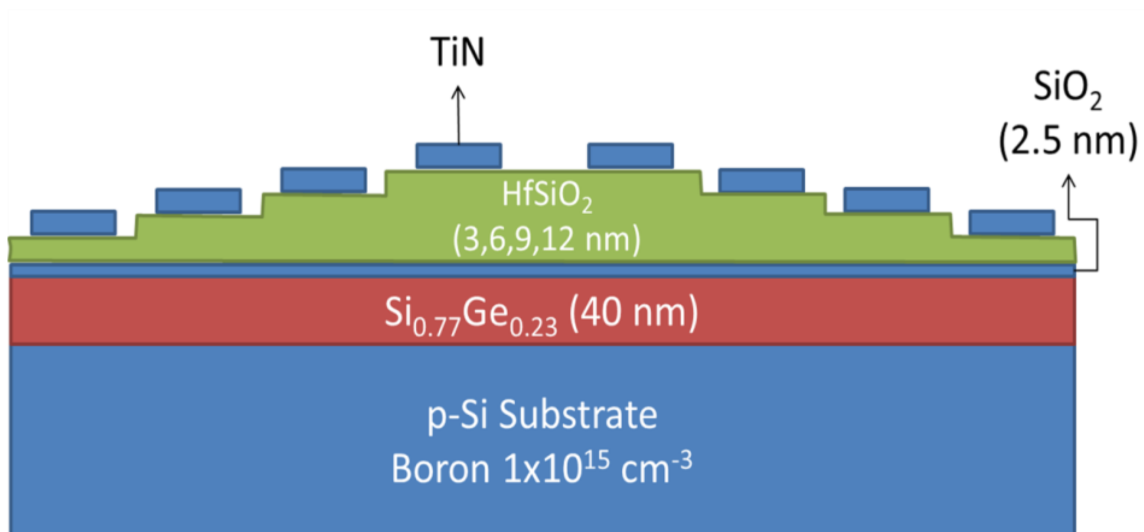

Fig. 19. Schematics of $HfSiO_2/SiO_2$/SiGe/p-Si stack.

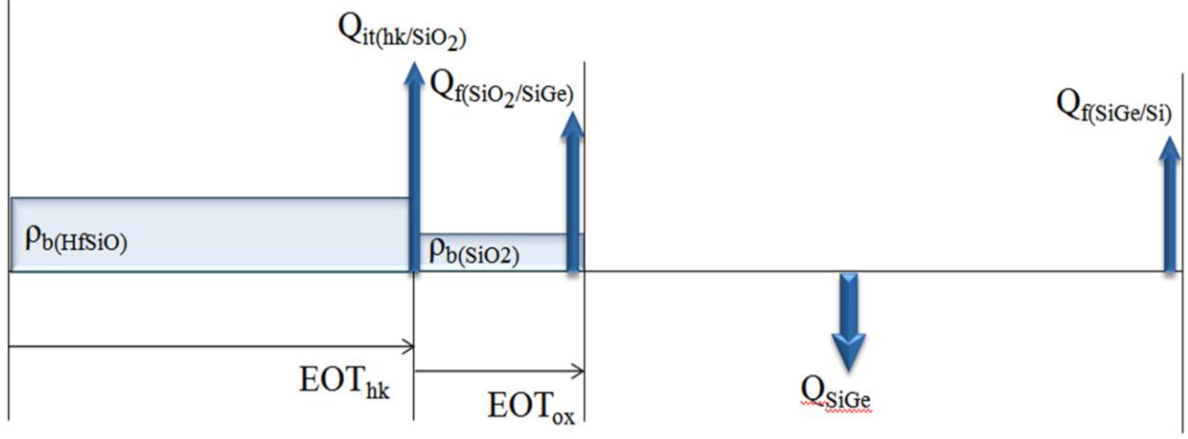

Fig. 20. Charge schematic of $HfSiO_2/SiO_2$/SiGe/p-Si stack. The variables shown are defined in Table 2 and throughout the text.

Table 2. Tabulation of charges potentially affecting the flat band voltage including the symbols used to represent the charges throughout the paper along with assumptions regarding the charges explained within the paper.

Charges Potentially Affecting V_{FB}	Symbol	Assumptions
Bulk $HfSiO_2$ layer	$\rho_{b(HfSiO_2)}$	$\rho_{b(HfSiO_2)} = 0$
High-κ/SiO_2 Interface	$Q_{it\left(\frac{HfSiO_2}{SiO_2}\right)}$	$Q_{it(\frac{HfSiOx}{SiO2})} \gg \rho_{b(HfSiO)} EOT_{hk}$ & $Q_{it(\frac{HfSiOx}{SiO2})} \cong 0eV$
Bulk SiO_2 Interfacial layer	$\rho_{b(SiO_2)}$	$\rho_{b(SiO_2)} = 0$
$SiO_2/Si_{0.77}Ge_{0.23}$ Interface	$Q_{f(\frac{SiO2}{SiGe})}$	$Q_{f(\frac{SiO2}{SiGe})} \gg \rho_{b(SiO_2)} EOT_{ox}$
Space Charge in the $Si_{0.77}Ge_{0.23}$	Q_{SiGe}	$Q_{SiGe} \neq 0$
$Si_{0.77}Ge_{0.23}$/Si Interface	$Q_{f(\frac{SiGe}{Si})}$	$Q_{f\left(\frac{SiGe}{Si}\right)} \cong 0$
Space Charge in the Si	Q_{Si}	$Q_{Si} = 0$

ε_{SiO_2} is the permittivity of SiO_2 and Φ_{ms} is the work function difference between the gate and the substrate, the high-κ, $HfSiO_2$, gate dielectric charge distribution per unit volume is $\rho_{b(HfSiO_2)}(x)$, the $HfSiO_2$ dielectric EOT is defined as EOT_{hk}, the SiO_2 dielectric effective oxide thickness is defined as EOT_{ox}, and $EOT = EOT_{hk} + EOT_{ox}$. A bilayer stack is a reasonable assumption based on previous materials characterization of this gate stack (*89*). If $Q_{f\left(\frac{SiO_2}{SiGe}\right)} >> \rho_{b(SiO_2)} EOT_{ox}$ and $Q_{it\left(\frac{HfSiO_2}{SiO_2}\right)} >> \rho_{b(HfSiO_2)} EOT_{hk}$, then $\rho_{b(SiO_2)} = \rho_{b(HfSiO_2)} = 0$ (*18*). For the system being considered, a more extensive equation is required to account for the bilayer stack, $HfSiO_2/SiO_2$, and the heterojunction, $Si_{0.77}Ge_{0.23}/Si$. Ja, *et al*'s bi-layer dielectric stack capacitor equation can be rewritten to incorporate the heterojunction and the interfacial trapped charge per unit area at the $HfSiO_2/SiO_2$ interface, $Q_{it\left(\frac{HfSiO_2}{SiO_2}\right)}$ as:

$$V_{FB} = (\Phi_{ms}) - \left[\frac{Q_s}{\varepsilon_{SiO_2}} + \frac{Q_{f\left(\frac{SiO_2}{SiGe}\right)}}{\varepsilon_{SiO_2}} \right] EOT - \frac{Q_{it\left(\frac{HfSiO_2}{SiO_2}\right)}}{\varepsilon_{SiO_2}} EOT_{hk} \tag{1}$$

$$\text{where } Q_s = Q_{Si} + Q_{SiGe} = (-\varepsilon_{Si} E_{Si}) + (-\varepsilon_{SiGe} E_{SiGe}) \tag{2}$$

Q_s is the semiconductor space charge per unit area and takes into account the space charge in both the substrate (Q_{Si}) and semiconductor layer (Q_{SiGe})Q_{SiGe}, (ε_{Si}: permittivity of Si, E_{Si}: surface perpendicular electric field of Si, ε_{SiGe}: permittivity of $Si_{0.77}Ge_{0.23}$, E_{SiGe}: surface perpendicular electric field of $Si_{0.77}Ge_{0.23}$). The elementary charge is included in Φ_{ms}. In the case of a lightly doped substrate and an intrinsically doped SiGe layer, Q_{Si} is assumed to be zero. This is a reasonable assumption as will be shown later in the chapter. Equation (1) can be written as:

$$V_{FB} = (\Phi_{ms}) - \frac{Q_{it\left(\frac{HfSiO_2}{SiO_2}\right)}}{\varepsilon_{SiO_2}} EOT_{hk} - \left[\frac{-\varepsilon_{\mathrm{SiGe}} \mathrm{E}_{\mathrm{SiGe}}}{\varepsilon_{SiO_2}} + \frac{Q_{f\left(\frac{SiO_2}{SiGe}\right)}}{\varepsilon_{SiO_2}} \right] EOT \quad (3)$$

If EOT_{hk} is kept constant and *EOT* varies by only changing EOT_{ox}, then V_{FB} is a function of *EOT*. Equation (3) can also be written in terms of *EOT* and EOT_{ox} as:

$$V_{FB} = (\Phi_{ms}) + \frac{Q_{it\left(\frac{HfSiO_2}{SiO_2}\right)}}{\varepsilon_{SiO_2}} EOT_{ox} + \left[\frac{\varepsilon_{\mathrm{SiGe}} \mathrm{E}_{\mathrm{SiGe}}}{\varepsilon_{SiO_2}} + \frac{-Q_{f\left(\frac{SiO_2}{SiGe}\right)}}{\varepsilon_{SiO_2}} - \frac{Q_{it\left(\frac{HfSiO_2}{SiO_2}\right)}}{\varepsilon_{SiO_2}} \right] EOT \quad (4)$$

Thus V_{FB} is a linear function of *EOT* with a slope of $\left[\frac{\varepsilon_{\mathrm{SiGe}} \mathrm{E}_{\mathrm{SiGe}}}{\varepsilon_{SiO_2}} + \frac{-Q_{f\left(\frac{SiO_2}{SiGe}\right)}}{\varepsilon_{SiO_2}} - \frac{Q_{it\left(\frac{HfSiO_2}{SiO_2}\right)}}{\varepsilon_{SiO_2}} \right]$ and a y-intercept of $\left[(\Phi_{ms}) + \frac{Q_{it\left(\frac{HfSiO_2}{SiO_2}\right)}}{\varepsilon_{SiO_2}} EOT_{ox} \right]$. Compared to the relationship between the V_{FB} and *EOT* for a bilayer stacked capacitor (*18*), the addition of Q_s for a bilayer stacked heterojunction capacitor does not theoretically affect the work function calculation.

3.3 Experiment Methodology

A 200 mm Si substrate with p-type doping density of 1×10^{15} cm^{-3} was used as the platform for capacitor formation. Using field isolation dielectrics, 30 nm of $Si_{1-x}Ge_x$ with x = 0.23 was selectively grown. Given that native oxide on Ge is unfavorable; a pre-clean process (*89*) was employed followed by a 15 nm thick atomic layer deposition (ALD) Hf dielectric layer. However, due to the inherently small variation in capacitance with thickness in high-κ materials such as HfO_2, a lower-κ dielectric was employed by incorporating cycles of Si in the ALD process to achieve a Si/Hf ratio of 3/2. Using a

circular injection etch process previously described (*19*), portions of the dielectric were etched back to 10, 8, 6 and 4 nm. Following an NH_3 anneal process at 700°C to reduce leakage current, varying thickness of ALD TiN metal gate was deposited and patterned. The subsequent capacitance-voltage curves were collected and numerically modeled using the NCSU CVC program for flat band voltage (V_{FB}) and equivalent oxide thickness (*EOT*) (*90*), taking into account substrate material difference. Error in numerical modeling (actual versus modeled C-V) is below 3% in all cases, with most error arising from gate leakage in accumulation. The data was correlated with spatially-dependent dielectric thickness to verify extraction of appropriate *EOT*.

3.4 Results and Discussion

With the introduction of the heterostructures that complicates the classical capacitive extraction of work function, we have to understand how the depletion region will form in a metal/dielectric/heterostructure (MOH) device. Reasonable understanding of the depletion region around the heterostructure will assist us in better determining an appropriate initial substrate doping that will alleviate complications during work function extraction calculations. To this end, we employ numerical simulations of the MOH device, extract depletion region extension into the substrate and examine how this impacts the work function methodology.

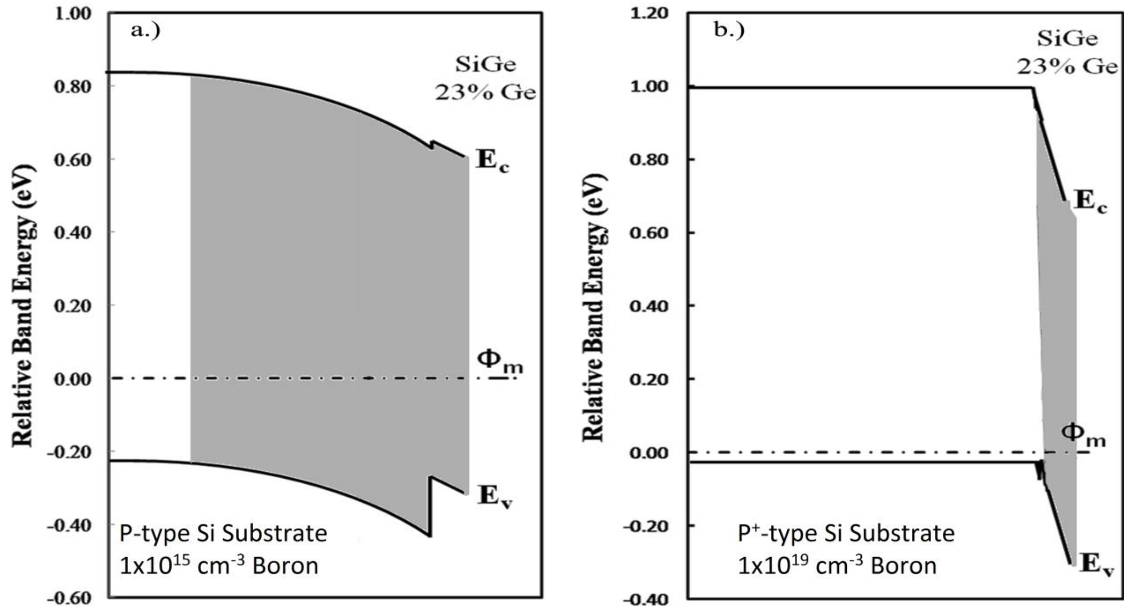

Fig. 21. Schematic band diagrams of the SiGe/p-Si heterojunction with Si substrate Boron doping concentrations of (a) 1×10^{15}cm^{-3} and (b) 1×10^{19}cm^{-3} at $V_g = 0$ V. The depletion region is shaded.

Fig. 21 shows schematic band diagrams of the heterojunction at $V_g = 0$ V for a p-Si substrate ($N_a = 1x10^{15}/cm^3$) and p^+-Si substrate ($N_a = 1x10^{19}/cm^3$). For the p-Si substrate, the low doping concentration causes the depletion region of the device to fall significantly into the p-Si substrate. Such a large depletion region causes the surface potential of Si to be much larger than that of SiGe, $\Phi_{Si} >> \Phi_{SiGe}$. In the case of the p^+-Si substrate, the doping concentration causes the depletion region to remain primarily in the SiGe layer. The notably thinner depletion region causes the surface potential of Si to be much smaller than that of SiGe, $\Phi_{Si} << \Phi_{SiGe}$. Significant differences in surface potentials for both doping concentrations results in the summation of surface potential for either case to never reach zero. Thus, the flat band voltage condition $\varepsilon_s E_s = \varepsilon_{Si} E_{Si} + \varepsilon_{SiGe} E_{SiGe} = 0$ C/cm^2 does not apply in the case of significant differences in surface potentials at the heterojunction, Equation (2). Therefore, apparent flat band voltage will occur when $\varepsilon_{Si} E_{Si} = 0$ C/cm^2 and $\varepsilon_{SiGe} E_{SiGe} \neq 0$ C/cm^2 for the p-Si substrate (N_a =

$1x10^{15}/cm^3$) and $\varepsilon_{Si}E_{Si} \neq 0$ C/cm^2 while $\varepsilon_{SiGe}E_{SiGe} = 0$ C/cm^2 for the p$^+$-Si substrate (N_a = $1x10^{19}/cm^3$).

As previously stated for the experimental device in this chapter the $Q_{Si} = 0$, which leads to the simplification from Equation (1) to Equation (3). This simplification is valid due to depletion region of the device falling significantly into the p-Si substrate, as shown in Fig. 21. Such a large depletion region causes the surface potential of Si to be much larger than that of SiGe, $\Phi_{Si} >> \Phi_{SiGe}$, allowing for the simplified work function extraction. Equation (1) takes into account other doping concentrations and is not limited to a low doped substrate.

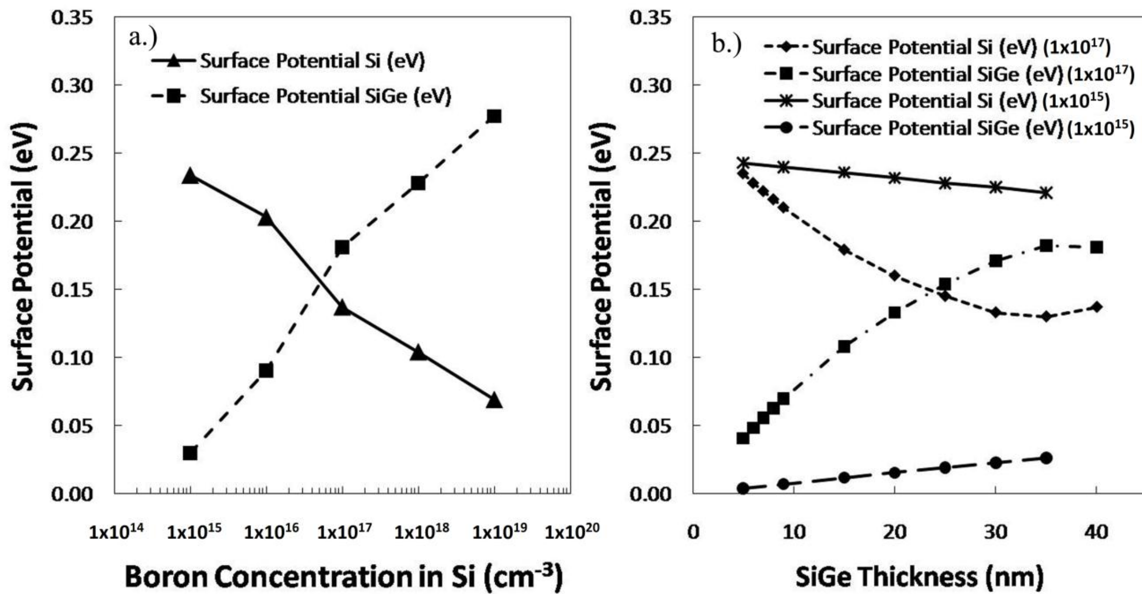

Fig. 22. Dependence of the Si and SiGe Surface Potentials on the (a) doping concentration of Si for the TiN/HfO_2/SiO_2/SiGe with a SiGe thickness of 40 nm and (b) thickness of SiGe for the TiN/HfO_2/SiO_2/SiGe with a doping concentration of $N_a = 1 \times 10^{15}/cm^3$ and $1 \times 10^{17}/cm^3$. All simulations were run using a HfO_2 thickness of 6 nm.

To better understand the effect of heterojunction doping and thickness, the effect of surface potential on doping was studied using the Sentaurus Device simulation tool.

As seen in Fig. 22, the surface potential of Si decreases while the surface potential of SiGe increases as the doping concentration increases due to the decrease in the depletion region. For doping concentrations near and including $1x10^{17}/cm^3$ the difference between the surface potential of Si and SiGe is relatively small leading to the typical flat band voltage condition, $\varepsilon_s E_s = 0$ C/cm^2, to apply, resulting in Equations (3) and (4) to be modified to Equations (5) and (6), respectively.

$$V_{FB} = (\Phi_{ms}) - \frac{Q_{it\left(\frac{HfSiO_2}{SiO_2}\right)}}{\varepsilon_{SiO_2}} EOT_{hk} - \left[\frac{Q_{f\left(\frac{SiO_2}{SiGe}\right)}}{\varepsilon_{SiO_2}}\right] EOT \quad (5)$$

$$V_{FB} = (\Phi_{ms}) + \frac{Q_{it\left(\frac{HfSiO_2}{SiO_2}\right)}}{\varepsilon_{SiO_2}} EOT_{ox} + \left[\frac{-Q_{f\left(\frac{SiO_2}{SiGe}\right)}}{\varepsilon_{SiO_2}} - \frac{Q_{it\left(\frac{HfSiO_2}{SiO_2}\right)}}{\varepsilon_{SiO_2}}\right] EOT \quad (6)$$

Another important parameter to surface potential is the semiconductor thickness. For low doped Si ($N_a = 1x10^{15}/cm^3$), as SiGe thickness increases from 5 nm to 40 nm the surface potential of Si decreases while the surface potential of SiGe increases, Fig. 22(b). This was expected due to the shift in the location and length of the depletion region as the thickness of SiGe is increased. For $N_a = 1x10^{17}/cm^3$, the surface potentials follow the same trend as the low doped Si, however, the rate of change in the surface potential decreases as SiGe increases in thickness, Fig. 22(b) (*91*).

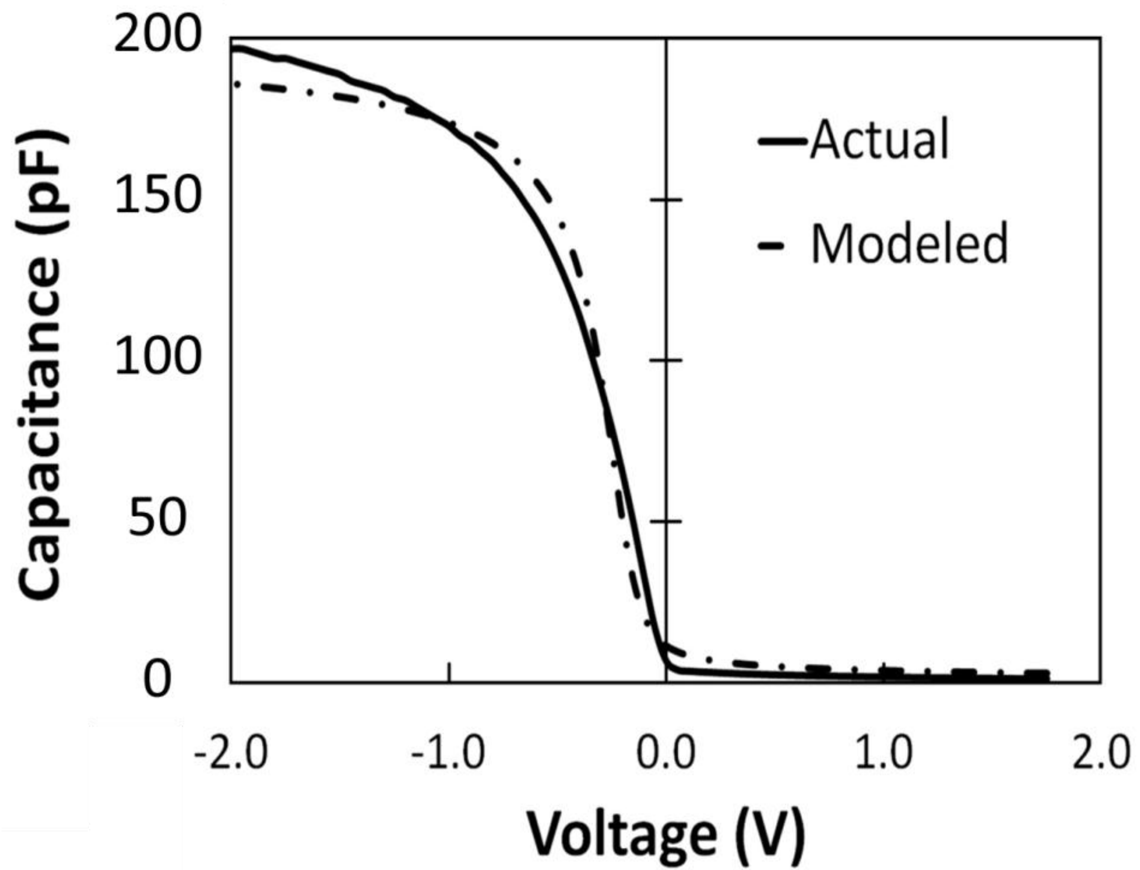

Fig. 23. C-V curve corresponding to a specific EOT device with a heterojunction plotted against a simulated device with the same EOT without a heterojunction using SiGe as the substrate.

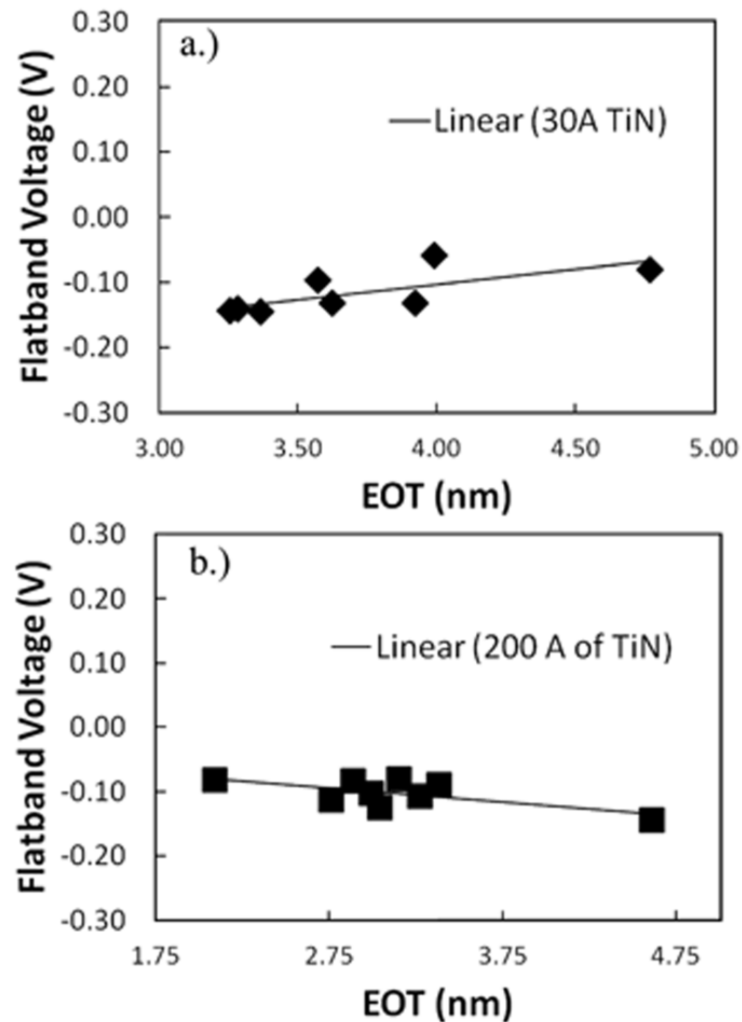

Fig. 24. Flat band voltage vs. *EOT* for effective work function extraction of devices with fixed interfacial SiO_2 layer, varying $HfSiO_2$ layers and a TiN contact thickness of (a) 3 nm and (b) 20 nm.

Following the simulation results for suggested Si doping, devices were developed with low Si doping density. The SiGe thickness was increased to test the efficiency of this technique. A thickness variation of TiN was chosen as the metal gate because the extracted work function of TiN for varying thicknesses is well understood in the Si/HfO_2 system (*83*). Fig. 24(a) and Fig. 24(b) show the V_{FB} versus *EOT* curves for devices with varying $HfSiO_2$ layer and either a 3 nm or 20 nm thick TiN contact, respectively. The V_{FB} versus *EOT* curves are fit to a straight line using "least square fit (*18*)." The linear

relationship suggests minimal influence from the high-κ bulk charge density, $\rho_{b(HfSiO_2)}$ (*83*). The extracted effective work function (EWF) for a 3 nm and 20 nm thick TiN contact device is 4.27 ± 0.07 eV and 4.53 ± 0.03 eV, respectively, using Equation (4). Inconsistencies in the intrinsic epitaxial SiGe carrier densities due to auto doping and defects have been described in literature (*92*). For this reason, the effective work function was calculated for several intrinsic concentrations to demonstrate its minimal impact on the EWF extraction. The results are shown in Table 3. The error was calculated by determining the standard error of the y-intercept and slope of the best linear fit with 68% confidence, in accordance with the error calculated in Jha, *et al* (*18*). The calculated EWFs are within 5% error of previously published data for a TiN/$HfSiO_2$/SiO_2/Si stack, Table 3 (*83*). It was assumed that $Q_{it\left(\frac{HfSiO_2}{SiO_2}\right)} \cong 0$ #/cm^2 (*83*).

The linear relationship of the data and accuracy of the calculated results indicate that heterojunction and substrate doping-optimized test structures can be used to evaluate the effect of work function in heterostructure systems, Fig. 23 and Fig. 24. The defect density and heterojunction quality can be discerned by other experimental methods.

Table 3. Tabulation of the numerical values of the variables used in this work. The charges located at the $HfSiO_2$/SiO_2 interface, SiO_2/Si interface + permittivity of SiGe multiplied by the surface perpendicular electric field of SiGe and the extracted effective work function values using Equation (4) using different values for the intrinsic concentrations. This analysis indicates that the calculated effective work function is within 5% of the reference.

	20 nm Thick TiN			3 nm Thick TiN		
n_i (cm^{-3}) (*92*)	5.1x10^{10}	1.0x10^{11}	4.6x10^{12}	5.1x10^{10}	1.0x10^{11}	4.6x10^{12}
E_c-E_i (eV)	0.521	0.503	0.404	0.521	0.503	0.404
$Q_{it\left(\frac{HfSiO_2}{SiO_2}\right)}$		≈ 0 #/cm^2			≈ 0 #/cm^2	
$\varepsilon_{SiGe}E_{SiGe} - Q_{f\left(\frac{SiO_2}{SiGe}\right)}$		- 4.75x10^{11}± 2.02x10^{11} #/cm^2			- 1.00x10^{12}± 4.10x10^{11} #/cm^2	
Ref Φ_m (eV) (*83*)		4.70			4.45	
Φ_m (eV)	4.53±0.03	4.51±0.03	4.41±0.03	4.27±0.07	4.25±0.07	4.15±0.07
% Error	3.7	4.1	6.2	4.1	4.4	6.7

3.5 Summary and Conclusions

The effect of a SiGe/Si heterostructure on the extraction of work function is evaluated. Modifications to the terraced oxide EWF extraction method were implemented by adaptation of lower-κ Hf-containing dielectric to realize an appropriate level of effective oxide thickness change. Device simulations were used to find appropriate doping profiles for EWF extraction. The resulting structures with ALD TiN show excellent agreement with published literature values of EWF as the TiN thickness is varied.

3.6 Acknowledgements

Financial support from the National Excellence Fellowship and NSF grant #1028910 and #0901699 is gratefully acknowledged.

CHAPTER IV
BAND OFFSET MEASUREMENTS OF THE GaN/DIELECTRIC INTERFACES*

With the knowledge of the effect of the heterostructure on the effective work function extraction calculation completed a better understanding of the chemical states at the dielectric/ACM is needed. X-ray and ultraviolet photoelectron spectroscopy are used to observe the interface electronic states at the GaN (0001) and high-κ dielectric interfaces. GaN was chosen as the alternate channel material based on the polarization effects of GaN and recent research regarding HEMTs has resulted in the deposition of a thin GaN layer on top of the AlGaN/GaN HEMTs prior to high-κ/metal gate stack deposition (*93, 94*). The GaN is aqueous HCl cleaned prior to atomic layer deposition of Al_2O_3 and HfO_2, then followed by a post deposition anneal. The GaN/HfO_2 and GaN/Al_2O_3 interfaces exhibited dipoles of 1.6 eV and 0.4 eV ± 0.2 eV, respectively. It is found that the formation of an interfacial layer at the GaN/HfO_2 interface is the primary cause of the larger dipole.

4.1 Introduction

Currently, enhancement-mode (E-mode) III-N-based devices are needed for analog applications and low-loss high-voltage switching. To achieve E-mode III-N-based devices, the threshold voltage (V_{th}) must be controlled, i.e. positive or negative and within a certain voltage range depending on doping or heterostructures engineering. One of the potential methods to control the V_{th} is using a metal/high-κ dielectric stack in place of a Schottky gate, and varying the work function of the gate metal (*27, 95, 96*). To accomplish this task, a better understanding of the band alignment, including dipole formation, at the III-N/dielectric interface is needed. The III-N/ high-κ interface has

*Parts of this chapter have been submitted to the *Journal of Applied Physics*.

been shown to influence the work function of the gate metal and therefore the threshold voltage (*27, 29*). Many III-N-based devices with varying gate stacks using high-κ materials such as HfO_2 and Al_2O_3 have been studied (*26, 27, 30-32*). However, previous experiments only use X-ray photoelectron spectra (XPS) to determine the band offsets (*34, 35*). UPS is needed to accurately determine the valence band offset between III-N/dielectric due to precision issues with XPS at low binding energies (*97*).

Typical experimental procedures for determining the band offsets of a high-κ dielectric on GaN require the GaN to be cleaned using in situ surface cleaning methods (*33, 98*). However, *in situ* surface cleaning is not always practical when fabricating GaN-based devices since wet chemistry is used to remove the native oxide on the GaN surface (*98*). Aqueous HCl (aq-HCl) is commonly used to remove the GaN native oxide (*34, 35, 98*). Therefore, the authors use aq-HCl to remove the GaN surface oxide prior to photoelectron measurements and dielectric depositions to explore the impact of this pre-clean on the interfacial dipole formation. We present X-ray photoelectron spectra (XPS) and UV photoelectron spectra (UPS) of GaN/HfO_2 and GaN/Al_2O_3. The position and origin of the interfacial dipoles are discussed.

4.2 Experimental Methodology

The unintentionally doped (0001)-oriented GaN samples were grown on sapphire substrates by hydride vapor phase epitaxy (HVPE) with a thickness of ~ 5 μm ± 1.5 μm, a resistivity < 0.5 Ohm-cm, a dislocation density < $1x10^9$ cm^{-2}, and a carrier concentration of ~ $10x10^{17}$ cm^{-3} (*99*). Further information regarding the growth of GaN has been previously published (*99*). All GaN samples were immersed for 15 min in a solution of HCl (~ 6 M) and rinsed using DI water, prior to the introduction of the GaN sample to ultra-high vacuum (UHV) analysis chamber (for reference analysis) or atomic layer deposition (ALD) chamber for high-κ deposition. The high-κ HfO_2 film with a thickness of 3 nm was grown by ALD using Tetrakis(ethylmethylamino)hafnium (TEMAH) and water at a chamber temperature of 200 °C. The high-κ Al_2O_3 film with a

thickness of 3 nm was grown by ALD using Trimethylaluminium (TMA) and water with a chamber temperature of 250 °C. The post deposition anneal (PDA) treatment at a temperature of 700 °C for 1 min in N_2 ambient was carried out for all high-κ deposited samples.

Ex situ XPS and UPS were performed. XPS spectra were recorded using a monochromated Al-K_{α} X-ray source (hν = 1486.5 eV), hybrid optics (employing a magnetic and electrostatic lens simultaneously) and a multi-channel plate and delay line detector coupled to a hemispherical analyzer. The photoelectrons take-off angle was normal to the surface of the sample and 45° with respect to the X-ray beam. All spectra were recorded using a single sweep and an aperture slot of 300 x 700 microns, and high resolution spectra were collected with a pass energy of 20 eV. Error analysis of the XPS data was completed by monitoring the XPS spectra of a clean gold sample. UPS spectra were recorded using He (I) UV-ray source (hν = 21.2 eV), hybrid optics (employing a magnetic and electrostatic lens simultaneously) and a multi-channel plate and delay line detector coupled to a hemispherical analyzer. The photoelectrons take-off angle was normal to the surface of the sample and 45° with respect to the UV beam. All spectra were recorded using a single sweep and an aperture slot of ~ 1000 x 1000 microns, and high resolution spectra were collected with a pass energy of 5 eV.

Error analysis of the UPS data was completed by monitoring the valence band maxima region of a clean gold sample. Due to the fitting of the linear regression line used to determine the valance band maxima and the slight variation in the valence band maxima of the gold sample, the overall UPS spectra error was found to be ± 0.1 eV. The pressure in the analysis chamber was typically $4x10^{-9}$ Torr during all data acquisition. XPS analysis software was used to determine the stoichiometry of samples from corrected peak areas and employing sensitivity factors for each element of interest. The Fermi level energy of the system was located using linear-regression at the valence-band edge of a sputtered gold foil sample.

The cleaned GaN sample was mounted and inserted into the load lock chamber within 10 min of the aq-HCl clean. All samples were mounted on a sample plate with copper foil in contact with the top of the samples to ensure electrical grounding. The charge neutralizer was turned on. XPS survey scans were taken once the samples were loaded into the analysis chamber using the Al K_{α} line (1486.6 eV). Fig. 25 shows the XPS survey scans of aq-HCl GaN, GaN/Al_2O_3, and GaN/HfO_2. UPS spectra of the four samples were acquired without the charge neutralizer following the XPS survey scans for all samples using a He I line (21.2 eV). The analyzer was biased 9.0 V with respect to the sample in order to overcome the work function of the system. Individual C1*s*, N 1*s*, O 1*s*, Ga 2*p*, Ga 3*d* and Al 2*p* (for Al_2O_3 samples only) scans, with the charge neutralizer turned on, of all samples were recorded following the UPS scans. The core-level positions and intensities were acquired by linear background subtraction and fitting to a Gaussian line shape resulting in peak positions within ± 0.1 eV uncertainty. The method used for calculating the GaN/dielectric band offsets are reported in several previous publications (*33, 34, 62*).

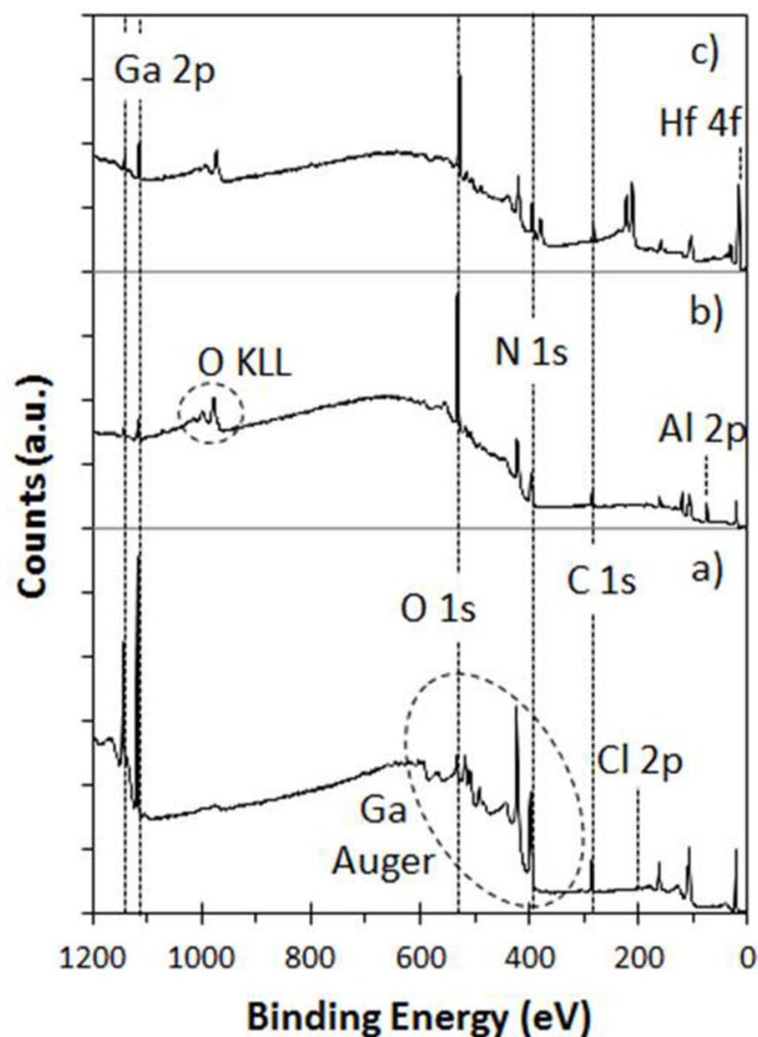

Fig. 25. XPS survey spectra of: a) aq-HCl GaN, b) GaN/Al_2O_3 after PDA, and c) GaN/HfO_2 after PDA. Some of the core level peaks are identified using a dotted line along with some Auger peaks with dotted circles.

4.3 Results and Discussion

The UPS spectra from the aq-HCl cleaned GaN, GaN/HfO_2, and GaN/Al_2O_3 are shown in Fig. 26. The valance band maximum (VBM) of the aq-HCl GaN was determined using linear regression to be 3.5 eV ± 0.1 eV with a spectral width of 13.75 eV ± 0.1 eV (referenced to the Fermi level) (Table 4). The electron affinity of the aq-HCl GaN was determined from the UPS spectra and the relation $\chi = h\nu - W - E_g$, where

χ is the electron affinity, hν is the photon energy (21.2 eV), W is the width of the spectra from the VBM to the secondary electron cut-off and E_g is the band gap of the material (*33, 62*). For aq-HCl GaN the electron affinity was determined to be 4.05 eV ± 0.1 eV which correlates to previously published data (*54, 100*).

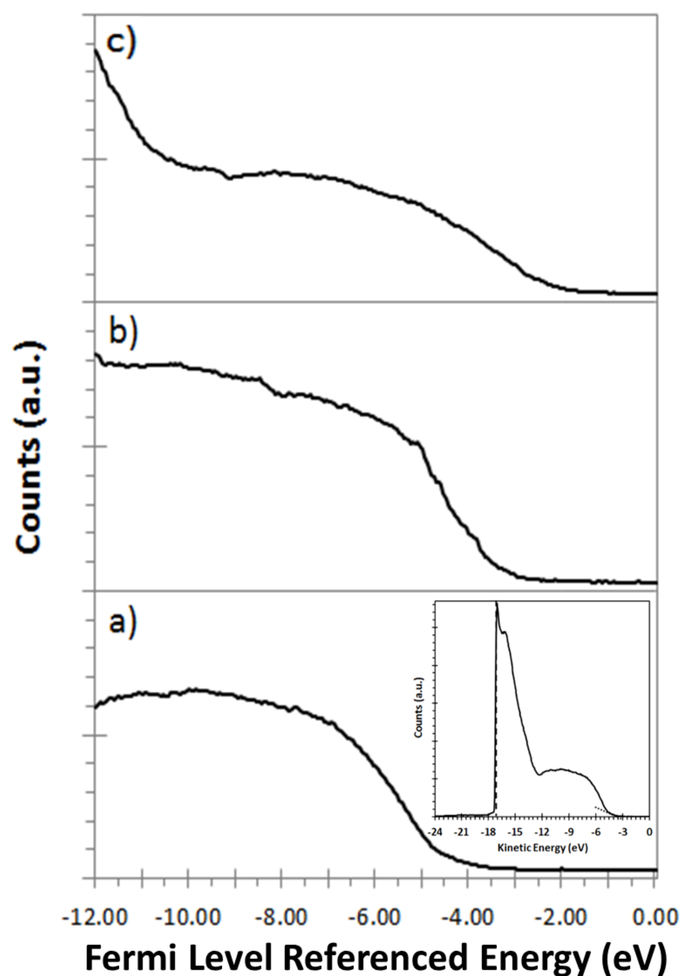

Fig. 26. UPS spectra of the valence band maximum of: a) aq-HCl GaN, b) GaN/Al_2O_3 after PDA, and c) GaN/HfO_2 after PDA. (insert) UPS spectra of aq-HCl GaN showing the linear regressions used to determine the valence band maxima and the on-set of the secondary electrons.

Table 4. UPS valence band maximum (VBM) fitting results and XPS core level fitting results for the O 1*s*, N 1*s*, Ga 3*d*, Al 2*p*, and Hf 4*f* energy levels. All XPS data has an uncertainty of ± 0.1 eV. All UPS data has an uncertainty of ± 0.1 eV.

Sample	VBM	O 1*s*		N 1*s*		Ga 3*d*		Al 2*p*		Hf 4*f*	
	(eV)	Center (eV)	FWHM (eV)	Center (eV)	FWHM (eV)	Center (eV)	FWHM (eV)	Center (eV)	FWHM (eV)	Center (eV)	FWHM (eV)
aq-HCl GaN	3.50	532.0	2.3	397.3	0.8	19.8	1.2	…	…	…	…
GaN/Al_2O_3	2.70	530.5	1.9	396.4	0.8	19.1	1.2	74.3	1.5	…	…
GaN/HfO_2	1.65	530.2	1.8	397.2	0.9	19.7	1.6	…	…	18.5	1.1

The Fermi level of aq-HCl GaN is shifted towards the conduction band due to nitrogen vacancies and surface states (*34, 35*). The N-vacancies are created as a result of the aq-HCl surface treatment, which also results in chemisorbed chlorine onto the surface of the GaN (*35*). The shift in the Fermi Level towards the conduction band is further emphasized by the Ga 3*d* core level peak position and there is potential contribution to this shift from the clear Cl 2*p* peak in the XPS survey. Typical GaN Ga 3*d* peaks have a binding energy of 19.54 – 19.70 eV (*101*), a shift towards a higher binding energy could indicate a shift in the Fermi level towards the conduction band (*35*). In Fig. 27, the Ga 3*d* peak position is determined to be 19.80 eV ± 0.1 eV (Table 4) indicating a shift in the surface Fermi level towards the conduction band. A shift in the Fermi level towards the conduction band indicates a decrease in band bending at the GaN surface compared to chemical vapor cleaned (CVC) GaN, upward band bending of 0.3 eV (*33*). In the case of aq-HCl GaN, the Fermi level is shifted towards the conduction band by 0.9 eV ± 0.1 eV, resulting in downward band bending at the surface. Downward band bending suggests that the negatively bound charge at the surface of GaN due to spontaneous polarization is over compensated for or screened by the chemisorbed chlorine and N-vacancies formed during the aq-HCl cleaning. Fig. 28 displays the calculated band line-up of the aq-HCl GaN surface.

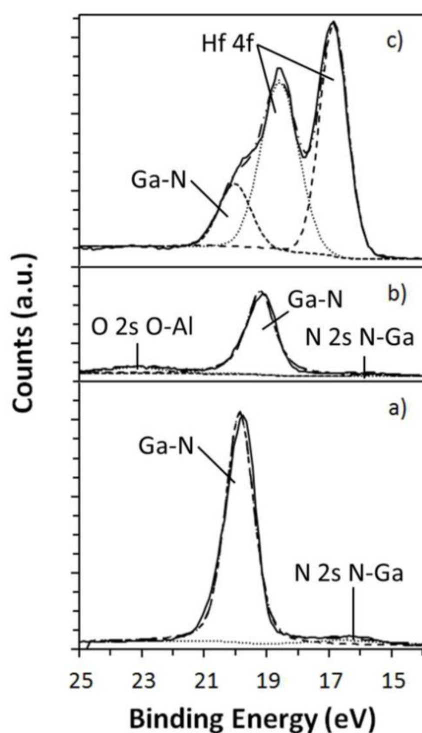

Fig. 27. Ga 3*d* XPS spectra for: a) aq-HCl GaN, b) GaN/Al_2O_3 after PDA, and c) GaN/HfO_2 after PDA. Peak fittings are the dotted and dashed lines, there are two or three peaks fitted to each plot.

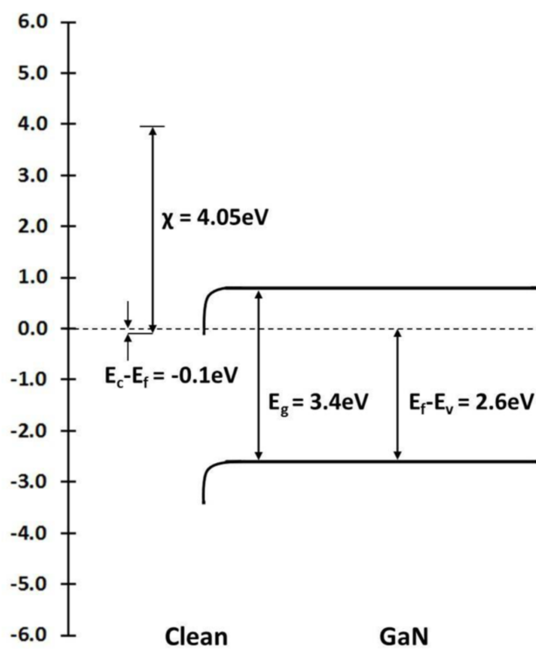

Fig. 28. Deduced bands for the aq-HCl cleaned GaN surface and GaN.

The valence band maximum for the annealed GaN/HfO_2 was determined using linear regression to be 1.65 eV ± 0.1 eV below the Fermi level of the aq-HCl GaN with a spectral width of 14.0 eV ± 0.1 eV (Fig. 26 and Table 4). The electron affinity was found to be 1.4 eV ± 0.1 eV assuming a band gap of 5.8 eV which corresponds to previous values (*58*). The Ga 3*d* and N 1*s* peaks were monitored to determine if band bending occurred at the GaN/dielectric interface, Fig. 27 and Fig. 29. There is a 0.13 eV ± 0.1 eV difference between the aq-HCl GaN Ga 3*d* peak (E^1_{Ga3d}) and GaN/HfO_2 Ga 3*d* peak (E^2_{Ga3d}), $\Delta E_{Ga3d} = E^1_{Ga3d} - E^2_{Ga3d}$, which indicates a 0.13 eV ± 0.1 eV upward band bending at the GaN/HfO_2 interface compared to that of aq-HCl GaN surface resulting in an overall 0.77 eV downward band bending at the GaN/HfO_2 interface. However, due to the minimal change in the Ga 3*d* peaks the difference is within error, resulting in no change in band bending at the GaN/HfO_2 interface compared to that of aq-HCl GaN (0.9 eV ± 0.1 eV downward band bending).

The valence and conduction band offsets, VBO and CBO, are expressed as

$$VBO = E^2_{VBM} - E^1_{VBM} + \Delta E_{Ga3d} \tag{1}$$

$$CBO = (E^2_g - E^2_{VBM}) - (E^1_g - E^1_{VBM}) + \Delta E_{Ga3d} \tag{2}$$

where E^2_{VBM} and E^1_{VBM} are the measured VBMs of the high-κ dielectric deposited on aq-HCl GaN and the substrate (aq-HCl GaN), respectively, E^2_g and E^1_g are the band gaps of the high-κ dielectric and GaN, respectively, and ΔE_{Ga3d} is the change in band bending defined by the shift of the Ga 3*d* core level. It is important to note that a shift in the N 1*s* core level also indicates band bending, thus ΔE_{Ga3d} can be replaced by $\Delta E_{N1s} = E^1_{N1s} - E^2_{N1s}$ if the change in the core level is larger for N 1*s* versus Ga 3*d* peaks (*33*). ΔE_{N1s} is the change in band bending defined by the shift of the N 1*s* core level, E^1_{N1s} is the aq-HCl GaN N 1*s* peak, and E^2_{N1s} is the GaN/dielectric N 1*s* peak.

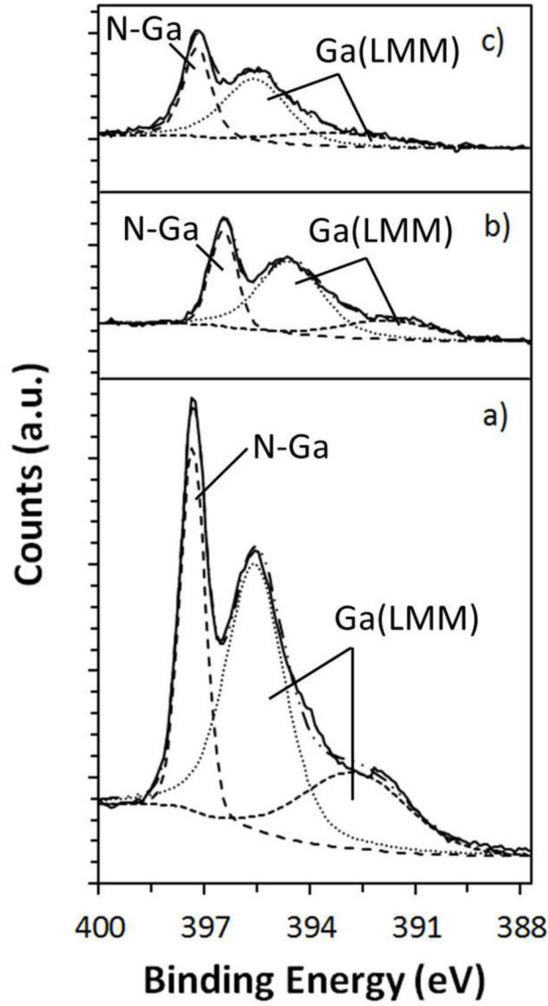

Fig. 29. N 1*s* XPS spectra for: a) aq-HCl GaN, b) GaN/Al_2O_3 after PDA, and c) GaN/HfO_2 after PDA. Peak fittings are the dotted and dashed lines, there are three peaks fitted to each plot.

Fig. 30 displays the calculated band line-up for the annealed GaN/HfO_2 interface. The VBO and CBO for the annealed GaN/HfO_2 interface were determined to be -1.85 eV and 4.25 eV ± 0.2 eV respectively (Table 5). With these values and the electron affinities of aq-HCl and HfO_2 the interfacial dipole is determined using

$$\Delta = \left(\chi_2 + \left(E_g^2 - E_{VBM}^2\right)\right) - \left(\chi_1 + \left(E_g^1 - E_{VBM}^1\right) + \Delta E_{Ga3d}\right) \quad (1)$$

where χ_1 and χ_2 are the electron affinities of the aq-HCl GaN and the dielectric, respectively, and Δ is the aq-HCl GaN/dielectric interfacial dipole. An interface dipole of 1.6 eV ± 0.2 eV was deduced (Table 5). An interfacial dipole of 2.0 eV at the GaN/HfO_2 interface using a n-type CVC-GaN substrate has been previously published (*33*). The variation in interfacial dipole is attributed to the different GaN surface preparations, CVC vs. aq-HCl, which leads to a shift in the VBM. However, previous publications (*33*) attribute the 2.0 eV interfacial dipole to interface states while we observed a 2.5 nm interfacial layer at the GaN/HfO_2 interface, Fig. 31. We attribute the 1.6 eV ± 0.2 eV interfacial dipole to the interfacial layer as well as potential interface states at both the GaN-side and HfO_2-side of the interface layer. The interface is a Type II band alignment which indicates that the valence band maximum of the aq-HCl GaN lies below that of the HfO_2 valence band, and is consistent with previous work (*33*).

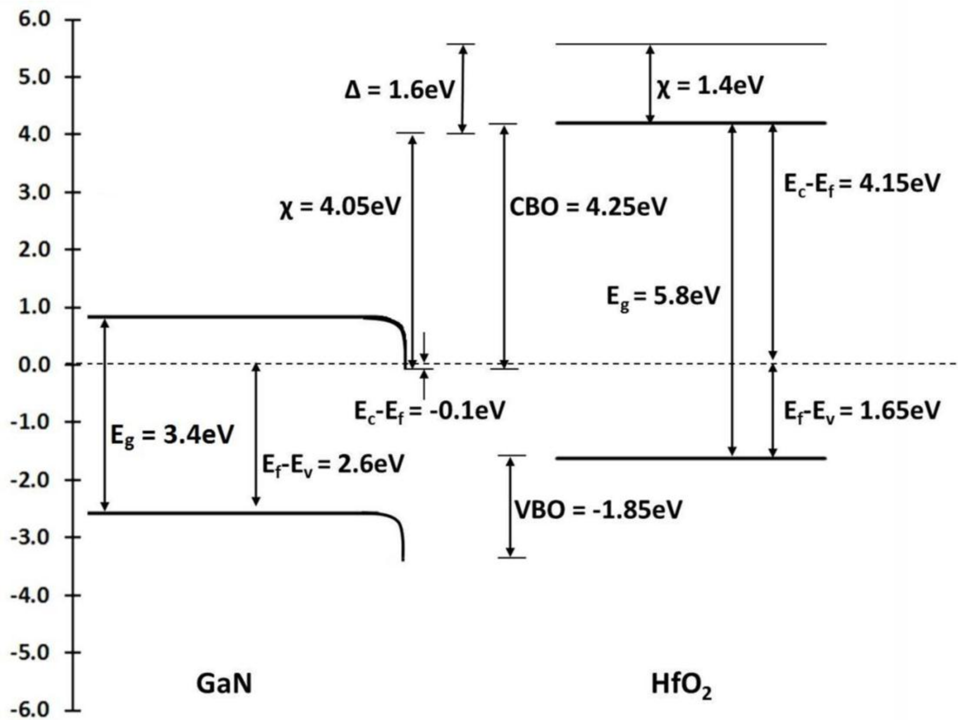

Fig. 30. Deduced bands for the interface between GaN and HfO_2 after PDA. The valence band offset (VBO), conduction band offset (CBO), band bending, and interface dipole (Δ) are represented.

Table 5. Parameters used to calculate the GaN/dielectric interface dipole, where E_g is the band gap of the surface material, E_F is the Fermi level of the sample, E_v is the valence band of the surface material, E_c is the conduction band of the surface material, χ is the electron affinity of the surface material, ΔE_{Ga3d} is the difference in the Ga 3*d* core level of the aq-HCl GaN and the sample, ΔE_{N1s} is the difference in the N 1*s* core level of the aq-HCl GaN and the sample, VBO is the valence band offset, CBO is the conduction band offset, and Δ is the dipole at the GaN/dielectric interface.

	E_g (eV)	E_F-E_v (eV ± 0.1 eV)	E_c-E_F (eV ± 0.1 eV)	χ (eV ± 0.1 eV)	ΔE_{Ga3d} (eV ± 0.1 eV)	ΔE_{N1s} (eV ± 0.1 eV)	VBO (eV ± 0.2 eV)	CBO (eV ± 0.2 eV)	Δ (eV ± 0.2 eV)
aq-HCl GaN	3.4	3.5	-0.1	4.1	…	…	…	…	…
GaN/Al_2O_3	6.4	2.70	3.7	1.5	0.7	0.9	0.1	3.0	0.4
GaN/HfO_2	5.8	1.65	4.15	1.4	0.1	0.1	-1.9	4.3	1.6

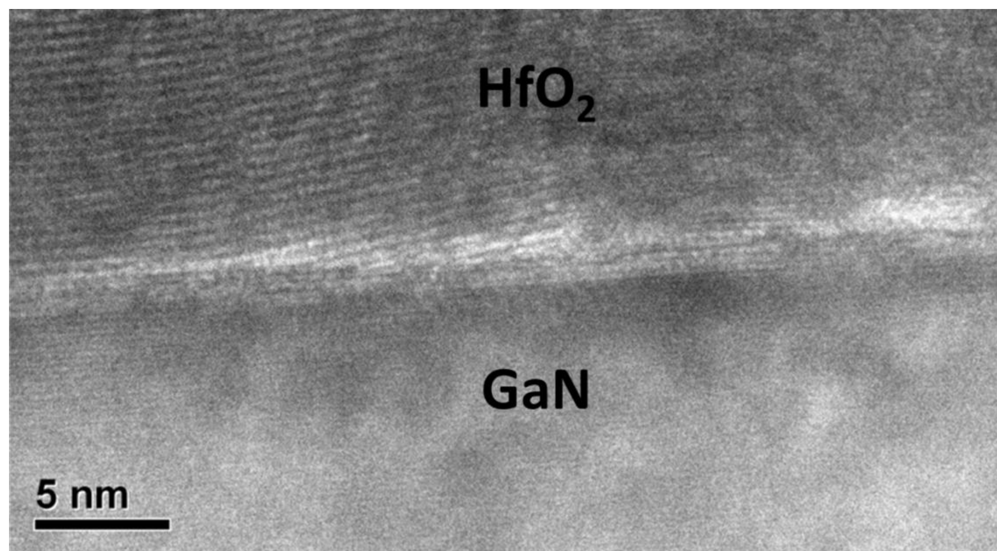

Fig. 31. Cross-sectional TEM image of high-κ HfO_2 (9 nm) deposited using ALD on aq-HCl cleaned GaN grown on Si, an interfacial GaON or GaON with Hf layer (2.5nm) is formed during deposition of HfO_2. No post deposition anneal was done.

It is important to note that during ALD deposition of HfO_2 and Al_2O_3 the sample is heated to 200 and 250°C, respectively, and exposed to water vapor which may allow for the chemisorbed chlorine on both samples to be partially desorbed (*35*). Annealed aq-HCl GaN at 200°C for 10 min has been reported to shift the Ga 3*d* peak 0.4 eV ± 0.1

eV towards the valence band, which correlates to a downward shift in Fermi level compared to that of the as-cleaned aq-HCl GaN (*35*). In a more recent paper, the shift in the Ga 3*d* peak between aq-HCl GaN and 550°C annealed aq-HCl GaN is correlated to the removal of surface states from atmospheric contamination not the desorption of chlorine (*34*). In this chapter, there is no shift observed between the Ga 3*d* peaks for aq-HCl GaN and GaN/HfO_2 samples. It is concluded that while the chlorine and the surface states due to contamination are partially desorbed during the ALD process the formation of a GaON interfacial layer compensates for any change in the Ga 3*d* peak that would be observed without the interfacial layer.

The band offset measurement for annealed GaN/Al_2O_3 was also completed, Fig. 32. The turn-on for the annealed GaN/Al_2O_3 sample was determined using linear regression to be 2.70 eV ± 0.1 eV below the Fermi level of the aq-HCl GaN with a spectral width of 13.30 eV ± 0.1 eV (Fig. 26 and Table 4). The electron affinity was found to be 1.50 eV ± 0.1 eV assuming a band gap of 6.4 eV,(*102*) which corresponds to previously published data (*56, 57*). The Ga 3*d* and N 1*s* peaks were monitored to determine if band bending occurred at the GaN/Al_2O_3 interface, Fig. 27 and Fig. 29. Here it is found that there is a 0.85 eV ± 0.1 eV between the aq-HCl GaN N 1*s* peak (E^1_{N1s}) and GaN/Al_2O_3 N 1*s* peak (E^2_{N1s}), which indicates a 0.85 ± 0.1 eV upward band bending at the GaN/Al_2O_3 interface compared to that of aq-HCl GaN surface resulting in an overall 0.05 eV ± 0.1 eV downward band bending or approximately a flat band condition at the GaN/Al_2O_3 interface. Accounting for band bending the VBO, CBO and dipole are calculated to be 0.05 eV, 2.95 eV and 0.40 eV ± 0.2 eV, respectively (Table 5). The 0.7 eV ± 0.1 eV shift in the Ga 3*d* peak is expected due to desorption of chlorine and surface states during ALD at 250°C, however, the magnitude of the shift is larger than previously reported for an annealed aq-HCl GaN sample at 200°C, 0.4 eV (*35*). The larger shift in the Ga 3*d* peak is indicative of a decrease in surface states at the GaN/Al_2O_3 interface. Currently there is no reported data that shows the formation of an interfacial layer at the GaN/Al_2O_3 interface (*32, 41*). Furthermore, this small dipole, in

contrast to GaN/HfO_2, indicates that the larger dipole is due to the formation of an interfacial layer when reaction kinetics allow for the formation of such.

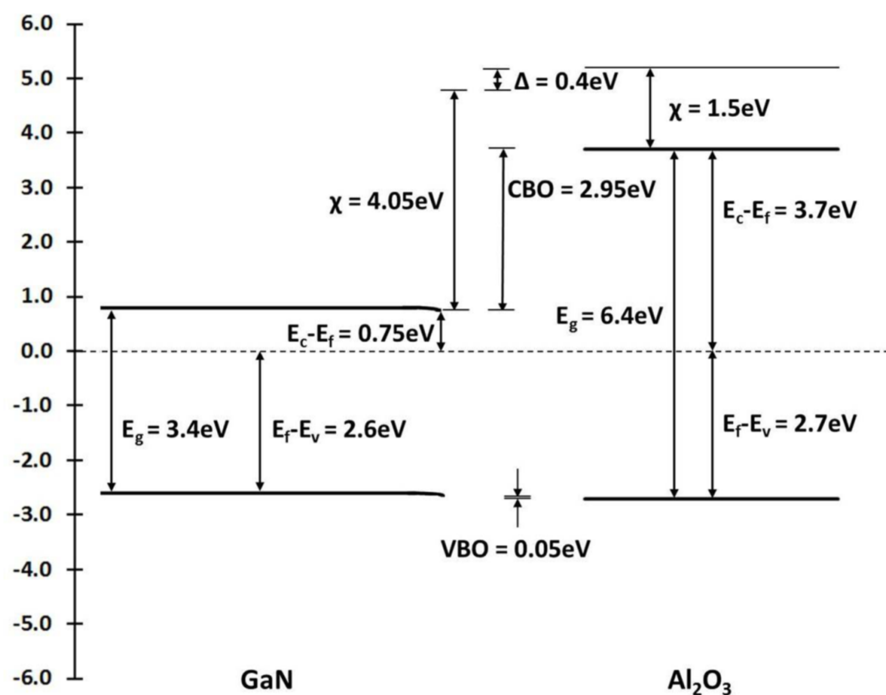

Fig. 32. Deduced bands for the interface between GaN and Al_2O_3 after a post deposition anneal. The valence band offset (VBO), conduction band offset (CBO), band bending, and interface dipole (Δ) are represented.

4.4 Conclusions

In summary, the band alignment of Al_2O_3 and HfO_2 on aq-HCl cleaned GaN has been investigated. To the authors knowledge this is the first time the band offset measurements for GaN/Al_2O_3 have been calculated using UPS and XPS. The electron affinities and valence band maxima for aq-HCl GaN, Al_2O_3 and HfO_2 were measured using UV photoelectron spectroscopy (UPS). Downward band bending of 0.9 eV on the aq-HCl GaN surface was deduced from UPS measurements. Band bending at the GaN/Al_2O_3 and GaN/HfO_2 was determined using the shifts in the Ga 3*d* and N 1*s* core-level peaks measured using X-ray photoelectron spectroscopy (XPS). Downward band

bending of 0.05 eV and 0.9 eV ± 0.1 eV existed at the GaN/Al_2O_3 and GaN/HfO_2 interfaces. An interface dipole of 0.4 eV ± 0.2 eV for GaN/Al_2O_3 and 1.6 eV ± 0.2 eV for GaN/HfO_2 was calculated. The data suggests that the interfacial oxide formed during the ALD of HfO_2 may cause the dipole at the HfO_2/GaN interface.

4.5 Acknowledgements

We thank the National Science Foundation (Grant No. 0618242) for funding the X-ray Photoelectron Spectrometer used in this work. Financial support from the National Excellence Fellowship and NSF grant #1028910 and #0901699 is gratefully acknowledged.

CHAPTER V
BAND-OFFSET MEASUREMENTS OF THE GaN/GaON INTERFACE

Due to the knowledge of the formation of an interfacial GaO_x or GaON layer during atomic layer deposition of HfO_2, a better understanding of the GaN/GaON interface is needed. To accomplish this task, the interface electronic states at the GaN(0001) and GaON interface are observed using X-ray and ultraviolet photoelectron spectroscopy. The GaN is cleaned prior to thermal dry oxidation using aqueous hydrochloric acid. Resulting in GaN/GaON exhibited a dipole of -2.7 eV ± 0.2 eV assuming that the core level shifts are only representative of the GaN band bending at the interface. If it is assumed that the core level shifts are only due to the oxidation of GaN then the exhibited dipole at the GaN/GaON is -1.8 eV ± 0.2 eV. The observed dipole is found to be primarily due to the polarization of the GaN.

5.1 Introduction

Analog applications and low-loss high-voltage switching are currently in need of enhancement-mode (E-mode) III-N-based devices. One of the potential methods to fabricate E-mode III-N devices is to control the V_{th} is using a metal/high-κ dielectric stack in place of a Schottky gate, and varying the work function of the gate metal (*27, 95, 96*). The III-N/ high-κ interface has been shown to influence the work function of the gate metal and therefore the threshold voltage (*27, 29*). It has been discovered that during atomic layer deposition (ALD) of HfO_2 on GaN an interfacial layer is formed and remains after post deposition annealing (*30*).

This interface plays a key role in understanding the band alignment at the HfO_2/GaN interface and therefore the expected threshold voltage. It also affects the overall reproducibility of devices due to the lack of uniformity. An intentionally grown thin uniform GaO_x or GaON layer could potentially fix the devices reproducibility and

form discrete interfaces. The interfacial oxide is believed to be some form of GaO_x or GaON that is approximately 2-3 nm thick (*30*). A better understanding of the band alignment, including dipole formation, at the GaN/HfO_2 interface is needed. While XPS and UPS analysis of the HfO_2/GaN interface has been previously completed and the respective band alignments have been determined, assuming no interfacial layer formation (*33*), no band alignment information regarding thin (2-3 nm thick) thermally grown GaOx or GaON on GaN have been published to the author's knowledge. Therefore the author uses XPS and UPS to determine the band alignment at the GaN/GaON interface.

Typical experimental procedures for determining the band offsets of a high-κ dielectric on GaN require the GaN to be cleaned using in situ surface cleaning methods (*33, 98*). However, *in situ* surface cleaning is not always practical when fabricating GaN-based devices since wet chemistry is used to remove the native oxide on the GaN surface (*98*). Aqueous HCl (aq-HCl) is commonly used to remove the GaN native oxide (*34, 35, 98*). Therefore, the authors use aq-HCl to remove the GaN surface oxide prior to photoelectron measurements and dielectric depositions to explore the impact of this pre-clean on the interfacial dipole formation. We present X-ray photoelectron spectra (XPS) and UV photoelectron spectra (UPS) of GaN/GaON. The position and origin of the interfacial dipole is discussed.

5.2 Experimental Methodology

The unintentionally doped (0001)-oriented GaN samples were grown on sapphire substrates by hydride vapor phase epitaxy (HVPE) with a thickness of ~ 5 μm ± 1.5 μm, a resistivity < 0.5 Ohm-cm, a dislocation density < $1x10^9$ cm^{-2}, and a carrier concentration of ~ $10x10^{17}$ cm^{-3} (*99*). Further information regarding the growth of GaN has been previously published (*99*). All GaN samples were immersed for 15 min in a solution of HCl (~ 6 M) and rinsed using DI water, prior to the introduction of the GaN sample to ultra-high vacuum (UHV) analysis chamber (for reference analysis) or furnace

for GaON growth. The formation of a 3 nm thick GaON film was conducted in a conventional horizontal quartz tube furnace. Immediately following the aq-HCl clean, the sample was inserted into an approximately 800 °C heated quartz tube with 40 sccm of ultra-high purity oxygen. Dry oxidation of the sample was conducted for 30 min. Following the completion of the oxidation run, the sample was removed from the quartz tube and was allowed to cool to room temperature within 5 min.

Ex situ XPS and UPS were performed. XPS spectra were recorded using a monochromated Al-K_{α} X-ray source (hν = 1486.5 eV), hybrid optics (employing a magnetic and electrostatic lens simultaneously) and a multi-channel plate and delay line detector coupled to a hemispherical analyzer. The photoelectrons take-off angle was normal to the surface of the sample and 45° with respect to the X-ray beam. All spectra were recorded using a single sweep and an aperture slot of 300 x 700 microns, and high resolution spectra were collected with a pass energy of 20 eV. UPS spectra were recorded using He (I) UV-ray source (hν = 21.2 eV), hybrid optics (employing a magnetic and electrostatic lens simultaneously) and a multi-channel plate and delay line detector coupled to a hemispherical analyzer. The photoelectrons take-off angle was normal to the surface of the sample and 45° with respect to the UV beam. All spectra were recorded using a single sweep and an aperture slot of ~ 1000 x 1000 microns, and high resolution spectra were collected with a pass energy of 5 eV. Due to the fitting of the linear regression line used to determine the valance band maxima and the slight variation in the valence band maxima of the gold sample, the overall UPS spectra error was found to be ± 0.1 eV. The pressure in the analysis chamber was typically $4x10^{-9}$ Torr during all data acquisition. XPS analysis software was used to determine the stoichiometry of samples from corrected peak areas and employing sensitivity factors for each element of interest. The Fermi level energy of the system was located using linear-regression at the valence-band edge of a sputtered gold foil sample.

The cleaned GaN sample was mounted and inserted into the load lock chamber within 10 min of the aq-HCl clean. Both samples were mounted on a sample plate with copper foil in contact with the top of the samples to ensure electrical grounding. The

charge neutralizer was turned on. XPS survey scans were taken once the samples were loaded into the analysis chamber using the Al K_α line (1486.6 eV). Fig. 33 shows the XPS survey scan of aq-HCl GaN and GaN/GaON. UPS spectra of both samples were acquired without the charge neutralizer following the XPS survey scans for all samples using a He I line (21.2 eV). The analyzer was biased 9.0 V with respect to the sample in order to overcome the work function of the system. Individual C1*s*, N 1*s*, O 1*s*, Ga 2*p*, and Ga 3*d* scans, with the charge neutralizer turned on, of all samples were recorded following the UPS scans. The core-level positions and intensities were acquired by linear background subtraction and fitting to a Gaussian line shape resulting in peak positions within ± 0.1 eV uncertainty. The method used for calculating the GaN/dielectric band offsets is reported in several previous publications (*33, 34, 62*).

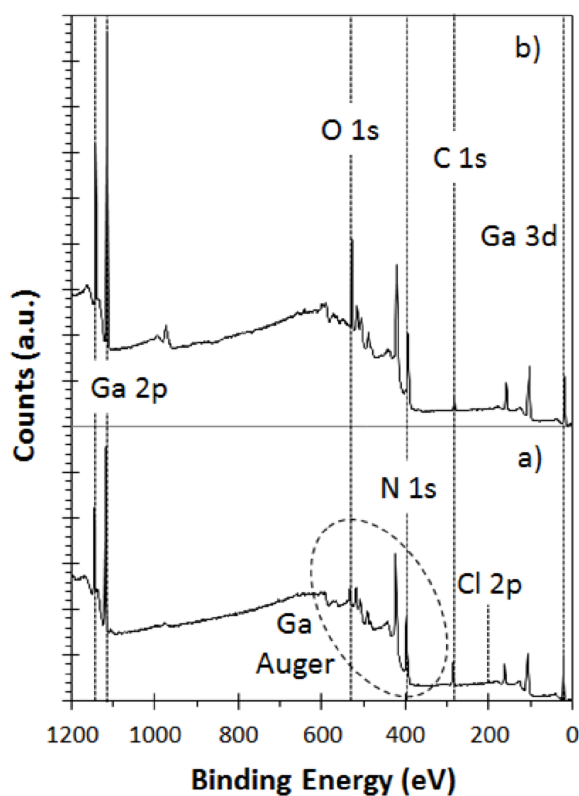

Fig. 33. XPS survey spectra of: a) aq-HCl GaN and b) GaN/GaON. Some of the core level peaks are identified using a dotted line along with Ga Auger peaks with the dotted circle.

5.3 Results and Discussion

The thickness of the GaON layer is determined using TEM analysis to be ~ 3nm, Fig. 34. The Ga/N and Ga/O ratios for aq-HCl GaN are determined to be 1.40 and 3.00, respectively. The Ga/N ratio indicates a nitrogen deficit GaN surface after the aq-HCl clean which is in agreement with previously published data (*34*). The Ga/N and Ga/O ratios for GaN/GaON are determined to be 2.64 and 1.45, respectively. These ratios indicate the formation of a GaON layer (*103*). The complete UPS spectra of the aq-HCl cleaned GaN and GaN/GaON are shown in Fig. 35. The valence band maximums of aq-HCl GaN and GaN/GaON are shown in Fig. 36. The valance band maximum (VBM) of the aq-HCl GaN was determined using linear regression to be 3.5 eV ± 0.1 eV with a spectral width of 13.75 eV ± 0.1 eV (referenced to the Fermi level) (Table 6). The electron affinity of the aq-HCl GaN was determined from the UPS spectra and the relation $\chi = h\nu - W - E_g$, where χ is the electron affinity, $h\nu$ is the photon energy (21.2 eV), W is the width of the spectra from the VBM to the secondary electron cut-off and E_g is the band gap of the material (*33, 62*). For aq-HCl GaN the electron affinity was determined to be 4.05 eV ± 0.1 eV which correlates to previously published data (*54, 100*).

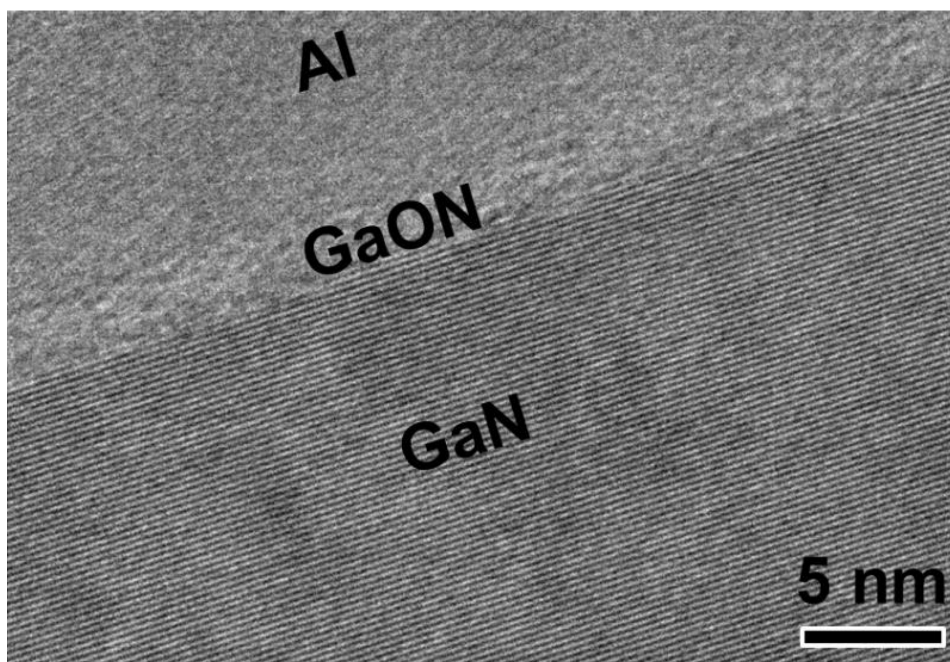

Fig. 34. Cross-sectional TEM image of GaON (3 nm) thermally grown on aq-HCl cleaned GaN grown on Si. No post deposition anneal was done.

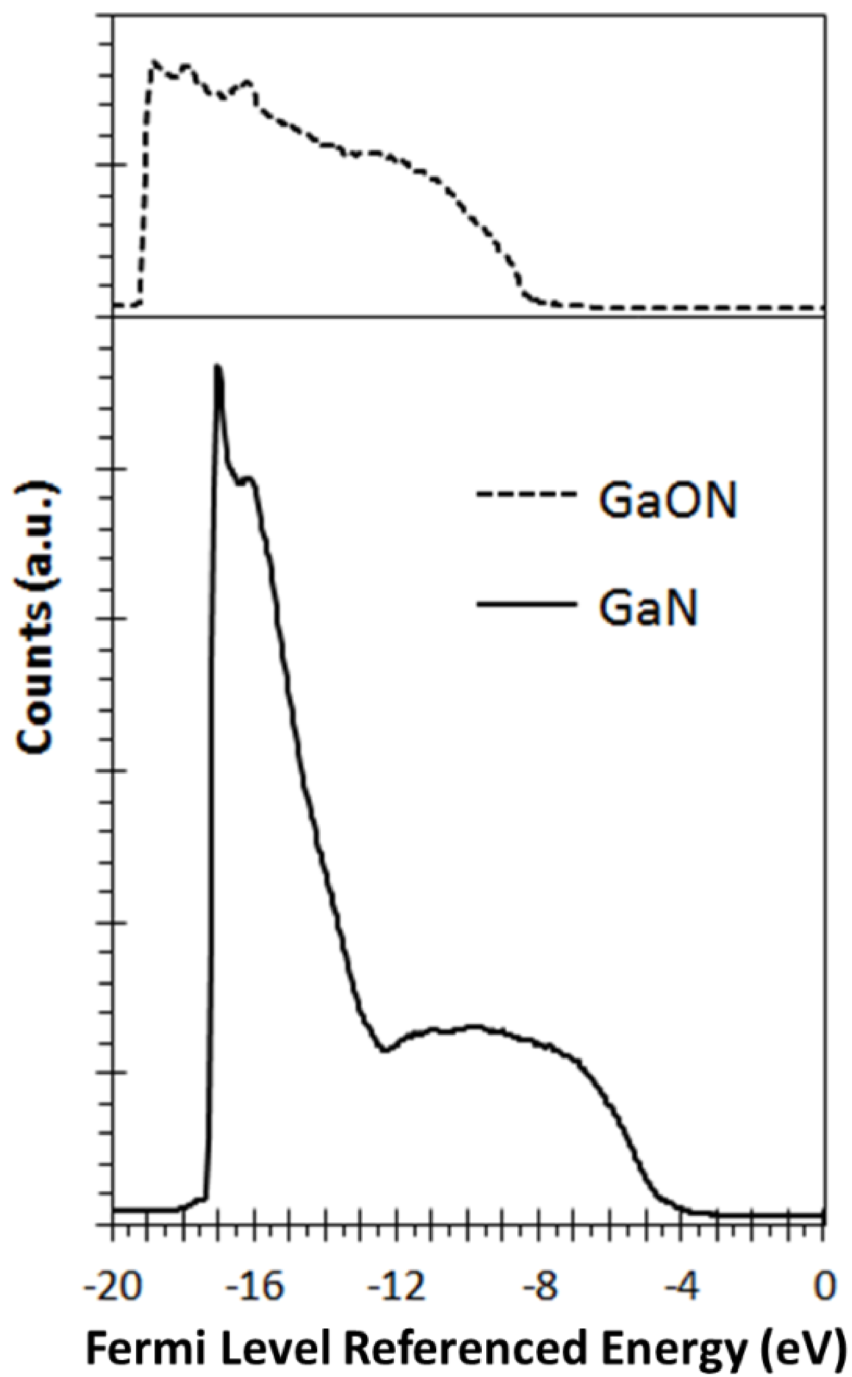

Fig. 35. UPS spectra of aq-HCl GaN (GaN) and GaN/GaON (GaON).

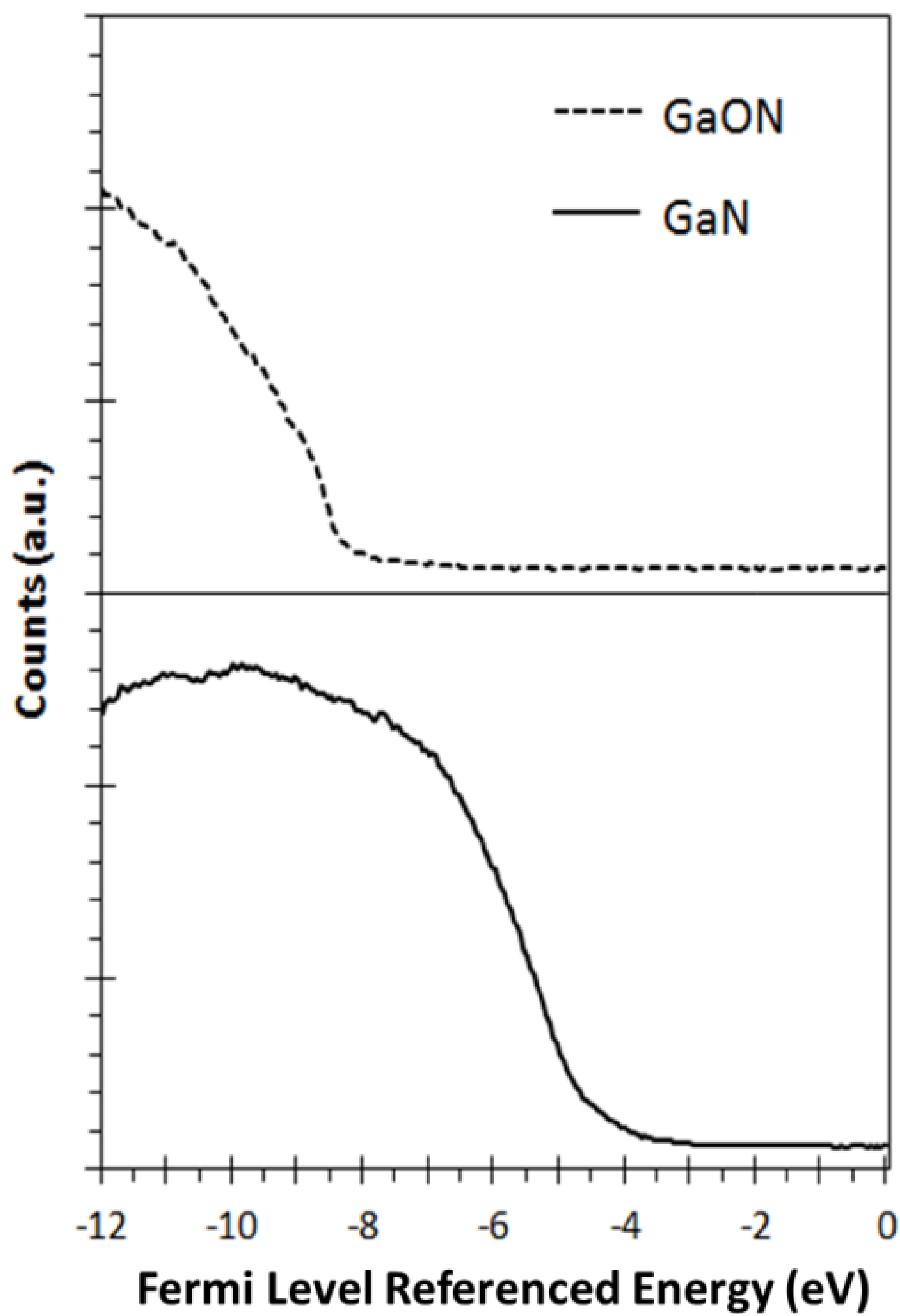

Fig. 36. UPS spectra of the valence band maximum of aq-HCl GaN (GaN) and GaN/GaON (GaON).

Table 6. UPS valence band maximum (VBM) fitting results and XPS core level fitting results for the O 1*s*, N 1*s*, and Ga 3*d* energy levels. The XPS and UPS data has an uncertainty of ± 0.1 eV.

Sample	VBM (eV)	O 1*s*		N 1*s*		Ga 3*d*	
		Center (eV)	FWHM (eV)	Center (eV)	FWHM (eV)	Center (eV)	FWHM (eV)
aq-HCl GaN	3.50	532.0	2.3	397.3	0.8	19.8	1.2
GaN/GaON	7.40	530.2	1.5	396.4	1.4	19.4	1.4

The Fermi level and surface band bending of the aq-HCl GaN have been previously discussed in Chapter V on page 51. To refresh the reader a general overview of the band alignment and valence band maxima are discussed here after. The Fermi level of aq-HCl is shifted towards the conduction band at the surface by 0.9 eV ± 0.1 eV, resulting in downward band bending. This shift is emphasized by the Ga 3*d* core level peak that is slightly shifted towards higher binder energies compared to typical Ga-N core levels, Fig. 37 and Table 6. Downward band bending suggests that the negatively bound charge at the surface of GaN due to spontaneous polarization is over compensated for or screened by the chemisorbed chlorine and N-vacancies formed during the aq-HCl cleaning. Fig. 38 displays the calculated band line-up of the aq-HCl GaN surface, which is a reprint of Fig. 28 and is for the readers review.

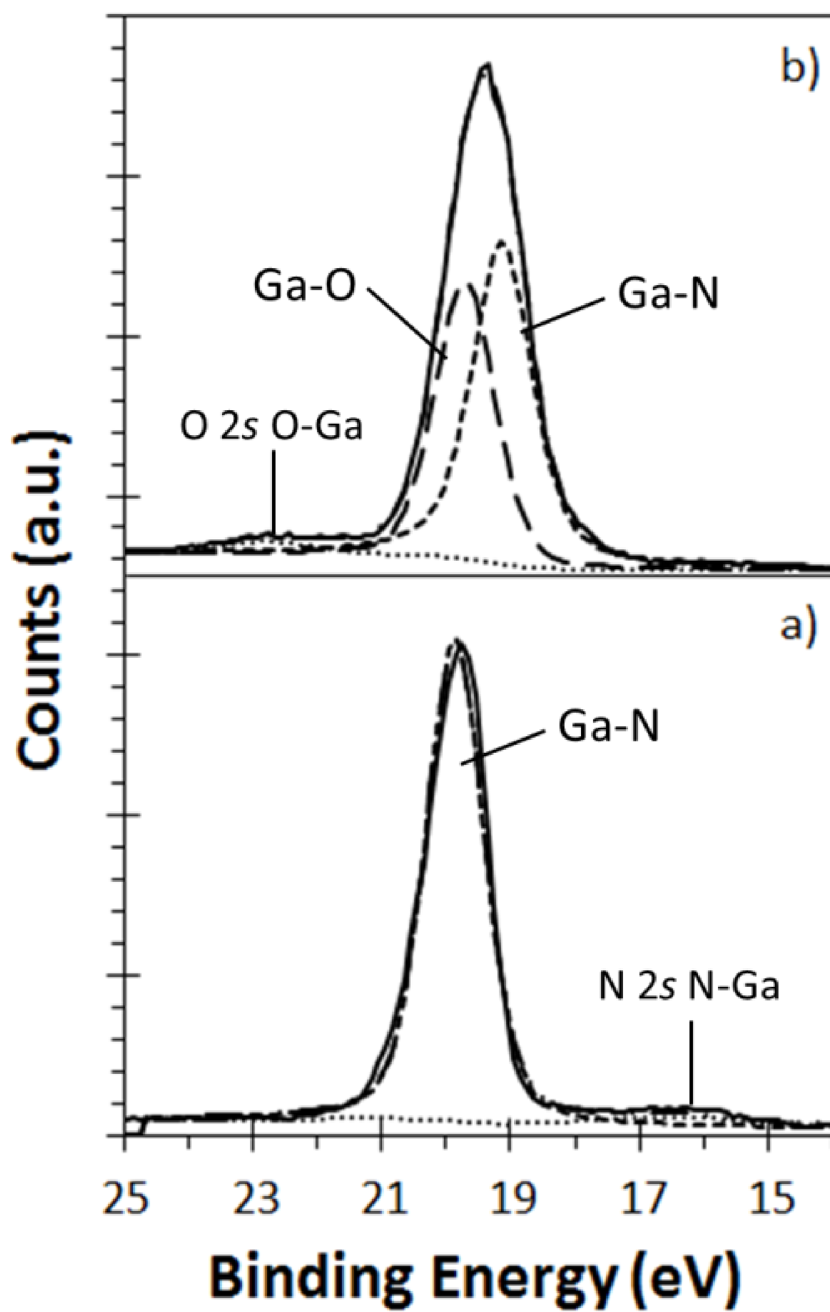

Fig. 37. Ga 3*d* XPS spectra for: a) aq-HCl GaN and b) GaN/GaON. Peak fittings are the dotted and dashed lines, there are two or three peaks fitted to each plot.

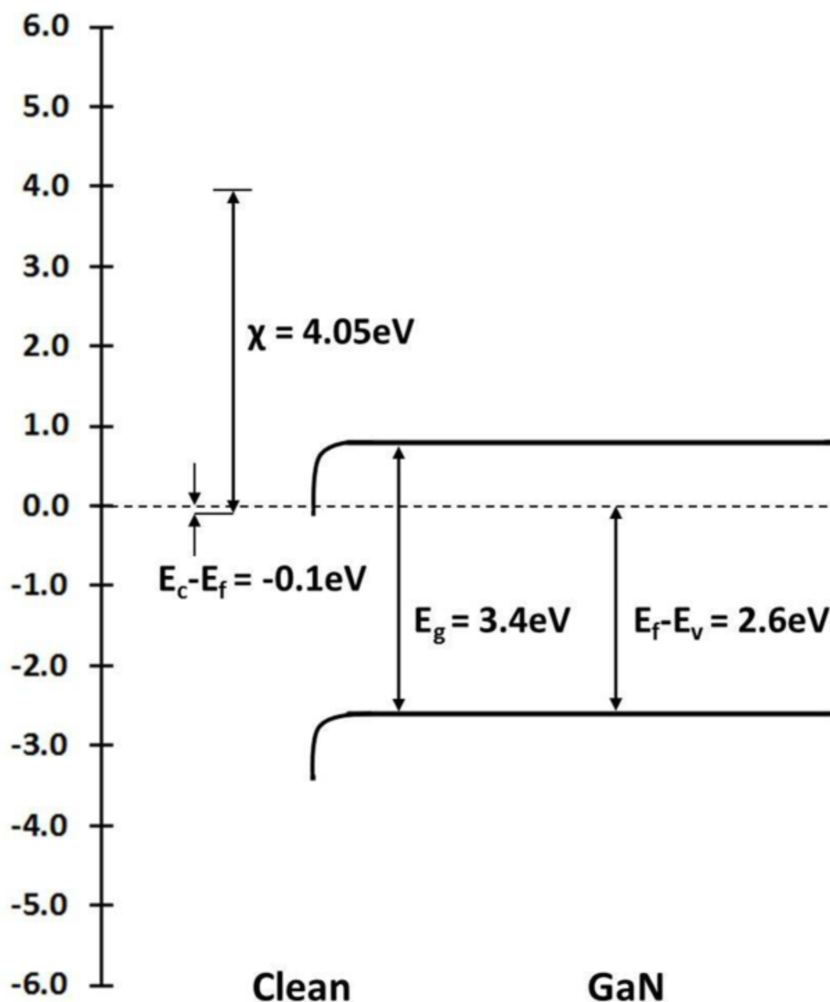

Fig. 38. Reprint of Fig. 28 from Chapter V for the readers review. Deduced bands for the aq-HCl cleaned GaN surface and GaN.

The valence band maximum for the annealed GaN/GaON was determined using linear regression to be 7.40 eV ± 0.1 eV below the Fermi level of the aq-HCl GaN with a spectral width of 11.65 eV ± 0.1 eV (Fig. 36 and Table 6). The shape and width of the GaON spectra is similar to previously published valence band spectra of gallium oxide obtained using XPS (*104*). The electron affinity was found to be 4.97 eV ± 0.1 eV assuming a band gap of 4.58 eV which is in between previously published electron

affinities of GaN and Ga_2O_3 (*54, 100, 105, 106*). The ionization energy of GaN/GaON is approximately 2.0 eV ± 0.1 eV above that of GaN, which is similar to previously published results of the oxidation of $Al_{0.55}Ga_{0.45}N$ which resulted in an increase of 2.0 eV after oxidation (*107*).

The Ga 3*d* and N 1*s* peaks were monitored to determine if band bending occurred at the GaN/GaON interface, Fig. 37 and Fig. 39. There is a 0.4 eV ± 0.1 eV difference between the aq-HCl GaN Ga 3*d* peak (E^1_{Ga3d}) and GaN/GaON Ga 3*d* peak (E^2_{Ga3d}), $\Delta E_{Ga3d} = E^1_{Ga3d} - E^2_{Ga3d}$, which indicates a 0.4 eV ± 0.1 eV upward band bending at the GaN/GaON interface compared to that of aq-HCl GaN surface. However, there is a larger shift, $\Delta E_{N1s} = E^1_{N1s} - E^2_{N1s}$, in the N 1*s* peak from aq-HCl GaN to GaON, ΔE_{N1s}= 0.9 eV ± 0.1 eV. This shift in the N 1s indicates an upward band bending of the GaN at the GaN/GaON interface resulting in no overall band bending in GaN at the interface which is in agreement with previously published work on the GaN/native oxide interface (*108*).

Due to the nature of GaON, core level shifts are known to occur due to changes in bonding not only band bending. With this in mind, two sets of valence and conduction band offsets, VBO and CBO, are calculated using the same theory shown in Chapter V, one assuming all core level shifts are due to band bending changes in bonding (GaN/GaON) and the other assuming all core level shifts are due to band bending in the GaN at the interface (GaN/GaON*). The core level shifts are convoluted because the shifts are due to both changes in bonding and changes in band bending at the interface.

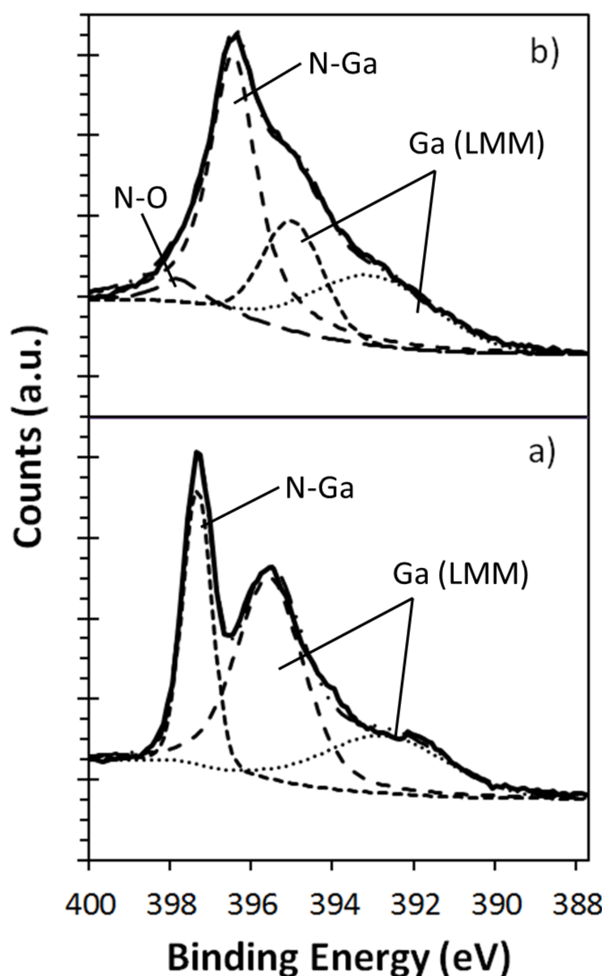

Fig. 39. N 1*s* XPS spectra for: a) aq-HCl GaN and b) GaN/GaON. Peak fittings are the dotted and dashed lines, there are three or four peaks fitted to each plot.

Fig. 40 and Fig. 41 display the calculated band line-up for the GaN/GaON and GaN/GaON* interfaces, respectively. The VBO and CBO for the GaN/GaON interface, assuming no shifts in the core level are affiliated with band bending, are determined to be 3.9 eV and -2.7 eV ± 0.2 eV respectively (Table 7). An interface dipole of -1.8 eV ± 0.2 eV was deduced (Table 7). The VBO and CBO for the GaN/GaON* interface, assuming shifts in the core level are affiliated with band bending, are determined to be 4.8 eV and -3.6 eV ± 0.2 eV respectively (Table 7). An interface dipole of -2.7 eV ± 0.2 eV was deduced (Table 7).

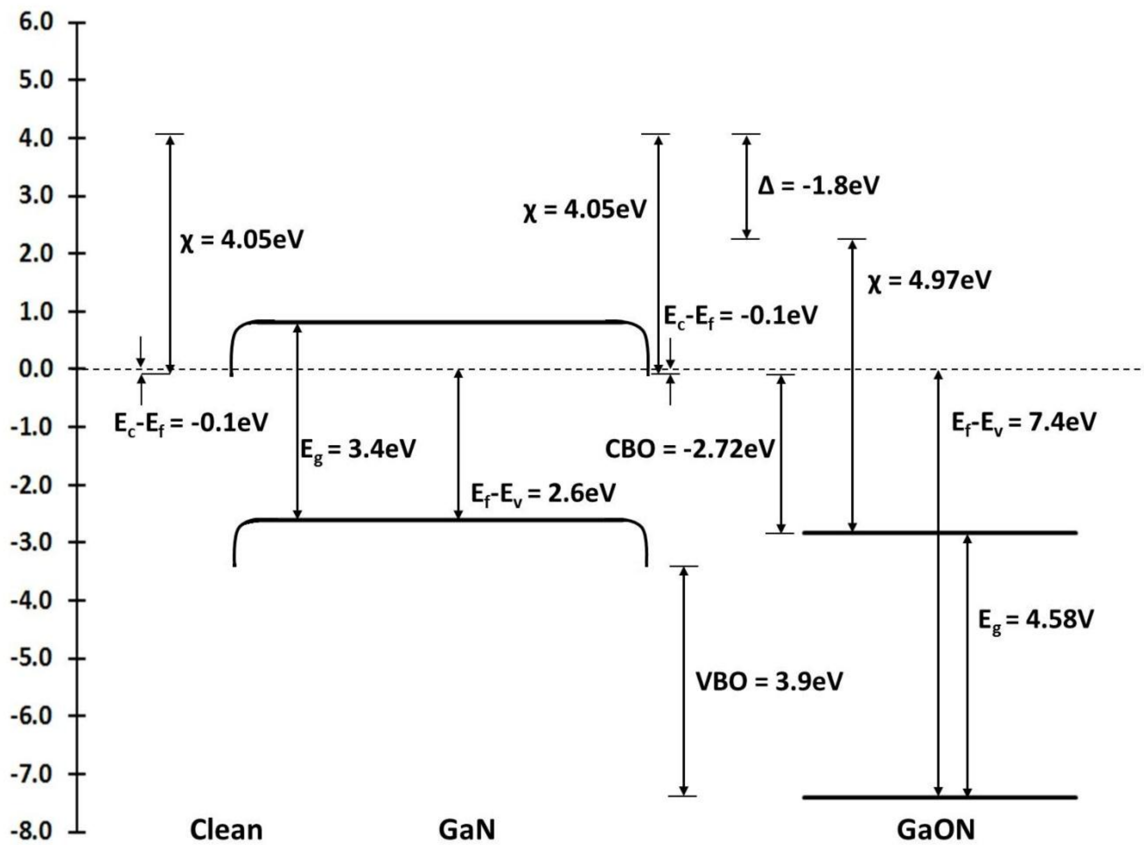

Fig. 40. Deduced bands for the interface between GaN and GaON assuming all core level shifts are due to changes in bonding. The valence band offset (VBO), conduction band offset (CBO), band bending, and interface dipole (Δ) are represented.

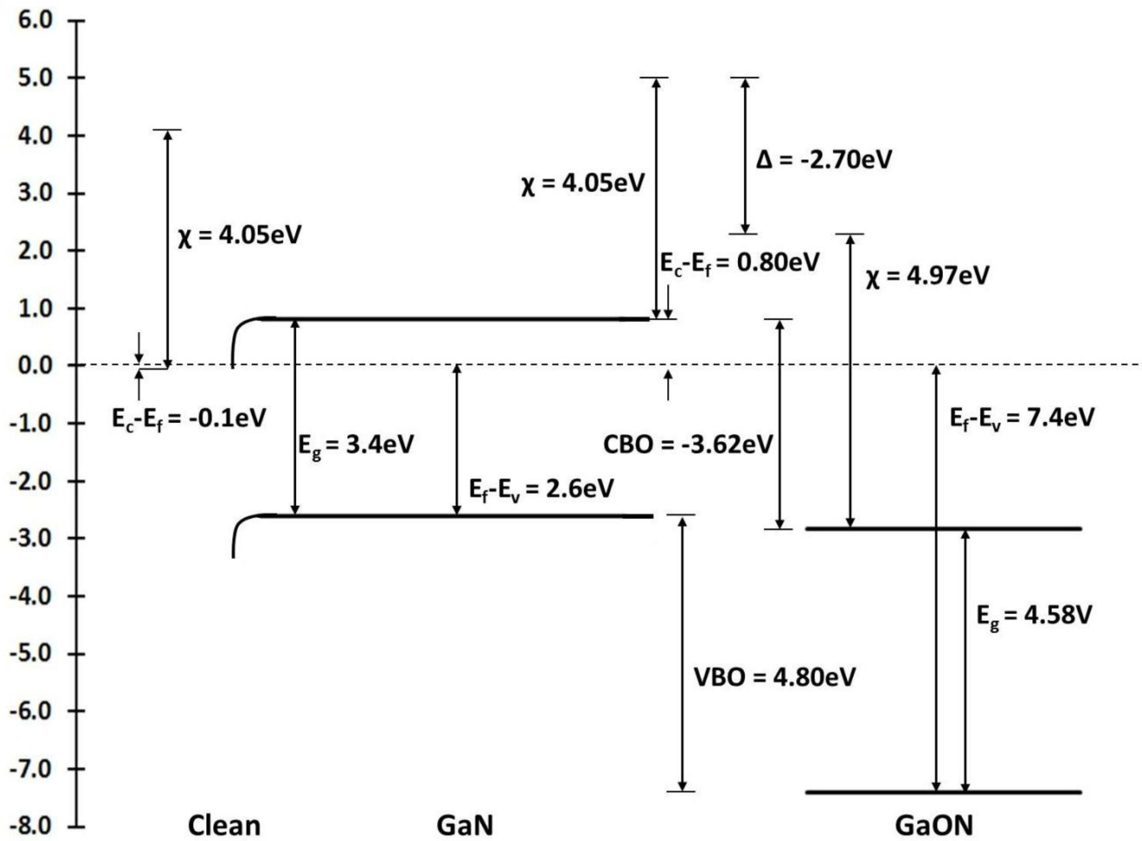

Fig. 41. Deduced bands for the interface between GaN and GaON* assuming all core level shifts are due to band bending at the interface in the GaN. The valence band offset (VBO), conduction band offset (CBO), band bending, and interface dipole (Δ) are represented.

Table 7. Parameters used to calculate the GaN/oxide interface dipole, where E_g is the band gap of the surface material, E_F is the Fermi level of the sample, E_v is the valence band of the surface material, E_c is the conduction band of the surface material, χ is the electron affinity of the surface material, ΔE_{Ga3d} is the difference in the Ga 3d core level of the aq-HCl GaN and the sample, ΔE_{N1s} is the difference in the N 1s core level of the aq-HCl GaN and the sample, VBO is the valence band offset, CBO is the conduction band offset, and Δ is the dipole at the GaN/dielectric interface. * represents calculations assuming that the core level shifts are only due to band bending at the GaN/GaON interface

	E_g (eV)	E_F-E_v (eV ± 0.1 eV)	E_c-E_F (eV ± 0.1 eV)	χ (eV ± 0.1 eV)	ΔE_{Ga3d} (eV ± 0.1 eV)	ΔE_{N1s} (eV ± 0.1 eV)	VBO (eV ± 0.2 eV)	CBO (eV ± 0.2 eV)	Δ (eV ± 0.2 eV)
aq-HCl GaN	3.4	3.5	-0.1	4.1	…	…	…	…	…
GaN/GaON	4.6	7.4	-2.8	5.0	…	…	3.9	-2.7	-1.8
GaN/GaON*	4.6	7.4	-2.8	5.0	0.4	0.9	4.8	-3.6	-2.7

For both assumptions large negative dipoles are determined. These negative dipoles are due to several factors including the crystalline structure of the GaON, the spontaneous polarization of GaN and potentially GaON, and the Ga-vacancies in the GaON. Previous research regarding GaON has resulted in three potential crystalline graphic structures, hexagonal wurzite, spinel-GaON (γ-GaON) similar to spinel-Ga_2O_3 (γ-Ga_2O_3), and a poly-type made up of hexagonal wurzite and cubic coexisting. The hexagonal wurzite has similar lattice coefficients to GaN; however, the c = 15.514 Å, γ-GaON has the following lattice coefficient: a = 5.85 or 8.2 Å (*109*), while the poly-type has the following coefficients: a = 4.494 Å for cubic and a = 3.185 Å and c = 15.514 Å for wurzite (*110*).

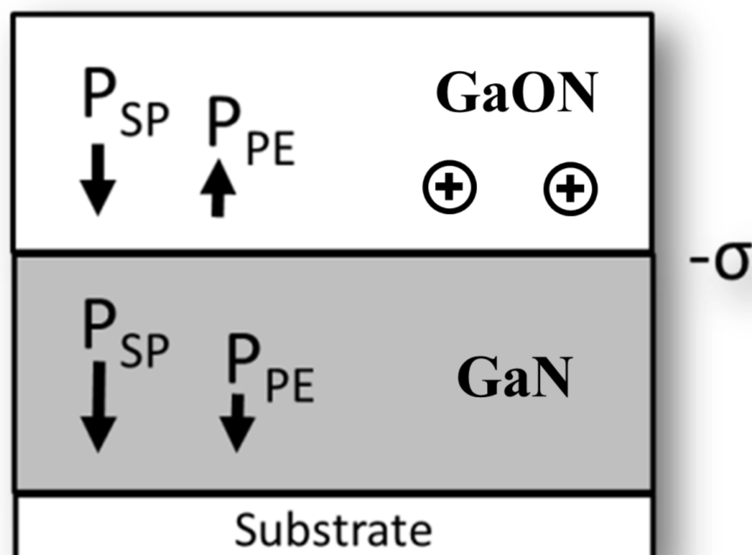

Fig. 42. Possible mechanisms behind the negative dipole at the GaN/GaON. Spontaneous and piezoelectric polarization, P_{SP} and P_{PE}, in the GaON and GaN resulting in an overall negative dipole, σ, at the GaN/GaON interface and Ga vacancies in the GaON, +.

Depending on the structure and elastic coefficients of the GaON, GaON may experience piezoelectric polarization in the positive direction due to compressive strain

and spontaneous polarization in the negative direction due to the Ga-O and Ga-N bonds, Fig. 42. GaN will experience compressive strain, while the magnitude of the strain is dependent on the crystalline structure of the GaON. The spontaneous polarization of GaN would be greater than that of the GaON due to the non-uniformity of the GaON film. Ga vacancies in GaON have been accounted for in previous work regarding GaON (*110*). Ga vacancies are considered to be acceptor defects, resulting in positive charges throughout the oxide (*54*). With all of these factors in mind a negative dipole would be expected at the GaN/GaON interface due to the overall polarization of the GaN, Fig. 42.

5.4 Conclusion

In summary, the band alignment of GaON on aq-HCl cleaned GaN has been investigated. To the authors knowledge this is the first time the band offset measurements for GaN/GaON have been calculated using UPS and XPS. The electron affinities and valence band maxima for aq-HCl GaN and GaON were measured using UV photoelectron spectroscopy (UPS). Band bending at the GaN/GaON was determined using the shifts in the Ga 3*d* and N 1*s* core-level peaks measured using X-ray photoelectron spectroscopy (XPS) assuming that either the shifts are only correlated to band bending or only due to the change in bond structure. Flat band existed at the GaN/GaON interface. An interface dipole of -2.7 eV ± 0.2 eV assuming that the core level shifts are only representative of the GaN band bending at the interface was calculated. If it is assumed that the core level shifts are only due to the oxidation of GaN then the exhibited dipole at the GaN/GaON interface is calculated to be -1.8 eV ± 0.2 eV. It is found that the observed dipole is primarily due to the polarization of the GaN. Future research is needed to determine the magnitude of the varying components.

5.5 Acknowledgements

We thank the National Science Foundation (Grant No. 0618242) for funding the X-ray Photoelectron Spectrometer used in this work. Financial support from the National Excellence Fellowship and NSF grant #1028910 and #0901699 is gratefully acknowledged.

CHAPTER VI
AB INITIO ANALYSIS OF THE INTERACTIONS OF GaN CLUSTERS WITH OXYGEN AND WATER*

Due to the formation of an interfacial layer during atomic layer deposition (ALD) of HfO_2 on GaN, a better understanding of the mechanisms behind GaN oxidation is needed. In this chapter we discuss the calculations of the interactions of oxygen and water with the Ga-face of GaN clusters, which could be used as testbeds for the actual Ga-face on GaN crystals of importance in electronics; however; an additional goal is the analysis of the nano-clusters for several other applications in nanotechnology. The results show that the local spin plays an important role in these interactions. It is found that the most stable interaction of O_2 and the GaN clusters results in the complete dissociation of the O_2 molecule to form two Ga-O-Ga bonds, while the most stable interaction between a H_2O molecule and the GaN clusters is the complete dissociation of one of the O-H bonds to form a Ga-O-H bond and a Ga-H bond.

6.1 Introduction

Enhancement-mode (E-mode) III-V based devices are currently needed for digital applications and low-loss high-power switching such as RF switches and transmitter/receiver switches for GPS receivers in mobile phones (*111*). E-mode devices are devices that are "OFF" when the gate source voltage is zero and are "ON" when the gate source voltage is pulled towards the drain voltage, positive for NMOS logic and negative for PMOS logic. To achieve E-mode III-V based devices the threshold voltage (V_{th}) of the device must be controlled, i.e. it should be positive or negative and be within

---

*Reprinted with permission from "Ab Initio Analysis of the Interactions of GaN Clusters with Oxygen and Water" by Mary R Coan, Paola Leon-Plata and Jorge M Seminario, 2012, *The Journal of Physical Chemistry C*. Copyright 2012 American Chemical Society. URL: http://pubs.acs.org/doi/abs/10.1021/jp302026n.

a certain voltage range, depending on the logic used (NMOS or PMOS) and their applications (*27, 95, 96*).

A current method being developed to control the threshold voltage is tuning the work function of the gate metal by varying the gate metal dielectric stack (*27, 95, 96*). To efficiently accomplish this task, the effects of the semiconductor and gate stack dipoles on the gate metal work function need to be thoroughly understood. The high-κ dielectric/III-V semiconductor interface has been shown to influence the work function of the gate metal and therefore the threshold voltage (*27, 29*). Several III-V based devices with varying gate stacks utilizing high-k materials such as HfO_2 and Al_2O_3 have been studied (*26, 27*). Previous research has shown that a thin GaON interfacial layer is formed during the atomic layer deposition (ALD) of HfO_2 on to clean Ga-face GaN (*30*).

Recently, GaN nanoclusters have been made by using the sequential ion implantation in a dielectric matrix (*112*). Another method to form GaN nanoclusters is to rinse the sample in a solution of a donor stabilized gallium-triazid (*113*). These may be considered nanoclusters of GaN adsorbed over the surface of a thin film. Materials made from or containing GaN have been extensively studied since the early 90's theoretically using *ab initio* electronic structure methods for GaN clusters (*114-123*). The theoretical studies of structural, dielectric, phonon dispersions and density of states for wurzite and/or zinc-blende GaN along with the stoichiometry and structure of the (0001) surface of GaN have been completed (*114, 116, 117*). The structural and electronic properties of GaN clusters have been previously modeled (*118-120, 123*). Theoretical calculations of the adsorption of O_2 onto GaN (0001) have previously been reported using density functional theory (DFT) within the generalized gradient approximation (GGA) (*124*) and other basis sets (*125, 126*) using only 2 x 2 super cell geometries. Theoretical calculations of the adsorption of H_2O onto GaN (0001) surface have been studied using DFT-GGA with an initial GaN geometry of a 2 x 2 super cell (*127*).

In this chapter, the oxidation of the Ga-face GaN surface with varying oxidation methods and surface structures are studied using the *ab initio* density functional theory

(DFT) using varying GaN structures with the intent to improve the development of materials and to investigate the features of these devices as they are scaled down to nanosizes. We believe forming individual devices with small nano-clusters could expand their applications beyond photonics and electronics areas such as catalysis, sensing equipment, and biomedical applications.

6.2 Methodology

The oxidation of a GaN surface is studied using hexagonal wurzite crystal geometries that resemble bulk GaN, a = 3.189 Å and c = 5.186 Å 24 (*54*). Hexagonal wurzite crystal geometries are considered the most thermodynamically stable structures for GaN. The surface Ga atoms are bonded to three N atoms and allowed to maintain one dangling bond. Three main surface structures are used to model bulk Ga-face GaN, Ga-centered, N-centered, and Hollow-centered surface structures. Four different forms of oxygen are used as the oxygen source during oxidation: an O atom, double bonded O_2, -OH molecules and H_2O. The oxygen source is within 2.50 Å of the surface or within a Ga-O and/or Ga-H bond length to a single Ga atom on the surface.

Calculations for the Ga-centered, N-centered, and Hollow-centered surface structures with and without an oxygen source are performed at the B3PW91/LANL2DZ (*75, 81, 128-134*) level of theory with varying multiplicities. The B3PW91 functional is a hybrid functional that uses the Becke exchange (*81*) combined with a Hartree-Fock (*135-137*) component and the correlation functional of Perdew-Wang (*75, 128-130, 134*). We have thoroughly tested the B3PW91 functional (*121, 138-140*). The basis set and effective core potential is the LANL2DZ (*131-133*). Optimizations were carried with the Berny method (*141, 142*). All structures are checked to be local minima by calculating the Hessian matrix, i.e., the second derivative of the energy with respect to all coordinates. Those that were found with negative eigenvalues were carefully analyzed and their geometry modified in order to get local minima; otherwise, their

imaginary frequencies are reported. All of the calculations are performed with the program GAUSSIAN-09 (*143*).

6.3 Results and Discussion

6.3.1 Testbeds

The formation of the Ga-face GaN cluster that represents localized regions of the bulk GaN are simulated and optimized. The optimized Ga-centered (Ga-GaN Testbed), N-centered (N-GaN Testbed), and Hollow-centered (Hollow-GaN Testbed) cluster surface structures are shown in Fig. 43. These nano-structures are chosen to approximate the local chemistry of the bulk surface of GaN that an O atom may come in contact with when the atom approaches the GaN surface. In this study, we are only interested in the oxidation of bulk GaN; therefore, hydrogen is added to the edges of the cluster to remove potential edge effects and to remove dangling bonds from non-surface atoms. The bulk surface Ga atoms are bonded to three N atoms and are allowed to have one dangling bond (*144*).

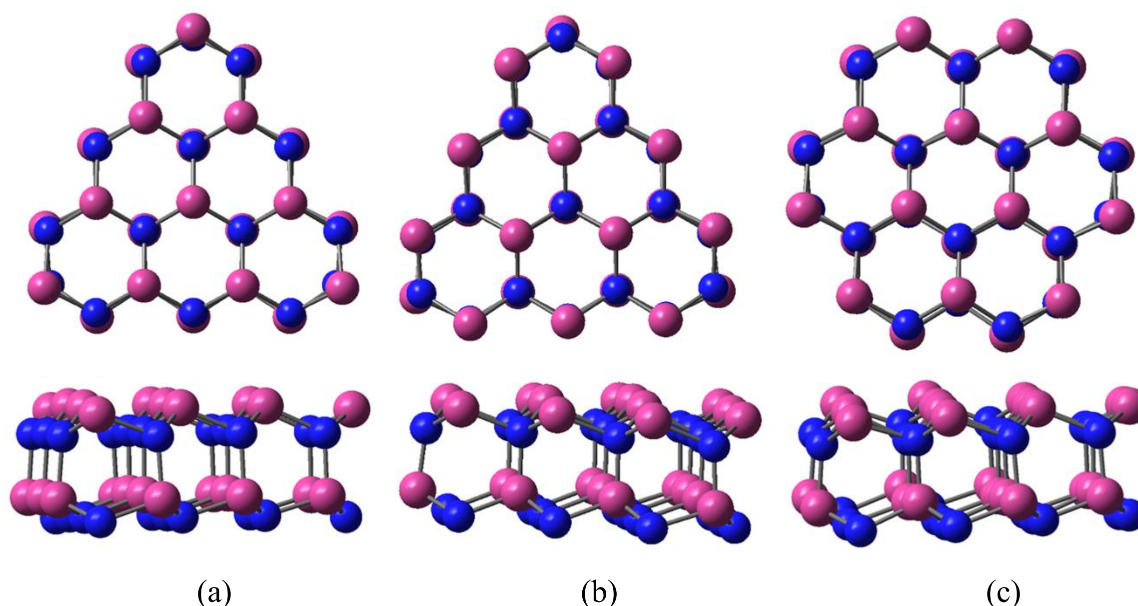

Fig. 43. Top and side views of the optimized GaN clusters used as surface reactive centers (testbeds) of a GaN surface (without H atoms) (a) Ga-centered, (b) N-centered, and (c) Hollow-centered. Ga is pink and N is Blue.

6.3.2 Oxidation of GaN Clusters Using Oxygen

Using the optimized GaN testbeds, oxygen is introduced to the Ga-centered, N-centered and hollow-centered clusters in two forms: a single O atom and double bonded O_2 to represent different oxidation techniques within 2.50 Å of the GaN surface. Oxygen is also introduced to the clusters within an O-Ga bond length to a single surface Ga atom that is part of the bulk GaN; a bond was not intentionally formed. All clusters are optimized using the B3PW91/LANL2DZ (*75, 81, 128-134*) level of theory with varying multiplicities (Fig. 44- Fig. 46). The total energies, are shown in Table 8 - Table 10 for the Ga-centered, N-centered, and hollow-centered structures, respectively. Also shown in Table 8 - Table 10 are the smallest initial and final distances of the oxygen atoms to the nearest Ga surface atom, the smallest initial and final angles from the O atom to the nearest surface Ga atom to the next N atom in the active region, and the shortest Ga-N bond length, where the N atom is part of the bulk GaN and the Ga atom is participating in the oxidation.

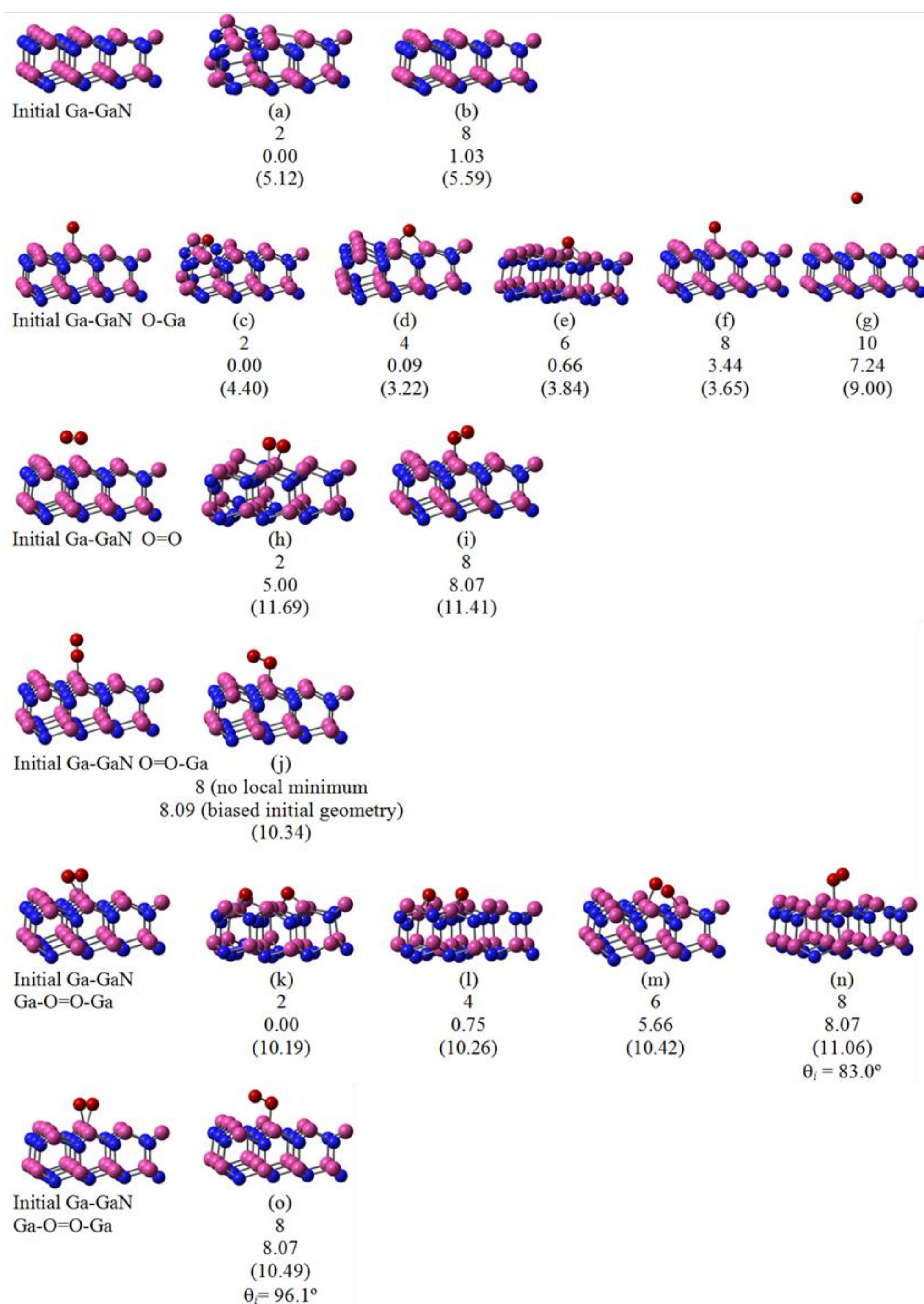

Fig. 44. Initial and final side views of the Ga-centered GaN structures (without H atoms) with and without oxygen being introduced to the cluster. (a-b) no oxygen atoms, (c-g) single O atom, (h) two O atoms, (i) O_2, (j) O_2 within a bonds length to a single surface Ga atom, and (k-o) O_2 with both O within a bond length to a single surface Ga atom. Below each diagram is the multiplicity, the optimized geometry relative energy, the initial geometry relative energy inside parentheses, and the smallest angle O-Ga-N (where applicable). Energies are in eV. Ga is pink, N is blue, and O is red.

Fig. 44 and Table 8 both illustrate the interaction between the Ga-centered GaN surface and oxygen atoms. More specifically, Fig. 44 (a)-(b) shows the optimization of the Ga-centered GaN testbed structure using a multiplicity of 2 and 8. While the GaN testbed with a multiplicity of 2 has the lowest relative energy, 0.00 eV, the testbed structure used in all subsequent simulations is the Ga-GaN testbed with a multiplicity of 8, 1.03 eV, due to the consistent Ga-N bond lengths, 2.00 Å, and wurzite configuration. Due to the methodology used to grow GaN on varying substrates (*145*), it is impractical to compare the surface structure of the Ga-GaN Testbed simulation to experimental results. However, it is known that Ga-terminated GaN has a wurzite or zinc blend structure (*145*), in this chapter we focus on the wurzite structure. With the optimization of the Ga-center GaN testbed structure complete, oxygen atoms were introduced to the system.

Table 8. Total optimized energies in Hartrees for Ga-centered GaN cluster, multiplicity (*m*), initial (d_i) and final (d_f) distances from the O atom to the nearest surface Ga atom, smallest initial (θ_i) and final (θ_f) O-Ga-N angles in the active region, and shortest Ga-N bond length ($d_{Ga\text{-}N}$) for the Ga atom that is taking part in the oxidation and the N atom that is part of the active region GaN.

Structures	*m*	Energy (Hartree)	Energy (eV)	d_i (Å)	θ_i (°)	d_f (Å)	θ_f (°)	$d_{Ga\text{-}N}$ (Å)
Ga-GaN Testbed	2	-1273.51286[a]	0.00					1.96
	8	-1273.47490	1.03					2.00
Ga-GaN O-Ga	2	-1348.79400	0.00	2.00	112.4	1.86	79.1	1.92
	4	-1348.79071	0.09	2.00	112.4	1.85	103.0	1.94
	6	-1348.76996	0.66	2.00	112.4	1.87	85.8	1.94
	8	-1348.66739	3.44	2.00	112.4	1.86	106.9	1.95
	10	-1348.52777[b]	7.24	2.00	112.4	4.26	110.9	2.00
Ga-GaN O=O	2	-1423.92661[c]	5.00	2.50	83.0	1.88	96.1	1.92
	8	-1423.81373	8.07	2.50	83.0	1.91	105.3	1.94
Ga-GaN O=O-Ga	8	-1423.81317	8.09	2.00	109.3	1.91	106.5	1.94
Ga-GaN Ga-O=O-Ga	2	-1424.11035	0.00	2.00	83.0	1.88	90.4	1.89
	4	-1424.08267	0.75	2.00	83.0	1.84	82.8	1.88
	6	-1423.90233	5.66	2.00	83.0	1.88	95.5	1.94
	8	-1423.81375	8.07	2.00	83.0	1.91	106.0	1.94
	8	-1423.81374	8.07	2.00	96.1	1.91	106.0	1.94

Imaginary frequencies (cm^{-1}): $16i$[a]; $11i$ and $9i$[b]; $28i$[c]

A single oxygen atom is first presented to the Ga-GaN testbed 2.00 Å from the center of Ga surface atom and allowed to optimize using varying multiplicities (Ga-GaN O-Ga). The initial and final structures with their respective multiplicities are found in Fig. 44 (c)-(g). During optimization of Ga-GaN O-Ga m = 4, the O atom shifted and formed two 1.85 Å bonds with two neighboring Ga atoms which resulted in the initial Ga-O bond being broken. Thus a Ga-O-Ga bond on the surface with a final relative energy of 0.00 eV, and Ga-O bond lengths of 1.85 Å (Table 8) which correspond to the Ga-O bond lengths in β-Ga_2O_3 (*146*).

O_2 is introduced to the Ga-GaN test bed 2.50 Å from the center Ga surface atom and allowed to optimize using a multiplicity of 2 and 8, (Ga-GaN O=O), Fig. 44 (h) and Fig. 44 (i). The optimization of the Ga-GaN O=O m = 2 structure results in the complete dissociation of the O_2 bond with an initial and final O to O distance of 1.16 Å and 1.54 Å, Fig. 44 (h). However, in the case of Ga-GaN O=O m = 8 structure the optimization results in a surface Ga atom bonding to an O atom, 1.91 Å, without completely dissociating the O_2 bond. The initial and final O_2 bond lengths are 1.16 Å and 1.39 Å, respectively.

O_2 is also introduced to the GaN active region 2.00 Å above the center Ga surface atom and allowed to optimize using varying multiplicities, (Ga-GaN O=O-Ga and Ga-GaN Ga-O=O-Ga). Fig. 44 (i)-(n) depicts the interaction between the O_2 and GaN surface. The mechanism of the O_2 and GaN interactions are tabulated in Table 8 for varying multiplicities. Table 8 shows that the most stable optimized Ga-centered test bed structure with O_2 is Ga-GaN Ga-O=O-Ga with a multiplicity of 2, 0.00 eV, with final bond lengths of 1.88 Å for three of the four Ga-O bonds and 2.00 Å for the last Ga-O bond and 1.90 Å for Ga-N. It is important to note that O_2, O=O bond length of 1.16 Å, was dissociated by the GaN surface resulting in a final O to O distance of 3.14 Å. The dissociation of the O_2 molecule is expected due to the strong positive surface dipole seen by the O atom due to the Ga-N bond.

Fig. 45 and Table 9 illustrate the interaction between the N-centered GaN cluster and oxygen atoms. The initial oxygen atoms are located above the center nitrogen atom

representing another potential oxygen-GaN surface interaction. The N-center GaN testbed used to test the oxygen/surface interaction is the N-GaN testbed with a multiplicity of 4 and a final relative energy of 0.08 eV, due to the consistent Ga-N bond lengths, 2.00 Å, and wurzite configuration, Fig. 45 (b). While N-GaN testbed with a multiplicity of 2 has a lower final relative energy, 0.00 eV, its configuration does not match a wurzite structure that is known to occur in grown and deposited GaN, (*145*) Fig. 45 (a).

In all cases tested, a single O atom initially located above the center N atom shifts towards a nearby surface Ga atom and bonds to the surface, Fig. 45 (c)-(e). For the most stable state, N-GaN O m = 2, the oxygen atom bonded to three surface Ga atoms resulting in deformation of the cluster, Fig. 45 (c). Deformation of the cluster is due to the electronegativity of the O and the N atoms. This deformation may indicate a mechanism for oxidation of surface defects. If enough oxygen is present the O atoms may continue to repulse the N atoms in defects and cause oxidation to occur along a dislocation. This may also be the mechanism behind the formation of gallium oxide. As the oxygen deforms the surface another oxygen atom attracted to the Ga surface will repulse the initial oxygen causing further deformation.

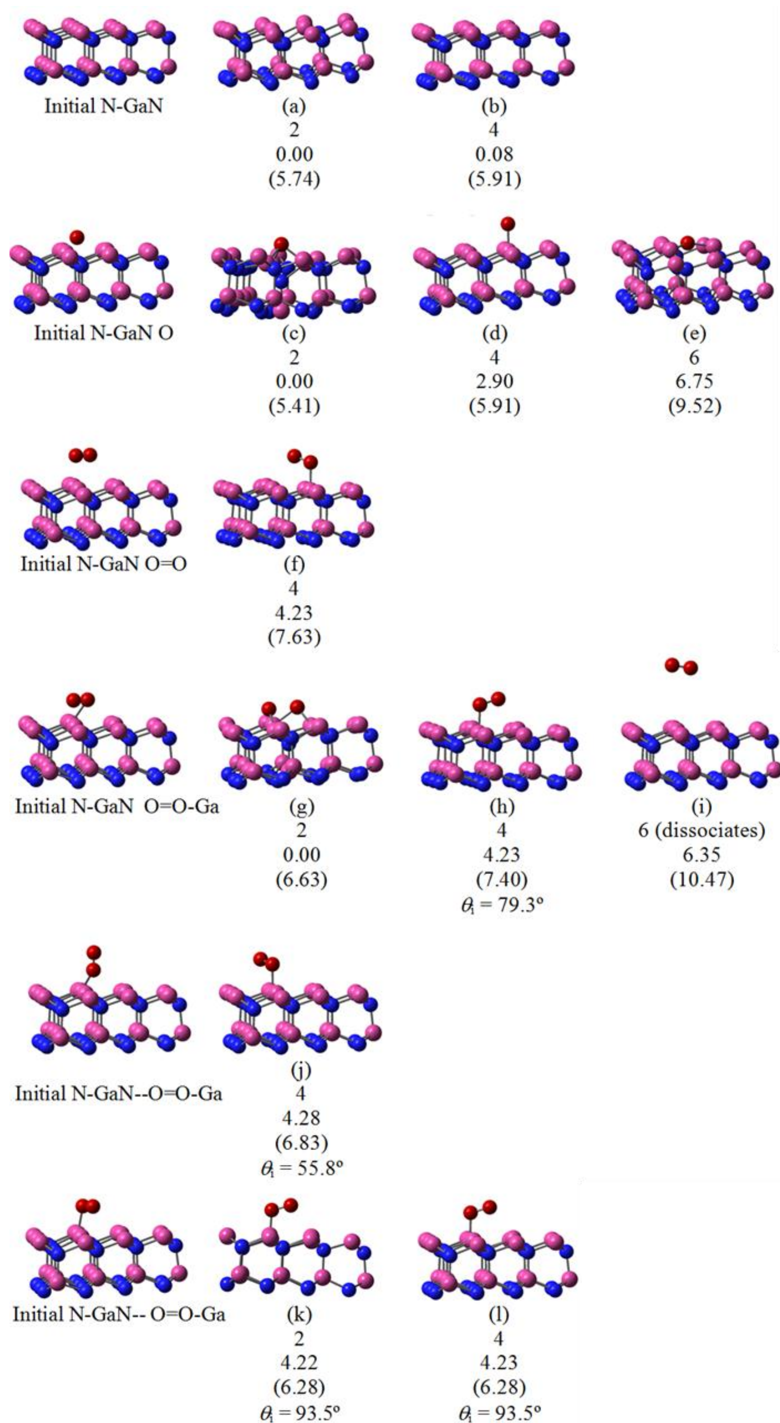

Fig. 45. Initial and final side views of the N-centered GaN clusters (H atoms not shown) with and without oxygen introduced to the cluster. (a,b) no oxygen atoms; (c-e) single O atom, (f) O_2, and (g-l) O_2 and within a bond length to a single surface Ga atom. Below each diagram is the multiplicity, , the optimized geometry relative energy, the initial geometry relative energy inside parentheses, and the smallest angle O-Ga-N (where applicable). Energies are in eV. Ga is pink, N is blue, and O is red.

Fig. 45 (f)-(k) shows the interaction between the N-centered GaN active region and O_2. Most of the interactions tested result in the movement of the O_2, O-O bond length of 1.16 Å, towards a nearby surface Ga atom followed by an O atom bonding to the closest surface Ga atom without completely dissociating the O_2 bond, final O-O bond lengths 1.39-1.40 Å, Table 9 and Fig. 45 (f), (h), (j)-(l). Only in one case does the O_2 completely dissociate: N-GaN O=O-Ga with a multiplicity of 2, Fig. 45 (g); the initial and final O-O distances were 1.16 Å and 2.34 Å. The most stable O_2 interaction with the N-centered GaN test bed is N-GaN O=O-Ga with a multiplicity of 2 and a final energy of 0.00 eV. From Table 9, the highest final energy is for N-GaN O=O-Ga with a multiplicity of 6, 6.35 eV, which resulted in no O_2/GaN surface interaction. While the complete dissociation of the O_2 molecule due to the GaN surface dipole is more stable, the partial dissociation of the O_2 molecule results in a lower final energy compared to that of no O_2/GaN surface interaction, Table 9.

Table 9. Total optimized energies in Hartrees for N-centered GaN cluster, multiplicity (m), initial (d_i) and final (d_f) distances from the O atom to the nearest surface Ga atom, smallest initial (θ_i) and final (θ_f) O-Ga-N angles in the active region, and shortest Ga-N bond length (d_{Ga-N}) for the Ga atom that is taking part in the oxidation and the N atom that is part of the active region GaN.

Structures	m	Energy (Hartree)	Energy (eV)	d_i (Å)	θ_i (°)	d_f (Å)	θ_f (°)	d_{Ga-N} (Å)
N-GaN Testbed	2	-1278.20431	0.00					2.00
	4	-1278.20117	0.08					2.02
N-GaN O	2	-1353.49744	0.00	2.03	48.2	2.00	74.6	1.92
	4	-1353.39073	2.90	2.03	48.2	1.85	108.0	1.95
	6	-1353.24951	6.75	2.03	48.2	1.88	47.6	2.00
N-GaN O=O	4	-1428.53438	4.23	2.50	85.2	1.90	108.3	1.94
N-GaN O=O-Ga	2	-1428.68994	0.00	2.01	79.3	1.86	83.0	1.94
	4	-1428.53445	4.23	2.01	79.3	1.90	108.3	1.94
	6	-1428.45673	6.35	2.01	79.3	4.27	99.3	2.02
	4	-1428.53260	4.28	2.00	55.8	1.89	110.1	1.94
	2	-1428.53464	4.22	2.00	93.5	1.90	108.3	1.94
	4	-1428.53452	4.23	2.00	93.5	1.87	108.3	1.94

Fig. 46 and Table 10 illustrate the interaction between the Hollow-centered GaN cluster and oxygen atoms. Several multiplicities are used to determine the Hollow-centered GaN Test bed that would be used to test the oxygen and GaN interactions, Fig. 46 (a)-(d). The most stable structure is the hollow-GaN test bed with a multiplicity of 3 and a final relative energy of 0.00 eV, Table 10. The hollow-GaN test bed has consistent Ga-N bond lengths and follows the wurzite structure.

A single oxygen atom is introduced to the Hollow-centered GaN active region in the center of the ring, and the system is optimized using multiplicities of 3, 5, 7, and 9, Fig. 46 (e)-(h). The most stable final structure is Hollow-GaN O with a multiplicity of 3 and a final energy of 0.00 eV, which resulted in the creation of two O-Ga bonds in the form of Ga-O-Ga where the Ga atoms are different surface atoms. Other interactions with higher energies are shown in Fig. 46 (f)-(h) and in Table 10 for comparison.

Two oxygen atoms are introduced to the Hollow-centered GaN testbed region close to the center of the hollow ring, but is slightly shifted towards one of the surrounding surface Ga atoms, Fig. 46 (i)-(l). The oxygen atoms are within a bonds length of the surface Ga atom; however no bond was initially formed. The most stable final structure resulted from Hollow-GaN Ga-O, Ga-O with a multiplicity of 5 and a final energy of 2.36 eV. One O atom remained bonded to a single surface Ga atom while the other shifted away from the first O atom and bonded to another surface Ga atom while remaining bonded to the original surface Ga atom.

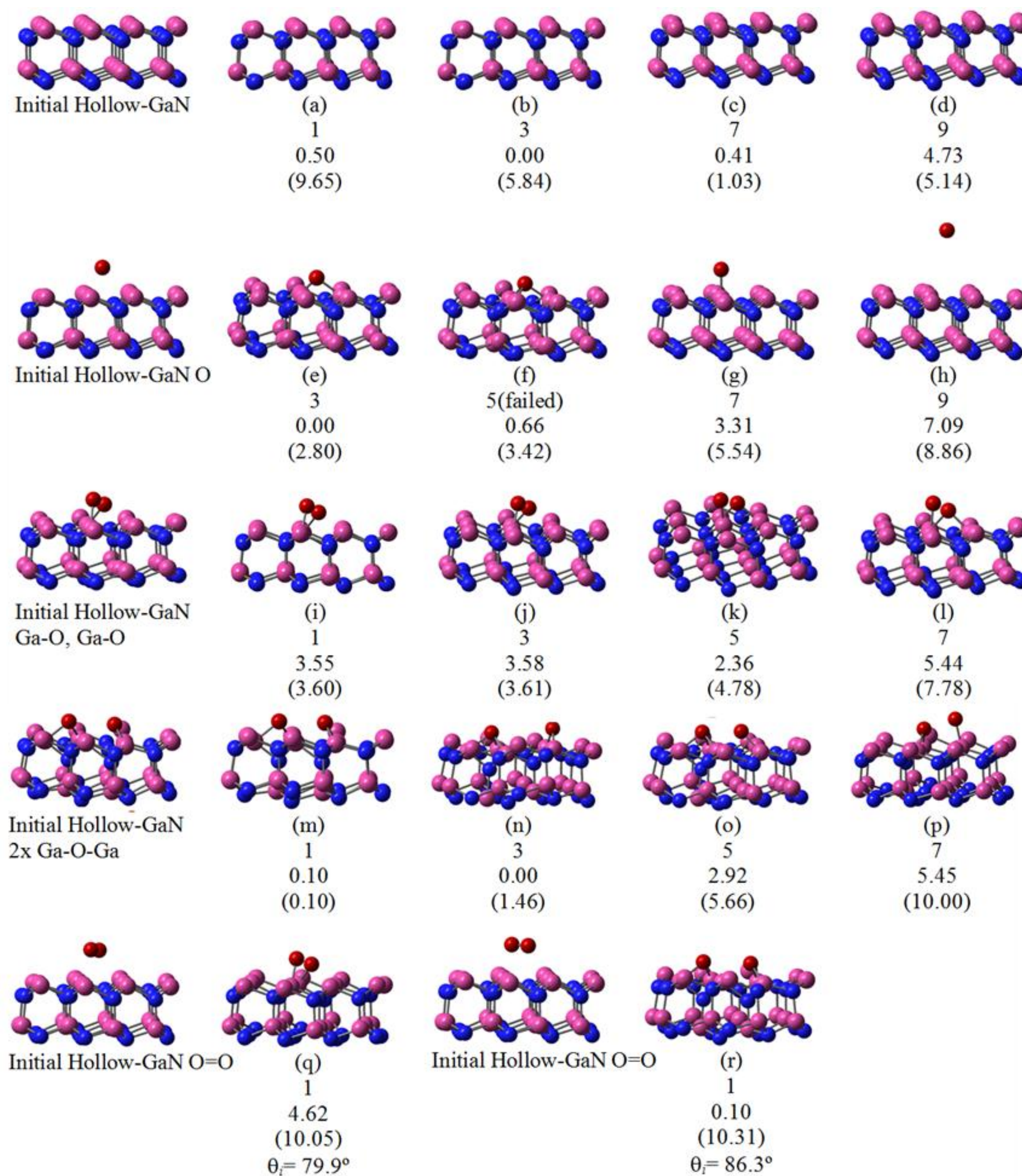

Fig. 46. Initial and final side views of the Hollow-centered GaN clusters (without H atoms) with and without oxygen being introduced to the system. (a-d) no oxygen atoms, (e-h) single O atom, (i-l) two O atoms each within a bonds length to a different surface Ga atom, (m-p) two O atoms each within a bonds length to two different surface Ga atoms, and (q-r) O_2 double bonded. Below each diagram is the multiplicity, the optimized geometry relative energy, the initial geometry relative energy inside parentheses, and the smallest angle O-Ga-N (where applicable). Energies are in eV. Ga is pink, N is blue, and O is red.

A different set of two single O atoms near the surface Ga atoms that make up the center ring were introduced. The optimized structures result in several varying geometries based on the multiplicity used, Fig. 46 (m)-(p). Hollow-GaN 2x Ga-O-Ga with a multiplicity of 3 results in the lowest final energy of 0.00 eV. One of the two O atoms bonded to three surface Ga atoms while the other retained its bond to the two original surface Ga atoms. The O atom that is bonded to three surface Ga atoms caused a deformation in the GaN cluster. This deformation is due to the electronegativity of the oxygen and nitrogen atoms. As previously stated, this deformation is believed to be a mechanism to oxidize surface dislocations and defects. However, the O atom that remained bonded to two Ga atoms forced the Ga atoms to shift towards each other creating a potential bond between two surface Ga atoms; the initial and final Ga-Ga distances are 2.72 and 2.65 Å. While there was a shift in the Ga surface atoms, it did not result in a Ga-N bond breaking.

The interaction between O_2 and the Hollow-centered GaN active region is tested. The O_2 is introduced to the system above the center hollow ring in two directions perpendicular to one another, Fig. 46 (q)-(r). Both optimizations result in the complete dissociation of the O_2 bond where the initial bond length was 1.16 Å and the two final lengths are 1.59 Å for Fig. 46 (q) and 3.23 Å for Fig. 46 (r). The lowest final energy results from Hollow-GaN O=O with a multiplicity of 1 and an initial O-Ga-N bond angle of 86.3° with a final energy of 0.10 eV, Fig. 46 (r) and Table 10.

The most stable interaction between the GaN active region and one O atom results in the formation of either two or three Ga-O bonds depending on the location of the original O atom and the local spin. By optimizing the same geometry with varying multiplicities the effect of the local spin is shown to play an important role in the oxidation of GaN. For an example, when an O atom is within 2.50 Å of a surface Ga atom and centered above a N atom three Ga-O bonds will form, Fig. 45 (c), when the local spin is S = ½ (m = 2). However, when the same geometry is optimized using a local spin of S = 3/2 (m = 4), only one Ga-O bond forms, Fig. 45 (d). The effect of local spin is also shown in Fig. 44 - Fig. 46.

Table 10. Total optimized energies in Hartrees for Hollow-centered GaN cluster, multiplicity (*m*), initial (d_i) and final (d_f) distances from the O atom to the nearest surface Ga atom, smallest initial (θ_i) and final (θ_f) O-Ga-N angles in the active region, and shortest Ga-N bond length ($d_{Ga\text{-}N}$) for the Ga atom that is taking part in the oxidation and the N atom that is part of the active region GaN.

Structures	*m*	Energy (Hartree)	Energy (eV)	d_i (Å)	θ_i (°)	d_f (Å)	θ_f (°)	$d_{Ga\text{-}N}$ (Å)
Hollow-GaN Testbed	1	-1390.21377[a]	0.50					1.97
	3	-1390.23205	0.00					1.99
	7	-1390.21710	0.41					2.01
	9	-1390.05830	4.73					1.96
Hollow-GaN O	3	-1465.53053	0.00	2.50	84.5	1.93	85.5	1.93
	5	-1465.50627	0.66	2.50	84.5	1.95	85.8	1.94
	7	-1465.40866	3.31	2.50	84.6	1.86	106.9	1.95
	9	-1465.26986	7.09	2.50	84.6	4.42	96.9	2.01
Hollow-GaN Ga-O, Ga-O	1	-1540.66091	3.55	1.86	86.8	1.87	85.8	1.93
	3	-1540.65993	3.58	1.86	86.8	1.87	86.2	1.93
	5	-1540.70473	2.36	1.86	86.8	1.84	85.8	1.96
	7	-1540.59137	5.44	1.86	86.8	1.94	82.1	1.93
Hollow-GaN 2x Ga-O-Ga	1	-1540.78767	0.10	1.94	73.2	1.94	73.2	1.90
	3	-1540.79147	0.00	1.94	73.2	1.84	74.7	1.91
	5	-1540.68432	2.92	1.94	73.2	1.89	74.9	1.92
	7	-1540.59137	5.45	1.94	73.2	1.94	82.1	1.93
Hollow-GaN O=O	1	-1540.62187	4.62	2.50	79.9	1.86	86.8	1.93
	1	-1540.78767	0.10	2.50	86.3	1.94	73.2	1.91

Imaginary frequencies (cm^{-1}): $39i$[a]

When the O atom is centered above a surface Ga atom or directly above the center of a ring and within 2.50 Å to the closest surface Ga atom, two Ga-O bonds will form a Ga-O-Ga structure, Fig. 44 (c) and Fig. 46 (e). The most stable interaction of O_2 and the active GaN region results in the complete dissociation of the O_2 molecule to form two Ga-O-Ga bonds for all tested scenarios, Fig. 44 (k), Fig. 45 (g), and Fig. 46 (n). However, the most stable interaction of two O atoms within a bonds length to the surface for a Hollow-GaN resulted in the formation of one oxygen atom bonded to three Ga atoms and the other oxygen atom bonded to two Ga atoms, Fig. 46 (n). The formation of three Ga-O bonds causes the deformation of the GaN cluster due to the electronegativity of the oxygen and nitrogen atoms. This deformation may indicate a mechanism for oxidation of surface defects such as dislocations. If enough oxygen is present the O atoms may continue to repulse the N atoms in defects and cause oxidation to occur beyond that of the initial surface.

6.3.3 Oxidation of GaN Clusters Using Water

Water is introduced to the Ga-centered, N-centered and hollow-centered systems in two forms: a single H_2O molecule and -OH to represent oxidation using water vapor and the stability of Ga-OH bonds on a Ga-terminated GaN surface. The stability of Ga-OH bonds are tested due to the formation of a Ga-OH bond and a single H atom as the optimized structure for the oxidation of the GaN active region with a water molecule. All systems are optimized using the B3PW91/LANL2DZ (*147*) level of theory with varying multiplicities, Fig. 47 - Fig. 49. The total energies are shown in Table 11 - Table 13 for the Ga-centered, N-centered, and hollow-centered structures, respectively.

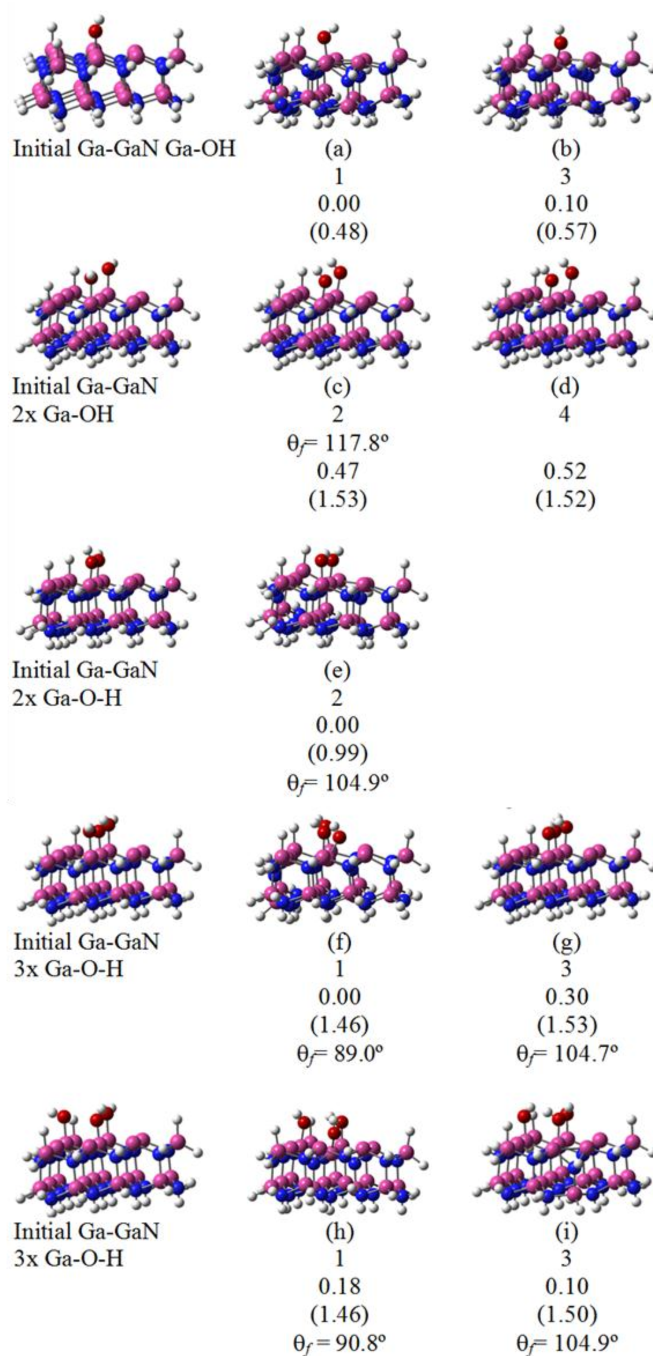

Fig. 47. Initial and final side views of the Ga-centered GaN clusters (with H atoms) with water or -OH being introduced to the system. (a-b) one –OH molecule within a Ga-O bonds length to the cluster, (c-e) two –OH molecules within a Ga-O bonds length to the cluster, (f-i) three –OH molecules each within a bonds length to a surface Ga atom, (j-q) one water molecule in varying rotations and distances from a surface. Below each diagram is the multiplicity, the optimized geometry relative energy, the initial geometry relative energy inside parentheses, and the smallest angle O-Ga-N (where applicable). Energies are in eV. Ga is pink, N is blue, and O is red. Ga atom. Ga is pink, N is blue, and O is red.

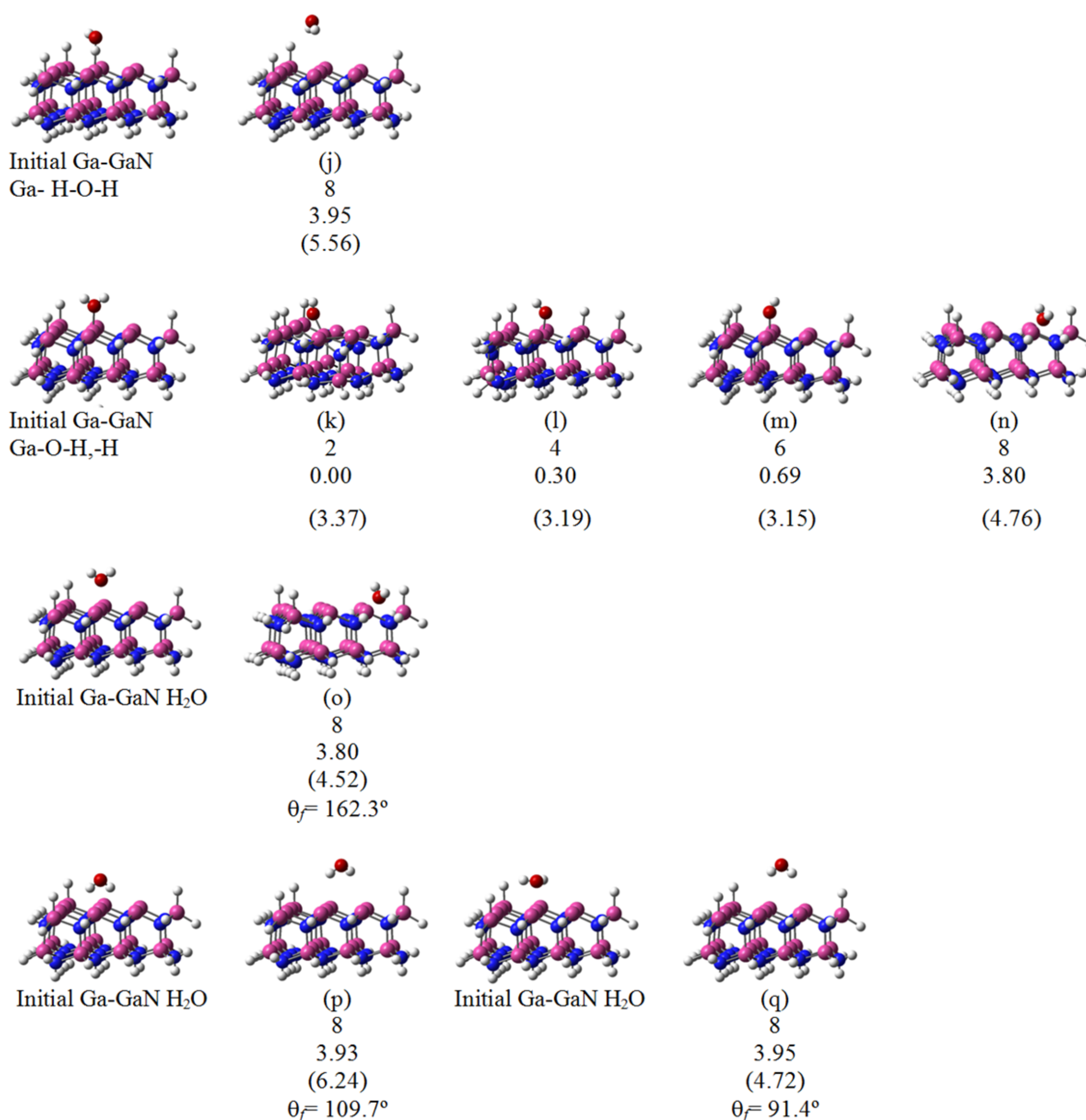

Fig. 47 Continued. Initial and final side views of the Ga-centered GaN clusters (with H atoms) with water or -OH being introduced to the system. (a-b) one –OH molecule within a Ga-O bonds length to the cluster, (c-e) two –OH molecules within a Ga-O bonds length to the cluster, (f-i) three –OH molecules each within a bonds length to a surface Ga atom, (j-q) one water molecule in varying rotations and distances from a surface. Below each diagram is the multiplicity, the optimized geometry relative energy, the initial geometry relative energy inside parentheses, and the smallest angle O-Ga-N (where applicable). Energies are in eV. Ga is pink, N is blue, and O is red. Ga atom. Ga is pink, N is blue, and O is red.

Fig. 47 and Table 11 illustrate the interaction between the Ga-centered GaN cluster and H_2O or -OH molecules. The Ga-centered GaN testbed is exposed to one, two or three –OH molecules and optimized using differing multiplicities, Fig. 47 (a)-(i). When the Ga-centered active region is exposed to a single –OH molecule, the GaN lattice became distorted and a Ga-Ga bond formed as a result of distortion and edge effects for all multiplicities tested Fig. 47 (a)-(b). The least distorted and most stable exposed Ga-centered testbed resulted from the optimized Ga-GaN Ga-O-H structure with a multiplicity of 1. The addition of two –OH molecules to the Ga-centered GaN active region resulted in similar optimized structures with the most stable being optimized using a multiplicity of 2 with a final bond angle of 104.9º, 0.00 eV, as seen in Fig. 47 (e) and Table 11. The most stable structure is the only structure that resulted in a distorted GaN lattice in the form of a Ga-Ga bond due to edge effects. The placement of the –OH molecules on the active region was tested by adding three –OH molecules to the Ga-GaN Test bed in two different configurations and optimizing the structures using a multiplicity of 1 and 3. The most stable Ga-GaN 3x Ga-O-H structure was optimized using a multiplicity of 1 with a final Ga-O bond angle of 88.97º, Fig. 47 (f).

A single water molecule is introduced to the Ga-GaN active region in several different orientations and distances from the surface and optimized using a multiplicity of 2, 4, 6 and 8. The most stable structure resulting in the formation of a Ga-O bond is Ga-GaN Ga-O-H,-H (m = 2) with a final Ga-O bond angle and length of 90.1º and 1.81 Å, seen in Fig. 47 (k) and Table 11). During the optimization of Ga-GaN Ga-O-H,-H (m = 2), one of the hydrogen atoms broke away from the water molecule allowing for the oxygen atom to bond with the nearest surface Ga atom. The free H atom shifted towards the nearest surface Ga atom with a dangling bond to form a Ga-H bond, Fig. 47 (k). The GaN lattice became distorted during optimization of the Ga-GaN Ga-O-H,-H (m = 2) and a Ga-Ga bond formed as a result of the deformation and edge effects. Two other structures resulted in the formation of a Ga-O bond, Ga-GaN Ga-O-H,-H (m = 4 and 6). Both of these structures did not result in the formation of a Ga-Ga bond. All other

structures resulted in no interaction between the Ga surface and water molecules and higher final energies.

Table 11. Total optimized energies in Hartrees for water oxidized Ga-centered GaN cluster, multiplicity (m), initial (d_i) and final (d_f) distances from the O atom to the nearest surface Ga atom, smallest initial (θ_i) and final (θ_f) O-Ga-N angles in the active region, and shortest Ga-N bond length (d_{Ga-N}) for the Ga atom that is taking part in the oxidation and the N atom that is part of the active region GaN.

Structures	M	Energy (Hartree)	Energy (eV)	d_i (Å)	θ_i (°)	d_f (Å)	θ_f (°)	d_{Ga-N} (Å)
Ga-GaN Ga-OH	1	-1349.38598	0.00	1.77	104.1	1.79	109.1	1.95
	3	-1349.38235	0.10	1.77	104.1	1.83	94.9	1.93
Ga-GaN 2x Ga-OH	2	-1425.24857	0.47	1.91	113.1	1.78	117.8	1.94
	2	-1425.26589	0.00	1.73	109.2	1.77	104.9	1.94
	4	-1425.24686	0.52	1.91	113.1	1.77	119.1	1.94
Ga-GaN 3x Ga-OH	1	-1501.13918	0.00	1.77	104.1	1.77	89.0	1.90
	1	-1501.13246	0.18	1.77	104.1	1.78	90.8	1.89
	3	-1501.12813	0.30	1.77	104.1	1.77	104.7	1.94
	3	-1501.13564	0.10	1.77	104.1	1.78	104.9	1.94
Ga-GaN Ga-H-O-H	8	-1349.86848	3.95	2.50	109.0	4.01	86.4	2.00
Ga-GaN Ga-O-H,-H	2	-1350.01348	0.00	1.90	109.5	1.81	90.1	1.93
	4	-1350.00241	0.30	1.90	109.5	1.78	101.2	1.95
	6	-1349.98835	0.69	1.90	109.5	1.77	104.1	1.96
	8	-1349.87374	3.80	1.90	109.5	3.37	162.4	1.97
Ga-GaN H_2O	8	-1349.87374	3.80	2.20	109.5	3.37	162.3	1.97
	8	-1349.86922[a]	3.93	2.20	109.7	3.83	109.7	1.97
	8	-1349.86831	3.95	2.20	111.2	3.88	91.4	1.97

Imaginary frequencies (cm^{-1}): $17i$[a]

Fig. 48 and Table 12 illustrate the interaction between the N-centered GaN cluster and H_2O or -OH molecules. The N-centered GaN testbed is exposed to one, two or three –OH molecules and optimized using differing multiplicities, Fig. 48 (a)-(f). The optimization of the N-GaN Ga-OH structure using a multiplicity of 1 did not result in the formation of bonds or the degradation of bonds, however the optimization resulted in the most stable structure with a final energy of 0.00 eV, Fig. 48 (a). The addition of two –OH molecules to the N-centered GaN system resulted in slight shifts in the Ga-O-H bonds when optimized, using a multiplicity of 2 or 4, Fig. 48 (c)-(d). However, during the optimization of N-GaN 2x Ga-OH (m = 4) two of the H atoms broke away from the edge Ga-H bond which resulted in a higher final energy of 2.70 eV compared to that of N-GaN 2x Ga-OH (m = 2) with all Ga-H bonds intact, 0.00 eV, as seen in Table 12.

It is important to note that the optimization of N-GaN 2x Ga-OH (m = 4) resulted in one of the Ga-OH bonds to form a -OH molecule bonded to two surface Ga atoms, Fig. 48 (d). While the formation of such a bond is not the most probable in this case, it is stable thus the bond structure may form. The optimization of N-GaN 3x Ga-OH was completed using multiplicities of 1 and 3. Both systems resulted in similar structures, i.e. no bonds were broken or formed, with final energies of 0.00 and 3.69 eV, respectively. The most stable geometry, N-GaN 3x Ga-O-H m = 1, was unable to reach the minimum energy, however the exact minimum energy should be around -1505.83584 Hartree, Table 12.

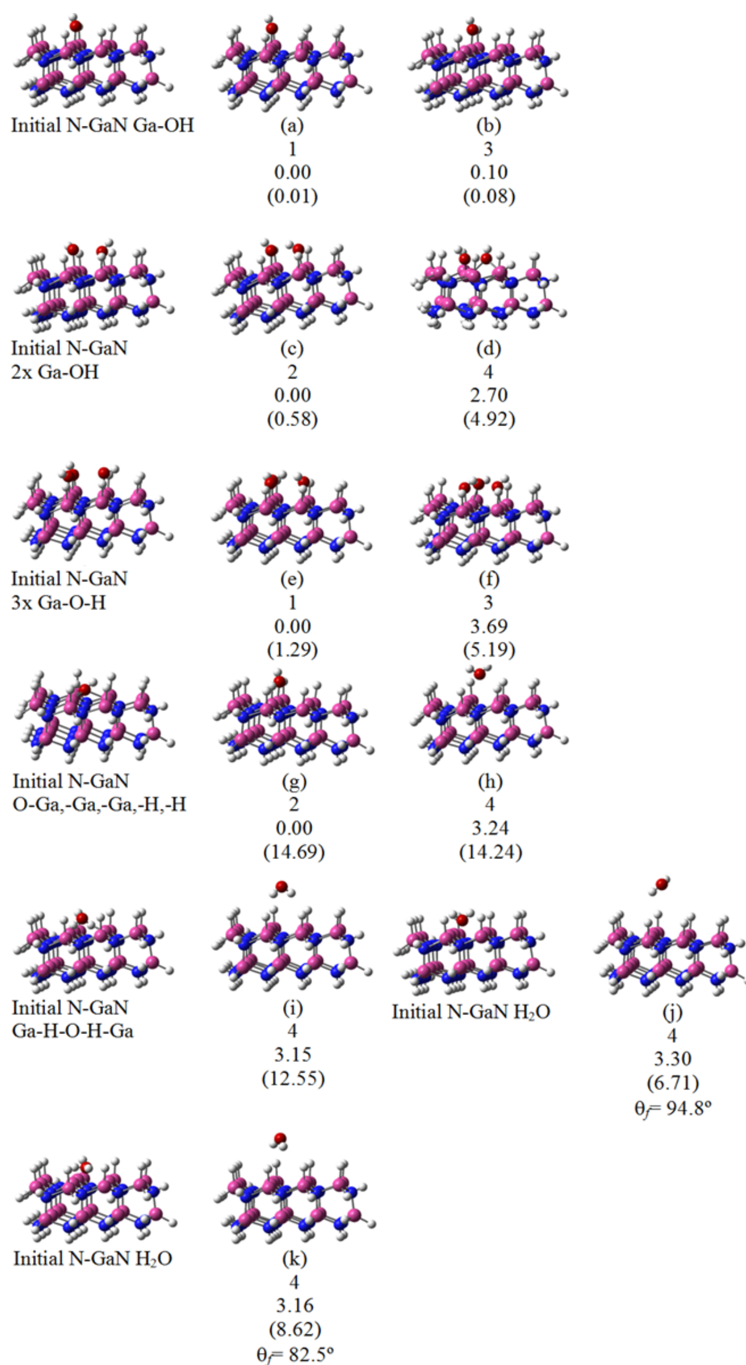

Fig. 48. Initial and final side views of the N-centered GaN structures (with H atoms) with water or -OH being introduced to the system. (a-b) one –OH molecule within a Ga-O bond length to the cluster, (c-d) two –OH molecules within a Ga-O bond length to the cluster, (e-f) three –OH molecules each within a bond length to a surface Ga atom, (g-k) one water molecule in varying rotations and distances from a surface Ga atom. Below each diagram are the multiplicity, the optimized geometry relative energy, and the initial geometry relative energy inside parentheses, and the smallest angle O-Ga-N (where applicable). Energies are in eV. Ga is pink, N is blue, and O is red.

A single water molecule is introduced to the N-GaN active region in several different orientations and distances from the surface and optimized using a multiplicity of 2 and 4. The most stable and only structure resulting in the formation of a Ga-O bond is N-GaN O-Ga,-Ga,-Ga,-H,-H (m = 2) with a final Ga-O bond angle and length of 105.4° and 1.76 Å, as seen in Fig. 48 (g) and Table 12. During the optimization of N-GaN O-Ga,-Ga,-Ga,-H,-H (m = 2), one of the hydrogen atoms broke away from the water molecule allowing for the oxygen atom to bond with the nearest surface Ga atom. The free H atom shifted towards the nearest surface Ga atom with a dangling bond to form a Ga-H bond, Fig. 48 (g). All other structures resulted in unbounded water molecules with higher final energies, Fig. 48 (h)-(k) and Table 12.

Table 12. Total optimized energies in Hartrees for water oxidized N-centered GaN cluster, multiplicity (*m*), initial (d_i) and final (d_f) distances from the O atom to the nearest surface Ga atom, smallest initial (θ_i) and final (θ_f) O-Ga-N angles in the active region, and shortest Ga-N bond length ($d_{Ga\text{-}N}$) for the Ga atom that is taking part in the oxidation and the N atom that is part of the active region GaN.

Structures	*m*	Energy (Hartree)	Energy (eV)	d_i (Å)	θ_i (°)	d_f (Å)	θ_f (°)	$d_{Ga\text{-}N}$ (Å)
N-GaN Ga-OH	1	-1354.08265	0.00	1.76	105.4	1.77	103.8	1.96
	3	-1354.07889	0.10	1.76	105.4	1.76	104.0	1.96
N-GaN 2x Ga-OH	2	-1429.95972	0.00	1.76	105.4	1.77	104.9	1.95
	4	-1429.86057	2.70	1.76	105.4	1.88	85.9	1.94
N-GaN 3x Ga-OH	1	-1505.83584	0.00	1.76	105.4	1.77	109.3	1.99
	3	-1505.70033	3.69	1.76	105.4	1.76	100.0	1.93
N-GaN O-Ga,-Ga,-Ga,-H,-H	2	-1354.70974	0.00	2.00	43.8	1.76	105.4	1.96
	4	-1354.59057 [a]	3.24	2.00	43.8	2.94	79.3	2.02
N-GaN Ga-H-O-H-Ga	4	-1354.59380 [b]	3.15	2.21	54.8	4.04	82.7	2.01
N-GaN H_2O	4	-1354.58847 [c]	3.30	2.18	54.1	4.45	94.8	1.97
	4	-1354.59364 [d]	3.16	2.20	54. 6	3.98	82.5	2.01

Imaginary frequencies (cm^{-1}): 44*i* [a], 15*i* [b], 84*i* and 12*i* [c], 496*i*, 409*i* and 55*i* [d], all of them correspond to the movement of the water over the surface

Fig. 49 and Table 13 illustrate the interaction between the Hollow-centered GaN surface and H_2O or -OH molecules. The Hollow-centered GaN testbed is exposed to one, two or three –OH molecules and optimized using varying multiplicities, Fig. 49 (a)-(j). The optimization of the Hollow-GaN Ga-OH structure using a multiplicity of 2 resulted in the formation of a new Ga-OH bond while maintaining the original Ga-OH bond. This is the only time that the most stable structure for any system resulted in a –OH molecule bonded to two surface Ga atoms in this research. The formation of such a bond may indicate how an interfacial layer will form given the correct reaction kinetics during deposition or growth of an oxide. The final O-Ga-N energy and bond angle are 0.00 eV and 80.8º, Fig. 49 (a). The addition of two –OH molecules to the Hollow-centered GaN system resulted in slight shifts in the Ga-O-H bonds when optimized, using a multiplicity of 1 or 3, Fig. 49 (d)-(e). However, during the optimization of Hollow-GaN 2x Ga-OH (m = 3) one of the -OH molecules shifted towards another surface Ga atom forming a new Ga-O bond without breaking the original Ga-O bond which resulted in a higher final energy of 0.23 eV compared to that of Hollow-GaN 2x Ga-OH (m = 1) with all O-H bonds intact, 0.00 eV (Table 13). The optimization of Hollow-GaN 3x Ga-OH was completed using multiplicities of 2 and 4. Both systems resulted in similar structures, i.e. no bonds were broken or formed, with final energies of 0.00, 0.16 and 0.17 eV, respectively.

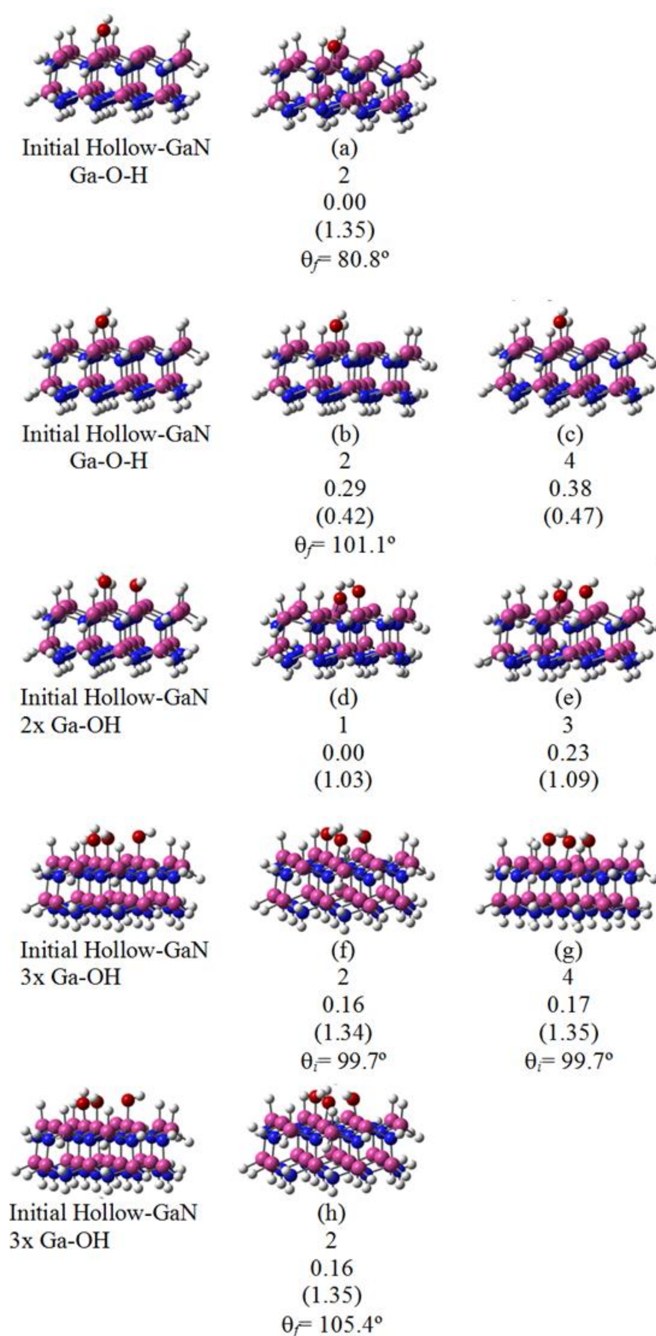

Fig. 49. Initial (top) and final (bottom) side views of the Hollow-centered GaN structures (with H atoms) with water or -OH being introduced to the system. (a-c) one –OH molecule within a Ga-O bond length to the cluster, (d-e) two –OH molecules within a Ga-O bond length to the cluster, (f-j) three –OH molecules each within a bond length to a surface Ga atom, (k-n) one water molecule in varying rotations and distances from a surface Ga atom. Below each diagram are the multiplicity, the optimized geometry relative energy, and the initial geometry relative energy inside parentheses, and the smallest angle O-Ga-N (where applicable). Energies are in eV. Ga is pink, N is blue, and O is red.

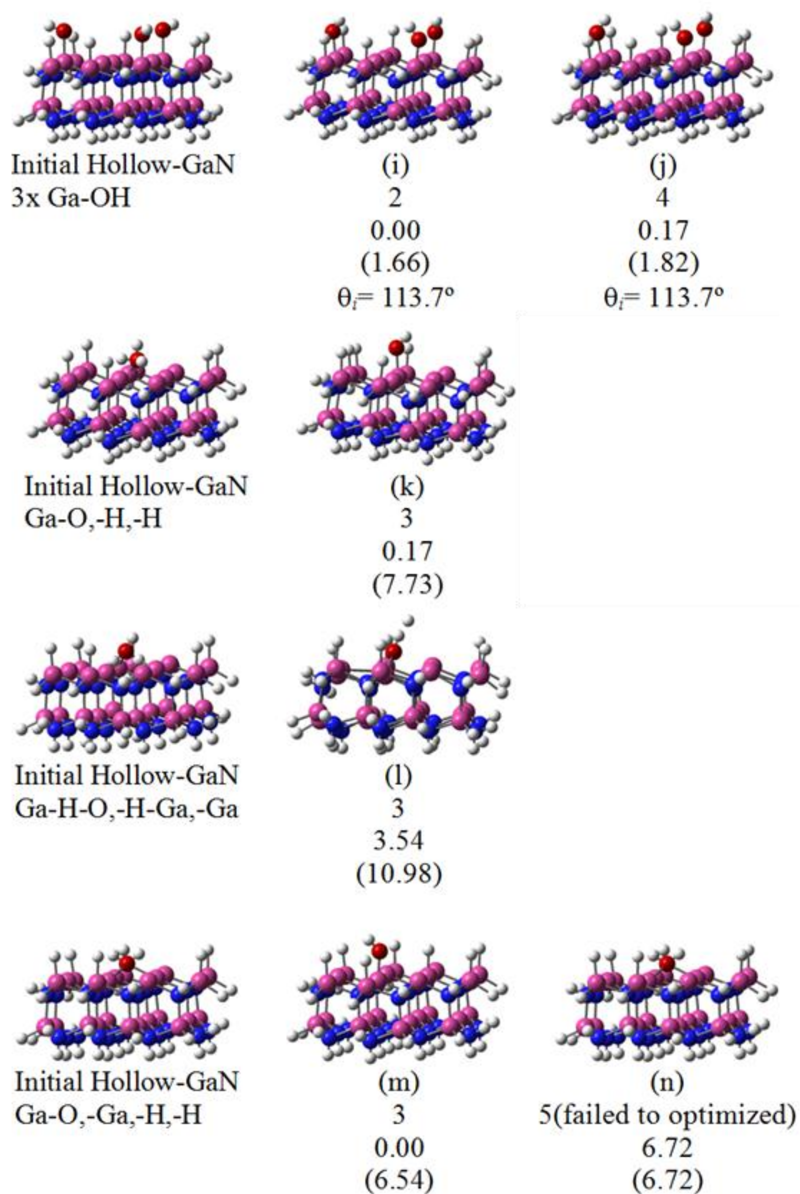

Fig. 49 Continued. Initial (top) and final (bottom) side views of the Hollow-centered GaN structures (with H atoms) with water or -OH being introduced to the system. (a-c) one –OH molecule within a Ga-O bond length to the cluster, (d-e) two –OH molecules within a Ga-O bond length to the cluster, (f-j) three –OH molecules each within a bond length to a surface Ga atom, (k-n) one water molecule in varying rotations and distances from a surface Ga atom. Below each diagram are the multiplicity, the optimized geometry relative energy, and the initial geometry relative energy inside parentheses, and the smallest angle O-Ga-N (where applicable). Energies are in eV. Ga is pink, N is blue, and O is red.

A single water molecule is introduced to the Hollow-GaN active region in several different orientations and distances from the surface and optimized using a multiplicity of 3 and 5, seen in Fig. 49 (k)-(n) and Table 13. Three of the four Hollow-GaN structures exposed to a single water molecule tested resulted in a Ga-O-H bond and the formation of a Ga-H bond, Fig. 49 (k) - Fig. 49 (m), with final energies of 0.17, 3.54 and 0.00 eV, respectively. The most stable Hollow-GaN structure exposed to water is Hollow-GaN Ga-O,-Ga,-H,-H (m = 3) with a final Ga-O bond angle and length of 105.6º and 1.77Å , Fig. 49 (m) and Table 13. During the optimization of Hollow-GaN Ga-O,-Ga,-H,-H (m = 3), one of the hydrogen atoms broke away from the water molecule allowing for the oxygen atom to bond with the nearest surface Ga atom. The free H atom shifted towards the nearest surface Ga atom with a dangling bond to form a Ga-H bond, Fig. 49 (m).

Table 13.Total optimized energies in Hartrees for water oxidized Hollow-centered GaN cluster, multiplicity (*m*), initial (d_i) and final (d_f) distances from the O atom to the nearest surface Ga atom, smallest initial (θ_i) and final (θ_f) O-Ga-N angles in the active region, and shortest Ga-N bond length ($d_{Ga\text{-}N}$) for the Ga atom that is taking part in the oxidation and the N atom that is part of the active region GaN.

Structures	*m*	Energy (Hartree)	Energy (eV)	d_i (Å)	θ_i (°)	d_f (Å)	θ_f (°)	$d_{Ga\text{-}N}$ (Å)
Hollow-GaN Ga-OH	2	-1466.11656	0.00	1.77	99.7	1.96	80.8	1.91
	2	-1466.10606	0.29	1.77	105.4	1.77	101.1	1.95
	4	-1466.10279	0.38	1.77	105.4	1.77	104.0	1.96
Hollow-GaN 2x Ga-OH	1	-1541.99330	0.00	1.91	110.6	1.77	91.2	1.90
	3	-1541.98470	0.23	1.91	110.6	1.77	83.3	1.91
Hollow-GaN 3x Ga-OH	2	-1617.85910	0.16	1.77	99.7	1.77	103.0	1.95
	2	-1617.85898	0.16	1.77	105.4	1.77	103.0	1.95
	2	-1617.86466	0.00	1.91	113.7	1.77	119.3	1.94
	4	-1617.85864	0.17	1.77	99.7	1.77	103.0	1.95
	4	-1617.85832	0.17	1.91	113.7	1.77	120.2	1.95
Hollow-GaN Ga-O,-H,-H	3	-1466.72637	0.17	2.00	77.0	1.78	106.9	1.95
Hollow-GaN Ga-H-O, -H-Ga,-Ga	3	-1466.60246[a]	3.54	2.00	77.5	1.88	86.9	1.90
Hollow-GaN Ga-O,-Ga, -H,-H	3	-1466.73253	0.00	2.00	81.6	1.77	105.6	1.96
	5	-1466.48548	6.72	2.00	81.6	2.00	81.6	1.99

Imaginary frequencies (cm^{-1}): 352i[a]

The most stable interaction between the GaN active region and one, two or three -OH molecules results in neither the formation nor degradation of the Ga-O bonds only slight shifting of the Ga-O-H bond lengths and angles, seen in (Fig. 47 (a), Fig. 47 (e), Fig. 47 (f), Fig. 48 (a), Fig. 48 (c), Fig. 48 (e), Fig. 49 (d) and Fig. 49 (i), depending on the location of the hydroxyl group and the local spin. Optimization of the same geometry with varying multiplicities emphasizes the effect of the local spin on the oxidation of GaN using water. For an example, when a water molecule is within 2.00 Å of a surface Ga atom and centered above a Ga atom one Ga-OH bonds will form, Fig. 47 (k)-(m), when the local spin is S = 1/2, 3/2, 5/2 (m = 2, 4, 6). However, when the same geometry is optimized using a local spin of S = 7/2 (m = 8), only no Ga-O bond forms, Fig. 47 (n). The effect of local spin is also shown in Fig. 47 - Fig. 49. One of the most stable interactions between the GaN active region and one –OH molecule resulted in the formation of the –OH molecule bonded to two surface Ga atoms Fig. 49 (a). The formation of such a bond may indicate how an interfacial layer will form given the correct reaction kinetics during deposition or growth of an oxide. The most stable interaction of a H_2O molecule and the active GaN region is the complete dissociation of one of the O-H bonds to form a Ga-O-H bond and a Ga-H bond for all tested scenarios, represented in Fig. 47 (k), Fig. 48 (g), and Fig. 49 (m).

6.4 Conclusions

In this chapter, the oxidation of the Ga-face GaN surface with varying oxidation methods and hydrolyzed surface structures are studied using the *ab initio* density functional theory (DFT). The interactions between the GaN active region and varying forms oxygen and water have been discussed. The most notable interactions are between the GaN active region and O_2 and H_2O. The most stable interaction of O_2 and the active GaN region results in the complete dissociation of the O_2 molecule. While the most stable interaction between a H_2O molecule and the active GaN region is the complete dissociation of one of the O-H bonds to form a Ga-O-H bond and a Ga-H bond

for all tested scenarios. The local spin plays an important role in the oxidation of GaN using either oxygen or water. These results are consistent with the suspected Hf-reactant + O-reactant mechanism used during atomic layer deposition of HfO_2 onto a substrate (*37*). Other notable interactions include the formation of a single oxygen atom bonded to three surface Ga atoms causing deformation of the cluster and a –OH molecule bonded to two surface Ga atoms. Both of these interactions indicate the possible mechanism behind the formation of an interfacial layer during the atomic layer deposition of HfO_2.

CHAPTER VII
AB INITIO ANALYSIS OF THE INTERACTIONS OF HYDROLYZED GaN CLUSTERS WITH ALD REACTANTS

With the knowledge of the formation of an interfacial layer during atomic layer deposition (ALD) of HfO_2 on GaN, a better understanding of the mechanisms behind the reaction of hydrolyzed GaN and the Hf-reactant is needed. However, to better understand why an interfacial layer forms during ALD of HfO_2 and not Al_2O_3 both reaction mechanisms are calculated. In this chapter we discuss the calculations of the interactions of Trimethylaluminium (TMA) and Tertrakis(EthylMethylAmino)Hafnium (TEMAH) with the hydrolyzed Ga-face of GaN clusters, which could be used as testbeds for the actual Ga-face on GaN crystals. However, an additional goal is the analysis of the nano-clusters for several other applications in nanotechnology. It is found that while further research is needed in this area to grasp a better understanding of the interactions of TMA or TEMAH with hydrolyzed GaN clusters, it was found that the formation of a Ga-N(CH_3)(CH_2CH_3) bond can form during the deposition of HfO_2 using ALD and TEMAH as the reactant without breaking the Hf-N bond. It is important to note that a Ga-CH3 bond did not form in any fully optimized stable structures when analyzing the interaction of TMA with hydrolyzed GaN.

7.1 Introduction

Enhancement-mode (E-mode) III-V based devices are currently needed for digital applications and low-loss high-power switching such as RF switches and transmitter/receiver switches for GPS receivers in mobile phones (*111*). To achieve E-mode III-V based devices the threshold voltage (V_{th}) of the device must be controlled, one current method is using high-k metal gate stacks (*27, 95, 96*). Through this research, the formation of an interfacial layer at the ALD HfO_2 – GaN interface has been

discovered (*30*), while no interfacial layer has been found for ALD of Al_2O_3 on GaN (*32, 41*). The formation of an interfacial layer at the semiconductor/dielectric interface can cause detrimental effects on the performance and the reproducibility of the device along with the threshold voltage of the device. A better understanding of the mechanism responsible for the formation of an interfacial layer during the atomic layer deposition of HfO_2 on GaN would give insight into determining the removal or non-formation of the interfacial layer.

Recently, GaN nanoclusters have been made by using the sequential ion implantation in a dielectric matrix (*112*). Another method to form GaN nanoclusters is to rinse the sample in a solution of a donor stabilized gallium-triazid (*113*). These may be considered nanoclusters of GaN adsorbed over the surface of a thin film. Materials made from or containing GaN have been extensively studied since the early 90's theoretically using *ab initio* electronic structure methods for GaN clusters (*114-123*). The theoretical studies of structural, dielectric, phonon dispersions and density of states for wurzite and/or zinc-blende GaN along with the stoichiometry and structure of the (0001) surface of GaN have been completed (*114, 116, 117*). The structural and electronic properties of GaN clusters have been previously modeled (*118-120, 123*).

It is necessary to understand the mechanisms for oxidation of GaN prior to understanding the mechanisms for atomic layer deposition of HfO_2 or Al_2O_3. Theoretical calculations of the adsorption of O_2 onto GaN (0001) have previously been reported using density functional theory (DFT) within the generalized gradient approximation (GGA) (*124*) and other basis sets (*125, 126*) using only 2 x 2 super cell geometries. Theoretical calculations of the adsorption of H_2O onto GaN (0001) surface have been studied using DFT-GGA with an initial GaN geometry of a 2 x 2 super cell (*127*). Theoretical calculations of the oxidation of GaN using DFT B3PW91/LANL2DZ level of theory have been reported in CHAPTER VI, page 84. To the author's knowledge no theoretical calculations have been published to date regarding the atomic layer deposition process of HfO_2 or Al_2O_3 on hydrolyzed GaN. In this chapter, the

interactions of HfO2 and Al2O3 ALD reactants with hydrolyzed Ga-face GaN are studied using the *ab initio* density functional theory (DFT) using varying GaN structures.

7.2 Methodology

The reaction mechanisms of two atomic layer deposition reactants with hydrolyzed GaN(0001) surface are studied using hexagonal wurzite crystal geometries that resemble bulk GaN, a = 3.189 Å and c = 5.186 Å (*54*). Hexagonal wurzite crystal geometries are considered the most thermodynamically stable structures for GaN. The surface Ga atoms are bonded to three N atoms and allowed to maintain one dangling bond. The GaN clusters are hydrolyzed using 1, 2 or 3 –OH molecules bonded to the GaN surface. Three main surface structures are used to model hydrolyzed bulk Ga-face GaN, Ga-centered, N-centered, and Hollow-centered surface structures. Two different atomic layer deposition (ALD) reactants are used: Trimethylaluminium (TMA) and Tertrakis(EthylMethylAmino)Hafnium (TEMAH). TMA is used as the reactant in ALD when Al_2O_3 is being deposited, while TEMAH is used when HfO_2 is being deposited.

Calculations for the Ga-centered, N-centered, and Hollow-centered surface structures with the presence of an ALD reactant are modeled at the B3PW91/LANL2DZ (*75, 81, 128-134*) level of theory with varying multiplicities. In some cases atoms of the reactants and of the –OH molecule were shifted to try to induce interactions. Once a stable interaction between the ALD reactant and the hydrolyzed GaN cluster occurred, further tests were completed to determine stability of the Ga-O-(Hf or AL). The B3PW91 functional is a hybrid functional that uses the Becke exchange (*81*) combined with a Hartree-Fock (*135-137*) component and the correlation functional of Perdew-Wang (*75, 128-130, 134*). We have thoroughly tested the B3PW91 functional (*121, 138-140*). The basis set and effective core potential is the LANL2DZ (*131-133*). Optimizations were carried with the Berny method (*141, 142*). All structures are checked to be local minima by calculating the Hessian matrix, i.e., the second derivative

of the energy with respect to all coordinates. All of the calculations are performed with the program GAUSSIAN-09 (*143*).

7.3 Results and Discussion

7.3.1 TMA

7.3.1.1 TMA interactions with Hydrolyzed GaN

Trimethylaluminium (TMA) is introduced to the hydrolyzed Ga-centered, N-centered and hollow-centered systems to represent the atomic layer deposition (ALD) process of Al_2O_3 on GaN. All systems are optimized using the B3PW91/LANL2DZ (*147*) level of theory with varying multiplicities, Fig. 50 - Fig. 52. The total energies are shown in Table 14 - Table 16 for the Ga-centered, N-centered, and hollow-centered structures, respectively. Generally, only geometries tested that resulted in stable molecules are shown.

A single TMA molecule is introduced to the singly hydrolyzed Ga-GaN cluster, Ga-GaN 1x –OH, in several orientations and distances from the surface and optimized using a multiplicity of 1 and 3, seen in Fig. 50 (a)-(f) and Table 14. The most common stable interaction resulted in the TMA bonding to the –OH molecule without breaking any bonds in the system, Fig. 50 (a)-(b) and (e)-(f). However, the most stable interaction resulted in the formation of a CH_4 molecule and an O-Al bond from a TMA molecule that had been modified by breaking the Al-CH_3 bond, Fig. 50 (c). The CH_3 molecule is placed approximately 2.63 Å away from the Al atom (typical Al-O bond length in TMA is 2.00 Å), while the H atom of the –OH molecule is 1.16 Å away from the O atom compared to the typical O-H bond of 0.98 Å. These shifts are necessary to form a Ga-O-Al bond and a CH_4 molecule which are believed to be the result of TMA reacting with an –OH molecule. Without shifting any atoms in the system, the most stable interaction between TMA and Ga-GaN 1x –OH resulted in a final relative energy (RE) of 0.78 eV, Fig. 50 (a).

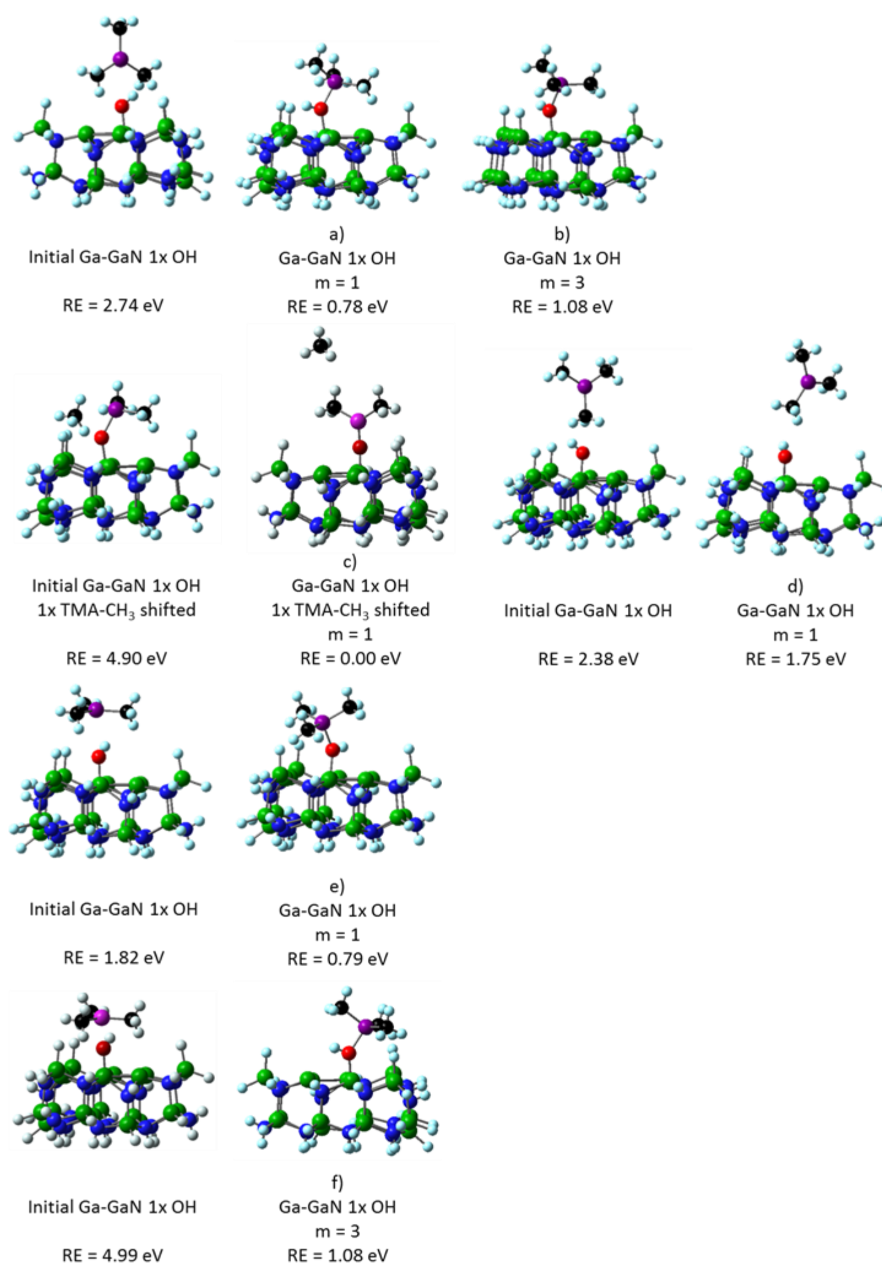

Fig. 50. Initial and final side views of the Ga-centered hydrolyzed (1, 2 or 3 –OH molecules bonded to the surface) GaN structures (with H atoms) with 1 or 2 TMA molecules being introduced to the system. Each figure is labeled with the name and the multiplicity of each molecule. (a)-(f) one –OH molecule bonded to the GaN surface with 1 TMA molecule introduced, (g)-(j) two –OH molecule bonded to the surface with 1 TMA molecule introduced, (k)-(n) three –OH molecule bonded to the surface with 1 TMA molecule introduced, (o)-(p) two –OH molecule bonded to the surface with 2 TMA molecules introduced, and (q)-(t) three –OH molecules bonded to the surface with 2 TMA molecules introduced. Ga is Green, N is blue, O is red, H is white, C is black, and Al is purple. RE is Relative Energy (eV) and m is the multiplicity. (F) Signifies that the geometry failed to optimize completely due to an error, (NS) signifies that the geometry has not finished optimizing, and (Osc) signifies the geometry failed to converge due to oscillations.

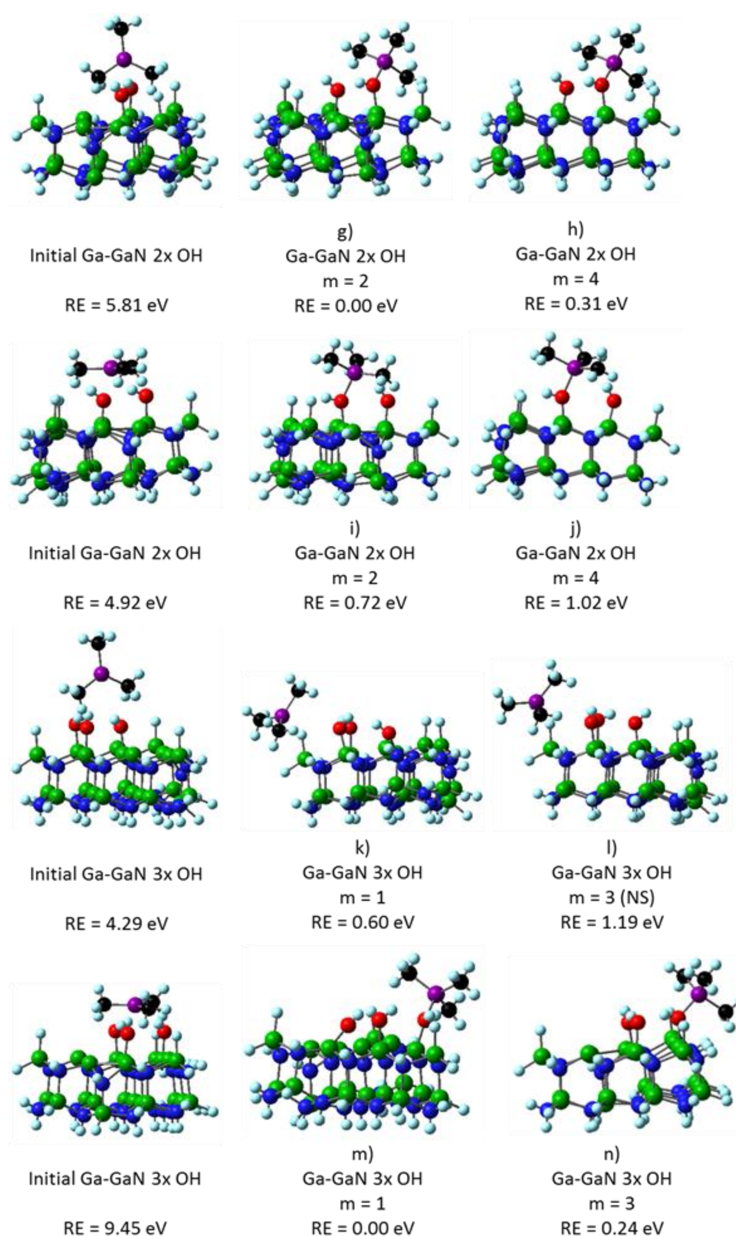

Fig. 50 Continued. Initial and final side views of the Ga-centered hydrolyzed (1, 2 or 3 –OH molecules bonded to the surface) GaN structures (with H atoms) with 1 or 2 TMA molecules being introduced to the system. Each figure is labeled with the name and the multiplicity of each molecule. (a)-(f) one –OH molecule bonded to the GaN surface with 1 TMA molecule introduced, (g)-(j) two –OH molecule bonded to the surface with 1 TMA molecule introduced, (k)-(n) three –OH molecule bonded to the surface with 1 TMA molecule introduced, (o)-(p) two –OH molecule bonded to the surface with 2 TMA molecules introduced, and (q)-(t) three –OH molecules bonded to the surface with 2 TMA molecules introduced. Ga is Green, N is blue, O is red, H is white, C is black, and Al is purple. RE is Relative Energy (eV) and m is the multiplicity. (F) Signifies that the geometry failed to optimize completely due to an error, (NS) signifies that the geometry has not finished optimizing, and (Osc) signifies the geometry failed to converge due to oscillations.

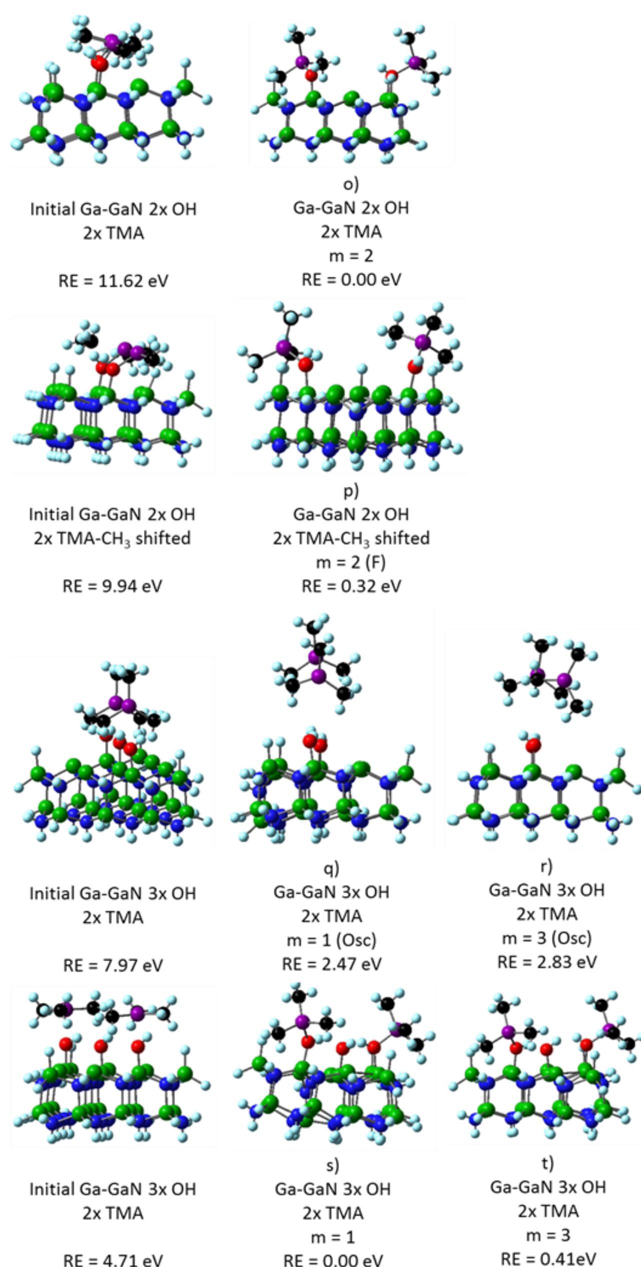

Fig. 50 Continued. Initial and final side views of the Ga-centered hydrolyzed (1, 2 or 3 –OH molecules bonded to the surface) GaN structures (with H atoms) with 1 or 2 TMA molecules being introduced to the system. Each figure is labeled with the name and the multiplicity of each molecule. (a)-(f) one –OH molecule bonded to the GaN surface with 1 TMA molecule introduced, (g)-(j) two –OH molecule bonded to the surface with 1 TMA molecule introduced, (k)-(n) three –OH molecule bonded to the surface with 1 TMA molecule introduced, (o)-(p) two –OH molecule bonded to the surface with 2 TMA molecules introduced, and (q)-(t) three –OH molecules bonded to the surface with 2 TMA molecules introduced. Ga is Green, N is blue, O is red, H is white, C is black, and Al is purple. RE is Relative Energy (eV) and m is the multiplicity. (F) Signifies that the geometry failed to optimize completely due to an error, (NS) signifies that the geometry has not finished optimizing, and (Osc) signifies the geometry failed to converge due to oscillations.

Table 14. Total optimized energies in Hartrees for hydrolyzed Ga-centered GaN cluster interacting with 1, 2 or 3 TMA molecules, the number of –OH molecules bonded to the GaN cluster, the number of TMA molecules, the multiplicity (*m*) used, the initial (d_i) and final distances (d_f) from the O atom to the nearest Al atom, the formation of a CH_4 molecule is determined and the shortest Ga-N bond length for the Ga atom that is taking part in the reaction and the N atom that is part of the active region GaN. (F) Signifies that the geometry failed to optimize completely due to an error, (NS) signifies that the geometry has not finished optimizing, and (Osc) signifies the geometry failed to converge due to oscillations. RE stands for relative energy.

Structure Label from **Error! Reference source not found.**	TMA	-OH	*m*	Energy (Hartree)	RE (eV)	d_i (Å)	d_f (Å)	CH_4 Formation?	Ga-N Bond Length (Å)
A	1	1	1	-1471.13034	0.78	3.00	1.99	-	1.93
B			3	-1471.11951	1.08	3.00	2.01	-	1.93
C			1	-1471.15905	0.00	3.00	1.72	Yes	1.95
D			1	-1471.09484	1.75	2.50	5.57	-	1.94
E			1	-1471.13018	0.79	3.00	1.98	-	1.92
F			3	-1471.11952	1.08	2.00	2.01	-	1.93
G	1	2	2	-1547.02606	0.00	2.50	1.94	-	1.94
H			4	-1547.01456	0.31	2.50	1.94	-	1.94
I			2	-1546.99949	0.72	2.00	2.01	-	1.92
J			4	-1546.98843	1.02	2.00	2.01	-	1.93
K	1	3	1	-1622.88044	0.60	3.60	4.05	-	1.96
L			3	-1622.85887[a]	1.19	3.60	4.13	-	1.95
M			1	-1622.90255	0.00	2.50	1.99	-	1.94
N			3	-1622.89368	0.24	2.50	1.95	-	1.94
O	2	2	2	-1668.74865	0.00	1.50	1.99	-	1.93
P			2	-1668.73673[b]	0.33	1.98	1.99	-	1.93
Q	2	3	1	-1744.55794[c]	2.47	2.70	4.41	-	1.95
R			3	-1744.54447[c]	2.83	2.70	4.64	-	1.96
S			1	-1744.64855	0.00	2.20	1.96	-	1.93
T			3	-1744.63338	0.41	2.20	1.94	-	1.93

[a] NS, [b] F, and [c] Osc

A single TMA molecule is introduced to the double and triple hydrolyzed Ga-GaN cluster, Ga-GaN 2x –OH and Ga-GaN 3x –OH, in several orientations and distances from the surface and optimized using a multiplicity of 2 and 4 for Ga-GaN 2x –OH and 1 and 3 for Ga-GaN 3x –OH, seen in Fig. 50 (g)-(n) and Table 14. The most stable interaction of TMA with either Ga-GaN 2x –OH or Ga-GaN 3x –OH resulted in the TMA bonding to one of the –OH molecules without breaking any bonds in the system, Fig. 50 (g) and Fig. 50 (m). However, other optimized geometries also resulted in similar structures with slightly higher energies, Table 14. The formation of a CH_4

molecule did not occur for any geometry tested, including non-stable geometries. None of the atoms were shifted to induce a reaction in the Ga-GaN 2x –OH or Ga-GaN 3x –OH geometries, Fig. 50 (g)-(n).

Two TMA molecules were introduced to the double and triple hydrolyzed Ga-GaN cluster, Ga-GaN 2x –OH, 2x TMA and Ga-GaN 3x –OH, 2x TMA in several orientations and distances from the surface and optimized using a multiplicity of 2 for Ga-GaN 2x –OH, 2x TMA and 1 and 3 for Ga-GaN 3x –OH, 2x TMA, seen in Fig. 50 (o)-(t) and Table 14. The most stable interaction of TMA with either Ga-GaN 2x –OH, 2x TMA or Ga-GaN 3x –OH, 2x TMA resulted in each of the TMA molecules bonding to one of the –OH molecules without breaking any bonds in the system, Fig. 50 (o) and Fig. 50 (s). However, other optimized geometries also resulted in similar structures with slightly higher energies, Table 14. The formation of a CH_4 molecule did not occur for any geometry tested, including non-stable geometries. Atoms were shifted to induce a reaction in the Ga-GaN 2x –OH, 2x TMA however shifting the atoms did not result in the formation of a CH_4 molecule, in fact the geometry failed to converge, Fig. 50 (p).

A single TMA molecule is introduced to a single and hydrolyzed N-GaN cluster, N-GaN 1x –OH and N-GaN 3x –OH, in several orientations and distances from the surface and optimized using a multiplicity of 1, seen in Fig. 51 (a)-(b) and Table 15. The only stable interactions of TMA with N-GaN 1x –OH and N-GaN 3x –OH are shown in Fig. 51 (a)-(b). Other geometries were tested and failed to stabilize. The only geometry that resulted in an interaction between TMA and hydrolyzed GaN is N-GaN 3x –OH. The interaction resulted in TMA bonding to one of the –OH molecules without breaking any bonds in the system, Fig. 51 (b). The formation of a CH_4 molecule did not occur for any geometry tested, including non-stable geometries.

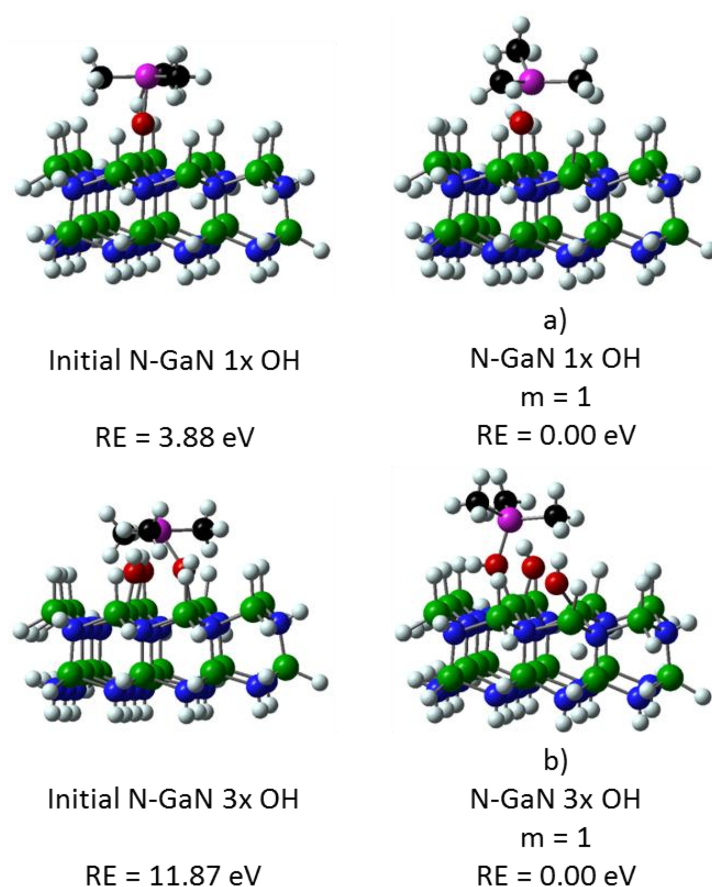

Fig. 51. Initial and final side views of the N-centered hydrolyzed (1, 2 or 3 –OH molecules bonded to the surface) GaN structures (with H atoms) with 1 or 2 TMA molecules being introduced to the system. Each figure is labeled with the name and the multiplicity of each molecule. (a) one –OH molecule bonded to the GaN surface with 1 TMA molecule introduced and (b) three –OH molecule bonded to the surface with 1 TMA molecule introduced. Ga is Green, N is blue, O is red, H is white, C is black, and Al is purple. RE is Relative Energy (eV) and m is the multiplicity.

Table 15. Total optimized energies in Hartrees for hydrolyzed N-centered GaN cluster interacting with 1 or 3 TMA molecules, the number of –OH molecules bonded to the GaN cluster, the number of TMA molecules, the multiplicity (*m*) used, the initial (d_i) and final distances (d_f) from the O atom to the nearest Al atom, the formation of a CH_4 molecule is determined and the shortest Ga-N bond length for the Ga atom that is taking part in the reaction and the N atom that is part of the active region GaN. RE stands for relative energy.

Structure Label from Fig. 51	TMA	-OH	*m*	Energy (Hartree)	RE (eV)	d_i (Å)	d_f (Å)	CH_4 Formation?	Ga-N Bond Length (Å)
A	1	1	1	-1475.81611	0.00	2.00	2.03	-	1.93
B	1	3	1	-1627.57598	0.00	2.00	1.98	-	1.98

A single TMA molecule is introduced to the singly hydrolyzed Hollow-GaN cluster, Hollow-GaN 1x –OH, in several orientations and distances from the surface and optimized using a multiplicity of 2, seen in Fig. 52 (a)-(c) and Table 16. The most stable interaction resulted in the formation of an O-Al bond and a CH_4 molecule from a TMA molecule that had been modified by breaking the Al-CH_3 bond, Fig. 52 (c). It is important to note the formation of a Ga-OH-Al bond accompanied by the formation of a Ga-CH_3 bond in Fig. 52 (b). While the overall lowest energy was not able to be obtained due to a potential sharp local minimum which causes the system to oscillate in energy, the lowest energy is near the energy reported.

Two TMA molecules were introduced to the double hydrolyzed Hollow-GaN cluster, Hollow-GaN 2x –OH, 2x TMA, and optimized using a multiplicity of 1, seen in Fig. 52 (d) and Table 16. The TMA is modified by shifting a CH_3 molecule away from the Al atom. The only stable interaction of TMA with Hollow-GaN 2x –OH, 2x TMA resulted in the formation of two O-Al bonds, two Ga-O-Ga and two CH_4 molecules. This is the first time the formation of an O bonded to two surface Ga atoms and an Al atom as taken place within this study. However, due to the lack of other stable Hollow-GaN 2x –OH, 2x TMA systems it is difficult to draw any definitive conclusions about this structure, further research is necessary.

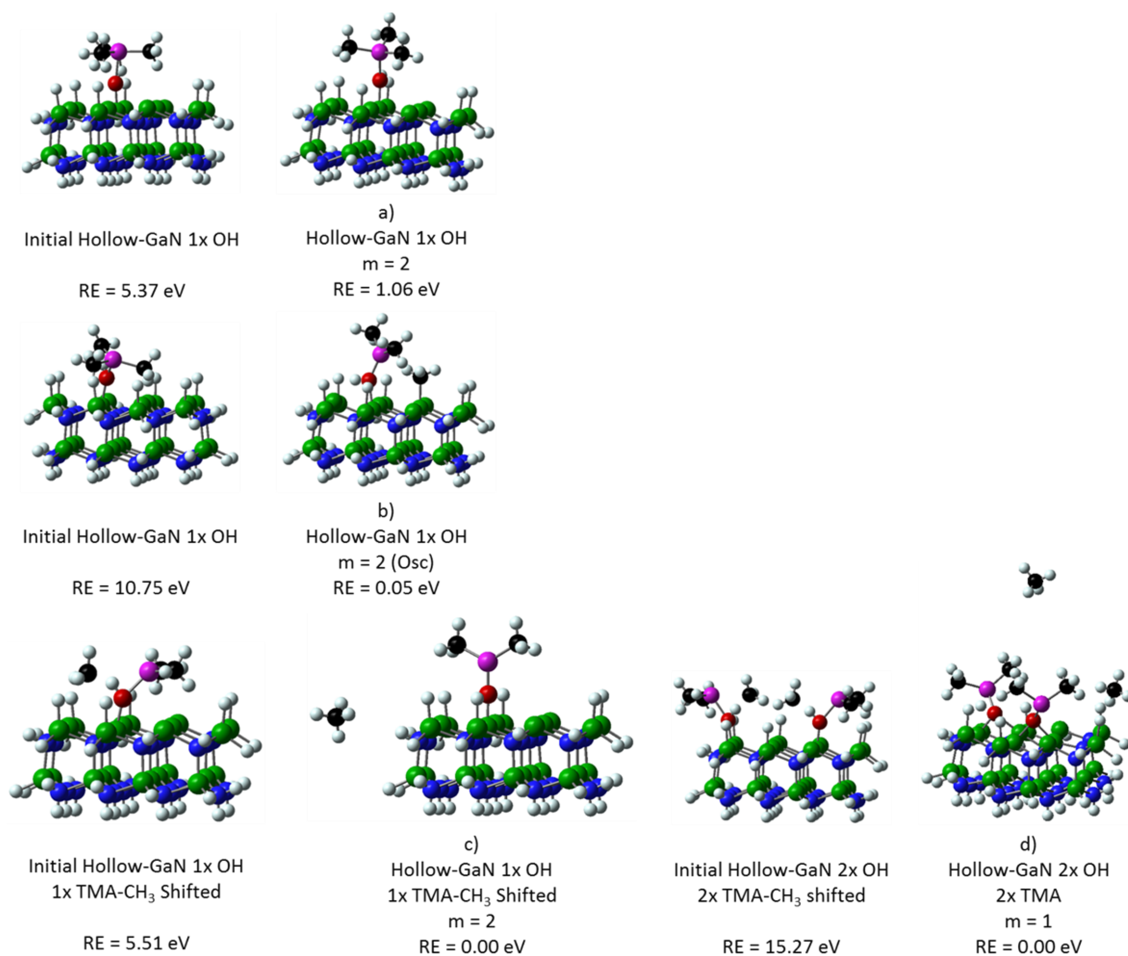

Fig. 52. Initial and final side views of the Hollow-centered hydrolyzed (1, 2 or 3 –OH molecules bonded to the surface) GaN structures (with H atoms) with 1 or 2 TMA molecules being introduced to the system. Each figure is labeled with the name and the multiplicity of each molecule. (a)-(c) one –OH molecule bonded to the GaN surface with 1 TMA molecule introduced and (d) two –OH molecule bonded to the surface with 2 TMA molecules introduced. Ga is Green, N is blue, O is red, H is white, C is black, and Al is purple. RE is Relative Energy (eV) and m is the multiplicity. (Osc) signifies failure to converge due to oscillations.

Table 16. Total optimized energies in Hartrees for hydrolyzed Hollow-centered GaN cluster interacting with 1, 2 or 3 TMA molecules, the number of –OH molecules bonded to the GaN cluster, the number of TMA molecules, the multiplicity (*m*) used, the initial (d_i) and final distances (d_f) from the O atom to the nearest Al atom, the formation of a CH_4 molecule is determined and the shortest Ga-N bond length for the Ga atom that is taking part in the reaction and the N atom that is part of the active region GaN. (F) Signifies that the geometry failed to optimize completely due to an error, (NS) signifies that the geometry has not finished optimizing, and (Osc) signifies the geometry failed to converge due to oscillations. RE stands for relative energy.

Structure Label from Fig. 52	TMA	-OH	*m*	Energy (Hartree)	RE (eV)	d_i (Å)	d_f (Å)	CH_4 Formation?	Ga-N Bond Length (Å)
A	1	1	2	-1587.84313	1.06	2.00	2.02	-	1.94
B			2	-1587.88016[a]	0.05	1.45	1.90	-	1.76
C			2	-1587.88218	0.00	1.98	1.73	Yes	1.96
D	2	2	1	-1785.58088	0.00	1.98	1.82	Yes	1.89

[a] Osc

The most common stable interactions between the hydrolyzed GaN region and one or two TMA molecules generally results in the formation of a Ga-OH-Al bond with only slight shifting of the bond lengths and angles, seen in Fig. 50 (a)-(b), (e)-(j), (m)-(p) and (s)-(t), Fig. 51 (b), and Fig. 52 (a)-(b). In the ALD of Al_2O_3 it is believed that O reacts with the Al to form a bond followed by the formation of CH_4. However in this study it appears that the H prefers to remain bonded to the O rather than the CH_3. This could be due to the fact that under deposition conditions the reactants and substrate are heated to 250 °C thus increasing the kinetic energy of the molecules which may allow for the formation of CH_4, as seen in some of the modified TMA systems, Fig. 50 (c) and Fig. 52 (c)-(d). The modification of TMA results in some of the most stable interactions for hydrolyzed Ga-GaN and Hollow-GaN which form a Ga-O-Al bond and at least one CH_4 molecule, Fig. 50 (c) and Fig. 52 (c). The Al-O bond lengths are in agreement with previously published data (*148, 149*). It is important to mention the formation of a Ga-O-Ga bond where the O atom is bonded to Al. This geometry only occurs once throughout this research and is the only stable structure for the given system; therefore no definitive conclusions can be drawn.

7.3.1.2 Stability of the O-Al bond that forms from the interaction of TMA with Hydrolyzed GaN

The most stable Trimethylaluminium (TMA) interaction with a single hydrolyzed GaN is used as the initial geometry to determine the stability of the O-Al bond with hydrolyzed GaN. Other geometries are also used to determine the stability of the O-Al bond with other –OH molecules or Ga-O bonds on GaN next to or near the O-Al bond, Fig. 53 - Fig. 55. All systems are optimized using the B3PW91/LANL2DZ (*147*) level of theory with varying multiplicities. The total energies are shown in Table 17 - Table 19 for the Ga-centered, N-centered, and hollow-centered structures, respectively. Generally, only geometries tested that resulted in stable molecules are shown.

The stability of a single Ga-O-Al$(CH_3)_2$ geometry is tested using varying geometries bonded to the Ga-GaN cluster, Step 2 Ga-GaN 1x O, Fig. 53 (a)-(b). The optimization of these geometries resulted in neither the formation nor degradation of any bonds. The stability of the Ga-O-Al$(CH_3)_2$ geometry near an –OH molecule is tested using two geometries, Step 2 Ga-GaN 1x OH, 1x O, Fig. 53 (c)-(d). The most stable optimization results in the formation of a Ga-O-Al$(CH_3)_2$-O-Ga bond, Fig. 53 (c) and Table 17. Finally the stability of two Ga-O-Al$(CH_3)_2$ geometries on a single GaN cluster is tested using three separate geometries, Step 2 Ga-GaN 2x O, 2x TMA, Fig. 53 (e)-(g). The overall most stable optimization from Step 2 Ga-GaN 2x O, 2x TMA is non-fully optimized structure that forms a Ga-O-Al$(CH_3)_2$-O-Ga bond and a Ga-O-AlCH_3-Ga bond with a Ga-CH_3 bond at the cluster edge. Due to the nature of this optimization, no conclusions can be drawn from this structure; however conclusions can be drawn from the structure with the second lowest energy, Fig. 53 (e) and Table 17. Fig. 53 (e) fully optimizes to form a O-Al$(CH_3)_2$-O-Al$(CH_3)_2$ bond where the oxygen atoms are bonded to surface Ga atoms with a final relative energy of 1.23 eV. If there is an –OH molecule bonded to a surface Ga atom next to the Ga-O-Al$(CH_3)_2$ then the Al$(CH_3)_2$ will shift and bond with both O atoms. However, if the –OH molecule is not close enough the Ga-O-Al$(CH_3)_2$ will remain unchanged.

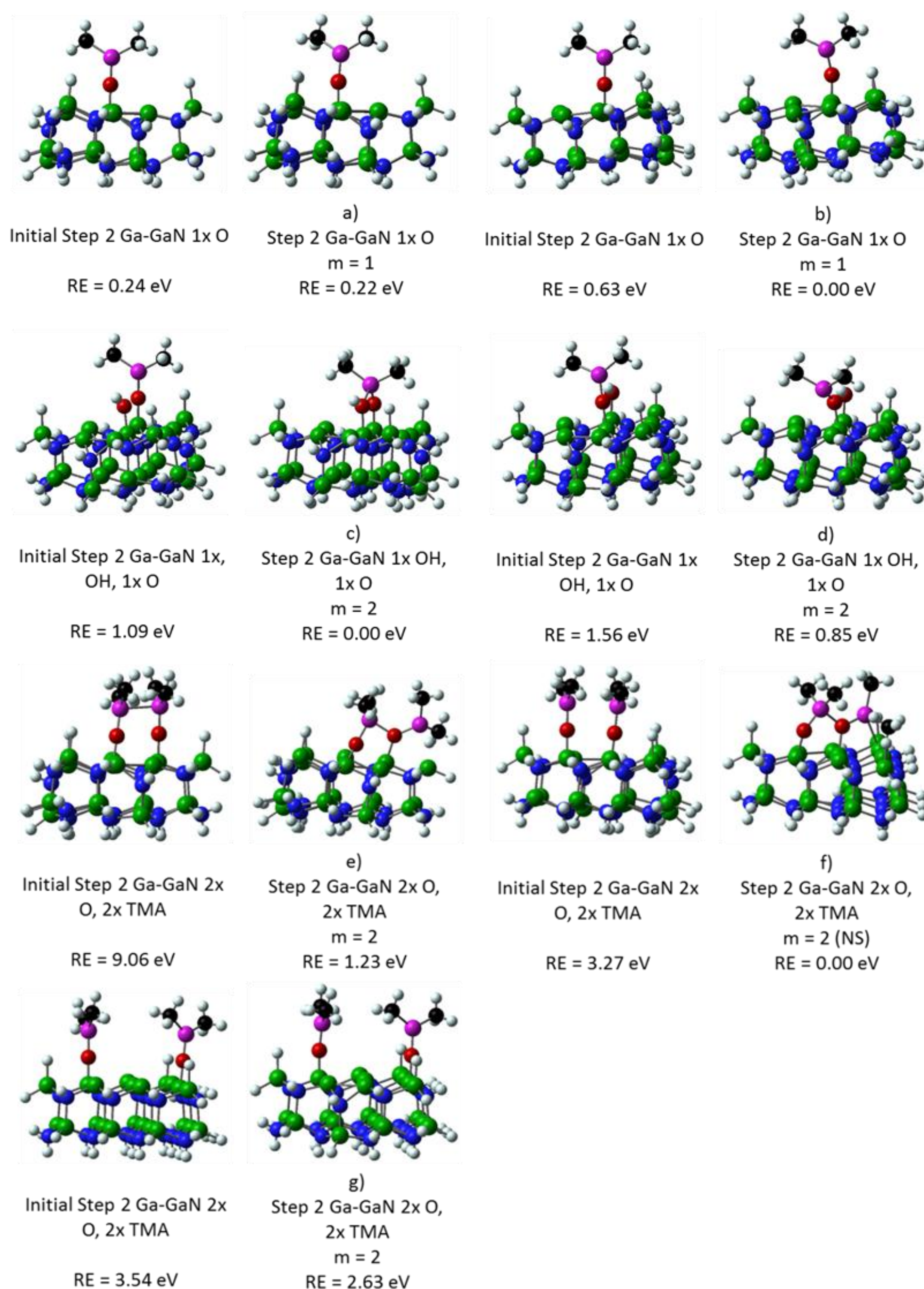

Fig. 53. Initial and final side views of Step 2, the stability of reacted TMA on hydrolyzed GaN. Ga-centered TMA reacted GaN structures (with H atoms) with 1 or 2 Ga-O bonds and 1 or 2 O-Al bonds. Each figure is labeled with the name and the multiplicity of each molecule. (a)-(b) one Al-O-Ga bond optimized, (c)-(d) one Al-O-Ga bond and one –OH molecule bonded to the GaN surface optimized and (e)-(g) two Al-O-Ga bonds optimized. Ga is Green, N is blue, O is red, H is white, C is black, and Al is purple. RE is Relative Energy (eV) and m is the multiplicity. (NS) signifies the molecule is not stable due to a failure in convergence.

Table 17. Total optimized energies in Hartrees for Step 2, the stability of reacted TMA on hydrolyzed Ga-centered GaN cluster, the number of –OH molecules bonded to the GaN cluster, the number of TMA molecules, the number of O atoms bonded to the GaN cluster, the multiplicity (*m*) used, the initial (d_i) and final distances (d_f) from the O atom to the nearest Al atom, the formation of any new or broken bonds is determined and the shortest Ga-N bond length for the Ga atom that is taking part in the reaction and the N atom that is part of the active region GaN. (F) Signifies that the geometry failed to optimize completely due to an error, (NS) signifies that the geometry has not finished optimizing. RE stands for relative energy.

System Label from Fig. 53	TMA	-OH	O	*m*	Energy (Hartree)	RE (eV)	d_i (Å)	d_f (Å)	New/Broken Bonds?	Ga-N Bond Length (Å)
A	1	-	1	1	-1430.65807	0.22	1.72	1.72	-	1.95
B				1	-1430.66615	0.00	1.72	1.73	-	1.95
C	1	1	1	2	-1506.56724	0.00	1.72	1.78	Yes	1.93
D				2	-1506.53610	0.85	1.72	1.79	-	1.93
E	2	-	2	2	-1587.85396	1.23	1.72	1.81	Yes	1.93
F				2	-1587.89912[a]	0.00	1.72	1.78	Yes	1.94
G				2	-1587.80229	2.63	1.72	1.72	-	1.94

[a] NS

The stability of a single Ga-O-Al(CH_3)$_2$ geometry is tested using varying geometries bonded to the N-GaN cluster, Step 2 N-GaN 1x O, Fig. 54 (a). The optimization of this geometry resulted in the formation of a Ga-O bond resulting in an overall geometry of O-Al(CH_3)$_2$ where the O atom is bonded to two surface Ga atoms. The stability of the Ga-O-Al(CH_3)$_2$ geometry near an –OH molecule is tested using two geometries, Step 2 N-GaN 1x OH, 1x O, Fig. 54 (b). The optimization results in neither the formation nor degradation of any bonds. Finally the stability of two Ga-O-Al(CH_3)$_2$ geometries on a single GaN cluster is tested using three separate geometries, Step 2 N-GaN 2x O, 2x TMA, Fig. 54 (c)-(d). The optimization results in neither the formation nor degradation of any bonds only slight shifts in bond lengths and angles, Table 18.

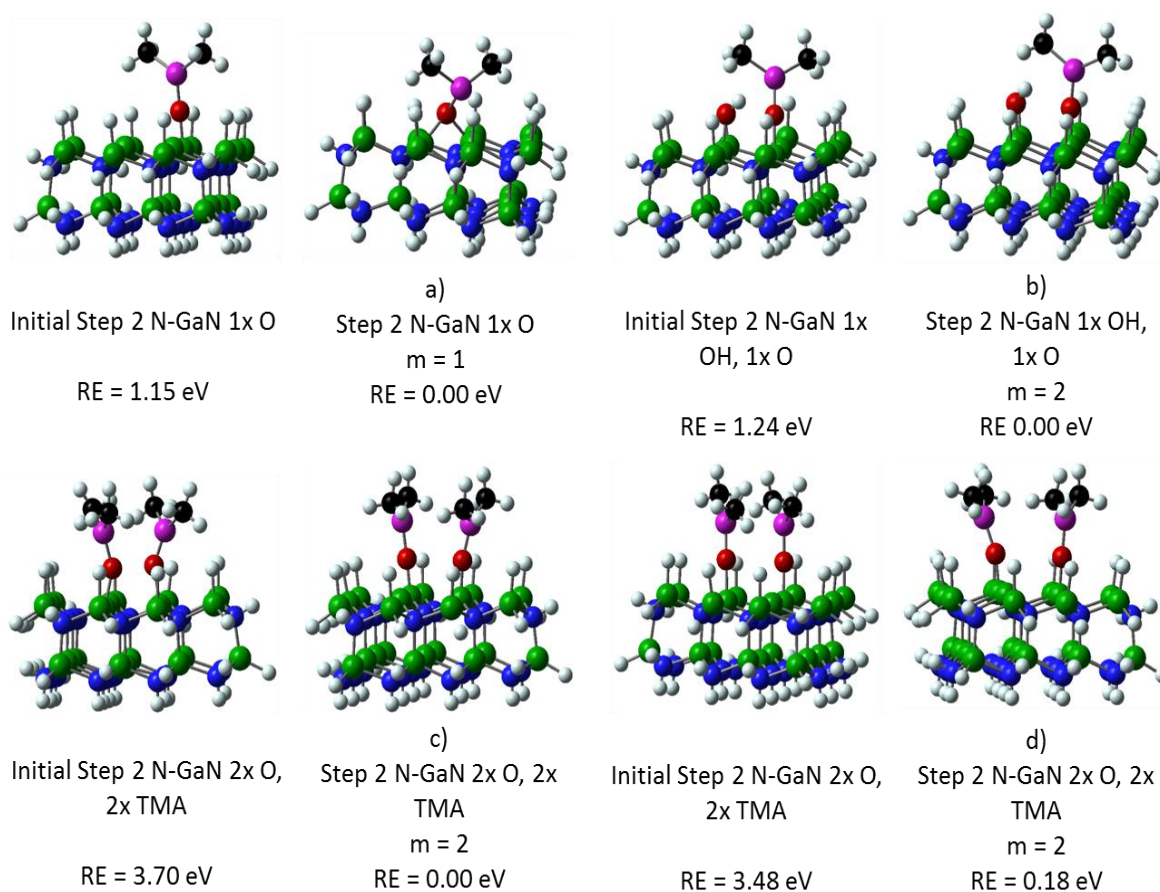

Fig. 54. Initial and final side views of Step 2, the stability of reacted TMA on hydrolyzed N-GaN. N-centered TMA reacted GaN structures (with H atoms) with 1 or 2 Ga-O bonds and 1 or 2 O-Al bonds. Each figure is labeled with the name and the multiplicity of each molecule. (a) one Al-O-Ga bond optimized, (b) one Al-O-Ga bond and one –OH molecule bonded to the GaN surface optimized and (c)-(d) two Al-O-Ga bonds optimized. Ga is Green, N is blue, O is red, H is white, C is black, and Al is purple. RE is Relative Energy (eV) and m is the multiplicity.

Table 18. Total optimized energies in Hartrees for Step 2, the stability of reacted TMA on hydrolyzed N-centered GaN cluster, the number of –OH molecules bonded to the GaN cluster, the number of TMA molecules, the number of O atoms bonded to the GaN cluster, the multiplicity (*m*) used, the initial (d_i) and final distances (d_f) from the O atom to the nearest Al atom, the formation of an any new or broken bonds is determined and the shortest Ga-N bond length for the Ga atom that is taking part in the reaction and the N atom that is part of the active region GaN. RE stands for relative energy.

System Label from Fig. 54	TMA	-OH	O	*m*	Energy (Hartree)	RE (eV)	d_i (Å)	d_f (Å)	New/Broken Bonds?	Ga-N Bond Length (Å)
A	1	-	1	1	-1435.38572	0.00	1.72	1.93	Yes	1.95
B	1	1	1	2	-1511.22984	0.00	1.72	1.73	-	1.97
C	2	-	2	2	-1592.50047	0.00	1.72	1.72	-	1.99
D				2	-1592.49980	0.02	1.72	1.72	-	1.99

The stability of a single Ga-O-Al$(CH_3)_2$ geometry is tested using varying geometries bonded to the Hollow-GaN cluster, Step 2 Hollow-GaN 1x O, Fig. 55 (a). The optimization results in neither the formation nor degradation of any bonds. The stability of the Ga-O-Al$(CH_3)_2$ geometry near an –OH molecule is tested using two geometries, Step 2 Hollow-GaN 1x OH, 1x O, Fig. 55 (b). The optimization of this geometry resulted in the formation of a Ga-O bond resulting in an overall geometry of Ga-O-Ga and a floating H atom while the Ga-O-Al$(CH_3)_2$ geometry shifted in angle and in bond lengths. The stability of two Ga-O-Al$(CH_3)_2$ geometries on a single GaN cluster is tested using one geometry, Step 2 Hollow-GaN 2x O, 2x TMA, Fig. 55 (c). The optimization results in the formation of a Ga-O-Ga bond where the O is bonded to Al$(CH_3)_2$. The other Ga-O-Al$(CH_3)_2$ geometry shifted in angle and in bond lengths. Finally the stability of three Ga-O-Al$(CH_3)_2$ geometries on a single GaN cluster is tested using one geometry, Step 2 Hollow-GaN 3x O, 3x TMA, Fig. 55 (d). The optimization resulted in neither the formation nor degradation of any bonds only slight shifts in bond lengths and angles, Table 19.

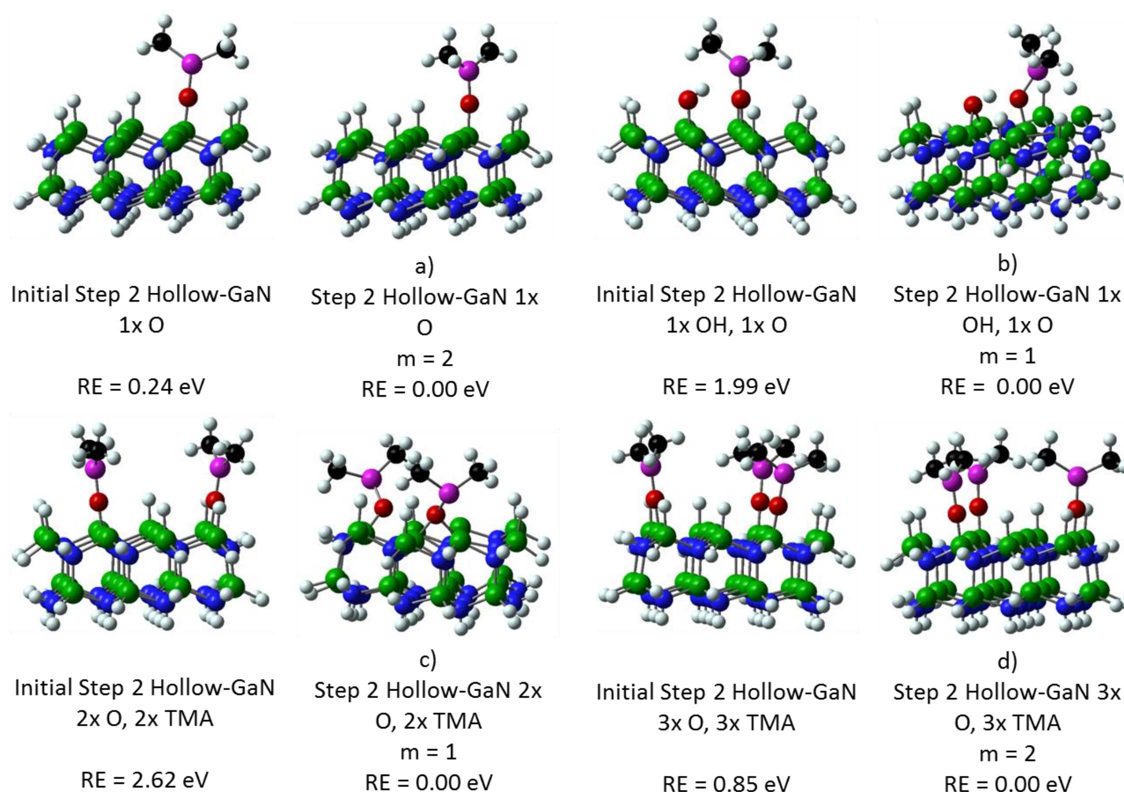

Fig. 55. Initial and final side views of Step 2, the stability of reacted TMA on hydrolyzed Hollow-GaN. Hollow-centered TMA reacted GaN structures (with H atoms) with 1, 2, or 3 Ga-O bonds and 1, 2 or 3 O-Al bonds. Each figure is labeled with the name and the multiplicity of each molecule. (a) one Al-O-Ga bond optimized, (b) one Al-O-Ga bond and one –OH molecule bonded to the GaN surface optimized, (c) two Al-O-Ga bonds optimized, and (d) three Al-O-Ga bonds optimized. Ga is Green, N is blue, O is red, H is white, C is black, and Al is purple. RE is Relative Energy (eV) and m is the multiplicity.

Table 19. Total optimized energies in Hartrees for Step 2, the stability of reacted TMA on hydrolyzed Hollow-centered GaN cluster, the number of –OH molecules bonded to the GaN cluster, the number of TMA molecules, the number of O atoms bonded to the GaN cluster, the multiplicity (*m*) used, the initial (d_i) and final distances (d_f) from the O atom to the nearest Al atom, the formation of new or broken bonds is determined and the shortest Ga-N bond length for the Ga atom that is taking part in the reaction and the N atom that is part of the active region GaN. RE stands for relative energy.

System Label from Fig. 55	TMA	-OH	O	*m*	Energy (Hartree)	RE (eV)	d_i (Å)	d_f (Å)	New/Broken Bonds?	Ga-N Bond Length (Å)
A	1	-	1	1	-1547.38087	0.00	1.72	1.72	-	1.95
B	1	1	1	2	-1623.25510	0.00	1.72	1.80	-	1.91
C	2	-	2	1	-1704.57937	0.00	1.72	1.82	Yes	1.89
D	3	-	3	2	-1861.68456	0.00	1.72	1.72	-	1.94

Out of the geometries that resulted in stable systems typically the Ga-O-Al$(CH_3)_2$ structure is preserved during optimization if no other structures surround it, Fig. 53 (a)-(b), (d), and (g) and Fig. 55 (a) and (d). However, in some cases the O atom or the Al$(CH_3)_2$ molecule shifts to form new bonds, Fig. 53 (c) and (e)-(f), Fig. 54 (a) and Fig. 55 (b)-(c). For an example the Ga-O-Al$(CH_3)_2$ on the N-centered GaN geometry the O atom shifts to form a Ga-O-Ga bond without breaking any other bonds, Fig. 54 (a). It is important to note that due to the lack of multiple stable structures it is impossible to know if the structures shown here are the lowest energies achievable. However, some conclusions can be made. First, it is possible to form O-Al(CH3)2-O and Ga-O-Ga geometries during ALD of Al_2O_3 on GaN clusters. Second, the Ga-O-Al$(CH_3)_2$ geometry may interact with unreacted Ga-OH and other Ga-O-Al$(CH_3)_2$ geometries. Research is currently continuing in this area.

7.3.2 TEMAH

7.3.2.1 TEMAH interactions with Hydrolyzed GaN

Tertrakis(EthylMethylAmino)Hafnium (TEMAH) is introduced to the hydrolyzed Ga-centered and hollow-centered systems to represent the atomic layer deposition (ALD) process of HfO_2 on GaN. All systems are optimized using the B3PW91/LANL2DZ (*147*) level of theory with varying multiplicities, Fig. 56 - Fig. 57. The total energies are shown in Table 20 - Table 21 for the Ga-centered and hollow-centered structures, respectively. The N-centered system is tested; however, no stable geometries have resulted from the system. Generally, only geometries tested that resulted in stable molecules are shown.

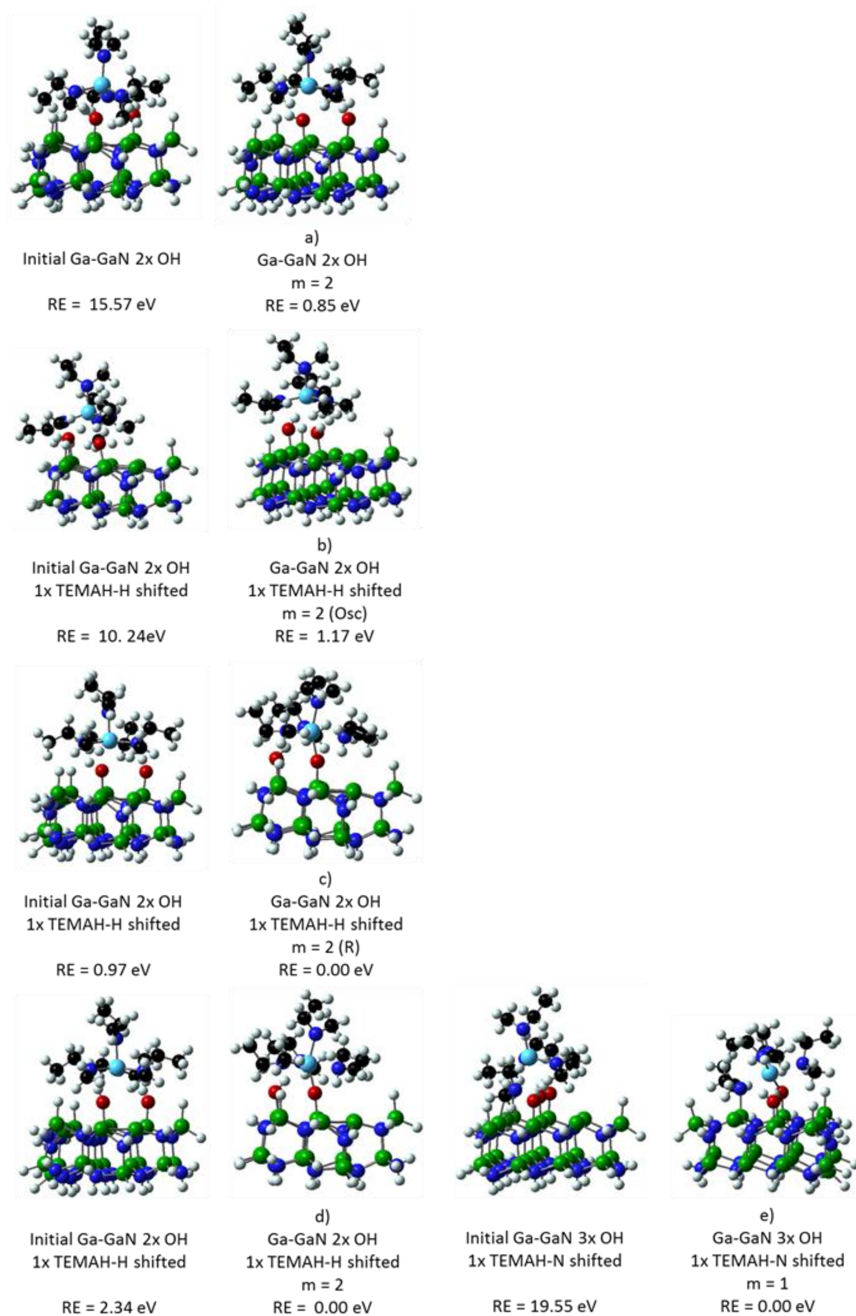

Fig. 56. Initial and final side views of the Ga-centered hydrolyzed (2 or 3 –OH molecules bonded to the surface) GaN structures (with H atoms) with 1 TEMAH molecule being introduced to the system. Each figure is labeled with the name and the multiplicity of each molecule. (a) two –OH molecules bonded to the GaN surface with 1 TEMAH molecule introduced, (b)-(d) two –OH molecules bonded to the GaN surface with 1 TEMAH molecule introduced and varying H atoms being shifted, and (e) three –OH molecules bonded to the surface with 1 TEMAH molecule introduced with a N atom shifted. Ga is Green, N is blue, O is red, H is white, C is black, and Al is purple. RE is Relative Energy (eV) and m is the multiplicity. (Osc) signifies failure to converge due to oscillations and (R) signifies the molecule is still running and has not reached its final stable state.

A single TEMAH molecule is introduced to the double and triple hydrolyzed Ga-GaN cluster, Ga-GaN 2x –OH and Ga-GaN 3x –OH, in several orientations using varying bond lengths of C-H and N-Hf. These structures are optimized using a multiplicity of 1 and 2, Fig. 56 (a)-(e) and Table 20. The most stable interaction resulted in the TEMAH bonding to the –OH molecule which caused Hf-N(CH2CH3) bond to break and react with the H from the –OH molecule forming an H-N bond, Fig. 56 (c)-(e). A shift in either the N-Hf bond or the O-H bond is necessary to form O-Hf and H-N(CH_2CH_3) bonds. Without shifting any atoms in the system, the most stable interaction between TEMAH and Ga-GaN 1x –OH resulted in a final relative energy (RE) of 0.85 eV and no interaction between the hydrolyzed surface and TEMAH, Fig. 56 (a) and Table 20.

Table 20. Total optimized energies in Hartrees for hydrolyzed Ga-centered GaN cluster interacting with 1 TEMAH molecule, the number of –OH molecules bonded to the GaN cluster, the number of TEMAH molecules, the multiplicity (*m*) used, the initial (d_i) and final distances (d_f) from the O atom to the nearest Hf atom, the formation of a N-H bond is determined and the shortest Ga-N bond length for the Ga atom that is taking part in the reaction and the N atom that is part of the active region GaN. (R) Signifies that the geometry has not fully optimized and is still running and (Osc) signifies the geometry failed to converge due to oscillations. RE stands for relative energy.

Structure Label from Fig. 56	TEMAH	-OH	*m*	Energy (Hartree)	RE (eV)	d_i (Å)	d_f (Å)	N-H Formation?	Ga-N Bond Length (Å)
A	1	2	2	-2169.54182	0.85	2.40	2.47		1.94
B			2	-2169.53025[a]	1.17	2.49	2.76		1.94
C			2	-2169.57318[b]	0.00	2.29	2.05	Yes	1.97
D			2	-2169.57321	0.00	2.71	2.05	Yes	1.97
E	1	3	1	-2245.51539	0.00	2.70	1.99	Yes	1.94

[a] Osc and [b] R

A single TEMAH molecule is introduced to the double and triple hydrolyzed Hollow-GaN cluster, Hollow-GaN 2x –OH and Hollow-GaN 3x –OH, in several orientations using varying bond lengths of C-H and N-Hf. These structures are optimized using a multiplicity of 1 and 2, Fig. 57 (a)-(c) and Table 21. The most stable

interaction between TEMAH and the double hydrolyzed Hollow-GaN cluster resulted in the formation of a Ga-O-Ga bond without interacting with the TEMAH. The only stable interaction between TEMAH and the triple hydrolyzed Hollow-GaN cluster resulted in the TEMAH bonding to the –OH molecule which caused Hf-N(CH2CH3) bond to break and react with the H from the –OH molecule forming an H-N bond, Fig. 57 (c). A shift in the N-Hf bond is necessary to form O-Hf and H-N(CH_2CH_3) bonds.

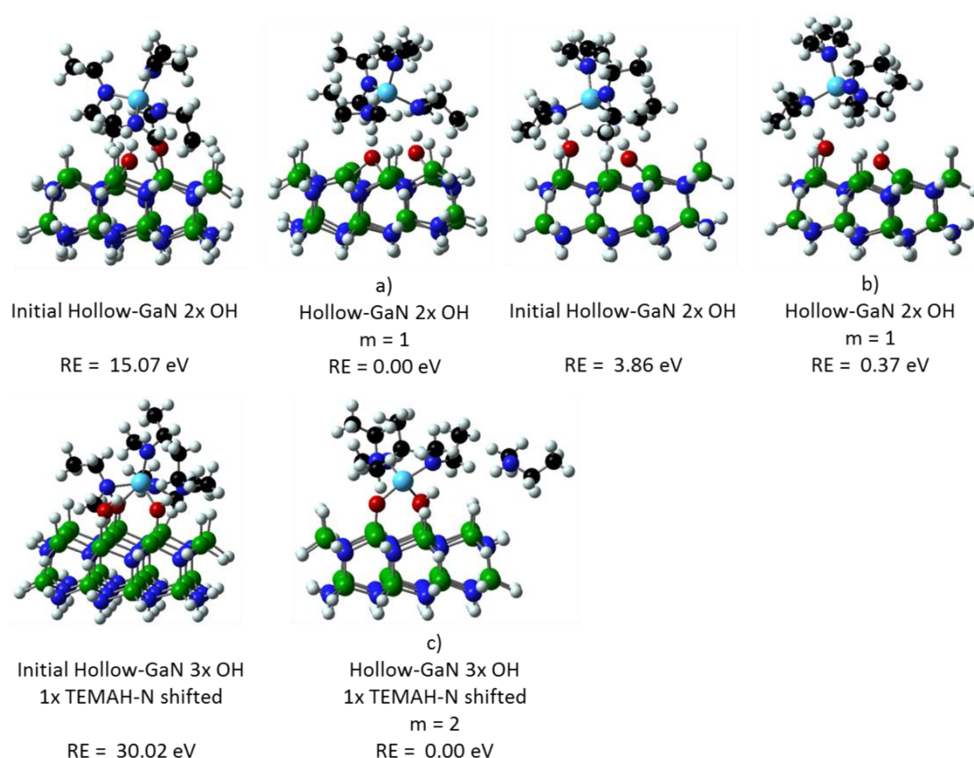

Fig. 57. Initial and final side views of the Hollow-centered hydrolyzed (2 or 3 –OH molecules bonded to the surface) GaN structures (with H atoms) with 1 TEMAH molecule being introduced to the system. Each figure is labeled with the name and the multiplicity of each molecule. (a)-(b) two –OH molecules bonded to the GaN surface with 1 TEMAH molecule introduced and (c) three –OH molecules bonded to the surface with 1 TEMAH molecule introduced with a N atom shifted. Ga is Green, N is blue, O is red, H is white, C is black, and Al is purple. RE is Relative Energy (eV) and m is the multiplicity.

Table 21. Total optimized energies in Hartrees for hydrolyzed Hollow-centered GaN cluster interacting with 1 TEMAH molecule, the number of –OH molecules bonded to the GaN cluster, the number of TEMAH molecules, the multiplicity (*m*) used, the initial (d_i) and final distances (d_f) from the O atom to the nearest Hf atom, the formation of a N-H bond is determined and the shortest Ga-N bond length for the Ga atom that is taking part in the reaction and the N atom that is part of the active region GaN. RE stands for relative energy.

Structure Label from Fig. 57	TEMAH	-OH	*m*	Energy (Hartree)	RE (eV)	d_i (Å)	d_f (Å)	N-H Formation?	Ga-N Bond Length (Å)
A	1	2	1	-2286.29151	0.00	3.28	3.99		1.89
B			1	-2286.27809	0.37	3.13	3.76		1.92
C	1	3	2	-2362.22720	0.00	2.00	1.98	Yes	1.96

The formation of H-N(CH_2CH_3) and O-Hf only occurs when the either the Hf-N or the O-H bond lengths are increased significantly. Deposition temperatures of the substrate and TEMAH are around 200 °C and 150 °C, respectively. These temperatures correspond to increases in the kinetic energy of the molecules which leads to changes in bond lengths. The research shows that the most stable interaction between TEMAH and hydrolyzed GaN clusters results in formation of H-N(CH_2CH_3) and Ga-O-Hf when reaction kinetics allow, i.e. temperatures beyond that of room temperature. The Hf-O bond lengths, for those molecules that formed N-H bonds, are similar to previously published data (*150, 151*). It is important to mention the formation of a Ga-O-Ga bond where the O atom is bonded to Hf. This geometry only occurs once throughout this research and is the only stable structure for the given system; therefore no definitive conclusions can be drawn.

7.3.2.2 Stability of the O-Al bond that forms from the interaction of TEMAH with Hydrolyzed GaN

The most stable Tertrakis(EthylMethylAmino)Hafnium (TEMAH) interaction with a double hydrolyzed GaN that matched the generally accepted initial structure O-Hf structure during ALD is used as the initial geometry to determine the stability of the O-Hf bond with hydrolyzed GaN. Other geometries are also used to determine the stability of the O-Hf bond with other –OH molecules or Ga-O bonds on GaN next to or near the

O-Hf bond, Fig. 58 - Fig. 60. All systems are optimized using the B3PW91/LANL2DZ (*147*) level of theory with varying multiplicity. The total energies are shown in Table 22 - Table 24 for the Ga-centered, N-centered, and hollow-centered structures, respectively. Generally, only geometries tested that resulted in stable molecules are shown.

The stability of a single Hf-$(N(CH_3)(CH_2CH_3))_2$ geometry where the Hf is bonded to two O atoms is tested using several geometries with the O atoms bonded to the Ga-GaN cluster; however only one system resulted in a stable structure, Step 2 Ga-GaN 2x O, Fig. 58 (a). The optimization of this geometry resulted in neither the formation nor degradation of any bonds only shifts in bond angles and lengths. The stability of the Hf-$(N(CH_3)(CH_2CH_3))_2$ geometry near an –OH molecule is tested, Step 2 Ga-GaN 1x OH, 2x O, Fig. 58 (b). The most stable optimization results in the deformation of the GaN cluster, causing it to curve upward, Fig. 58 (b).

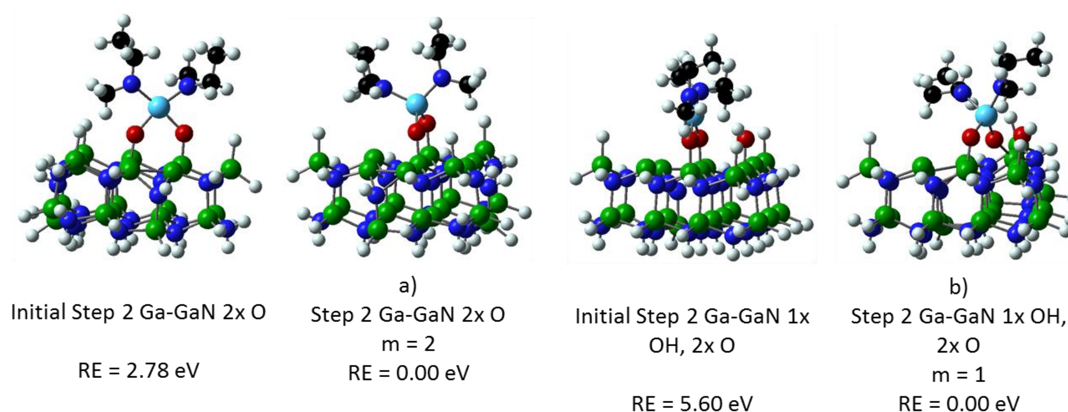

Fig. 58. Initial and final side views of Step 2, the stability of reacted TEMAH on hydrolyzed Ga-GaN. Ga-centered TEMAH reacted GaN structures (with H atoms) with 2 or 3 Ga-O bonds and 2 O-Hf bonds. Each figure is labeled with the name and the multiplicity of each molecule. (a) one Ga-O-Hf$(NCH_2CH_3)_2$-O-Ga bond optimized and (b) one Ga-O-Hf$(NCH_2CH_3)_2$-O-Ga bond optimized and one –OH molecule bonded to the GaN surface optimized. Ga is Green, N is blue, O is red, H is white, C is black, and Al is purple. RE is Relative Energy (eV) and m is the multiplicity.

Table 22. Total optimized energies in Hartrees for Step 2, the stability of reacted TEMAH on hydrolyzed Ga-centered GaN cluster, the number of –OH molecules bonded to the GaN cluster, the number of TEMAH molecules, the number of O atoms bonded to the GaN cluster, the multiplicity (*m*) used, the initial (d_i) and final distances (d_f) from the O atom to the nearest Hf atom, the formation of new or broken bonds is determined and the shortest Ga-N bond length for the Ga atom that is taking part in the reaction and the N atom that is part of the active region GaN. RE stands for relative energy.

System Label from Fig. 58	TEMAH	-OH	O	*m*	Energy (Hartree)	RE (eV)	d_i (Å)	d_f (Å)	New/Broken Bonds?	Ga-N Bond Length (Å)
A	1	-	2	2	-1820.82067	0.00	2.00	1.94	-	1.94
B	1	1	2	1	-1896.70358	0.00	2.00	1.96	-	1.90

While the interaction between hydrolyzed N-GaN and TEMAH did not result in any stable structures, the stability of a single Hf-(N(CH_3)(CH_2CH_3))$_2$ geometry where the Hf is bonded to two O atoms is tested with the O atoms bonded to the N-GaN cluster, Step 2 N-GaN 2x O, Fig. 59 (a). The optimization of this geometry resulted in neither the formation nor degradation of any bonds only shifts in bond angles and lengths. The stability of the Hf-(N(CH_3)(CH_2CH_3))$_2$ geometry near an –OH molecule is tested, Step 2 N-GaN 1x OH, 2x O, Fig. 58 (b). Again the optimization of this geometry resulted in neither the formation nor degradation of any bonds only shifts in bond angles and lengths, Table 23.

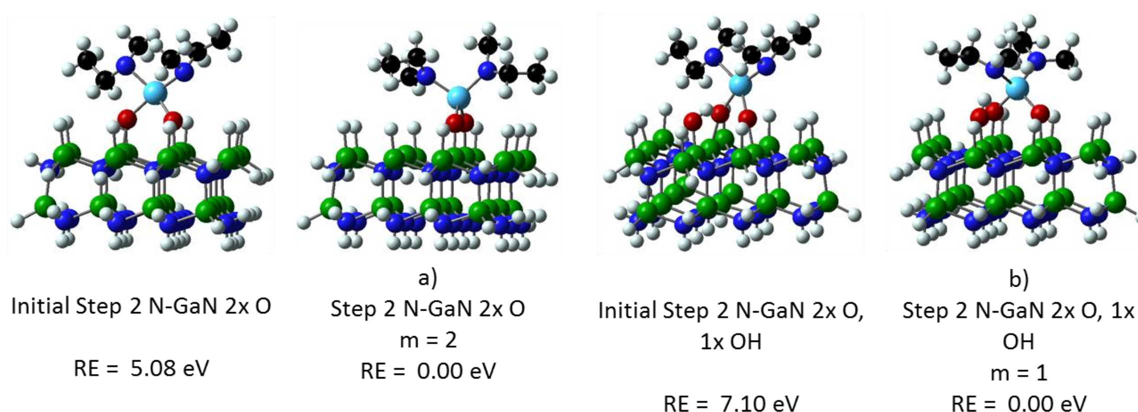

Fig. 59. Initial and final side views of Step 2, the stability of reacted TEMAH on hydrolyzed N-GaN. N-centered TEMAH reacted GaN structures (with H atoms) with 2 or 3 Ga-O bonds and 2 O-Hf bonds. Each figure is labeled with the name and the multiplicity of each molecule. (a) one Ga-O-Hf(NCH_2CH_3)$_2$-O-Ga bond optimized and (b) one Ga-O-Hf(NCH_2CH_3)$_2$-O-Ga bond optimized and one –OH molecule bonded to the GaN surface optimized. Ga is Green, N is blue, O is red, H is white, C is black, and Al is purple. RE is Relative Energy (eV) and m is the multiplicity.

Table 23. Total optimized energies in Hartrees for Step 2, the stability of reacted TEMAH on hydrolyzed N-centered GaN cluster, the number of –OH molecules bonded to the GaN cluster, the number of TEMAH molecules, the number of O atoms bonded to the GaN cluster, the multiplicity (*m*) used, the initial (d_i) and final distances (d_f) from the O atom to the nearest Hf atom, the formation of new or broken bonds is determined and the shortest Ga-N bond length for the Ga atom that is taking part in the reaction and the N atom that is part of the active region GaN. RE stands for relative energy.

System Label from Fig. 59	TEMAH	-OH	O	*m*	Energy (Hartree)	RE (eV)	d_i (Å)	d_f (Å)	New/Broken Bonds?	Ga-N Bond Length (Å)
A	1	-	2	2	-1825.51620	0.00	2.00	1.95	-	1.96
B	1	1	2	1	-1901.39807	0.00	2.00	1.93	-	1.95

The stability of a single Hf-(N(CH_3)(CH_2CH_3))$_2$ geometry where the Hf is bonded to two O atoms is tested using two geometries with the O atoms bonded to the Hollow-GaN cluster, Step 2 Ga-GaN 2x O, Fig. 60 (a)-(b). The optimization of this geometry, given the O atoms are attached to neighboring Ga surface atoms, results in the formation of a Ga-N(CH_3)(CH_2CH_3) bond without breaking any bonds. While this is not the most stable interaction it may be the mechanism behind the formation of in

interfacial layer during the ALD of HfO_2 on GaN. The optimization of this geometry when the O atoms are separated by four Ga-N bond lengths results in neither the formation nor degradation of any bonds only shifts in bond angles and lengths, Fig. 60 (b). The stability of the Hf-$(N(CH_3)(CH_2CH_3))_2$ geometry near an –OH molecule is tested, Step 2 Hollow-GaN 1x OH, 2x O, Fig. 60 (c). The most stable optimization, which failed to reach a minimum due to oscillations, results in the formation of a H-$N(CH_3)(CH_2CH_3)$ bond and an additional O-Hf bond, Fig. 60 (c).

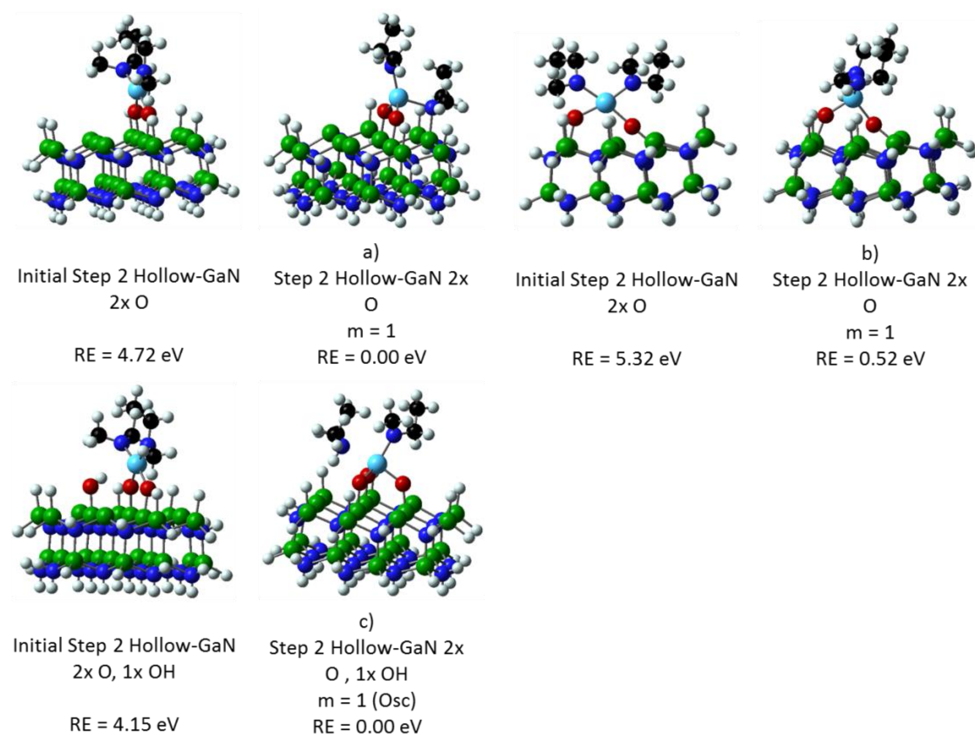

Fig. 60. Initial and final side views of Step 2, the stability of reacted TEMAH on hydrolyzed Hollow-GaN. Hollow-centered TEMAH reacted GaN structures (with H atoms) with 2 or 3 Ga-O bonds and 2 O-Hf bonds. Each figure is labeled with the name and the multiplicity of each molecule. (a)-(b) one Ga-O-Hf$(NCH_2CH_3)_2$-O-Ga bond optimized and (c) one Ga-O-Hf$(NCH_2CH_3)_2$-O-Ga bond optimized and one –OH molecule bonded to the GaN surface optimized. Ga is Green, N is blue, O is red, H is white, C is black, and Al is purple. RE is Relative Energy (eV) and m is the multiplicity. Osc signifies the system did not reach a minimum due to oscillations.

Table 24. Total optimized energies in Hartrees for Step 2, the stability of reacted TEMAH on hydrolyzed Hollow-centered GaN cluster, the number of –OH molecules bonded to the GaN cluster, the number of TEMAH molecules, the number of O atoms bonded to the GaN cluster, the multiplicity (*m*) used, the initial (d_i) and final distances (d_f) from the O atom to the nearest Hf atom, the formation of new or broken bonds is determined and the shortest Ga-N bond length for the Ga atom that is taking part in the reaction and the N atom that is part of the active region GaN. RE stands for relative energy. Osc signifies the system did not reach a minimum due to oscillations.

System Label from Fig. 60	TEMAH	-OH	O	*m*	Energy (Hartree)	RE (eV)	d_i (Å)	d_f (Å)	New/Broken Bonds?	Ga-N Bond Length (Å)
A	1	-	2	1	-1937.55161	0.00	2.00	1.90	Yes	1.92
B	1	-	2	1	-1937.53263	0.52	2.00	1.95	-	1.92
C	1	1	2	1	-2013.45367[a]	0.00	2.00	1.97	Yes	1.96

[a] Osc

Many structures were tested to determine the stability of the O-Hf bond, but few resulted in stable systems. With this in mind no definitive conclusions can be drawn without further research. It is important to note the formation of a stable Ga-$N(CH_3)(CH_2CH_3)$ bond. While this geometry was not the most stable it was within 0.52 eV of the most stable structure signifying that this bond structure may form during ALD of HfO_2 on GaN and may be the cause of the interfacial layer formation as no such structure is found in this research of TMA interacting with hydrolyzed GaN clusters for fully optimized and stable systems.

7.4 Conclusions

Additional research is needed in the theoretical approximation of ALD on GaN to grasp a better understanding of the interactions of TMA or TEMAH with hydrolyzed GaN clusters. It was discovered that the formation of a Ga-$N(CH_3)(CH_2CH_3)$ bond can form during the deposition of HfO_2 using ALD and TEMAH as the reactant without breaking the Hf-N bond. The formation of a Ga-$N(CH_3)(CH_2CH_3)$ bond is significant because with the introduction of water into the system the methyl and ethyl methyl groups may reach to form a Ga-N-O bond which is believed to be the interfacial oxide found during deposition of HfO_2 using ALD on GaN. It is important to note that a Ga-

CH_3 bond did not form in any fully optimized stable structures when analyzing the interaction of TMA with hydrolyzed GaN.

CHAPTER VIII
CONCLUSIONS AND FUTURE RESEARCH

In this dissertation, combinations of experimental and theoretical approaches were taken to determine the effects of chemical states on the effective work function. The experimental approaches were used to determine the flat band voltage, band bending at GaN – dielectric interfaces, valence band maximum and electron affinities of the various dielectrics and aq-HCl GaN. The measurements resulted in the inclusion of a heterojunction in the effective work function calculation and the calculation of interfacial dipoles that are known to affect the effective work function at the GaN – dielectric interface. The theoretical approaches were used to determine the effect of the heterojunction (material thickness and doping concentration) on the effective work function calculation, the mechanism behind the oxidation of GaN using oxygen and water, and the mechanism behind atomic layer deposition of Al_2O_3 and HfO_2 on GaN(0001) clusters.

The initial research was to determine the effect of a heterojunction on the effective work function calculation. An experimental and theoretical approach was taken to determine the effects of a heterojunction on the effective work function in a metal/high-κ gate stack. The investigation found that if a Ge/Si heterostructure on silicon is low doped and sufficiently thin, the work function can be extracted in a manner similar to that on a simple silicon substrate. In other words, the heterojunction does not play a significant role in the work function calculation in this work. The extracted work functions of TiN with an underlying heterojunction were found to be in agreement with that of TiN on a silicon substrate.

With the knowledge of the effect of the heterojunction determined, the next step of the research was to understand the effects of the semiconductor – dielectric interface on the effective work function. Numerous studies mentioned throughout this dissertation have shown that a dipole at the III-N/dielectric interface affects the flat band

voltage and thus the effective work function of high electron mobility transistors. Therefore the next step of research was to determine the III-N/dielectric interfacial dipole. An experimental approach was taken to fulfill this goal. X-ray and ultraviolet photoelectron spectroscopy were used to observe the interface electronic states at the GaN (0001) and Al_2O_3, HfO_2 and GaON dielectric interfaces. GaN was chosen as the III-N semiconductor due to recent advancements in the structure of high electron mobility transistors which resulted in the metal gate stack being deposited on a thin GaN layer. The GaN was aqueous HCl cleaned prior to thermal oxidation to form GaON and prior to atomic layer deposition of Al_2O_3 and HfO_2, which were followed by a post deposition anneal. An aqueous HCl clean was performed instead of high temperature ammonia clean to the interfacial dipole that would form during typical manufacturing. The GaN/HfO_2 and GaN/Al_2O_3 interfaces exhibited dipoles of 1.6 eV and 0.4 eV, respectively. The formation of an interfacial layer at the GaN/HfO_2 interface was the primary cause of the larger dipole.

Due to the knowledge of the formation of an interfacial GaO_x or GaON layer during atomic layer deposition of HfO_2, a better understanding of the GaN/GaON interface was needed. To accomplish this task, the interface electronic states at the GaN(0001) and GaON interface were observed using X-ray and ultraviolet photoelectron spectroscopy (XPS and UPS). The experimental analysis of the GaN/GaON interface resulted in the calculation of a -2.7 eV dipole based on the assumption that the core level shifts are only representative of the GaN band bending at the interface. If it is assumed that the core level shifts are only due to the oxidation of GaN, therefore only changes in bonds, then the exhibited dipole at the GaN/GaON was calculated to be -1.8 eV. Due to the research of the GaN/GaON interface, the observed dipole was determined to be primarily due to the polarization of the GaN. While this research resulted in the determination of the interfacial dipole, a more complete understanding of the formation of the interfacial layer was needed.

The mechanisms behind the formation of a GaON interfacial layer during atomic layer deposition of HfO_2 were evaluated using a theoretical approach. First, density

functional theory was used to calculate the interactions of oxygen and water with the Ga-face of GaN clusters, which could be used as testbeds for the actual Ga-face on GaN crystals. The results demonstrated that the local spin plays an important role in these interactions. The most stable interaction of O_2 and the GaN clusters resulted in the complete dissociation of the O_2 molecule to form two Ga-O-Ga bonds, while the most stable interaction between a H_2O molecule and the GaN clusters is the complete dissociation of one of the O-H bonds to form a Ga-O-H bond and a Ga-H bond. In some cases, oxygen became bonded to three surface Ga atoms resulting in the deformation of the crystalline structure directly below this structure. Another stable structure that formed during oxidation using water was the formation of a –OH molecule bonded to two surface Ga atoms. This may be a mechanism behind the formation of an interfacial layer. Second, density functional theory was used to calculate the interaction of the reactants used to deposit HfO_2 and Al_2O_3 during atomic layer deposition with hydrolyzed Ga-face GaN clusters. It was determined from the results, that further research is needed in this area to grasp a better understanding of the interactions of TMA or TEMAH with hydrolyzed GaN clusters. It was found that the formation of a Ga-$N(CH_3)(CH_2CH_3)$ bond can form during the deposition of HfO_2 using ALD and TEMAH as the reactant without breaking the Hf-N bond. The formation of a Ga-$N(CH_3)(CH_2CH_3)$ bond is significant because with the introduction of water into the system the methyl and ethyl methyl groups may reach to form a Ga-N-O bond which is believed to be the interfacial oxide found during deposition of HfO_2 using ALD on GaN. It is important to note that a Ga-CH_3 bond did not form in any fully optimized stable structures when analyzing the interaction of TMA with hydrolyzed GaN.

The work presented in this dissertation is a systematic investigation of the effects of chemical states on the EWF. There are substantial issues that are unresolved and some that have not been investigated in this work. To have high quality enhancement mode high electron mobility transistors, further investigation must be conducted with the suggestions presented here after.

The immediate next step is to better understand the factors that contribute to the GaN/GaON interfacial dipole. The magnitude of each contributing factor needs to be investigated. One contributor to the interfacial dipole that can be tested next is the amount of physical strain from the lattice mismatch. To do this one can measure the valence band maxima and width using UPS and XPS of GaN and GaN/GaON, followed by the samples under mechanical stress, such as bending, and then measured once the samples have recovered. One would be able to determine the amount of strain the top film would experience and model the results. This type of test would indicate the amount of change that can be seen in the UPS and XPS data from mechanical stress, either in the tensile or compressive directions and the magnitude that would be expected. Once a mechanical stress test is completed, only the spontaneous polarization and Ga vacancies are left to be accounted for.

Further investigation of the mechanism of the GaON interfacial layer that is formed during atomic layer deposition of HfO_2 is needed. It is suggested that *in situ* XPS and UPS be taken during the deposition of HfO_2 on GaN. This experiment was not completed during this study due to a lack of equipment that is capable of doing such an experiment. However, the experiment is necessary to provide experimental proof concept of the mechanisms laid out in this work that were theoretically determined using density functional theory.

Another investigation that should be completed is photoemission study of high-κ dielectrics on GaN/AlGaN/GaN heterostructures. Due to the heterojunctions, the UPS and XPS measurements may vary and the interface dipoles may change slightly due to the polarization fields taking place in the AlGaN and bottom GaN. The same basic experiments laid out in this study and previously can be used to determine the effect of the heterostructures. Once this type of study is completed, the scientific community will have a better understanding of the effects of polarization on the gate stack and the gate stack on the formation of a 2-dimensional electron gas.

Finally, a continued photoemission study of AlGaN/dielectric and GaN/dielectric interfaces could lead to a more complete understanding of the role of spontaneous and

piezoelectric polarization effects on the effective work function. With this knowledge, enhancement-mode high electron mobility transistors could be fabricated and possibly integrated into silicon based technologies. While further research must be completed on GaN/dielectric interfaces, this dissertation provides the groundwork for future work regarding the gate stack of high electron mobility transistors.

REFERENCES AND NOTES

1. D. A. Buchanan, Scaling the gate dielectric: Materials, integration, and realiability. *IBM Journal of research and Development* **43**, 245 - 264 (1999).

2. G. D. Wilk, R. M. Wallace, J. M. Anthony, High-κ gate dielectrics: Current status and materials properties considerations. *Journal of Applied Physics* **89**, 5243 - 5276 (2001).

3. R. Liu, *Materials and Fundamentals of Gate Dielectrics. Chapter X*. A. Demkov, A. Navrotsky, Eds., (Springer, Netherlands, 2005).

4. S. Guha, E. P. Gusev, M. Copel, L.-A. Ragnarsson, D. A. Buchanan, Compatibility challenges for high-κ materials integration into CMOS technology. *MRS Bulletin* **27**, 226 - 229 (2002).

5. R. Degraeve, J. Schmitz, L. Pantisano, E. Simoen, M. Houssa *et al.*, *Dielectric Films for Advanced Microelectronics. Chapter IV Electrical Characterization of Advanced Gate Dielectrics.* M. G. M. Baklanov, and K. Maex, Ed., (John Wiley and Sons, West Sussex, 2007).

6. G. Bersuker, P. Zeitzoff, J. H. Sim, B. H. Lee, R. Choi *et al.*, Mobility evaluation in transistors with charge trapping gate dielectrics. *Applied Physics Letters* **87**, 042905-042903 (2005).

7. H. N. Alshareef, H. C. Wen, H. R. Harris, K. Choi, H. F. Luan *et al.*, Modulation of the work function of silicon gate electrode using thin TaN interlayers. *Applied Physics Letters* **87**, 052109-052103 (2005).

8. J. Schaeffer, S. Samavedam, L. Fonseca, C. Capasso, O. Adetutu *et al.*, Investigations of metal gate electrodes on HfO2 gate dielectrics. *Mat. Res. Soc. Symp. Proc.* **811**, 137-147 (2004).

9. R. Lin, Q. Lu, P. Ranade, T. J. King, C. M. Hu, An adjustable work function technology using Mo gate for CMOS devices. *IEEE Electron Device Letters* **23**, 49-51 (2002).

10. S. H. Bae, W. P. Bai, H. C. Wen, S. Mathew, L. K. Bera *et al.*, Laminated metal gate electrode with tunable work function for advanced CMOS. *VLSI Technology Conference, 2004. Digest of Technical Papers. 2004*, 188 - 189 (15 - 17 June, 2004).

11. S. Zafar, V. Narayanan, A. Callegari, F. R. McFeely, P. Jamison *et al.*, HfO2 metal stacks: Determination of energy level diagram, work functions & their dependence on metal deposition. *VLSI Technology Conference, 2005. Digest of Technical Papers. 2005*, 44-45 (14-16 June, 2005).

12. L. Kang, B. H. Lee, W.-J. Qi, Y. Jeon, R. Nieh *et al.*, Electrical characteristics of highly reliable ultrathin hafnium oxide gate dielectric. *IEEE Electron Device Letters* **21**, 181-183 (2000).

13. B. H. Lee, L. Kang, W.-J. Qi, R. Nieh, Y. Jeon *et al.*, Ultrathin hafnium oxide with low leakage and excellent reliability for alternative gate dielectric application. *IEDM Technical Digest International Electron Devices Meeting*, 133-136 (Dec. 5-8, 1999).

14. B. Streetman, S. Banerjee, *Solid State Electronic Devices*. (Prentice Hall, Upper Saddle River, NJ, 2000).

15. H. R. Harris, S. E. Thompson, S. Krishnan, P. Kirsch, P. Majhi *et al.*, Flexible, simplified CMOS on Si(110) with metal gate / high k for HP and LSTP. *IEDM*, 57-60 (Dec. 10-12, 2007).

16. P. D. Ye, G. D. Wilk, B. Yang, J. Kwo, S. N. G. Chu *et al.*, GaAs metal–oxide–semiconductor field-effect transistor with nanometerthin dielectric grown by atomic layer deposition. *Applied Physics Letter* **83**, 180 - 182 (2003).

17. S. Koveshnikov, W. Tsai, I. Ok, J. C. Lee, V. Torkanov *et al.*, Metal-oxide-semiconductor capacitors on GaAs with high-k gate oxide and amorphous silicon interface passivation layer. *Applied Physics Letters* **88**, 022106-022103 (2006).

18. R. Jha, J. Gurganos, Y. H. Kim, R. Choi, J. Lee *et al.*, A capacitance-bases methodology for work function extraction of metals on high-k. *IEEE Electron Device Letters* **25**, 420-423 (2004).

19. G. Brown, G. Smith, J. Saulters, K. Matthews, H. C. Wen *et al.*, An improved methodology for gate electrode work function extraction in. *Proc. IEEE SISC Conf.*, 15 (December 9-11, 2004).

20. M. Houssa, E. Chagarov, A. Kummel, Surface defects and passivation of Ge and III-V Interfaces. *MRS Bulletin* **34**, 504-513 (2006).

21. H. Kim, P. C. McIntyre, Atomic layer deposition of ultrathin metal-oxide films for nano-scale device applications. *Journal of the Korean Physical Society* **48**, 5 - 17 (2006).

22. A. Fet, V. Haublein, A. J. Bauer, H. Ryssel, L. Frey, Effective work function tuning in high-k dielectric metal-oxidesemiconductor stacks by fluorine and lanthanide doping. *Appl. Phys. Lett.* **96**, 053506-053503 (2010).

23. H. N. Alshareef, H. F. Luan, K. Choi, H. R. Harris, H. C. Wen *et al.*, Metal gate work function engineering using AlNx interfacial layers. *Applied Physics Letters* **88**, 112114-112113 (2006).

24. J. K. Efavi, T. Mollenhauer, T. Wahlbrink, H. D. B. Gottlob, M. C. Lemme *et al.*, Tungsten work function engineering for dual metal gate nano-CMOS. *Journal of Materials Science: Materials in Electronics* **16**, 433-436 (2005).

25. N. Goel, P. Majhi, W. Tsai, M. Warusawithana, D. G. Schlom *et al.*, High-indium-content InGaAs metal-oxide-semiconductor capacitor with amorphous laAlO3 gate dielectric. *Appl. Phys. Lett.* **91**, 093509-093503 (2007).

26. S. Sugiura, Y. Hayashi, S. Kishimoto, T. Mizutani, M. Kuroda *et al.*, Fabrication of normally-off mode GaN and AlGaN/GaN MOSFETs with HfO2 gate insulator. *Solid State Electron.* **54**, 79-83 (2010).

27. G. Li, T. Zimmermann, Y. Cao, C. Lain, X. Xing *et al.*, Threshold voltage control in Al0.72Ga0.28N/AlN/GaN HEMTs by work-function engineering. *IEEE Electron Device Lett.* **31**, 954-956 (2010).

28. J. Bernát, P. Javorka, A. Fox, M. Marso, H. Lüth *et al.*, Effect of surface passivation on performance of AlGaN/GaN/Si HEMTs. *Solid-State Electronics* **47**, 2097-2103 (2003).

29. K. Matocha, T. P. Chow, R. J. Gutmann, High-voltage normally off GaN MOSFETs on sapphire substrates. *IEEE Trans. Electron Devices* **52**, 6-10 (2005).

30. Y. C. Chang, H. C. Chiu, Y. J. Lee, M. L. Huang, K. Y. Lee *et al.*, Structural and electrical characteristics of atomic layer deposited high kappa HfO[sub 2] on GaN. *Appl. Phys. Lett.* **90**, 232904-232903 (2007).

31. D. Shahrjerdi, D. I. Garcia-Gutierrez, T. Akyol, S. R. Bank, E. Tutuc *et al.*, GaAs metal-oxide-semiconductor capacitors using atomic layer deposition of HfO[sub 2] gate dielectric: Fabrication and characterization. *Applied Physics Letters* **91**, 193503-193503 (2007).

32. P. Sivasubramani, T. J. Park, B. E. Coss, A. Lucero, J. Huang *et al.*, In-situ X-ray photoelectron spectroscopy of trimethyl aluminum and water half-cycle treatments on HF-treated and O3-oxidized GaN substrates. *physica status solidi (RRL) – Rapid Research Letters* **6**, 22-24 (2012).

33. T. E. Cook, C. C. Fulton, W. J. Mecouch, R. F. Davis, G. Lucovsky *et al.*, Band offset measurements of the GaN(0001)/HfO2 interface. *Journal of Applied Physics* **94**, 7155-7158 (2003).

34. J. J. Uhlrich, L. C. Grabow, M. Mavrikakis, T. F. Kuech, Practical Surface Treatments and Surface Chemistry of n -Type and p -Type GaN. *Journal of Electronic Materials* **37**, 439-447 (2008).

35. K. A. Rickert, A. B. Ellis, F. J. Himpsel, J. Sun, T. F. Kuech, n-GaN surface treatments for metal contacts studied via x-ray photoemission spectroscopy. *Applied Physics Letters* **80**, 204-206 (2002).

36. U. K. Mishra, P. Parikh, W. Yi-Feng, AlGaN/GaN HEMTs-an overview of device operation and applications. *Proceedings of the IEEE* **90**, 1022-1031 (2002).

37. X. Liu, S. Ramanathan, A. Longdergan, A. Srivastava, E. Lee *et al.*, ALD of hafnium oxide thin films from Tetrakis(ethylmethylamino)hafnium and Ozone. *J. Electrochem. Soc.* **152**, G213-G219 (2005).

38. M. Leskelä, M. Ritala, Atomic layer deposition (ALD): from precursors to thin film structures. *Thin Solid Films* **409**, 138-146 (2002).

39. M. Leskelä, M. Ritala, Atomic layer deposition chemistry: Recent developments and future challenges. *Angewandte Chemie International Edition* **42**, 5548-5554 (2003).

40. S. M. George, Atomic Layer Deposition: An overview. *Chemical Reviews* **110**, 111-131 (2009).

41. Y. C. Chang, M. L. Huang, Y. H. Chang, Y. J. Lee, H. C. Chiu *et al.*, Atomic-layer-deposited Al2O3 and HfO2 on GaN: A comparative study on interfaces and electrical characteristics. *Microelectronic Engineering* **88**, 1207-1210 (2011).

42. H. Kim, P. C. McIntyre, K. C. Saraswat, Effects of crystallization on the electrical properties of ultrathin HfO[sub 2] dielectrics grown by atomic layer deposition. *Applied Physics Letters* **82**, 106-108 (2003).

43. M. D. Groner, J. W. Elam, F. H. Fabreguette, S. M. George, Electrical characterization of thin Al2O3 films grown by atomic layer deposition on silicon and various metal substrates. *Thin Solid Films* **413**, 186-197 (2002).

44. M. D. Groner, F. H. Fabreguette, J. W. Elam, S. M. George, Low-temperature Al2O3 atomic layer deposition. *Chemistry of Materials* **16**, 639-645 (2004).

45. R. L. Puurunen, Surface chemistry of atomic layer deposition: A case study for the trimethylaluminum/water process. *Journal of Applied Physics* **97**, 121301-121352 (2005).

46. A. W. Ott, J. W. Klaus, J. M. Johnson, S. M. George, Al3O3 thin film growth on Si(100) using binary reaction sequence chemistry. *Thin Solid Films* **292**, 135-144 (1997).

47. R. A. Pollak, L. Ley, F. R. McFeely, S. P. Kowalczyk, D. A. Shirley, Characteristic energy loss structure of solids from x-ray photoemission spectra. *Journal of Electron Spectroscopy and Related Phenomena* **3**, 381-398 (1974).

48. R. Flitsch, S. I. Raider, Electron mean escape depths from x - ray photoelectron spectra of thermally oxidized silicon dioxide films on silicon. *Journal of Vacuum Science and Technology* **12**, 305-308 (1975).

49. N. W. Ashcroft, N. D. Mermin, *Solid State Physics*. (Harcourt College Publishers, Philadelphia, PA, ed. College Edition, 1976).

50. W. Liu, *Fundamentals of III-V devices: HBTs, MESFETs, and HFETs/HEMTs. Chapter I Basic Properties and Device Physics of III-V Materials.*, (John Wiley and Sons, New York, NY, 1999).

51. C. Kittel, *Introduction to Solid State Physics. Chapter VII Energy Bands.*, (John Wiley and Sons, New York, NY, ed. 8, 2005).

52. D. K. Schroder, *Semiconductor Material and Device Characterization. Chapter I - XI.*, (John Wiley and Sons, Hoboken, New Jersey USA, ed. 3, 2006).

53. S. M. Sze, K. K. Ng, *Physics of Semiconductor Devices*. (John Wiley & Sons New York, NY, 2006).

54. M. E. Levinshtein, S. L. Rumyantsev, M. Shur, *Properties of advanced semiconductor materials : GaN, AlN, InN, BN, SiC, SiGe. Chapter I GaN.*, (Wiley, New York, 2001).

55. J. Robertson, High dielectric constant gate oxides for metal oxide Si transistors. *Reports on Progress in Physics* **69**, 327-396 (2006).

56. J. Ren, B. Li, J.-G. Zheng, J. Liu, High-density NiSi nanocrystals embedded in Al2O3/SiO2 double-barrier for robust retention of nonvolatile memory. *Solid-State Electronics* **67**, 23-26 (2012).

57. S.-M. Oh, H.-w. You, K.-S. Kim, Y.-H. Lee, W.-J. Cho, Electrical properties of HfO2 charge trap flash memory with SiO2/HfO2/Al2O3 engineered tunnel layer. *Current Applied Physics* **10**, e18-e21 (2010).

58. E. Martinez, C. Leroux, N. Benedetto, C. Gaumer, M. Charbonnier *et al.*, Electrical and chemical properties of the HfO2/SiO2/Si stack: Impact of HfO2 thickness and thermal budget. *ECS Transactions* **16**, 161-169 (2008).

59. R. Schlaf, C. D. Merritt, L. A. Crisafulli, Z. H. Kafafi, Organic semiconductor interfaces: Discrimination between charging and band bending related shifts in frontier orbital line-up measurements with photoemission spectroscopy. *Journal of Applied Physics* **86**, 5678-5686 (1999).

60. R. Schlaf, O. Lang, C. Pettenkofer, W. Jaegermann, Band lineup of layered semiconductor heterointerfaces prepared by van der Waals epitaxy: Charge transfer correction term for the electron affinity rule. *Journal of Applied Physics* **85**, 2732-2753 (1999).

61. J. R. Waldrop, R. W. Grant, Semiconductor Heterojunction Interfaces: Nontransitivity of Energy-band Discontiuities. *Physical Review Letters* **43**, 1686-1689 (1979).

62. J. R. Waldrop, R. W. Grant, Measurement of AlN/GaN (0001) heterojunction band offsets by x-ray photoemission spectroscopy. *Applied Physics Letters* **68**, 2879-2881 (1996).

63. P. J. Goodhew, F. J. Humphreys, *Electron Microscopy and Analysis. Chapter IV Transmission Electron Microscope.*, (Taylor and Francis, London, UK, ed. 2, 1988).

64. S. TCAD, S. TCAD, Ed. (Sentaurus TCAD, 2007), vol. 2012.

65. A. R. Leach, *Molecular Modelling: Principles and Applications*. (Pearson Education Limitted, Singapore, 1996).

66. R. Ahlrichs, P. R. Taylor, The choice of gaussian-basis sets for molecular electronic-structure calculations. *Journal De Chimie Physique Et De Physico-Chimie Biologique* **78**, 315-324 (1981).

67. P. J. Hay, W. R. Wadt, Ab initio effective core potentials for molecular calculations. Potentials for K to Au including the outermost core orbitals. *J. Chem. Phys.* **82**, 299-310 (1985).

68. W. R. Wadt, P. J. Hay, Ab initio effective core potentials for molecular calculations. Potentials for main group elements Na to Bi. *J. Chem. Phys.* **82**, 284-298 (1985).

69. P. Hohenberg, W. Kohn, Inhomogeneous electron gas. *Physical Review* **136**, B864-B871 (1964).

70. W. Kohn, L. J. Sham, Self-consistent equations including exchange and correlation effects. *Physical Review* **140**, A1133-A1138 (1965).

71. W. Kohn, L. J. Sham, Quantum density oscillations in an inhomogeneous electron gas. *Physical Review* **137**, A1697-A1705 (1965).

72. D. S. Sholl, J. A. Steckel, *Density Functional Theory. Chapter: What is Density Functional Theory?* , (John Wiley & Sons, Inc., New York, NY, 2009).

73. W. Kohn, Density functional and density matrix method scaling linearly with the number of atoms. *Physical Review Letters* **76**, 3168–3171 (1996).

74. A. D. Becke, A new mixing of Hartree-Fock and local density-functional theories. *J. Chem. Phys.* **98**, 1372-1377 (1993).

75. J. P. Perdew, J. A. Chevary, S. H. Vosko, K. A. Jackson, M. R. Pederson *et al.*, Atoms, molecules, solids, and surfaces: Applications of the generalized gradient approximation for exchange and correlation. *Phys. Rev. B* **46**, 6671-6687 (1992).

76. J. P. Perdew, Y. Wang, Accurate and Simple Analytic Representation of the Electron-Gas Correlation Energy. *Phys. Rev. B* **45**, 13244-13249 (1992).

77. J. M. Seminario, M. G. Maffei, L. A. Agapito, P. F. Salazar, Energy Correctors for Accurate Prediction of Molecular Energies. *J. Phys. Chem. A* **110**, 1060-1064 (2006).

78. J. M. Seminario, Energetics using DFT: Comparisons to precise ab initio and experiment. *Chem. Phys. Lett.* **206**, 547-554 (1993).

79. A. D. Becke, Density-functional thermochemistry. V. Systematic optimization of exchange-correlation functionals. *The Journal of Chemical Physics* **107**, 8554 - 8561 (1997).

80. A. D. Becke, Density-functional thermochemistry. IV. A new dynamical correlation functional and implications for exact-exchange mixing. *The Journal of Chemical Physics* **104**, 1040 - 1046 (1996).

81. A. D. Becke, Density-functional thermochemistry. III. The role of exact exchange. *J. Chem. Phys.* **98**, 5648-5652 (1993).

82. A. D. Becke, Density-functional thermochemistry II. The effect of the Perdew-Wang generalized-gradient correlation correction. *J. Chem. Phys.* **97**, 9173-9177 (1992).

83. K. Choi, H.-C. Wen, H. Alshareef, H. R. Harris, P. Lysaght *et al.*, The effect of metal thickness, overlayer and high-k surface treatment on the effective work function of metal electrode. *Solid-State Device Research Conference, 2005. ESSDERC 2005. Proceedings of 35th European*, 101-104 (Sept. 12-16, 2005).

84. Q. Z. Nan Wu, Chunxiang Zhu, D. S. H. Chan, M. F. Li, N. Balasubramanian, Albert Chin, and Dim-Lee Kwong, Alternative surface passivation on germanium for metal-oxide-semiconductor applications with high-k gate dielectric. *Applied Physics Letters* **85**, 4127-4123 (2004).

85. S. C. Song, C. S. Park, J. Price, C. Burham, R. Choi *et al.*, Mechanism of V<inf>fb</inf> roll-off with high work function metal gate and low temperature oxygen incorporation to achieve PMOS band edge work function. *Electron Devices Meeting, 2007. IEDM 2007. IEEE International*, 337-340 (10-12 Dec., 2007).

86. H. Takeuchi, W. Hiu Yung, H. Daewon, K. Tsu-Jae, Impact of oxygen vacancies on high-κ gate stack engineering. *Electron Devices Meeting, 2004. IEDM Technical Digest. IEEE International*, 829-832 (13-15 Dec., 2004).

87. C. Chi On, S. Ramanathan, B. B. Triplett, P. C. McIntyre, K. C. Saraswat, Germanium MOS capacitors incorporating ultrathin high-k; Gate dielectric. *Electron Device Letters, IEEE* **23**, 473-475 (2002).

88. P. Ashburn, *SiGe Heterojunction Bipolar Transistors. Chapter VIII Silicon-Germanium Heterojunction Bipolar Transistors.*, (Wiley, West Sussex, England, 2003).

89. K. Choi, P. Lysaght, H. Alshareef, C. Huffman, H.-C. W. H. R. Harris *et al.*, Growth mechanism of TiN film on dielectric films and the effects on the work function. *Thin Solid Films* **486**, 141-144 (2005).

90. J. R. Hauser. (NCSU, Raliegh, NC, 1999), vol. 1, pp. Computer Program.

91. L. Kronik, M. Leibovitch, E. Fefer, V. Korobov, Y. Shapira, Electronic characterization of heterojunctions. *Journal of Electronic Materials* **24**, 893 - 901 (1995).

92. F. Schaffler, *Properties of Advanced semiconductor Materials - GaN, AlN, InN, BN, SiC, and SiGe. Chapter I GaN.* S. L. R. Michael E. Levinshtein, and Michael S. Shur, Ed., (John Wiley & Sons, New York, NY, 2001).

93. O. Ambacher, B. Foutz, J. Smart, J. R. Shealy, N. G. Weimann *et al.*, Two dimensional electron gases induced by spontaneous and piezoelectric polarization in undoped and doped AlGaN/GaN heterostructures. *J. App. Phys.* **87**, 334-344 (2000).

94. L. Shen, R. Coffie, D. Buttari, S. Heikman, A. Chakraborty *et al.*, High-power polarization-engineered GaN/AlGaN/GaN HEMTs without surface passivation. *Electron Device Letters, IEEE* **25**, 7-9 (2004).

95. C. Yong, Z. Yugang, K. M. Lau, K. J. Chen, Control of Threshold Voltage of AlGaN/GaN HEMTs by Fluoride-Based Plasma Treatment: From depletion mode to enhancement mode. *IEEE Trans. Electron Devices* **53**, 2207-2215 (2006).

96. S. Guha, V. K. Paruchuri, M. Copel, V. Narayanan, Y. Y. Wang *et al.*, Examination of flatband and threshold voltage tuning of HfO[sub 2]/TiN field effect transistors by dielectric cap layers. *Appl. Phys. Lett.* **90**, 092902-092903 (2007).

97. C. R. Brundle, C. A. Evans, S. Wilson, *Encyclopedia of materials characterization : surfaces, interfaces, thin films. Chapter V Electron Emission*

Spectroscopies., (Butterworth-Heinemann ; Manning, Boston; Greenwich, CT, 1992).

98. S. W. King, J. P. Barnak, M. D. Bremser, K. M. Tracy, C. Ronning *et al.*, Cleaning of AlN and GaN surfaces. *Journal of Applied Physics* **84**, 5248-5260 (1998).

99. T. Paskova, D. A. Hanser, K. R. Evans, GaN Substrates for III-Nitride Devices. *Proceedings of the IEEE* **98**, 1324-1338 (2010).

100. Q. Z. Liu, S. S. Lau, A review of the metal–GaN contact technology. *Solid-State Electronics* **42**, 677-691 (1998).

101. NIST-XPS-Team. (National Institute of Standards and Technology, Gaithersburg, 2003).

102. N. V. Nguyen, O. A. Kirillov, W. Jiang, W. Wang, J. S. Suehle *et al.*, Band offsets of atomic-layer-deposited Al[sub 2]O[sub 3] on GaAs and the effects of surface treatment. *Applied Physics Letters* **93**, 82105-82103 (2008).

103. S. D. Wolter, J. M. DeLucca, S. E. Mohney, R. S. Kern, C. P. Kuo, An investigation into the early stages of oxide growth on gallium nitride. *Thin Solid Films* **371**, 153-160 (2000).

104. T. Takeuchi, H. Ishikawa, N. Takeuchi, Y. Horikoshi, High resolution X-ray photoelectron spectroscopy of beta gallium oxide films deposited by ultra high vacuum radio frequency magnetron sputtering. *Thin Solid Films* **516**, 4593-4597 (2008).

105. E. G. Villora, K. Shimamura, T. Ujiie, K. Aoki, Electrical conductivity and lattice expansion of beta-Ga[sub 2]O[sub 3] below room temperature. *Applied Physics Letters* **92**, 202118-202113 (2008).

106. S. F. Matar, G. Campet, M. A. Subramanian, Electronic properties of oxides: Chemical and theoretical approaches. *Progress in Solid State Chemistry* **39**, 70-95 (2011).

107. H. Nienhaus, M. Schneider, S. P. Grabowski, W. Mönch, R. Dimitrov *et al.*, Ionization energy and electron affinity of clean and oxidized AlxGa1−xN(0001) surfaces. *MRS Proc.* **680E**, E4.5 (2001).

108. M. A. Garcia, S. D. Wolter, T.-H. Kim, S. Choi, J. Baier *et al.*, Surface oxide relationships to band bending in GaN. *Applied Physics Letters* **88**, 013506-013503 (2006).

109. P. Kroll, R. Dronskowski, M. Martin, Formation of spinel-type gallium oxynitrides: A density-functional study of binary and ternary phases in the system Ga-O-N. *Journal of Materials Chemistry* **15**, 3296-3302 (2005).

110. X. Cailleaux, M. d. C. M. d. Lucas, O. Merdrignac-Conanec, F. Tessier, K. Nagasaka *et al.*, Structural study of gallium oxynitrides prepared by ammonolysis of different oxide precursors. *Journal of Physics D: Applied Physics* **52**, 045408-045406 (2009).

111. A. Koudymov, H. Xuhong, K. Simin, G. Simin, M. Ali *et al.*, Low-loss high power RF switching using multifinger AlGaN/GaN MOSHFETs. *IEEE Electron Device Lett.* **23**, 449-451 (2002).

112. M. Giovanni, Alloy nanoclusters in dielectric matrix. *Nucl. Instrum. Methods Phys. Res., Sect. B* **191**, 323-332 (2002).

113. C. Winter, J. Kashammer, S. Mittler-Neher, R. A. Fischer, A new pathway to GaN: Deposition of GaN-clusters on functionalized thiol-SAMs on gold. *Opt. Mater.* **9**, 352-355 (1998).

114. C. Bungaro, K. Rapcewicz, J. Bernholc, Ab initio phonon dispersions of wurtzite AlN, GaN, and InN. *Phys. Rev. B* **61**, 6720 - 6725 (2000).

115. J. Nord, K. Albe, P. Erhart, K. Nordlund, Modelling of compound semiconductors: analytical bond-order potential for gallium, nitrogen and gallium nitride. *J. Phys. Condens. Matter* **15**, 5649-5662 (2003).

116. J. Fritsch, O. F. Sankey, K. E. Schmidt, J. B. Page, Ab initio calculation of the stoichiometry and structure of the (0001) surfaces of GaN and AlN. *Phys. Rev. B* **57**, 15360 - 15371 (1998).

117. K. Karch, J. M. Wagner, F. Bechstedt, Ab initio study of structural, dielectric, and dynamical properties of GaN. *Phys. Rev. B* **57**, 7043 - 7049 (1998).

118. A. Costales, R. Pandey, Density functional calculations of small anionic clusters of Group III nitrides. *J. Phys. Chem. A* **107**, 191-197 (2002).

119. B. Song, C.-H. Yao, P.-l. Cao, Density-functional study of structural and electronic properties of Ga_nN (n=1-19) clusters. *Phys. Rev. B* **74**, 035306-035308 (2006).

120. J. Zhao, B. Wang, X. Zhou, X. Chen, W. Lu, Structure and electronic properties of medium-sized Ga_nN_n clusters (n = 4-12). *Chem. Phys. Lett.* **422**, 170-173 (2006).

121. E. C. Perez-Angel, J. M. Seminario, Ab initio analysis and harmonic force fields of Gallium Nitride nanoclusters. *J. Phys. Chem. C* **115**, 6467-6477 (2011).

122. Y. Hua-Gen, An optimal density functional theory method for GaN and ZnO. *Chem. Phys. Lett.* **512**, 231-236 (2011).

123. B. Brena, L. O am e, Surface effects and quantum confinement in nanosized GaN clusters: Theoretical predictions. *J. Phys. Chem. C* **112**, 13516-13523 (2008).

124. C.-L. Hu, J.-Q. Li, Y.-F. Zhang, X.-L. Hu, N.-X. Lu *et al.*, A DFT study of O2 adsorption on periodic GaN (0001) and surfaces. *Chem. Phys. Lett.* **424**, 273-278 (2006).

125. L. Nai-Xia, L. Jun-Qian, X. Yi-Jun, C. Wen-Kai, Z. Yong-Fan, Theoretical study of O2 adsorption on GaN surfaces. *J. Mol. Struct. THEOCHEM* **668**, 51-55 (2004).

126. T. K. Zywietz, J. Neugebauer, M. Scheffler, The adsorption of oxygen at GaN surfaces. *Appl. Phys. Lett.* **74**, 1695-1697 (1999).

127. C.-L. Hu, Y. Chen, J.-Q. Li, First-principles calculations of H2O adsorption reaction on the GaN(0001) surface. *Chinese J. Struct. Chem.* **28**, 240 - 244 (2009).

128. J. P. Perdew, J. A. Chevary, S. H. Vosko, K. A. Jackson, M. R. Pederson *et al.*, Atoms, Molecules, Solids, and Surfaces - Applications of the Generalized Gradient Approximation for Exchange and Correlation (Vol 46, Pg 6671, 1992). *Phys. Rev. B* **48**, 4978-4978 (1993).

129. J. P. Perdew, K. Burke, Y. Wang, Generalized gradient approximation for the exchange-correlation hole of a many-electron system. *Phys. Rev. B* **54**, 16533 - 16539 (1996).

130. J. P. Perdew, *Electronic Structure of Solids. Chapter: Unified Theory of Exchange and Correlation beyond the Local Density Approximation*. P. Ziesche, H. Eschrig, Eds., (Akademie Verlag, Berlin, 1991).

131. P. J. Hay, W. R. Wadt, Ab initio effective core potentials for molecular calculations - potentials for the transition-metal atoms Sc to Hg *J. Chem. Phys.* **82** 270-283 (1985).

132. W. R. Wadt, P. J. Hay, Ab initio effective core potentials for molecular calculations - potentials for main group elements Na to Bi *J. Chem. Phys.* **82** 284-298 (1985).

133. P. J. Hay, W. R. Wadt, Ab initio effective core potentials for molecular calculations - potentials for K to Au including the outermost core orbitals *J. Chem. Phys.* **82** 299-310 (1985).

134. K. Burke, Perdew, J. P., Wang, Y., *Electronic Density Functional Theory: Recent Progress and New Directions*. G. V. Ed. J. F. Dobson, and M. P. Das, Ed., Electronic Density Functional Theory: Recent Progress and New Directions (Plenum, New York, NY, 1998).

135. C. C. J. Roothaan, New Developments in Molecular Orbital Theory. *Rev. Mod. Phys.* **23**, 69-89 (1951).

136. J. A. Pople, R. K. Nesbet, Self-consistent orbitals for radicals,. *J. Chem. Phys.* **22**, 571 - 572 (1954).

137. R. McWeeny, G. Diercksen, Self-consistent perturbation theory. II. Extension to open shells. *J. Chem. Phys.* **49**, 4852-4856 (1968).

138. G. I. C r denas- ir n, P . Leon-Plata, D. Cortes-Arriagada, J. M. Seminario, Electrical characteristics of cobalt phthalocyanine complexes adsorbed on graphene. *J. Phys. Chem. C* **115**, 16052-16062 (2011).

139. Y. Liuming, J. B. Eddy, M. S. Jorge, Ab initio analysis of electron currents through benzene, naphthalene, and anthracene nanojunctions. *Nanotechnology* **18**, 485701-485708 (2007).

140. M.-L. Fu, N. Rangel, R. Adams, J. Seminario, Synthesis, crystal structure, photophysical properties, and DFT calculations of a Bis(tetrathia-calix[4]arene) Tetracadmium complex. *Journal of Cluster Science* **21**, 867-878 (2010).

141. C. Peng, P. Y. Ayala, H. B. Schlegel, M. J. Frisch, Using redundant internal coordinates to optimize equilibrium geometries and transition states. *J. Comp. Chem.* **17**, 49 - 56 (1996).

142. X. Li, M. J. Frisch, Energy-represented DIIS within a hybrid geometry optimization method. *J. Chem. Theory Comput.* **2**, 835 - 839 (2006).

143. M. J. Frisch, G. W. Trucks, H. B. Schlegel, G. E. Scuseria, M. A. Robb *et al.*, W. CT, Ed. (Gaussian, Inc., 2009).

144. P. Ruterana, M. Albrecht, J. Neugebauer, *Nitride Semiconductors Handbook on Materials and Devices. Chapter VI Surface Structure and Adatom Kinetics of Group-III nitrides.*, (Wiley-VCH GmbH & Co. KGaA, Federal Republic of Germany, ed. 1, 2003).

145. O. Ambacher, Growth and applications of Group III-nitrides. *J. Phys. D: Appl. Phys.* **31**, 2653 - 2710 (1998).

146. S. Gowtham, M. Deshpande, A. Costales, R. Pandey, Structural, energetic, electronic, bonding, and vibrational properties of Ga3O, Ga3O2, Ga3O3, Ga2O3, and GaO3 clusters. *J. Phys. Chem. B* **109**, 14836-14844 (2005).

147. J. P. Perdew, Y. Wang, Accurate and simple analytic representation of the electron-gas correlation energy. *Phys. Rev. B* **45**, 13244 - 13249 (1992).

148. Y. Xu, C. B. Musgrave, A DFT Study of the Al2O3 Atomic Layer Deposition on SAMs: Effect of SAM termination. *Chemistry of Materials* **16**, 646-653 (2004).

149. A. Stierle, F. Renner, R. Streitel, H. Dosch, W. Drube *et al.*, X-ray Diffraction Study of the Ultrathin Al2O3 Layer on NiAl(110). *Science* **303**, 1652-1656 (2004).

150. J. Ren, Y.-T. Zhang, D. W. Zhang, Density functional theory study of initial stage of HfO2 atomic layer deposition on hydroxylated SiO2 surface. *Journal of Molecular Structure: THEOCHEM* **803**, 23-28 (2007).

151. J. Robertson, P. W. Peacock, *Materials Fundamentals of Gate Dielectrics. Chapter V: Atomic Structure, Interfaces and Defects of High Dielectric Constant*

Gate Oxides. A. A. Demkov, A. Navrotsky, Eds., (Springer, Dordrecht, Netherlands, 2005).

VITA

Mary Rachel Coan received her Bachelor of Science in Chemical Engineering from the University of Rochester in Rochester, New York in May 2007. She entered the Chemical Engineering program at Texas A&M University in September 2007 and received her Doctor of Philosophy degree in August 2012. Her research interests include microelectronics, nanotechnology, III-V materials, heterostructures and device fabrication.

Her email address is mcoan2@gmail.com and she may be reached at either the Harris Integrated Photonic and Electronics Laboratory at Texas A&M University, at the following address:

c/o Dr. H. Rusty Harris
Department of Electrical and Computer Engineering
Texas A&M University
TAMU 3128
College Station, TX 77843-3122
Rusty. Harris@tamu.edu

Or at the Molecular Engineering Group at Texas A&M University, at the following address:

c/o Dr. Jorge M. Seminario
Department of Chemical Engineering
Texas A&M University
TAMU 3122
College Station, TX 77843-3122
seminario@tamu.edu